Investigations of Low- and Equatorial-Latitude Upper Atmospheric Processes using Optical and Radio Techniques

A thesis submitted in partial fulfilment of the requirements
for the degree of

Doctor of Philosophy

by

Sovan Saha
(Roll No. 17330031)

Under the guidance of

Prof. Duggirala Pallamraju
Space and Atmospheric Sciences Division
Physical Research Laboratory, Ahmedabad, India

Discipline of Physics
Indian Institute of Technology Gandhinagar, India
2022

Dedicated to my parents

Declaration

I, Sovan Saha, declare that this written submission represents my ideas in my own words, and where others' ideas or words have been included, I have adequately cited and referenced the original sources. I also declare that I have adhered to all principles of academic honesty and integrity and have not misrepresented or fabricated or falsified any idea/data/fact/source in my submission. I understand that any violation of the above can cause disciplinary action by the Institute and can also evoke penal action from the sources which have thus not been properly cited or from whom proper permission has not been taken when needed.

Sovan Saha
(Roll no. 17330031)

Date: 08 August 2022

Certificate

It is certified that the work contained in the thesis entitled ***"Investigations of Low- and Equatorial-Latitude Upper Atmospheric Processes using Optical and Radio Techniques"*** by Mr. Sovan Saha (Roll no. 17330031), has been carried out under my supervision and this work has not been submitted elsewhere for any degree or diploma.

(Prof. Duggirala Pallamraju)
Thesis Supervisor
Space and Atmospheric Sciences Division
Physical Research Laboratory
Unit of Department of Space, Government of India
Ahmedabad-380009, Gujarat, India.

Date: 08 August 2022

Acknowledgments

It was a great experience throughout this 5-year of period at PRL. I take this opportunity to acknowledge all of them, without their support and blessings the journey could not be possible.

First and foremost, I express my heartfelt gratitude to my thesis supervisor Prof. Duggirala Pallamraju for his guidance in the completion of this thesis work. I feel myself great fortunate for having a supervisor like him. His vast knowledge in the field of the upper atmosphere, expertise in the instrumentation helped me gain interest and knowledge in this field. His hard-working ability, strong mental strength, calm and compose character always inspired me. His unique way of understanding scientific problems, valuable suggestions, and ideas always kept me motivated in the research work. Apart from that, the Diwali sweets, the tasty foods at his home were filled with love and affection. I also thank Bhuvaneswari ma'am for providing me the homely atmosphere and the delicious food at her home.

I express my sincere gratitude to my Doctoral Studies Committee (DSC) members, Prof. D. Chakrabarty, Dr. A. Guharay, Prof. S. Ganesh for their constant support, critical questions, comments which helped me to improve my understanding the concept in the subject. I was greatly benefitted from the interactions and discussions with them. I also thank the members of academic review committee of PRL for their comments and suggestions which also helped me groom my research career.

I am grateful to (late) Dr. B. V. Krishnamurthy for his appreciation on the results where we have used the relative variations of meridional winds at low-latitudes as estimated using digisondes. Even he encouraged to extend this work to get the latitudinal behaviour of winds.

I am obliged to the Department of Space, Government of India, for the research grant offered during my tenure at PRL. I acknowledge Dr. Anil Bhardwaj, Director of PRL, for his support regarding the reimbursement of registration fees for various conferences and other guidance. I also thank Prof. P. Janardhan, former Dean; Prof. D. Pallamraju, present Dean, Mr. Deekshitulu, former Registrar for providing the necessary facilities which helped me to carry out my research work. I express my gratitude to Prof. R. D. Deshpande for his incredibly kind behaviour to me. I thank to Nishtha Ma'am and other staff in the library for managing library, processing the book grants, organizing book fairs, and managing journal subscriptions. I express my sincere thanks to Dr. Bhushit Vaishnav, head of academics, for his support in academic related matters. I also thank the computer centre of PRL for providing excellent internet facility, and software support. I thank all the faculty members of PRL for providing an overall research atmosphere here in PRL. I also thank the administration, canteen, accounts, dispensary, CMG, and purchase section of PRL for providing facilities in various aspects. I also thank the academic and administrative personnel of IITGn for providing various resources and processing the official formalities in a very smooth way.

I would like to acknowledge Jawaharlal Nehru Technological University, Hyderabad (JNTUH) for the logistic support during the field trip to JNTUH. I also thank all the staff of

PRL at Mt. Abu campus for providing me nice stay during the field trip there. I am grateful to Space Physics Laboratory, Thiruvananthapuram and Indian Institute of Geomagnetism, Navi Mumbai, for providing me the digisonde and magnetometer data, respectively. I am thankful to Dr. Tarun K. Pant for providing the digisonde data of Trivandum. I also express my gratitude to Dr. Rupesh Ghodpage for providing me the all-sky imager data from Kolhapur. I also thank several others for providing the datasets in open sources.

I am really grateful to the colleagues of the Space and Atmospheric Sciences division Prof. S. Ramachandran, Prof. L. Sahu, Prof. S. Sharma, Dr. H. Gadhvi, Dr. N. Ojha, Dr. R. P. Singh, Dr. T. A. Rajesh, Dr. K. Venkatesh, Mr. S. Venkataramani, Mr. A. Manke, Mr. M. Bhavsar, Mr. T. K. S. Kumar, Mr. Malaidevan, Ms. Sourita, Dr. Tanzil, Dr. Sumanjit, Dr. Subarna, Sneha di, Anil, Aditya, Rahul, Vishnu, Jacob, Abhishek for providing me such a nice working ambiance. I am blessed to have seniors like Kuldeep, Sandeep, Avik, Dipti, Fazlul in this division. I thank Ankit for the scientific discussions and various enjoying moments. I enjoyed interacting with the juniors Yogesh, Bijoy, Gaurav, Kamran, Dharmendra, Meghna, Kiran, Haritha at different division activities. Participation in drama, winning tournaments like football (2019), volleyball (2022), and table tennis (2022) are some unforgettable moments. I thank all my teammates for making this possible.

I am thankful to my colleagues in the Optical Aeronomy group for providing such a friendly atmosphere. I have spent a wonderful time with them playing table tennis, adda, weekend cooking, having lunch and dinner outside, Diu trip, etc. I am really thankful to Subir, Pradip, Shashank, Pankaj, Sunil, Chithra, Mohit, Kshitiz for providing such wonderful moments. I thank my seniors Deepak and Subir for their support and suggestions. It was a big strength for me to have Subir da at my side. Scientific discussions with my seniors (Deepak and Subir) and juniors (Sunil and Kshitiz) always helped me to improve my understanding of the subject. I am thankful to Dupinder, Narayan for their help and suggestions at different point of time whenever it was required.

I convey my heartfelt thanks to the friends of my batchmates Ramanuj, Sudipta, Pravin. It was an overwhelming experience staying with them. I thank Sarika, Satyajeet, Upamanyu for the wonderful times spent with them as well. I also thank my other batchmates Aravind, Tanmay, Amit, Ankit, Vishal, Atif, Milan, Deepak, Vipin, Biswajit, Ritu, Shivani, Hrushi, Anshika, Abhay, Shanwlee, Subith, Partha, Sushant, Himanshu, Madhu, Sana, Neeraj, and Alka for providing memorable moments at various occasions.

I have met wonderful seniors like, Anirban da, Manu, Ikshu di, Venki, Niharika di, Avdesh, Soumik da, Ashish, Bhavesh, Anil, Naman in the Navrangpura hostel. Those were some precious moments playing Volleyball, Football, Cricket, table tennis at the hostel premises, adda at the canteen table, celebrating festivals, etc., I will never forget. I can recall those priceless times spent with Anirban da. We (me, Ramanuj, Sudipta, Tanmay, Anirban da) used to roam at midnight, and had tea outside. His knowledge in vast areas has always fascinated me. We were just listeners in front of him. I thank Ashim da who has helped me in many ways. I will always be grateful to him. It was sorrowful moments saying adieu *when they left PRL. I express my sincere thanks to my dear juniors Yogesh, Arijit, Sidharth, Deva, Supriya, Kshitiz, Bijoy, Gourav, Sourabh, Bharti, Debashish, Kamran, Dharmendra, Guru, in the hostel for making my hostel life so lively.*

I thank Subir da, Suman da for preparing delicious lunches during weekends. I remember those times walking with Suman da, Subir da, and Yogesh after dinner. I really miss those days.

I cherish the time playing football which acted as a refreshing agent for me. I thank Gautam Sir, R P Sir, Sachindra Sir, Lokesh Sir, Arvind Sir, Manu, Zabir, Ali, Bivin, Venki, Sabir, Varun, Subir, Aravind, Kaustav, Soumya, Rishi, Deepak, Anil, Chandan, Kalyan, Yatharth, Sunaram and many more inside and outside of PRL for being part of the football matches.

I express my heartfelt thanks to my friends, Dibyendu, Pritam, Aniruddha, Arpan, Protin, Riaz, Souvik, Shubham, Sayan, and Sucheta for their constant love and support.

My deepest gratitude to Swapan Samanta Sir, who developed love for physics inside me during school time. I sincerely thank my math teacher Ashoke Sir. I thank my teachers during college periods, Sanoar da, U N Nandi Sir, Sanghamitra ma'am, Mitali ma'am, Swati ma'am for their excellent teaching. I thank Prof. Somendra Mohan Bhattacharjee, Prof. Partha Sarathi Majumdar, Dr. Abhijit Bandyopadhyay, Dr. Bobby Ezhuthachan, Prof. Debashish Gangopadhyay for their courses during my M.Sc. period. Even I was greatly benefitted and motivated in the subject of physics from the lectures of Prof. Walter Lewin, Prof. V. Balakrishnan, Prof. Ajay Ghatak, Prof. H C Verma, Prof. R Shankar available at online platform.

The journey would have been incomplete without the constant support and blessings from Ma-baba. Staying away from home was the most difficult part. I am indebted forever to them. I am thankful to my sister, cousin sisters and brothers (Mona, Tunu, Indira di, Lily, bhai, Alu) for providing me with such a wonderful childhood, and extending their affection and support till today. I thank Ashok da, boudi, mama-mami, jethu-jethi, pisi for their endless love and affection. I thank Radhashree (Mon) for tolerating me on various occasions. I also thank Mamoni for the love and affection, she extended to me.

Sovan Saha

Abstract

The ionosphere-thermosphere regions of the upper atmosphere consist of plasma and neutrals, which are intercoupled with each other, often referred to as the ionosphere-thermosphere system (ITS). Different electrodynamic processes, such as equatorial electrojet (EEJ), equatorial ionization anomaly (EIA), pre-reversal enhancement (PRE) in zonal electric field, and neutral dynamics play important roles in the distribution of plasma and neutrals over the equatorial and low-latitudinal regions. As a consequence, the magnitudes of the plasma and neutral densities, electric fields, and neutral winds get altered. Further, on occasions, plasma irregularities get generated over the magnetic equator due to the onset of Rayleigh-Taylor (R-T) instability which can span scale sizes of around seven orders of magnitudes and extend to the low-latitudes and beyond. These plasma irregularities adversely affect the radio wave communications at different frequencies. A comprehensive understanding is required on all these variations in plasma-neutral dynamics, in order to gain not only fundamental understanding of ITS science, but also aspects related to applications.

Therefore, systematic observations and accurate measurements of different parameters are needed for a critical understanding of the upper atmospheric processes. Optical, radio, and magnetic techniques have been used in this work to infer the intricate behaviour of the ITS. In this thesis, the OI 630.0 nm nightglow emissions (red line), which serve as tracers to the behaviour in the ITS, are used as the primary data. High Throughput Imaging Echelle Spectrograph (HiTIES) is used to measure the red line emissions at Mt. Abu, a low-latitudinal location over Indian longitude, typically situated under the crest of the EIA during high-solar activity periods. Data from digisonde and the magnetometer are also used to carry out a comprehensive study of the various dynamical processes which occur in the upper atmosphere.

The peak emissions of OI 630.0 nm nightglow emanate from around 250 km and

provide information of the upper atmospheric dynamics prevalent, essentially in the bottomside of F-region. Dissociative recombination of molecular oxygen with the thermal electrons is responsible for the nighttime red line emissions. A photo-chemical model has been generated to estimate the OI 630.0 nm nightglow emissions wherein the digisonde measured electron densities are used as an input. The red line emissions primarily depend on the densities of electron, O^+, and O_2^+ present at these altitudinal regions. Therefore, the variabilities in the OI 630.0 nm emissions provide information on the subtle changes occurring at those altitudes. Different kinds of variabilities have been observed in the OI 630.0 nm nightglow emissions from this location which fall in four broad types. The causes of such variabilities have been addressed rigorously and the new understanding of the systemic behaviour that has emerged is reported in this thesis.

Investigation into the effect of equatorial electrodynamics on the latitudinal movement of the EIA crest has shown that, on several occasions, airglow emissions are larger along the northern direction after sunset compared to the southern direction. This is due to the movement of the EIA crest in response to the PRE. As the night progresses, the plasma motion changes towards the magnetic equator, which is known as reversal of the EIA. The speeds of this reversal range from 10 to 55 ms^{-1} and are caused by the nocturnal equatorial westward electric fields. In the absence of information on the nighttime electric fields over the Indian longitudes, we use the simultaneous variations in the daytime EEJ data from an opposite longitude sector and compared them with the measured nighttime reversal speeds. We show that these two are consistent, as the global equatorial electric fields follow the curl-free condition ($\nabla \times \mathbf{E} = 0$). An experimental evidence has been shown of the variation in the nighttime reversal speeds of the EIA in relation with the nighttime equatorial electric field. As a result of this information, it is proposed that the observed reversal speeds (equatorward movement) of the EIA crest can serve as a viable proxy to determine the behaviour of the nightly westward electric fields which are otherwise extremely difficult to obtain.

The OI 630.0 nm nightglow emission decreases monotonically with a decrease in the ionization after sunset. But, on several occasions, a bell-shaped enhancement in the OI 630.0 nm nightglow emissions were observed over Mt. Abu during post-sunset hours. The role of equatorial electrodynamics and meridional winds have been investigated to understand the plausible cause for such enhancements and found that the presence of poleward meridional winds or the cessation of equatorward winds over the low-latitudes can effectively account for the observed post-sunset emission enhancements. This effect of meridional winds on the thermospheric airglow emissions during the post-sunset time is a new finding, as it shows a consistent decrease in magnitude during Jan-Mar as predicted by climatological model winds in HWM-14. The OI 630.0 nm emission data considered was for the years 2013, 2014, and 2016 with varying solar activity, which asserts that the results arrived at are independent of the solar flux variation.

Multiple excursions in OI 630.0 nm nightglow emissions are seen over Mt. Abu. The presence of equatorial plasma bubbles simultaneously, as seen in the ionosonde data over Ahmedabad and the depletion in OI 630.0 nm emissions over Kolhapur, is further evidence of their influence. The strength of the PRE was found to be larger on the nights when the depletions in emissions were observed in the OI 630.0 nm emission over Mt. Abu. The zonal speeds of the plasma bubbles were found to vary from around 190 to 90 ms^{-1} over the night. The wave number spectral analyses for the emissions in the zonal direction using data from around 1300 images show that the scale sizes in the range of 250-300 km are omnipresent, whereas shorter scale sizes (50-250 km) are observed only during the presence of EPBs. It is inferred that these shorter scale size gravity waves played a significant role as the seed perturbations to trigger the R-T instability which is an interesting and important result in terms of understanding the generation of EPBs.

Contents

List of Tables

List of Figures

List of Abbreviations

AE	Atmospheric Explorer
CEJ	Counter electrojet
CHAMP	Challenging minisatellite payload
DE	Dynamic Explorer
EEJ	Equatorial electrojet
EIA	Equatorial ionization anomaly
EPB	Equatorial plasma bubble
ESF	Equatorial spread-F
ETWA	Equatorial temperature and wind anomaly
EUV	Extreme ultra-violet
FAL	False alarm limit
FPI	Fabry-Perot Interferometer
FOV	Field-of-view
GPS	Global Positioning System
GOLD	Global-scale Observations of the Limb and Disk
GW	Gravity wave
HIRISE	High Resolution Imaging Spectrograph using Echelle grating
HiTIES	High throughput Imaging Echelle Spectrograph
HWM	Horizontal wind model
ICON	Ionospheric Connection Explorer
ISR	Incoherent scatter radar

ITS	Ionosphere-thermosphere system
LT	Local time
MISE	Multiwavelength Imaging Echelle Spectrograph
MTM	Midnight Temperature Maximum
NIRIS	Near-Infrared Imaging Spectrograph
OGO	Orbiting geophysical observatory
PRE	Pre-reversal enhancement
PSD	Power spectral density
RADAR	Radio Detection and Ranging
RTI	Rayleigh-Taylor instability
Sq	Solar quiet
TIMED	Thermosphere Ionosphere Mesosphere Energetics and Dynamics
UA	Upper atmosphere
UARS	Upper Atmosphere Research Satellite
UVIS	ultraviolet imaging spectrograph
WATS	Wind and Temperature spectrometer

Chapter 1

Introduction

1.1 The structure of Atmosphere

The atmosphere of the Earth can be divided into three different regions, namely, lower atmosphere (up to 12-15 km from the surface), middle atmosphere (15-90 km), and upper atmosphere (above 90 km). The variation in temperature with altitude is not uniform. Depending on the gradient of temperature, the atmosphere of the Earth is divided into troposphere (0-15 km), stratosphere (15-50 km), mesosphere (50-90 km), and thermosphere (90-600 km) which is shown in figure 1.1a. The solar radiation in the range of around visible to near-infrared range falls on the surface and radiates the larger wavelength in the range of infrared radiation which keeps the region near the Earth's surface warm. The temperature drops at the rate of around 6.5 K km^{-1} with the increase in altitude. This negative temperature gradient continues up to tropopause heights which vary from 8-17 km from polar to equatorial latitudes. Due to the absorption of solar UV-B radiation (around 200-360 nm), the temperature increases with altitudes in the stratosphere region. This increase in temperature is majorly caused by the absorption of solar UV radiation by ozone, with small contribution from the photo-dissociation of molecular oxygen. This region of atmosphere is very stable due to the positive temperature gradient. Such kind of positive temperature gradient is seen up to around 50 km which is called stratopause. Above stratopause, the temperature gradient again becomes negative. Radiative cooling by CO_2 is responsible for the decrease in temperature. The sources of small amount of heating are the absorption of solar UV radiation by ozone, molecular oxygen, and down-

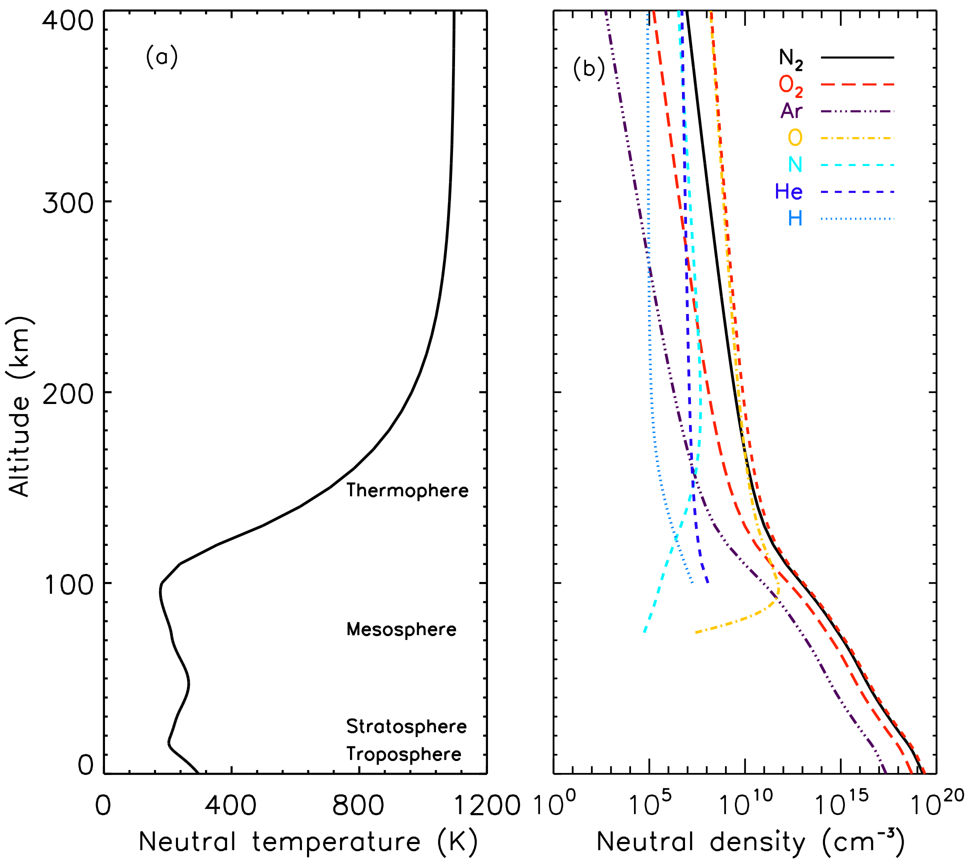

Figure 1.1: (a) Structure of atmosphere based on the neutral temperature which varies with altitudes. (b) Distribution of various neutral species in the atmosphere of Earth (based on NRLMSISE-00 outputs).

ward eddy transport from the thermosphere to the mesosphere. The mesopause region exists at an altitude of around 90 km which is the coldest region of the Earth's atmosphere. Above that altitude, due to the absorption of energetic solar photons of mostly EUV and X-rays with the neutral species that are present at that altitude, the temperature increases with altitudes sharply from 200K to around 1000K as shown in figure 1.1a. This region is called thermosphere (*Hargreaves*, 1992). The vertical propagation of atmospheric waves that deposits energy in the thermosphere through wave braking and precipitation of energetic charge particles in the high latitudes during geomagnetic disturbed events are some other sources which contribute to the total energy budget of the thermosphere. The region above the thermosphere (beyond 600 km) is called the exosphere. The density of this region is so low that the mean free path of the constituents like H and O exceeds the scale heights.

The mixing ratios of the major constituents are same in the atmosphere below 100 km. Therefore, this region is called homosphere. The homosphere consists of 78.1% Nitrogen, 20.9% Oxygen, 0.9% Argon, and some other trace gases, such as, CO_2, Ne, He, H_20, etc. (figure 1.1b). The region above 100 km is known as the heterosphere, where the constituents are distributed under gravity. Therefore, the composition varies with altitudes according to their molecular/atomic mass. The boundary between homosphere and heterosphere is called turbopause. Above the turbopause, the gaseous diffusion is more dominant than the mixing due to turbulence. We can see from figure 1.1b that the density of atomic oxygen becomes equal to the density of the Oxygen molecules around 110 km altitude. Above 200 km, the atomic oxygen dominates as compared to O_2 and N_2. The exosphere is dominated by helium and hydrogen.

The incoming solar radiations of different wavelengths, such as UV, EUV, and X-rays are absorbed in different altitudes of the upper atmosphere, which ionize the neutrals and form the ionosphere. The ionosphere can be extended from 60 km to 1000 km. The electron density varies from day to night, as well as, with the changes in the solar activity as shown in figure 1.2. The solar activity is defined by sunspot number which shows good correlation with the variation in the F10.7 cm solar flux. The whole ionosphere is divided into three regions: D region (60 km- 90 km), E region (90 km- 150 km), and F region (>150 km). During daytime, a ledge can be seen in the F-region and forms two layers, named F_1 and F_2 layers. It is predominantly observed in summer at low solar activity period. It has not been reported during winters at high solar activity periods. Depending upon the location, time, season, solar activity, etc., the electron density varies in the ionosphere. Although ions and electrons are present in the ionosphere, the neutral densities are always larger by three orders more than the plasma density.

The presence of electric and magnetic fields affects the motion of the charged particles in the ionosphere. Due to large neutral density present in the lower ionosphere, the ions and electrons are collision dependent in the D-region, i.e., collision frequencies with neutrals (ν_{in}, ν_{en}) are larger than their respective gyro-frequencies (ω_i, ω_e) for both ions and electrons ($\nu_{in} >> \omega_i$, $\nu_{en} >> \omega_e$). Whereas, in the F-region, gyro-frequencies dominate as compared to the collision frequencies of ions and electrons with the neutrals ($\nu_{in} < \omega_i$, $\nu_{en} << \omega_e$). However, ions and electrons show different behaviour in the ionospheric E-region ($\nu_{in} > \omega_i$, $\nu_{en} < \omega_e$). Being larger in dimension and, thereby larger collision cross-section, the motion of the ions is controlled by the neutral winds in the E-region.

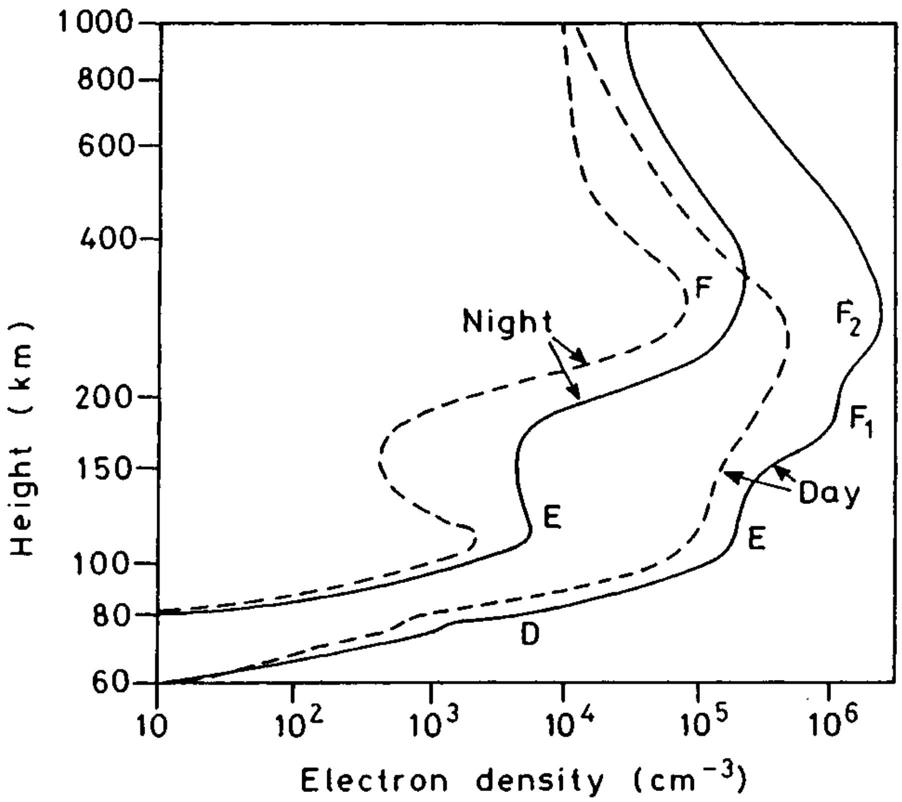

Figure 1.2: The variation of electron density with altitudes and different ionospheric layers during day and night time at high and low solar flux condition. (After *Hargreaves*, 1992)

The opposite behaviour is seen for the electrons, and they follow the electromagnetic forces.

The lower most part of the ionosphere is the D-region which extends from 60 to 90 km with electron density around 10^2-10^2 cm^{-3}. The major ions are NO^+, $O_2{}^+$, $N_2{}^+$ in this region (*Nicolet*, 1965; *Barth*, 1966; *Sechrist Jr*, 1967; *Narcisi and Bailey*, 1965). The main ionizing sources of this region are the Lyman-α, EUV, X-rays, and cosmic rays. The Lyman-α line of wavelength 121.5 nm ionizes the trace element NO, whereas, the EUV (102.7-111.8 nm) dissociates O_2 and N_2. Hard X-rays (0.2-0.8 nm) can ionize all the elements, mostly O_2 and N_2, as these are major constituents. The galactic cosmic rays are another important source of ionization of the ionospheric D-region. Ionization by the cosmic rays is efficient at this lower ionosphere as there are larger amount of neutral densities are present. During nighttime, as the ionization is absent and large neutral density is present, the charged particles recombine very quickly and the D-layer disappears.

The ionospheric E-region peaks around 105-110 km. After the discovery of radio wave transmission, several scientists, such as Edward Appleton, Arthur Kennelly, Oliver Heaviside etc. proved the existence of a reflecting layer, 'Kennelly-Heaviside layer', which is later known as E-layer. The E-layer contains ${N_2}^+$, ${O_2}^+$, NO^+, O^+, etc. EUV in the range of 80-102.7 nm ionizes O_2 and the X-rays in the shorter wavelength range (1-10 nm) can ionize all the neutral species in the E-region. The molecular ions undergo dissociative recombination process and produce atoms of higher energy states. Metallic ions such as Fe^+, Mg^+, Ca^+, Si^+ are also present in the E-region which mostly follow the radiative recombination. The daytime to nighttime electron density in the E-region is of the order around 10^5 to 10^3 cm^{-3}.

The primary reactions produce ${N_2}^+$, ${O_2}^+$, O^+, He^+, N^+ in the F-layer, whereas, the subsequent reactions produce an ample number of O^+, ${O_2}^+$, NO^+. The molecular and atomic ions dominate in the lower and upper F-layer, respectively. The electromagnetic radiation which provides the ionization potentials for various species, such as, N_2 (79.6 nm), O (91.1 nm), O_2 (102.7 nm), H (91.2 nm), HeI (58.4 nm), HeII (30.4 nm) are available in the F-layer as the solar spectrum between 17-91.1 nm is heavily absorbed in this region. The maximum ionization should be observed up to 180 km altitude as there is no radiation band that can further ionize any species. But, the F_2-layer peaks at 200-400 km altitude depending on day or nighttime due to the transportation of plasma. The peak electron density at F_2 layer is of the order 10^6 cm^{-3} during the daytime and reduce by one order of magnitude in the nighttime (figure 1.2).

So far, we have discussed the production mechanism for different altitudes in the ionosphere. The charged particles are also lost in different ways, such as dissociative recombination, radiative recombination, three-body recombination, etc. (*Bates and Massey*, 1946, 1947; *Biondi*, 1963). Depending upon different molecular species present at a given altitude, different loss mechanism takes place. At equilibrium conditions,

$$\frac{1}{q} = \frac{1}{\alpha N^2} + \frac{1}{\beta N} \tag{1.1}$$

where, q is the production rate and α, β are the loss rate.

The equation 1.1 satisfies the charge neutrality condition, which is, $N = N_A^+ + N_M^+$; where, N, N_{A^+}, and N_{M^+} are the density of electrons, atomic ions, and molecular ions, respectively. Now, when $N_M^+ >> N_A^+$, $q = \alpha N^2$, which occurs at the lower F-region, where molecular ions are larger in numbers than the atomic ions, and,

When, $N_M^+ << N_A^+$, $q = \beta N$, which occurs at higher altitudes of the F-region where atomic number densities are dominant.

Solving the equation 1.1 for N, we get,

$$N = \frac{q}{2\beta}[1 + \sqrt{1 + \frac{4\beta^2}{\alpha q}}]$$
$$N = \frac{q}{2\beta}[1 + \sqrt{1 + 4G}]$$

where, $G = \frac{\beta^2}{\alpha q}$, which decides the shape of the electron density distribution.

Now, for $4\beta^2 >> \alpha q$, $G >> \frac{1}{4}$: $N = \sqrt{\frac{q}{\alpha}}$, therefore, $q = \alpha N^2$.

$4\beta^2 << \alpha q$, $G << \frac{1}{4}$: $N = \frac{q}{\beta}$, therefore, $q = \beta N$.

The splitting of F-layer takes place around 160-200 km altitude. The loss mechanism, such that, αN^2 and βN, determines the occurrence and transition of F_1 and F_2 layers (*Ratcliffe*, 1956; *Setty*, 1960). If the transition height between α-type and β-type recombination is h_t, F_1 layer appears when $h_t > h_m$, where, h_m is the height of maximum ionization. In another way, value of G can decide the splitting of F-layer. A value of G greater than $\frac{1}{4}$ is required for the formation of F_1 layer. In the summer time, due to larger recombination at upper F-layer (β-type), F_1 layer forms, whereas, the decrease in production is responsible for the generation of F_1 layer in the solar minimum.

1.2 Equatorial/low-latitude processes

The neutrals and charged particles co-exist in the ionosphere-thermosphere system. As we discussed earlier, the production and loss mechanisms control the plasma density in the ionospheric system. The plasma transport also plays an essential role in the varying plasma densities observed over different latitudes. The electric field, magnetic field, and neutral winds affect the dynamics of the plasma and neutrals, and as a consequence, several processes get generated over the equatorial and low-latitude upper atmosphere.

The magnetic field of Earth is generated by various sources. The geodynamo at the core of Earth is the primary source of the geomagnetic field which is called the main

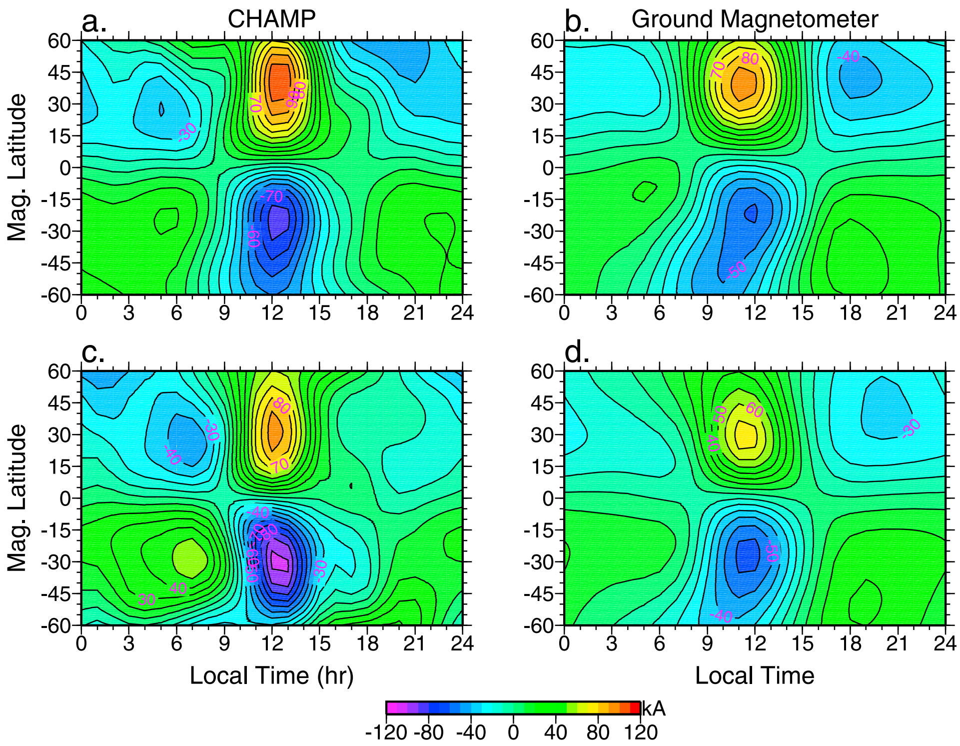

Figure 1.3: Sq current pattern during June solstice in the years of 2006 to 2008 obtained from (a) CHAMP satellite and (b) ground-based measurements. The same is shown in (c) and (d) for the December solstice. (After *Pedatella et al.*, 2011)

field. Other sources of geomagnetic field contribute up to a few percent of the main field. Solar quiet (Sq) current (an ionospheric current system) is one such source which induces magnetic field on the surface of Earth (*Matsushita*, 1968; *Rishbeth and Garriott*, 1969; *Campbell*, 1989). The differential heating by the Sun at different parts of the globe causes temperature and pressure gradient forces which generate neutral wind, and as a consequence, electric current forms. The existence of this global Sq current has been confirmed through rocket experiments (*Yabuzaki and Ogawa*, 1974; *Pfaff Jr et al.*, 1997) and satellite measurements (*Jadhav et al.*, 2002; *Vichare and Rajaram*, 2011; *Pedatella et al.*, 2011; *Alken et al.*, 2015). The magnitude of Sq current is of the order of several $\frac{\mu A}{m^2}$ flow in the dayside of the ionospheric E-layer, in the altitude range of 90-150 km. This region is also referred to as the dynamo region. The direction of the Sq current is opposite in two different hemispheres (counter-clockwise in northern hemisphere and clockwise in southern hemisphere). The ground-based and satellite measurement of Sq current is shown in figure 1.3 which shows the Sq current peaks at local noon time centered in the mid-latitude location.

The flow of charged particles in the ionosphere (ionospheric current) depends on the electrical conductivity of that medium. The ionosphere is anisotropic in nature. The current density equation: $\mathbf{j} = \boldsymbol{\sigma} \cdot \mathbf{E}$, where, $\boldsymbol{\sigma}$ is the electrical conductivity tensor (figure 1.4), which has a form like:

$$\sigma = \begin{pmatrix} \sigma_P & -\sigma_H & 0 \\ \sigma_H & \sigma_P & 0 \\ 0 & 0 & \sigma_\parallel \end{pmatrix}$$

where, $\sigma_\parallel = \sigma_0 = (\frac{n_e e^2}{m_e \nu_e})$ is the direct or parallel conductivity, which governs current along the electric field direction when the electric field is along the magnetic field.

$\sigma_P = (\frac{\nu_e^2}{\nu_e^2+\omega_e^2})\sigma_0$ is the Pedersen conductivity, which governs Pedersen current along the direction parallel to the electric field but perpendicular to the magnetic field.

$\sigma_H = -(\frac{\omega_e \nu_e}{\nu_e^2+\omega_e^2})\sigma_0$ is the Hall conductivity, which determines the Hall current in the direction perpendicular to both the electric field and magnetic field.

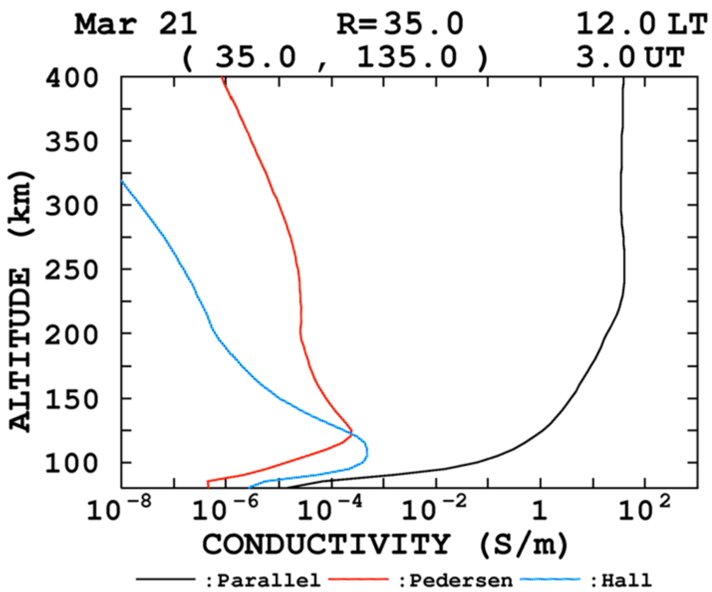

Figure 1.4: The variation of parallel, Pedersen, and Hall conductivities is shown with altitude over a mid-latitude location under noon-time March equinox time. (After *Yamazaki and Maute*, 2017).

1.2.1 Equatorial electrojet (EEJ)

The Sq current flows in the eastward direction over the geomagnetic equator which enhances the magnitude of Sq current density. Due to the geometry and the large conductivities in the ionospheric E-region over the dip-equator, the eastward current enhances in addition to the Sq current, which is known as equatorial electrojet (EEJ) (*Chapman*, 1951; *Forbes*, 1981; *Anandarao and Raghavarao*, 1987). To understand the generation mechanism of such current jet, the ionospheric E-region has been considered as a slab with thickness of 10 km from 100 to 110 km (figure 1.5). As discussed earlier, the electrons follow the electromagnetic forces in the ionospheric E-region, whereas, the ions are controlled by the neutral winds. During daytime, the zonal wind is in the westward direction over the equatorial E-region which carries the ions through ion-neutral collisions. This leads to the charge separation, which generates the primary electric field E_{py} directed in the eastward direction. Therefore, the current density due to this E_{py} is $\sigma_P E_{py}$ in the eastward direction. Due to the horizontal nature of geomagnetic field over the dip-equator and the presence of the eastward electric field, the electrons experience $\mathbf{E} \times \mathbf{B}$ drift over this region which is directed vertically upward. Although the $\mathbf{E} \times \mathbf{B}$ drift is charge and mass independent, the electrons move to higher altitudes in the E-region, but not the ions as their movement is controlled by the ion-neutral collisions. The polarization electric field drives a Hall current in the downward direction (negative sign indicates that the direction of current flow is opposite to the drift of the electrons).

$$-\mathbf{E}_{py} \times \mathbf{B} = -E_{py}B(\hat{\mathbf{y}} \times \hat{\mathbf{x}}) = -E_{py}B(-\hat{\mathbf{z}}) = E_{py}B\hat{\mathbf{z}} \tag{1.2}$$

This causes a charge separation with negative charges accumulating on the top of the E-region boundary and positive charges (ions) at the bottom of highly conducting layer. This space charge distribution creates a secondary electric field (E_{sz}) in the vertically upward ($-z$ direction). This secondary electric field (E_{sz}) drives a vertical Pedersen current opposing to the Hall current until this Pedersen current compensates the Hall current. In

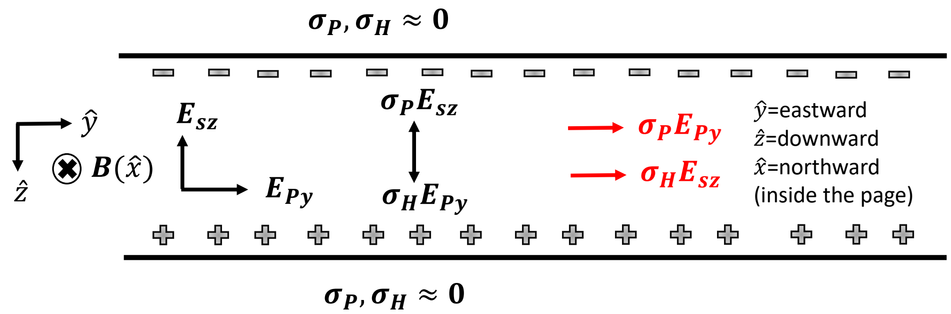

Figure 1.5: Equatorial electrojet model using slab geometry of the ionospheric E-region.

the equilibrium condition, there is no vertical current flow, therefore,

$$\begin{aligned} \sigma_H E_{py} &= \sigma_P E_{sz} \\ E_{sz} &= \frac{\sigma_H}{\sigma_P} E_{py} \end{aligned} \tag{1.3}$$

The secondary polarization electric field (*Anandarao*, 1976; *Pandey et al.*, 2016) generates a secondary Hall current flowing in the y-direction,

$$\begin{aligned} -\mathbf{E}_{sz} \times \mathbf{B} &= -E_{sz}B(-\hat{\mathbf{z}} \times \hat{\mathbf{x}}) = E_{sz}B(\hat{\mathbf{y}}) \\ J_{sy} &= \sigma_H E_{sz} = \frac{\sigma_H^2}{\sigma_P} E_{py} \end{aligned} \tag{1.4}$$

Therefore, the total eastward current ($\hat{y}$ direction) consists sum of primary Pedersen current and secondary Hall current.

$$\begin{aligned} J_y &= \sigma_P E_{py} + \sigma_H E_{sz} \\ &= (\sigma_P + \frac{\sigma_H^2}{\sigma_P}) E_{sz} \\ &= \sigma_P (1 + \frac{\sigma_H^2}{\sigma_P^2}) E_{sz} \\ &= \sigma_c E_{sz} \end{aligned} \tag{1.5}$$

where, $\sigma_c = \sigma_P(1+\frac{\sigma_H^2}{\sigma_P^2})$ is the Cowling conductivity which is enhanced by a large factor $(1+\frac{\sigma_H^2}{\sigma_P^2})$ and thereby, it can support the large current jet which is generated in the equatorial E-region.

The in-situ measurement of magnetic field through rocket experiments observed peak of E-region current at 105 km altitude (*Davis et al.*, 1967; *Sampath and Sastry*, 1979; *Pfaff Jr et al.*, 1997; *Chandra and RG*, 2000). Figures 1.6a and 1.6b show the measured eastward current density profile obtained through rocket flights over Thumba and Peru, at two dip-equatorial latitudes over different longitudinal sectors. Even the magnetic field induced due to the strong current jet at the ground can be measured through magnetometers. The estimation of the strength of EEJ using ground-based magnetometers has been discussed in section 2.5 of chapter 2. During nighttime, the electron density over the E-region becomes very less, conductivity also decreases. Even the electric field

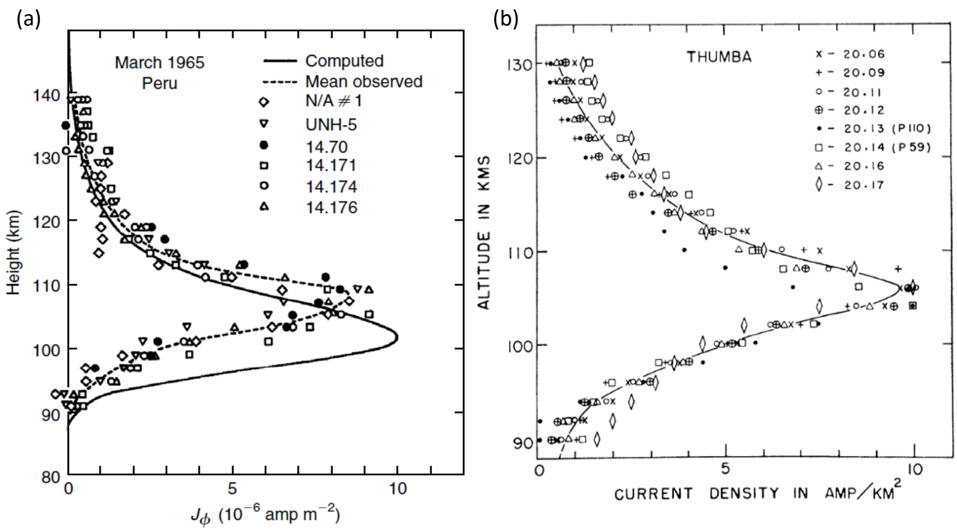

Figure 1.6: The current density at the equatorial E-region over South-American and Indian longitudes are shown in panels (a) and (b), respectively which are measured through rocket-borne instrument. The larger current around the 105 km altitude suggests the electrojet phenomena over the equator. (After *Richmond*, 1973; *Sampath and Sastry*, 1979).

also becomes westward, therefore, EEJ disappears at that time. However, on some occasions, the induced magnetic field during daytime decreases below the nighttime base value which is known as counter-electrojet (CEJ) (*Gouin*, 1962; *Rastogi*, 1975; *Raghavarao and Anandarao*, 1980; *Vichare and Rajaram*, 2011; *Singh et al.*, 2018). Figures 1.7a and 1.7b show the examples of electrojet and counter-electrojet for two given days which have been estimated using ground-based magnetometer data in the Indian sector.

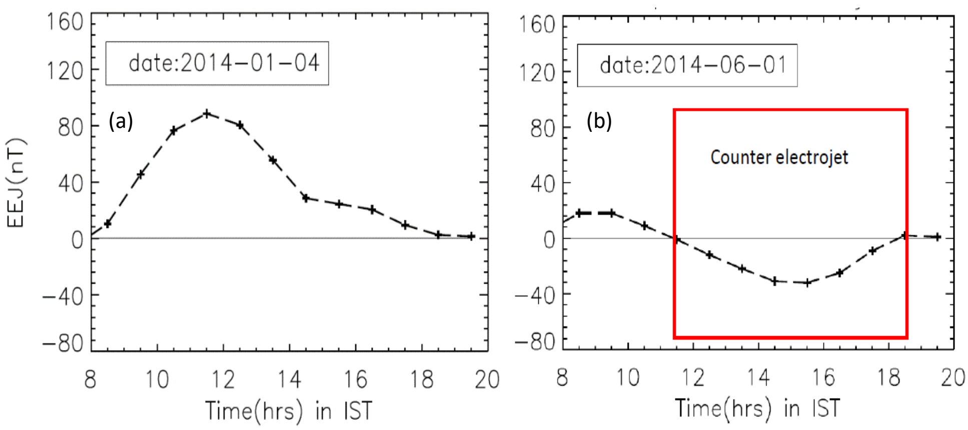

Figure 1.7: The variation of electrojet strength over Indian sector using the ground-based magnetometer data (hourly) for two sample days. The magnetometer data of Tirunelveli and Alibag are used in the estimation of EEJ strength over Indian sector. (a) shows typical electrojet variation, whereas, (b) shows the existence of counter-electrojet.

1.2.2 Equatorial ionization anomaly (EIA)

Equatorial ionization anomaly (EIA) plays an important role in the coupling between the equatorial and low-latitudinal regions. Due to this process, a double-humped structure in electron density is formed on either side of the dip-equator. The structure and behaviour of EIA have been investigated through various modes of measurement, such as, ionosonde (*Appleton*, 1946; *Croom et al.*, 1959), TEC measurement (*Rastogi and Klobuchar*, 1990; *Rodrigues et al.*, 2015), airglow emissions (*Sridharan et al.*, 1993b; *Pallamraju and Sridharan*, 1998b; *Immel et al.*, 2006; *Eastes et al.*, 2019) in the F-region, etc. The magnetic field lines of the off-equatorial E-region pass through the equatorial F-region. The eastward electric field generated in the E-region through the dynamo action gets mapped to the F-region through the equipotential magnetic field lines.

Theoretical works have been carried out to understand the processes behind such electron distribution over the equatorial and the low-latitudinal regions (e.g., *Mitra*, 1946; *Martyn*, 1955; *Rishbeth et al.*, 1963). The electrons and ions are lifted in the higher altitudes following the $\mathbf{E} \times \mathbf{B}$ drift in the F-region. This upward drifted plasma comes down to the off-equatorial and low-latitudinal regions along the magnetic field lines due to the ambipolar diffusion, which resembles a plasma fountain. A schematic of such plasma fountain is shown in figure 1.8a. In this way, plasma transported to the low-latitudes

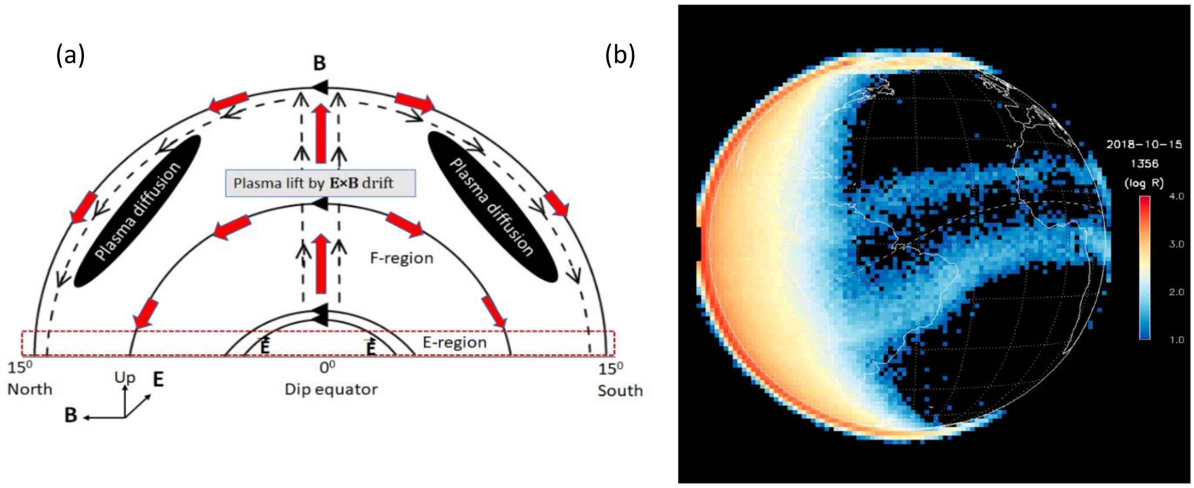

Figure 1.8: (a) Schematic of the plasma fountain process associated with EIA (adapted from *Rishbeth*, 1977). (b) The 135.6 nm atomic oxygen emissions show the structure of the EIA on either side of the dip-equator as observed from GOLD ultra-violet spectrograph (After *Eastes et al.*, 2019). Day-night transition can be seen over the American sector.

from dip-equator, forms crests in electron densities over ±15° to ±20° dip latitudes. A trough of the electron density is formed over the equator. Earlier, the trough over the magnetic equator and two crests on either side seemed to be anomalous as it was expected that the ionospheric plasma density should be larger at the equator as compared to low-latitudes at least during equinoxes when the solar EUV is expected to be greater over the equator side. That is the reason why this phenomenon was mentioned as the equatorial ionization anomaly (EIA). Later the process was explained and understood to be due to daytime electrodynamics which transport the plasma to the low-latitudes from the equator (*Hanson and Moffett*, 1966; *Rishbeth et al.*, 1963; *Anderson*, 1973). During nighttime, the electric field becomes westward, and the strength of EIA decreases. The daytime EIA process becomes reverse, known as reverse fountain effect (*Sridharan et al.*, 1993b; *Narayanan et al.*, 2013; *Saha and Pallamraju*, 2022). The importance of the strength of EIA over low-latitude plasma density variations has been investigated in this thesis work which has been shown in chapters 4, 5, and 6.

Apart from day-to-day variability, EIA exhibits variations depending on time, winds, seasons, solar flux, seasons, etc. (e.g., *Sastri*, 1990; *Rao et al.*, 2006; *Lin et al.*, 2007; *Luan et al.*, 2015; *Khadka et al.*, 2018). The strength of EIA also varies longitudinally depending upon the strength of magnetic field and the geometry of field lines (*Sharma*

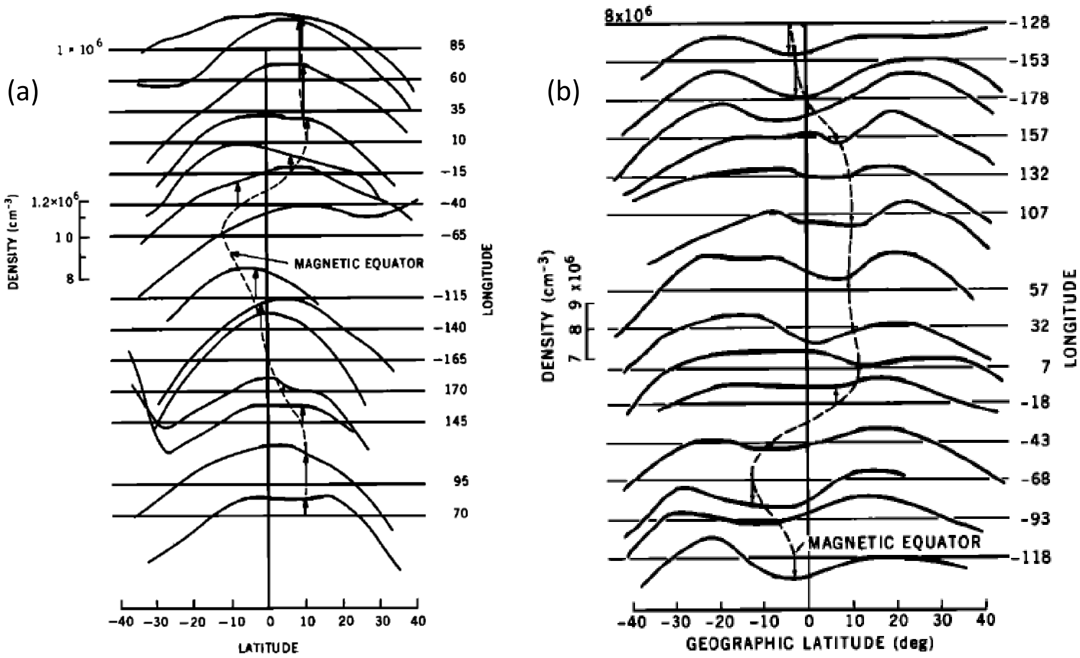

Figure 1.9: (a) and (b) show N_2 density measured on board OGO-6 satellite at morning and afternoon time, respectively. In the morning time, the EIA did not develop, whereas, it is already formed in the afternoon time which is reflected in the latitudinal variation of N_2 density. (After *Hedin and Mayr*, 1973)

and Raghavarao, 1989; *Immel et al.*, 2006; *Basu et al.*, 2009; *Eastes et al.*, 2021). The strength of the EIA is well correlated with the strength of EEJ showed that the strength of EIA follows one-to-one correlation with the integrated EEJ strength of the pre-noon time (8-12 LT) (*Rush and Richmond*, 1973; *Raghavarao et al.*, 1978, 1988b; *Sridharan et al.*, 1999; *England et al.*, 2006; *Pallamraju et al.*, 2010). The vertical uplift of the plasma depends upon the strength of the electric and magnetic fields over the equator. The rise of plasma fountain can be as high as 1000 km and is mapped to around ±30° latitudes during high solar active periods (*Balan et al.*, 1997). In this way, EIA plays a crucial role in the plasma distribution over the low-latitudinal regions.

1.2.3 Equatorial temperature and wind anomaly (ETWA)

Interestingly, the double-humped structure of the electron density caused by the plasma fountain process also affects the latitudinal distribution of neutral density, temperature, and wind. Neutral densities have been measured from OGO-6 satellite between 400 and 500 km altitudes during daytime (*Hedin and Mayr*, 1973). The N_2 and O density showed

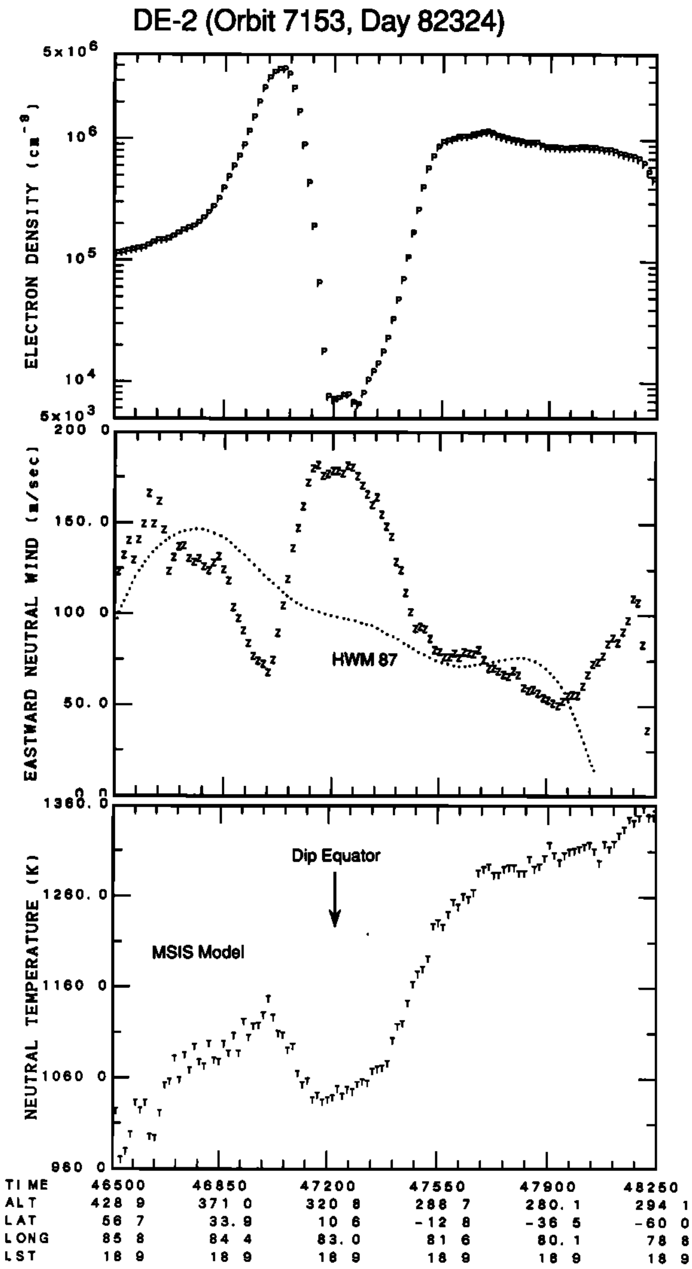

Figure 1.10: The measurement of electron density, zonal wind, and neutral temperature is shown from top to bottom panel observed from DE-2 satellite on 20 Nov 1982 at 18.9 LT. The values obtained from the empirical models HWM87 and MSIS have been compared with the measured value. (After *Raghavarao et al.*, 1991)

a decrease by about 20% and 10% over the equator, respectively, and a crest-like feature is observed at the ±20° latitude. This is known as neutral anomaly (*Heelis and Maute*, 2020). Figures 1.9a and 1.9b show the N_2 density variation during two different local times. The EIA structure is not formed at 6 LT (figure 1.9a), and so, the neutral density can be observed to be larger over the equator, whereas when the EIA is usually well developed at 17 LT (figure 1.9b), the double humped structure can be seen in the latitudinal distribution of neutral density. The ion drag associated with the EIA structure is understood to be responsible for the similar structure to the plasma density observed in neutral density distribution.

As a consequence of the double-humped structure in the neutral and plasma densities along latitudes, the neutral temperature and wind also show latitudinal structure in the daytime. The variations in neutral wind and temperature have been obtained from the Wind and Temperature spectrometer (WATS), and the electron densities measured from Langmuir probe (LP) onboard Dynamic Explorer-2 satellite are shown in figure 1.10 (*Raghavarao et al.*, 1991). The zonal neutral winds are decreased and the temperature is larger at a region collocated with the crest in electron density over the low-latitudes. The opposite behaviour in the distribution of the neutral temperature and zonal winds is seen over the equator. This kind of anomalous structure in neutral temperature and wind is known as equatorial temperature and wind anomaly (ETWA) (*Raghavarao et al.*, 1991, 1998; *Balan et al.*, 1997). The larger plasma density causes an increase in ion-neutral collision. Therefore, a reduction in wind speed and enhancement in temperature occurs due to the presence of a crest-like structure of neutral density over the low-latitudes. The differences in the wind and temperature between their crests and trough are about 100 ms^{-1} and 50 K, respectively. Vertically upward wind gets generated due to the temperature gradient at the equatorial and low-latitudes, which is downward at the equator and upward over the low-latitudes (*Raghavarao et al.*, 1993). The magnitude of the vertical winds had been observed in the range of 10-40 ms^{-1}.

1.2.4 Pre-reversal enhancement (PRE)

As we discussed earlier, the plasma gets drifted vertically upward over the dip-equator in the ionospheric F-region during daytime due to the $\mathbf{E} \times \mathbf{B}$ force and is transported over the low-latitudinal regions. While the E-region dynamo is active in the daytime, the F-region dynamo takes over at sunset. The neutral winds in the F-region change from west to east at the end of the day. The eastward wind creates downward electric field at the equatorial F-region in the presence of horizontal northward magnetic field

$\mathbf{E}_z = -\mathbf{U} \times \mathbf{B}$. This downward electric field is mapped to the off-equatorial E-region and the direction becomes equatorward ($\mathbf{E}_\theta$) (figure 1.11). Now, this equatorward electric field along with magnetic field drives $\mathbf{E} \times \mathbf{B}$ drift at the off-equatorial E-region which allows the electrons to move in the eastward direction, and a westward current is generated ($\mathbf{J}_{\theta\phi}$). As the conductivity of the medium decreases during the sunset time, the electrons will accumulate in the dayside wall of the day-night terminator. Therefore, an electric field will be generated in the eastward direction (($\mathbf{E}_\phi$) to maintain the curl-free condition of the ionospheric electric field ($\nabla \times \mathbf{E} = \mathbf{0}$). Thus, an enhancement in the eastward electric field is generated before the F-region electric field reverses its direction to the west and is called the Pre-reversal Enhancement (PRE) (e.g., *Rishbeth*, 1972; *Heelis et al.*, 1974; *Fejer*, 1981; *Fejer et al.*, 1991, 2008; *Fejer and Scherliess*, 1997; *Farley et al.*, 1986; *Scherliess and Fejer*, 1999).

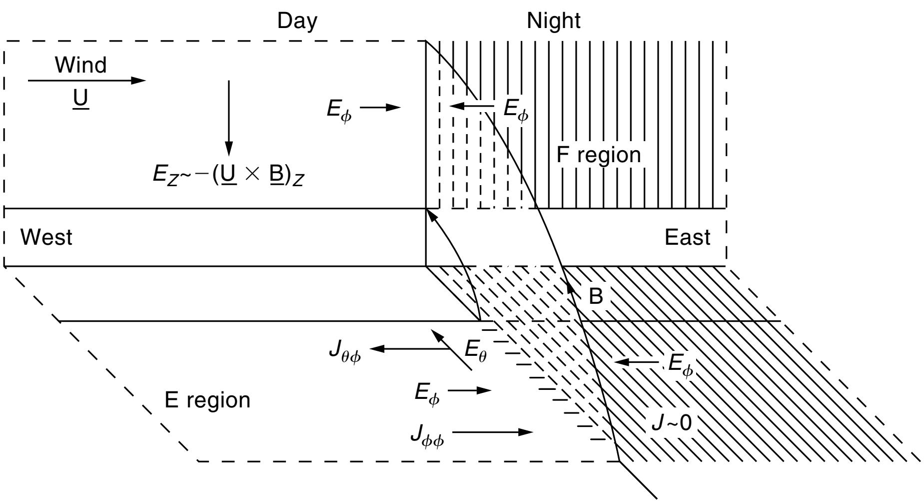

Figure 1.11: Schematic which describes the mechanism of pre-reversal enhancement (PRE). (After *Farley et al.*, 1986).

The off-equatorial E-region is coupled with the equatorial F-region through the equipotential geomagnetic field lines. The coupling factor between the E and F regions can be written as,

$$f = \frac{\Sigma_P^{FN}}{\Sigma_P^{EN} + \Sigma_P^{ES} + \Sigma_P^{FN}}$$

where, Σ_P is the Pedersen conductivity, the superscript E and F refer to E and F regions, and N and S refer to northern and southern hemisphere, respectively. During equinox

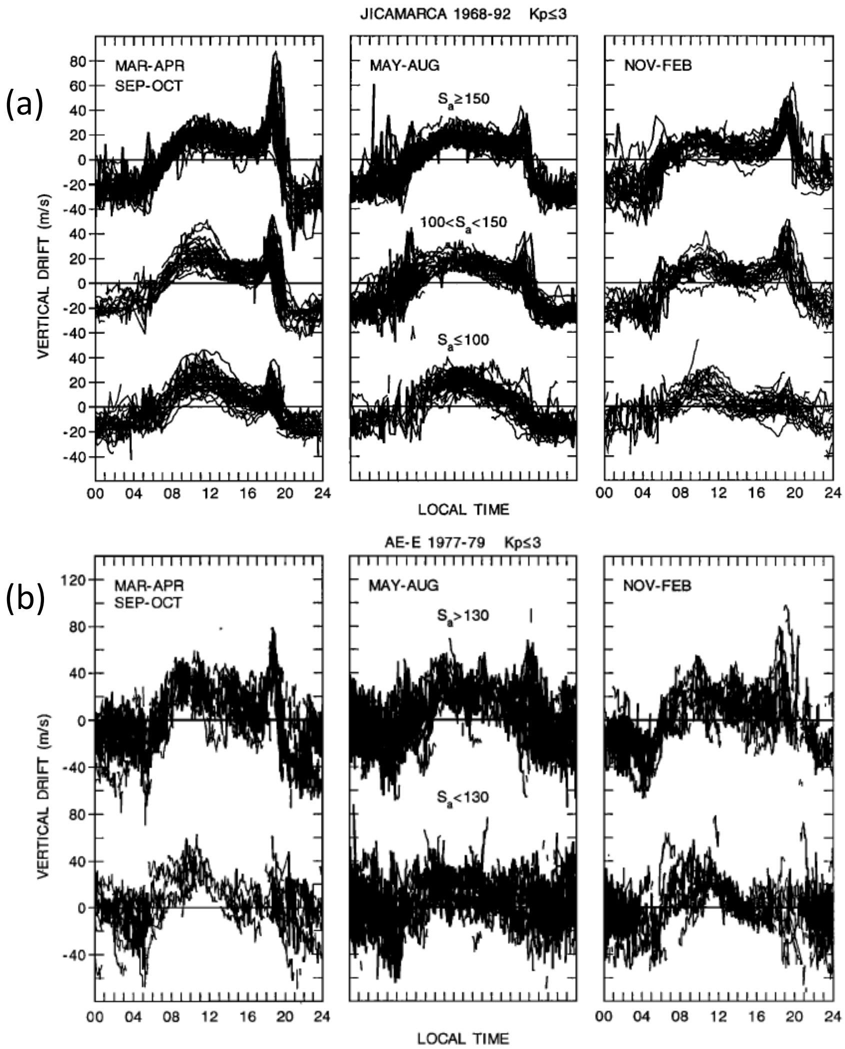

Figure 1.12: Vertical drift of the F-layer plasma measured by using incoherent scatter radar at Jicamarca (a) and ion-drift meter on board AE-E satellite (b) at different seasons and solar flux conditions (After *Scherliess and Fejer*, 1999)

time, sunset happens simultaneously in both the hemispheres. Therefore, Σ_P^E decreases to zero in both hemispheres at simultaneous time. The E and F region coupling factor approaches the value 1. Therefore, the F-region dynamo becomes stronger during the equinox time and shows larger vertical drift during PRE as compared to other seasons.

Figure 1.12a shows the F-region plasma vertical drift as measured from Jicamarca, a dip-equatorial station during various solar activity conditions and seasons (*Scherliess and Fejer*, 1999). The plasma drift shows sharp increase at the time of local sunset following the upward vertical drift during the daytime. The sunset time vertical drift in PRE shows large day-to-day variation depending on the speed of the zonal winds, the field line conductivity, zonal electric field during daytime, etc. During high solar active period, the plasma density becomes larger in amount which generates larger polarization electric field at sunset time in the E-region. Therefore, the zonal electric field at sunset time exhibits larger enhancement during the high solar active period as compared to the low solar active period. During equinox time, the vertical drift in PRE shows larger magnitude as compared to other seasons because of the simultaneous E and F-region coupling from both the hemisphere as discussed in the previous paragraph.

The measurement of plasma vertical drift through AE-E satellite is shown in figure 1.12b during both high and low solar active periods (*Scherliess and Fejer*, 1999). The phenomena of PRE have also been modelled theoretically (*Fesen et al.*, 2000; *Sousasantos et al.*, 2020). As the conductivity is low at sunset time, this electric field will be mapped to the equatorial F-region and enhance the eastward electric field as well as vertical drift of the plasma. The vertical drift due to the PRE in zonal electric field can cause resurgence of plasma following the fountain process over the low-latitudes, and the effect can be seen in the post-sunset time nightglow emissions. In this thesis work, we have investigated and characterized such various kinds of effects in greater detail in the subsequent chapters.

1.2.5 Equatorial plasma irregularities

Equatorial ionospheric irregularities give rise to plasma density distribution at a wide variety of scale sizes which impose significant impact in the radio wave propagation through the ionospheric medium. The GPS and HF receiver show scintillation in the signals during this period of the presence of these irregularities. This brings practical difficulties in navigation and satellite-based communications.

The instability in the nighttime ionosphere was observed for the first time as diffuse echoes in the reflected radio signals in the ionogram by *Booker and Wells* (1938) which was defined as spread-F (figure 1.13a). After that, several experiments and theoretical studies have been carried out to understand the mechanism and dynamics of the instability processes which are documented in various review articles (e.g., *Basu and Kelley*, 1977; *Fejer and Kelley*, 1980; *Ossakow*, 1981; *Makela*, 2006; *Kelley et al.*, 2011; *Sekar et al.*, 2008; *Yokoyama*, 2017). Linear perturbation theory based upon Rayleigh-Taylor instability (RTI) had been developed which was understood to be the cause of irregu-

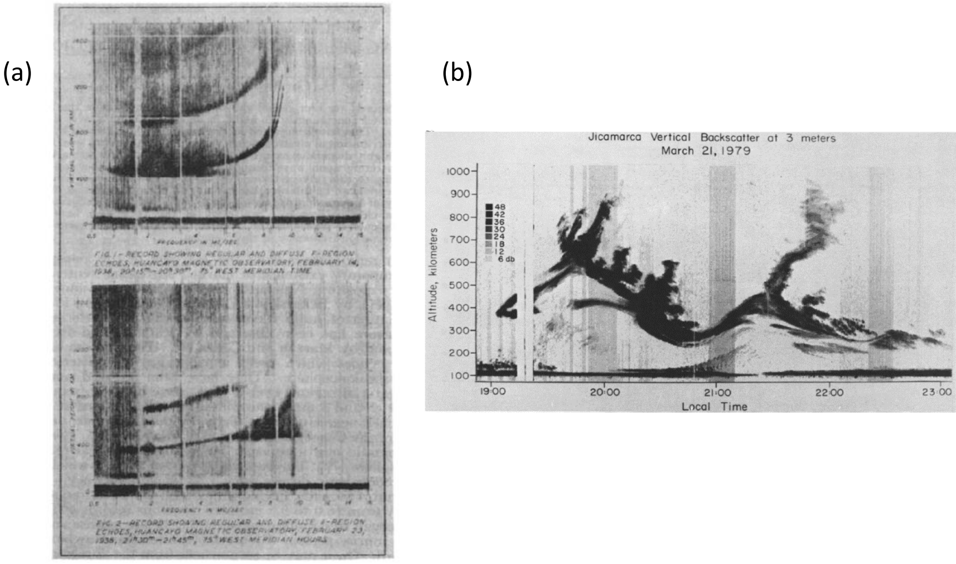

Figure 1.13: (a) Spread in reflected echoes of radio signal observed in ionogram. (After *Booker and Wells*, 1938). (b) The backscatter signal from 3-meter ionospheric irregularity observed over Jicamarca. (After *Kelley et al.*, 1981). The plume structures are the characteristic features of the ionospheric irregularities.

larities generated in the bottomside of the ionosphere as introduced by *Dungey* (1956) for the first time. After initial observations using the ionosonde, experiments have been carried out with the advent of radar, rocket, satellite platforms. The spread-F in the reflected radio echoes has also been investigated with the topside ionospheric observations by scintillations of radio stars, satellite signals as well as from the ground-based forward and backscatter signals by HF, VHF radar, for example, a backscatter signal from a radar operating at 50 MHz from a dip-equatorial station, Jicamarca. Such multi-instrument observations revealed many important information about this geomagnetic field-aligned ionospheric instability (*Farley et al.*, 1970; *Kelley and McClure*, 1981; *Kelley et al.*, 1981). figure 1.13b shows the backscatter signal obtained from 50 MHz radar operated over Jicamarca which provides information of the 3-m scale size irregularities. The growth rate, vertical movement of the irregularities, apex altitudes, strength of the backscatter signal, etc. can be estimated using such radar techniques.

The linear RTI theory as proposed by *Dungey* (1956) could not explain all of the features observed in the 50 MHz Jicamarca radar (*Farley et al.*, 1970). The rise of plasma plumes above the F-layer peak could not be explained by the bottomside instability. Later, the generation of the instability and growth have been understood in greater detail which has been described with the schematic in figure 1.14. During sunset time, a vertical plasma gradients are created. A larger plasma density (n_1) is found in the topside of the ionosphere as compared with the bottomside ionosphere (n_2). This is analogous to a heavier fluid being supported by the lighter fluid against gravity, which creates the hydrodynamic Rayleigh-Taylor instability. The gravitational force acts in the downward direction opposite to the density gradient (∇n). The net current flows in the eastward direction due to the gravity force is $J = \frac{nMg}{B}$, where, n is the number density, M is the mass of ions, g is the gravitational acceleration, and B is the geomagnetic field. If, a small perturbation is imparted in the medium, the charges pile up on the edges (as shown in figure 1.14). As a consequence, perturbation electric field ($\delta\mathbf{E}$) will be generated and the low-density region will be lifted up in the higher altitudes due to the $\delta\mathbf{E} \times \mathbf{B}$ force. The growth rate of the irregularities was considered to be an important factor in the development of plasma bubble apart from the seeding factor and has been investigated for several decades (e.g., *Scannapieco and Ossakow*, 1976; *Ossakow and Chaturvedi*, 1978; *Sultan*, 1996; *Shinagawa et al.*, 2018; *Das et al.*, 2021). Vertical drift during PRE in electric field has been observed as precursor of the RTI in many studies (e.g., *Fagundes et al.*, 1999; *Fejer et al.*, 1999; *Anderson et al.*, 2004; *Tulasi Ram et al.*, 2006; *Whalen*, 2002; *Lee et al.*, 2005; *Kudeki et al.*, 2007; *Kil et al.*, 2009b; *Abadi et al.*, 2015; *Tsunoda et al.*, 2018). Electric field, configuration of the geomagnetic field (horizontal in nature over the dip-equator), ion-neutral collisions, neutral winds have been observed as important factors in the growth rate (γ) of the irregularities which has been estimated to be $\gamma = (\frac{g}{\nu_{in}} + W_x \frac{\nu_{in}}{\Omega_i} - W_z) \cdot \frac{1}{n}(\frac{\partial n}{\partial h})$, (*Sekar and Raghavarao*, 1987; *Sultan*, 1996) where, W_x is the eastward wind, W_z is the upward wind, g is the gravitational acceleration, ν_{in} is ion-neutral collision frequency, $\frac{\partial n}{\partial h}$ is the density gradient.

Optical observations, using both ground and satellite-based instruments, have been carried out for the investigation of equatorial plasma bubbles (EPBs) which is an another manifestation of equatorial plasma irregularities. OI 630.0 nm nightglow emissions which emanate from around 250 km altitudes are used as tracer to observe the plasma depletions over the low-latitudinal regions (*Sobral et al.*, 1980; *Mendillo and Baumgardner*, 1982; *Mendillo and Tyler*, 1983; *Mendillo et al.*, 1992). Apart from the OI 630.0 nm emissions, 557.7 and 777.4 nm emissions are also used in the study of EPBs (*Takahashi et al.*, 2001; *Sinha et al.*, 2001; *Kelley et al.*, 2002; *Makela and Kelley*, 2003; *Rajesh et al.*, 2010).

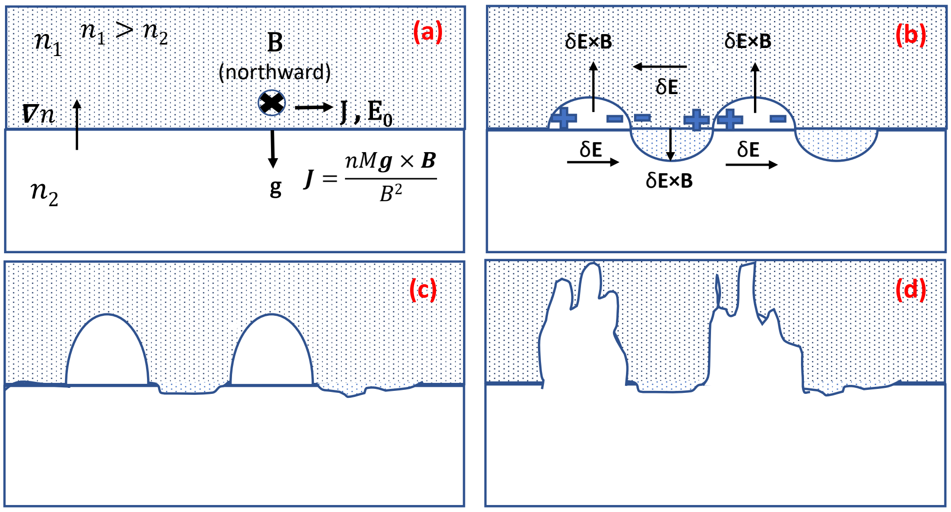

Figure 1.14: Schematic of generation of plasma bubbles. (Adapted from *Kelley*, 2009)

Nevertheless, it is not very convenient to study the EPBs by OI 557.7 nm emissions as it originates from lower F-region altitudes where the recombination rate is much higher. OI 630.0 nm emissions give the bottomside structure of plasma irregularities, whereas, OI 777.4 nm emissions which originate at the peak F-layer height can provide information

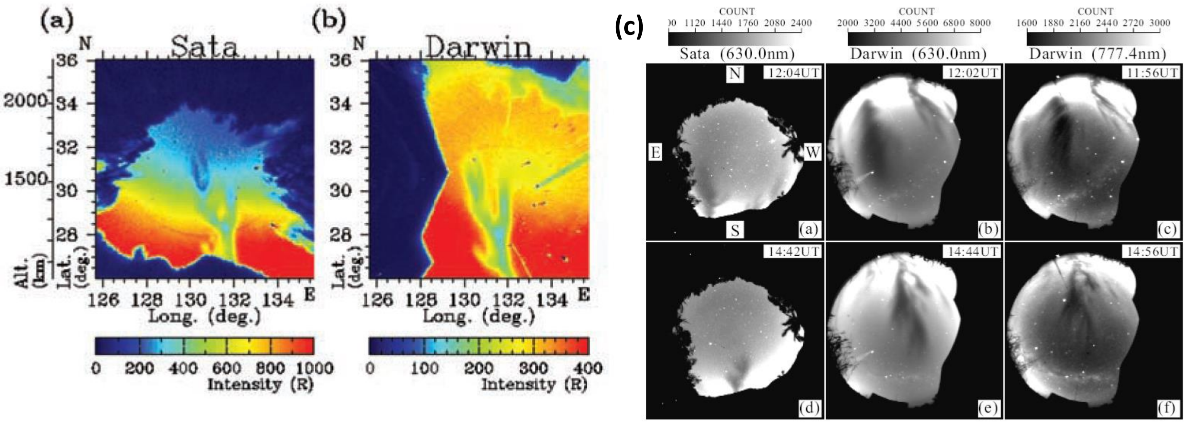

Figure 1.15: (a) Plasma depletions observed over two geomagnetic conjugate locations, Sata and Darwin in OI 630.0 nm nightglow emissions. (After *Otsuka et al.*, 2002). (b) A similar observation was carried out at two different wavelengths of nightglow emissions, OI 630.0 and 777.4 nm.(After *Shiokawa et al.*, 2004).

on the irregularities at altitudes higher above that of OI 630.0 nm (*Tinsley*, 1982; *Abalde et al.*, 2001, 2004; *Makela and Kelley*, 2003). The plasma bubbles generated over the dip-equator are lifted upwards and subsequently follow the geomagnetic field lines and get mapped over the low-latitudes. Simultaneous observations from two conjugate locations show the fascinating mirror image of the plasma depletion structure. OI 630.0 nm emissions observed using the all-sky imager from Sata (31°N, 130.7°E, 24°N mag) and Darwin (12.4°S, 131.0°E, 22°S mag) showed the evidence of geomagnetic field line mapping of the plasma bubbles as shown in figure 1.15 (*Otsuka et al.*, 2002; *Shiokawa et al.*, 2004). Even the small-scale structures of around 40-100 km in the zonal direction are observed to be mapped simultaneously at these two locations. This confirms that the polarization electric fields generated by the RTI process are mapped through the geomagnetic field lines. The zonal movement and the bifurcated structures also remained the same at both locations.

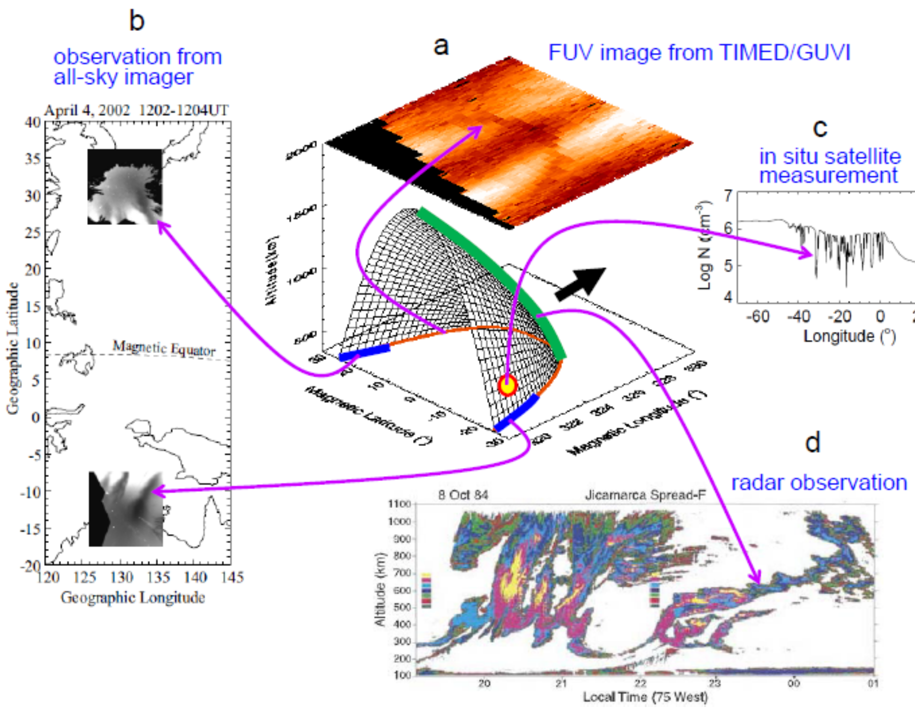

Figure 1.16: Structure of plasma shell where plasma depletion is observed at different parts of the shell from different locations using different modes of observation. (a) TIMED/GUVI satellite image shows the backward C-shaped structure, (b) image obtained from all-sky imager from two geomagnetically conjugate locations, (c) fluctuation of electron density as measured from in-situ satellite, and (d) plasma plume structures detected from radar experiment. (After *Kil*, 2015).

The irregularities are seen in different shapes and scale sizes spanning from few centimetres to several thousand of kilometres as seen through different observational techniques. These include a spread in reflected echoes as seen in the ionosonde, plasma bubbles with depleted plasma density as seen in optical imager, depletion in plasma density as seen from the satellite measurement, plasma plumes as observed over radar, etc. (*Abdu et al.*, 1983; *Takahashi et al.*, 2001; *Huang et al.*, 2013; *Huang and Roddy*, 2016). The shell structure shown in figure 1.16 provides a comprehensive picture of the plasma irregularities (*Kil*, 2015) and describes the different manifestations of the plasma irregularities by looking at different scale sizes. The black arrow suggests the movement of the plasma shell. The image obtained from the TIMED/GUVI observed the backward C-shaped plasma depletion at 350 km altitude (figure 1.16a) which is extended throughout the magnetic flux tubes. The orange band is the bottom part of the shell where the depletion is most significant as compared to background. The ground-based optical images obtained from two conjugate geomagnetic locations in Japan and Australia observed the poleward part of the shell as marked by blue bands (figure 1.16b). An In-situ measurement from space-based instrument measured the fluctuations in the electron density variation while passing through the plasma irregularities (figure 1.16c). The radar observation from equatorial station (figure 1.16d) observed the bottomside as well as topside plasma irregularity structures.

1.3 Modes of investigating the upper atmospheric variabilities

Various upper atmospheric parameters are measured to understand the variabilities of the ionosphere-thermosphere system caused by various processes as mentioned in the earlier section. Winds, Electric and magnetic fields, and temperature are some of the parameters associated with the atmospheric dynamics. Optical, radio, and magnetic measurements from both ground and space-based platforms are the means to investigate the ionosphere-thermosphere system.

1.3.1 Optical Measurements

Airglow emissions:

Various chemiluminescence processes emit photons of various wavelengths depending upon the excitation of energy levels of the neutral molecules and atoms. These are called as airglow. The atoms/molecules are excited to higher energy states by the energetic solar photons/ external sources and after the de-excitation, photons are emitted. The presence of sufficient neutral densities of the reactants and available ambient energies both contribute to the airglow emissions which are originated at a given altitudinal region. Depending on the daytime and nighttime emissions, these are referred to as dayglow and nightglow, respectively. During nighttime, there is no production from solar photons, the recombination of molecular and atomic ions is responsible for the nightglow. Airglow emissions act as tracers to understand the upper atmospheric dynamics of those altitudes from where the emissions originate. Observations of variation in emission brightness at multiple wavelengths from different altitudes provide information on the vertical coupling of the upper atmosphere. This is because, different emissions emanate from different altitudes depending on the number density of the reactants, the energy associated with the reactants, and the radiative lifetime of an excited species, - all are altitude dependent. Similarly, airglow observation from different latitudes and longitudes presents an opportunity to investigate the spatial (latitudes and longitudes) coupling of the upper atmosphere.

At the beginning of 20^{th} century, several astronomers recognized the emission of photons from the terrestrial atmosphere. Although, there are records of observation of such emissions even in the 18^{th} century. Such historical information was reported in the very beginning of the 20^{th} century by observing the nighttime airglow emissions (*Burns*, 1906; *Yntema*, 1909; *Jones and Harrison*, 1955; *Chamberlain*, 1961). There are several earlier reports which provided some rudimentary observations of oxygen green line, red line, and Na emissions which originate in the terrestrial atmosphere (e.g., *Rayleigh*, 1922; *Strutt*, 1931; *Frerichs*, 1930; *Slipher*, 1929). With the improvement in technology, these airglow emissions are measured with greater accuracy, and various thermospheric parameters, such as, temperature, wind, and plasma drift have been measured successfully. Ground-and space-based optical instruments have been operated to measure the airglow emissions of different altitudes. The ground-based observations provides higher temporal resolution, whereas, the satellite data yield better spatial coverage. Photometry, spectrometry, interferometry, imaging, etc., have been developed to study the nighttime mesospheric-thermospheric emissions (e.g., *Mukherjee et al.*, 2000; *Chakrabarti et al.*, 2001; *Makela et al.*, 2009, 2011; *Sharma et al.*, 2014).

Thermospheric winds and temperature are some important physical parameters in the aeronomy which can be measured from airglow emissions (*Meriwether et al.*, 1986; *Makela et al.*, 2011; *Shiokawa et al.*, 2012). Fabry-Perot interferometer is used to measure the thermospheric temperature and winds through Doppler shift and Doppler broadening of the emission lines. Coordinated measurement of thermospheric temperature over Mt. Abu, a low-latitudinal region in the Indian sector, using the OI 630.0 nm observation by Fabry-Perot interferometer revealed direct relation with the ionospheric base F-layer height (*Sridharan et al.*, 1991). The thermospheric winds are also measured from the same instrument over the same location (*Gurubaran and Sridharan*, 1993). The ionospheric heights and the nightglow emissions were found to vary with the variation of such thermospheric parameters, winds, and temperature (*Meriwether Jr et al.*, 1985; *Gurubaran et al.*, 1995; *Saha et al.*, 2021). The rotational temperature is measured from the mesospheric band emissions where the intensities of two rotational states are used (*Meriwether et al.*, 1984; *Taylor et al.*, 1999; *Shiokawa et al.*, 2007). OH (840.0, 846.5, 850.5 nm) and O_2 (866.0, 868.0 nm) rotational lines have been used to measure the rotational temperature at the mesospheric altitudes of around 87 and 94 km, respectively (*Singh and Pallamraju*, 2015, 2017).

Different airglow emissions originate at different altitudes depending on the constituents and ambient energy present at that altitude. The nighttime atomic oxygen emissions at 557.7, 630.0, and 777.4 nm wavelengths originate from around 150, 250 km, and peak F-layer, respectively. Atomic oxygen of higher energy states, ^{1}S and ^{1}D, produced through dissociative recombination. OI 557.7 and 630.0 nm emissions are produced due to the atomic transitions of ^{1}S - ^{1}D and ^{1}D - ^{3}P, respectively. The radiative lifetimes of these two excited states (^{1}S and ^{1}D) are 0.74 and 110 sec, respectively. These transitions are forbidden by electric-dipole radiation, whereas, the transitions are allowed by the electric-quadrupole (OI 557.7 nm) and magnetic-dipole (OI 630.0 nm) radiation.

Besides, the excited state (^{5}P) for the OI 777.4 nm emissions is produced by the radiative recombination of atomic oxygen ions with the ambient electrons, and the emissions occur due to the transition to the ^{5}S state. OI 135.6 nm far-ultraviolet emissions originate from the peak F-layer height following the atomic oxygen transition from ^{5}S to ^{3}P state. Sodium emissions (NaD) of 589.0 and 589.6 nm are produced at 92 km altitude. There are some molecular transitions at the mesospheric region which emit in band spectra. The hydroxyl (OH) emissions (6-2), molecular O_2 emissions (0-1) which emanate from 87 and 94 km altitudes, respectively, are examples of some molecular band emissions in the mesospheric region. The mechanism of these emissions is discussed with greater detail in chapter 3.

Observations:

The observations of OI 630.0 nm nightglow emissions have been carried out from different locations in the globe and several important results on thermospheric phenomena have been reported in the literature, such as, spread-F (e.g., *Otsuka et al.*, 2002; *Makela et al.*, 2004; *Sekar et al.*, 2007), plasma depletion as observed in nightglow emissions (e.g., *Sobral et al.*, 1980; *Mendillo and Baumgardner*, 1982; *Sekar et al.*, 2004), enhancement in nightglow emissions in the post-sunset hours (e.g., *Rao and Kulkarni*, 1973; *Kumar et al.*, 2021; *Saha et al.*, 2021), atmospheric waves (e.g., *Shiokawa et al.*, 2006; *Garcia et al.*, 1997; *Hecht et al.*, 2004; *Medeiros et al.*, 2004; *Lakshmi Narayanan et al.*, 2010; *Ghodpage et al.*, 2014), neutral wind and temperature (e.g., *Meriwether et al.*, 1986; *Sridharan et al.*, 1991; *Gurubaran and Sridharan*, 1993), midnight temperature maximum (e.g., *Faivre et al.*, 2006; *Makela et al.*, 2013), etc. Multiwavelength nightglow emissions of the thermospheric region are observed using a large field-of-view (FOV) instrument High Throughput Imaging Echelle Spectrograph (HiTIES) (*Chakrabarti et al.*, 2001). The infrared nightglow emissions from mesospheric region generated from OH and molecular O_2 band emissions are measured using Near-Infrared Imaging Spectrograph (NIRIS) over the low-latitudinal region. From this observation, the periodicities, and the scale sizes present at that altitudinal region from where these emissions originate, the latitudinal variation in rotational temperature, and the effect of sudden stratospheric warming had been investigated (*Singh and Pallamraju*, 2015, 2017).

The extraction of daytime airglow is more challenging because of the presence of a huge solar background. A dayglow photometer was fabricated using the pressure-tuned low resolution Fabry-Perot etalon along with the narrow band interference filter and a technique was developed to extract the dayglow emission intensities (*Narayanan et al.*, 1989; *Sridharan et al.*, 1992, 1993a, 1998). Later on, using the Echelle grating, high-resolution optical spectrographs, such as High Resolution Imaging Spectrograph using Echelle grating (HIRIES), Multiwavelength Imaging Echelle Spectrograph (MISE) had been developed to measure the thermospheric dayglow emissions of different wavelengths (*Pallamraju et al.*, 2002, 2013). OI 297.2 nm dayglow emissions were measured by a balloon-borne large FOV optical instrument called the Ultra-Violet Imaging Spectrograph (UVIS) (*Pallamraju et al.*, 2014). The investigation of daytime electrodynamics associated with the dayglow over low-latitudes (*Sridharan et al.*, 1992, 1994, 1999; *Pallam Raju et al.*, 1996; *Pallamraju et al.*, 2014; *Karan et al.*, 2016; *Karan and Pallamraju*, 2017), wave characteristics in the daytime thermosphere (*Pallamraju et al.*, 2010, 2016; *Laskar et al.*, 2013, 2015), and auroral emissions in the daytime had been carried out using various ground-based optical instruments (*Pallamraju and Sridharan*, 1998a; *Chakrabarti*, 1998; *Pallam Raju et al.*, 1995; *Pallamraju et al.*, 2001).

Various upper atmospheric parameters and processes have been investigated using the optical techniques onboard space-based platforms, such as series of Atmospheric Explorer (AE) (*Hays et al.*, 1973), Upper Atmosphere Research Satellite (UARS) (*Shepherd et al.*, 1993, 2012), Thermosphere Ionosphere Mesosphere Energetics and Dynamics (TIMED) (*Henderson et al.*, 2005b,a; *Immel et al.*, 2006), Global-scale Observations of the Limb and Disk (GOLD) (*Eastes et al.*, 2019, 2020; *Karan et al.*, 2020), Ionospheric Connection Explorer (ICON) (*Englert et al.*, 2017; *Makela et al.*, 2021), etc. Measurements of several optical emissions using instruments onboard satellites are also expected in the future. To complement and supplement the data from the satellite, several ground-based instruments and networks exist/ are being planned in order to characterize the ionosphere thermosphere system for better understanding.

1.3.2 Plasma Measurements

The propagation of radio waves is affected by the plasma present in the ionosphere. Radio techniques, such as ionosonde, RADAR (Radio Detection and Ranging), GPS (Global Positioning System), have been used to obtain information of the ionospheric constituents. In these radio techniques, radio waves of different ranges are transmitted into the ionosphere. The signals interact with the ionospheric plasma, match the frequency of the plasma oscillation, and are reflected back to the ground. Depending on the frequencies and power of the transmitted radio waves, backscattered signals are measured.

The oldest radio technique for ionospheric investigation is an ionosonde, and to this day, it continues to provide very useful information for ionospheric studies. Digital ionosonde is known as digisonde. The radio pulses of the frequencies in the range 1-30 MHz are transmitted upwards and the echo is received on the ground. The working principle of an ionosonde has been discussed in section 2.4 of chapter 2. The ionospheric electron density profile of the bottomside F-layer is measured using ionosonde. The typical electron density increases from morning time and peaks at noon based on the variation in solar zenith angle for a given day, whereas, due to the absence of ionization after sunset time, the electron density decreases monotonically. The variation in the electron density is reflected in the values of thermospheric airglow emissions during both day and nighttime. The nighttime plasma irregularities present in the ionosphere can also be identified as a spread in reflected echo signals. In this way, the ground-based digisonde provides useful information of the bottomside ionosphere, whereas, similar radio-sounding techniques carried out from space-based platforms provide the topside ionospheric information. Using such information obtained from digisonde data, the vertical propagation of gravity waves and their characteristics at different seasons and solar flux conditions during both geomagnetic quiet and disturbed periods have been studied (*Mandal et al.*, 2019, 2020; *Mandal and Pallamraju*, 2020). Vertical drift of the ionosphere during daytime, especially at the time of PRE is calculated vastly using the height information of the F-layer (*Murthy and Gupta*, 1972; *Bittencourt and Abdu*, 1981; *Krishna Murthy et al.*, 1990; *Woodman et al.*, 2006; *Saha et al.*, 2021). The thermospheric wind was also estimated using the ionosonde data (*Krishna Murthy et al.*, 1990; *Hari and Murthy*, 1995; *De Medeiros et al.*, 1997; *Miller et al.*, 1986). The topside radio sounding can provide the information on the top side of the ionosphere as it is operated from space-based platforms (*Tulasi Ram et al.*, 2009; *Venkatesh et al.*, 2011; *Sibanda and McKinnell*, 2011).

Radar is also a very powerful technique which uses different frequency range to probe different scale sizes of the ionosphere. Ultra-High Frequency (UHF) (300-3000 MHz), Very High Frequency (VHF) (30-300 MHz), High Frequency (HF) (3-30 MHz), Medium Frequency (MF) (0.3-3 MHz), and Meteor Radar (15-40 MHz) have been used for ionospheric-thermospheric studies (*Rao et al.*, 1995; *Patra et al.*, 1997). Ionospheric vertical drifts and plasma irregularities of different scale sizes are widely investigated using radar techniques (e.g., *Woodman and La Hoz*, 1976; *Fejer and Kelley*, 1980; *Kelley et al.*, 1981; *Rao et al.*, 1995; *Patra et al.*, 1997, 2005, 2014; *Tsunoda*, 2005; *Sekar et al.*, 2004, 2007, 2008). These are mostly coherent scatter radars which work on the principle of Bragg scattering. The successive echoes of the coherent scatter have the same amplitude and phase. Therefore, they can be added coherently, which improves the sensitivity of the instrument. The incoherent scatter radar (ISR) works based on the principle of Thomson scattering. This works at very high transmission power. ISR can provide information on bottomside and top side of the ionosphere, with better spatial resolution as compared to any other radio techniques. In addition, it provides information on neutral and ion densities (*Fejer*, 1981; *Fejer et al.*, 1991; *Holt et al.*, 1992; *Lei et al.*, 2005).

Global Positioning System (GPS) is a constellation of satellites which determine the position and velocity of an object on Earth (`https://urs.earthdata.nasa.gov/`). It is mostly used in the navigation system. NavIC (Navigation with Indian Constellation) is one such navigation system which works in Indian subcontinent (`https://www.isro.gov.in/irnss-programme`). The transmission is done in dual frequency range, L5 (1176.45 MHz) and S (2492.03 MHz) band, however, the future satellites are planned to transmit in L1 band (1575.42 MHz) also. While the radio signal propagates through the medium, it can also provide information of the plasma distribution in the ionosphere. The total electron content (TEC) can be provided by using GPS. The TEC can be defined as,

$$TEC = \int_{receiver}^{satellite} N \cdot ds$$

where, N is the electron density present in the column of unit cross-sectional area from the satellite to the ground receiver. GPS transmitter of L1-band (1575.42 MHz) and L2-

band (1227.6 MHz) are widely used in the ionospheric studies. There are several reports on the GPS system and its application, errors (e.g., *Parkinson and Spilker*, 1996; *Jin et al.*, 2014). The major contribution of TEC appears from the topside of the ionospheric F-region. The measurement of TEC provides useful information in the understanding of ionospheric dynamics with varying solar flux, seasons, electrodynamics under different geophysical conditions (*Rama Rao et al.*, 2006; *Abdu et al.*, 2008; *Chakrabarty et al.*, 2012; *Kumar et al.*, 2021, 2022a).

Different instruments which measure the density, and drift of the plasma, such as the Ion-drift meter (IDM), Langmuir probe (LP), Retarding potential analyser (RPA), ion Mass spectrometer have been used in various on-board satellites. They can provide in-situ measurement of ionospheric parameters. Atmospheric explorer (AE) (*Hays et al.*, 1978; *Solomon and Abreu*, 1989; *Scherliess and Fejer*, 1999), Dynamic explorer (DE) (*Spencer et al.*, 1981; *Raghavarao et al.*, 1991), Republic of China Satellite (ROCSAT) (*Burke et al.*, 2004; *Kumar et al.*, 2016), Challenging Minisatellite Payload (CHAMP) (*Lühr et al.*, 2004; *Stolle et al.*, 2006), ionosphere-thermosphere-Mesosphere-Energetics and Dynamics (TIMED) (*Paxton et al.*, 1999), Communication/ Navigation Outage Forecast System (C/NOFS) (*de La Beaujardiere et al.*, 2009; *Huang et al.*, 2013; *Kil et al.*, 2020), SWARM Satellite Constellation Application and Research Facility (*Friis-Christensen et al.*, 2006), Ionospheric Connection Explorer (ICON) (*Englert et al.*, 2017; *Sirk et al.*, 2017; *Immel et al.*, 2018) are some of the satellite missions which provide plasma information of the ionosphere and that had been used in the investigation of upper atmosphere.

1.3.3 Magnetic Measurements

The main source of the geomagnetic field is generated due to the geodynamo action. Various types of currents flow in the ionosphere and magnetosphere, which induce small amounts of magnetic field on the ground as well. Magnetometers are used to measure the magnetic field that is induced by those currents. Equatorial and auroral electrojets have been measured by ground-based magnetometers installed at equatorial and polar regions. The estimation of equatorial electrojet has been described in chapter 2. Various electrodynamics processes take place in the dynamo region which manifest as Sq current system (e.g., *Sastry*, 1970; *Sampath and Sastry*, 1979; *Davis et al.*, 1967; *Shuman*, 1970;

Pfaff Jr et al., 1997; *Rastogi*, 1974; *Rastogi and Iyer*, 1976; *Rastogi and Patil*, 1986; *Rastogi and Klobuchar*, 1990; *Gurubaran*, 2002; *Anderson et al.*, 2004; *Vichare and Rajaram*, 2011). In the equatorial region, a strong jet in eastward electric current generate which is known as EEJ, as described in section 1.2.1. Sometimes, this eastward current reverses in direction and known as counter electrojet. The strength of the geomagnetic storm is characterized by the value of Disturbance Storm Time (Dst) index, which is defined based on the variation of the horizontal component of geomagnetic field. The auroral electrojet is generated due to the precipitation of energetic particles of solar wind origin. The magnetic fields induced due to these currents are measured by the ground-based magnetometers deployed in the polar regions. Using the chain of magnetometer data spread over low to high latitudes, the changes in the horizontal component of the magnetic field ($D_{dyn} = \Delta H - S_R - Dst \times \cos L$) can be calculated during disturbed dynamo periods (*Le Huy and Amory-Mazaudier*, 2005; *Zaka et al.*, 2009; *Rastogi and Chandra*, 2012; *Amory-Mazaudier et al.*, 2017), where, ΔH is the horizontal component of the terrestrial magnetic field, S_R is the induced magnetic field due to the Sq current, and L is the geomagnetic latitude. The magnetometer from space-based instrument was used for the in-situ measurement of the induced magnetic field in the ionosphere (*Ivers et al.*, 2003; *Lühr et al.*, 2004; *Stolle et al.*, 2006; *Singh et al.*, 2018).

1.4 Summary

In this chapter, we have discussed the structure of the Earth's atmosphere, its composition, and chemistry at different altitudes. We have focused on the region of upper atmosphere in this thesis which consists of ionospheric-thermospheric system. The equatorial electrodynamics dynamics over the equatorial and low-latitudes, such as EEJ, EIA, and PRE have been described, which affect the plasma distribution over the equatorial and low-latitudinal region. The ionospheric-thermospheric parameters, such as electric field, neutral winds, and temperature vary with these dynamics in the ionospheric-thermospheric system. They also show variation with solar flux and seasons. The equatorial plasma irregularities that happened in the nighttime ionosphere are also discussed. Airglow emissions of different wavelengths act as tracers of those altitudinal regions from where they originate in the Earth's atmosphere. Different techniques have been developed to observe different phenomena which are occurring in the upper atmosphere. In this thesis work, we have used optical, radio, and magnetic instruments in the investigation of upper atmosphere. The OI 630.0 nm nightglow emissions are measured using the optical instrument over the low-latitudinal regions. The ionosonde has been used to obtain the electron density profile of the bottomside of ionosphere, the height of different ionospheric layers, and magnetometer data which provides the information about the ionospheric-magnetospheric currents which induces the magnetic field near the earth surface. Various results reported in many literatures using these different modes of investigation have also been discussed in this chapter.

1.5 The objective of the thesis

The main objective of this thesis work is to understand the thermospheric-ionospheric interactions in the low- and equatorial regions over small- and large-time scales at different geophysical conditions. In this chapter, we have discussed the atmospheric structure of the Earth, various species present at different altitudes, the chemical processes happening, etc. The processes of the ionosphere-thermospheric system which affect the upper atmospheric parameters have been discussed. Different modes of observation carried out from both ground- and space-based platforms have also been discussed. OI 630.0 nm nightglow emissions have been used as a tracer in this study which peaks around the altitudes of 250 km having a width of around 100 km. We have observed different kinds of variabilities in the OI 630.0 nm nocturnal emissions, such as enhancement in post-sunset emission intensity, reverse movement of the EIA crest during the nighttime, plasma bubbles over an off-equatorial and low-latitudinal region. There are very few observations and discussions reported of such post-sunset emission enhancement and reversal of EIA although clear reason for such variations was not explored. In our study, we discussed these phenomena with a larger number of datasets and offered explanations for the reason behind the observed variations in the emissions. To substantiate our interpretation, measurements from multiple stations around the globe have been used. The observations that have been addressed in this thesis work are listed below:

I. The latitudinal movement of the OI 630.0 nm nightglow emissions is observed in both, poleward and equatorward directions. What are the factors/ dynamics associated with such observations in emissions?

II. After sunset, the airglow decreases monotonically due to the absence of ionization. But, on several occasions, we have observed enhancement in emission after sunset. What is the reason behind such enhancement in emissions?

III. What are the characteristics of the equatorial plasma bubbles in terms of latitudinal and longitudinal extent, the effect of gravity wave scale sizes in the generation of equatorial plasma bubbles as seen from low-latitudes?

1.6 Overview of the thesis

As we discussed earlier, the optical instruments are used to observe the OI 630.0 nm nightglow emissions over low-latitudes. In this thesis work, we have used High Throughput Imaging Echelle Spectrograph (HiTIES) to measure the OI 630.0 nm nightglow emissions over a low-latitude location, Gurushikhar, Mt. Abu in Indian longitudes. HiTIES has a large database from high (2014) to moderately low solar activity period (2017) which is used in this thesis work. The instrument has a field-of-view of around 54° and makes observations in the meridional direction. The details of the instrument and image processing have been discussed in section 2.3 of chapter 2. Several types of OI 630.0 nm nightglow variations have been observed which have been addressed in this thesis work.

Chapter 1 explains the background of the upper atmospheric structure, processes and variabilities that occur in that region.

Chapter 2 describes the various instruments used in this thesis work. The data analysis of those instruments and the related theories are discussed.

Chapter 3 discussed the variations observed in the OI 630.0 nm nightglow emissions in relationship with the ionospheric height, electron densities under varying solar flux conditions.

Chapter 4 presents the latitudinal movement of the crest of EIA as seen in the latitudinal variation in OI 630.0 nm nightglow emissions. The effect of equatorial electrodynamics such as PRE and nighttime westward electric field is investigated in the context of movement of EIA crest.

Chapter 5 presents the cause of post-sunset emission enhancement in OI 630.0 nm nightglow emissions and the role of meridional wind in such emission enhancement.

Chapter 6 discusses the presence of EPBs over the low- and off-equatorial latitudes. The dynamics of the plasma bubbles and the contrasting scale sizes of gravity waves present between non-EPB and EPB nights are investigated.

Chapter 7 provides the summary and future plan of this thesis work.

Chapter 2

Observational techniques and data analysis

2.1 Background

Upper atmosphere is a natural laboratory where different processes are associated with the plasma and neutral interactions occur, and some of those are discussed in chapter 1. These upper atmospheric processes can be understood by the observations and measurements of different parameters. Airglow emissions, neutral winds, plasma dynamics in terms of drifts, electric and magnetic fields are some of the parameters which are aimed to be measured by the researchers in this field. In this chapter, we have discussed different kinds of instruments those are deployed at different locations to measure various parameters. The working principle of these instruments, data acquisition, and processing are discussed here.

2.2 Introduction

The atmospheric processes become different at different altitudes of the upper atmosphere and vary with the changes in latitudes and longitudes. Many direct and indirect techniques are used to understand the behaviour of the thermosphere-ionosphere system. The in-situ measurement by rocket and satellite can probe the upper atmosphere directly.

The measurement using the sounding rocket provides information with good altitudinal resolution during the flight. But it is not possible to conduct such measurements for a whole day or day-to-day basis. The on-board satellite measurement provides data over a wide range of spatial regions, although, it is difficult to get data with high temporal resolution for a particular location. Another way of probing the upper atmosphere is through remote sensing, which can be both in active and passive. For examples, radar measurements are direct remote sensing in which radio signals are transmitted towards the atmosphere, and the reflected echo is received after their interaction with the ambient plasma constituents of the target region. For aeronomy studies, VHF, HF, MF, and meteor radar are used, which works at higher transmission frequencies. There are various kinds of emissions that occur in the upper atmosphere during both day and nighttime, which act as passive remote sensor of the medium. These emissions are generated through different photo-chemical reactions, which produce photons of different wavelengths originating at different altitudes depending on the reaction rates and concentrations of the reactants present at those altitudes. Both ground-and space-based optical instruments can be designed to measure those emissions, which can provide the information corresponding to the altitudes in the upper atmosphere from where these emissions emanate. Besides this, magnetometers are used to measure the magnetic field which is induced due to the ionospheric and magnetospheric currents.

In this thesis work, OI 630.0 nm nightglow emissions are used in the investigation of upper atmosphere. Such measurements have been carried out using optical instruments, such as High Throughput Imaging Echelle Spectrograph (HiTIES) and All-Sky Imager (ASI), which are commissioned at Mt. Abu (24.6°N, 72.7°E, 19°N Mag) and Kolhapur (16.8°N, 74.2°E, 10.4°N Mag), respectively. Mt. Abu is located under the northern crest of the EIA, whereas Kolhapur is located between the trough and crest region. The details of the image processing and extraction of nightglow emissions are described in this chapter. In addition, ionosonde data over Ahmedabad (23.0°N, 72.6°E, 17.3°N Mag), a low-latitude location, and Trivandrum (8.5°N, 76.9°E, 1.1°N Mag), a dip-equatorial location have been used in this thesis work. The ground-based magnetometer data over Tirunelveli (8.7°N, 77.7°E, 0.2°N Mag) and Alibag (18.6°N, 72.9°E, 12.4°N Mag) in the Indian sector, and Jicamarca (11.9°S, 283.1°E, 0.05°S Mag) and Piura (5.2°S, 279.4°E, 6.4°N Mag) in the American sector have been used to obtain the strength of the EEJ at

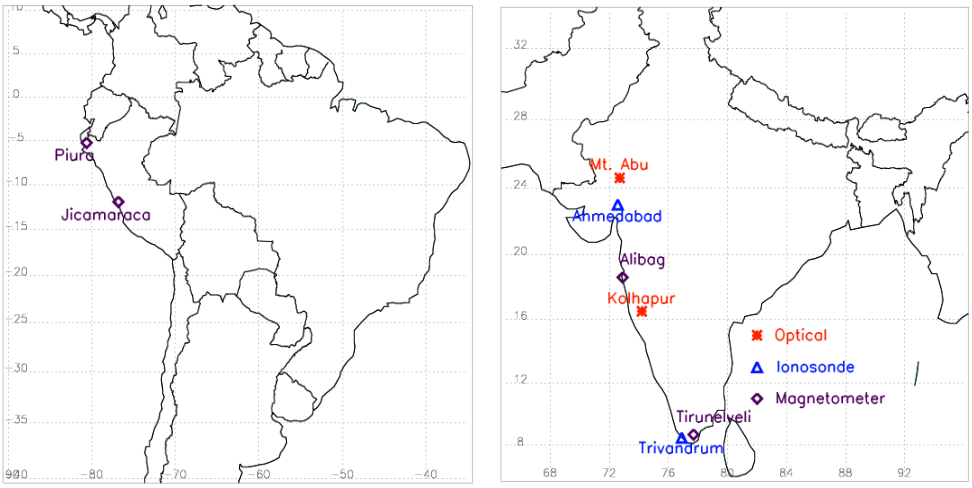

Figure 2.1: The locations of different Instruments, such as spectrograph, all-sky imager, ionosondes, and magnetometers used in the thesis work are shown here.

two different longitudinal sectors. The details of the estimation of EEJ are described in section 2.5 of this chapter. The different instruments located at different locations are depicted in figure 2.1. The geographic longitudes and latitudes are mentioned in the x- and y-axes, respectively.

2.3 Optical techniques

2.3.1 High Throughput Imaging Echelle Spectrograph (HiTIES)

HiTIES is a slit spectrograph oriented in the north-south direction with a field-of-view (FOV) of around 54°. HiTIES uses echelle grating as a dispersive element, field lens, collimator lens, imaging lens, mirror, interference filter, and CCD as detector (*Chakrabarti et al.*, 2001). The schematic of HiTIES is given in figure 2.2. A detailed description of the optical components and image processing techniques of the images obtained from HiTIES are discussed below.

2.3.1.1 Components of HiTIES

Fore optics: The fore optics of HiTIES consists of an objective lens, a slit (60 mm × 0.468 mm), and a field lens (plano-convex of 70 mm focal length). The focal length of the

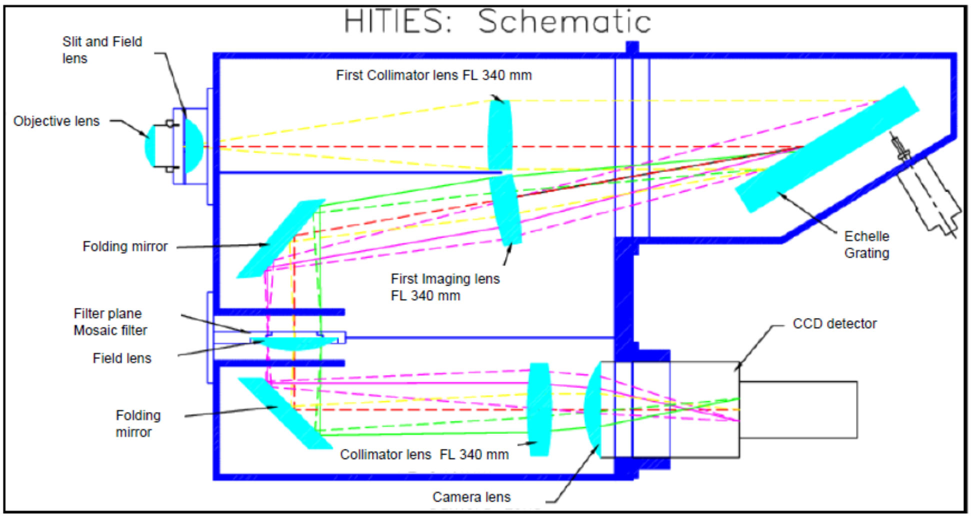

Figure 2.2: Schematic of HiTIES

objective lens decides the FOV of the instrument. The ray enters through the objective lens and is focused onto a narrow slit. A long slit has been used to increase the throughput. The width of the slit is calculated using the single slit interference experiment in the laboratory. He-Ne laser has been used as a source of light. When the laser light incident on the slit, yields interference pattern. Using the distance between the image and slit, and the separation between two constructive interference patterns, the slit width has been calculated, which has been found to be 0.468 mm. This high throughput makes the HiTIES capable of obtaining the nighttime sky spectrum and thereby capturing the faint nightglow emissions. As a consequence of the long slit, the spectral lines become curved as image forms on the detector, as shown in figure 2.3a. The aberration of the off-axis diffracted rays causes the curvature in the line spectra. Sodium and hydrogen lamps are used as light sources as shown in figure 2.3a. The simulated line spectra obtained using ray tracing is shown in figure 2.3b. A curved input slit is used to reduce this curvature in the image of the HiTIES. After passing through the slit, the light becomes divergent. A plano-convex field lens is used to reduce this divergence. The focal length used in the field lens is 70 mm.

Collimator and imaging lens: Two collimators and two imaging lenses are used in HiTIES. The main objective of the collimator is to make the light ray parallel, whereas, the imaging lens guides the light ray to converge on the focal point. Light rays passing through the first collimator lens fall on the dispersive element of HiTIES, the echelle grating. Two collimator lenses and the first imaging lens are of f/3.4 optics. F-number is defined by

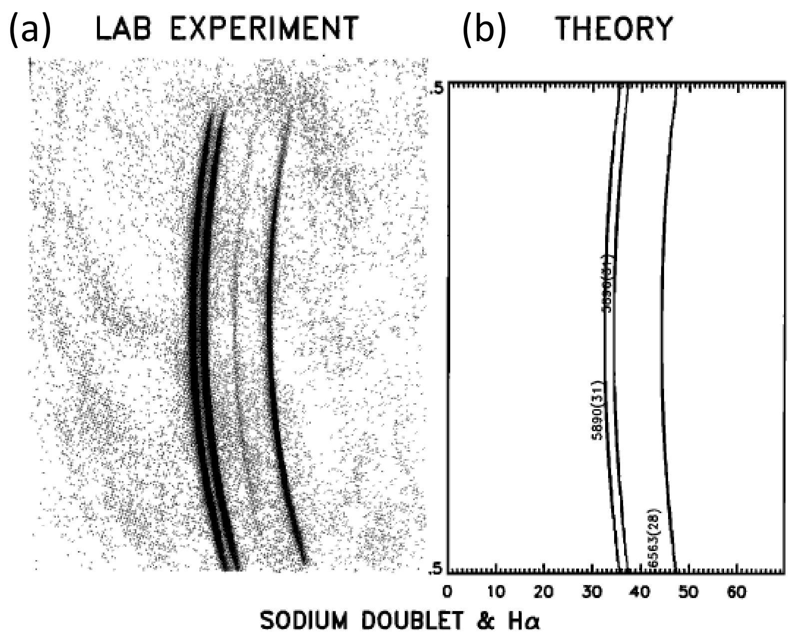

Figure 2.3: (a) The image formed using sodium and hydrogen lamps as light sources obtained during the lab experiment. (b) The result obtained by using the ray tracing for the same source wavelengths is shown.

the ratio of focal length to the aperture of the lens. The larger the f-number smaller the aperture and vice-versa for a given focal length. In other words, f-number decides the image size. The nighttime optical measurements require larger aperture (smaller f-number) to collect larger numbers of photons as the signals are low. The size of the image which can be optimally acceptable by the size of the CCD chip and the amount of light needed to be collected, are the aspects decided by the f-number of the lenses used in an optical instrument. After diffraction from the echelle grating, the light rays are focused on the filter by the first imaging lens. Another set of collimator and imaging lenses are used before the light is focused on the detector. The f-number used in the second imaging lens/ camera lens is 1.2 to reduce the image size by almost one-third so that it can be fit on the detector chip.

Echelle grating: The heart of the instrument is the echelle grating which helps in achieving high spectral resolution. Unlike normal gratings, echelle gratings are operated at higher spectral orders. The normal gratings (use to work in first or second diffraction order) have groove density of around thousand lines per mm, whereas the echelle gratings have groove density of the orders tens to a hundred lines per mm (works in higher

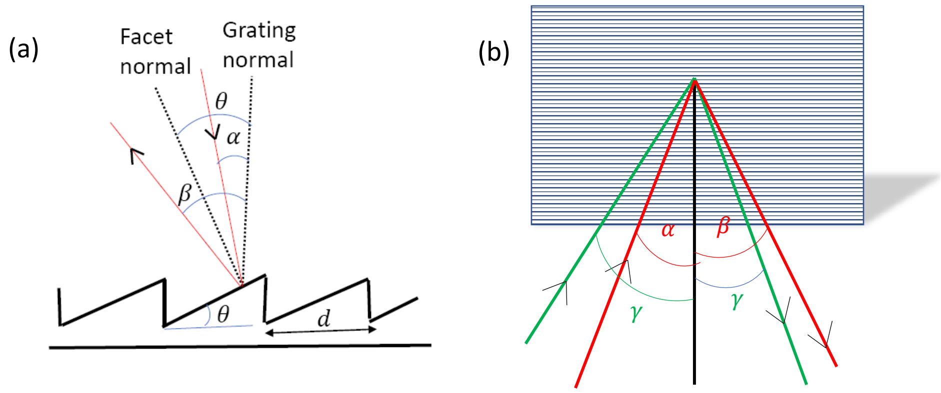

Figure 2.4: (a) Schematic structure of echelle grating and the parameters associated with it. α and β are incident and diffraction angles, respectively. (b) The lateral angle (γ) is depicted which creates curvature in the image.

diffraction order). HiTIES uses the echelle grating, having ruled area of around 102 mm $\times$ 206 mm, with line spacing of 98.76 grooves/mm. The grating equation is given by,

$$d(\sin\alpha + \sin\beta)\cos\gamma = n\lambda \tag{2.1}$$

where, α and β are incident and diffraction angles, respectively, d is the groove spacing, γ is the lateral angle, λ is wavelength, and n is the order of diffraction as shown in figure 2.4. The lateral angle, γ (figure 2.4b), the off-axis rays make the diffraction pattern curved while diffracted from the grating.

Differentiating equation 2.1 with respect to λ, we get,

$$\begin{aligned} d\cos\beta\frac{d\beta}{d\lambda} &= n \\ \frac{d\beta}{d\lambda} &= \frac{n}{d\cos\beta} \end{aligned} \tag{2.2}$$

Substituting $\frac{n}{d}$ from equation 2.1, we get equation 2.3 after considering the normal incidence ($\gamma = 0$),

$$\frac{d\beta}{d\lambda} = \frac{\sin\alpha + \sin\beta}{\lambda\cos\beta} \tag{2.3}$$

From equation 2.3, it can be noted that the angular dispersion ($\frac{d\beta}{d\lambda}$) depends upon the incident and diffraction angles. Therefore, to obtain the high spectral resolution, the light rays are designed to fall at high incident angles. The blaze angle of the grating, $\theta = (\alpha + \beta)/2$, is 63.5° where the incident angle (α) is 58.5°. The maximum angular dispersion can be achieved in the Littrow configuration ($\alpha = \beta$), and so, α and β are chosen close to θ. For greater efficiency (ratio of diffraction to incident intensity) of the grating, the facet length, $d\cos\theta$ is needed to be larger and as the blaze angle is high, the d should be large. When high values of the incident angle (α), diffracted angle (β), and small values of groove spacing (d) are considered in the relation 2.2, higher spectral resolution is possible at higher values of n. In HiTIES, the diffraction order is turns out to be 28 for 630.0 nm. Thus, HiTIES achieves higher dispersion by operating in high diffraction orders.

From the equation 2.1, it can be seen that different wavelengths of different orders are satisfied for a given α and β ($n_1\lambda_1 = n_2\lambda_2$), which means that different orders of different wavelengths are diffracted in the same direction. It is also seen through the ray trace computation (figure 2.5a) that the different wavelengths of different orders appear at the same diffraction angle. The order overlap depends on the free spectral range (FSR). The range of wavelengths in a given spectral order for which light does not coincide with the adjacent order is called the FSR. It can happen that the light of wavelength $\lambda + \delta\lambda$ is diffracted in a position with order m, whereas at the same location, light of wavelength λ is diffracted with order m+1, i.e., $m(\lambda + \delta\lambda) = (m+1)\lambda$. Figure 2.5b shows the FSR for a given set of diffraction orders where the values of angle of incidence and diffraction, and groove separation are used, as mentioned earlier. The wavelength gaps can be noted to be increasing with the increasing wavelength and with the decreasing diffraction order. As the objective of HiTIES is to observe multiple wavelengths, the diffraction orders fall in the range of 20 to 40 for the observation of desired wavelengths. Therefore, there are many possibilities for overlapping different wavelengths of different orders satisfying the $n_1\lambda_1 = n_2\lambda_2$ condition.

Mosaic Filter and Folding Mirrors: As discussed earlier, the echelle grating is used as the dispersing element in HiTIES which works in higher diffraction orders. We have also discussed that in the high diffraction orders FSR decreases which causes the problem of order overlapping. Due to this reason, even though the echelle grating provides the

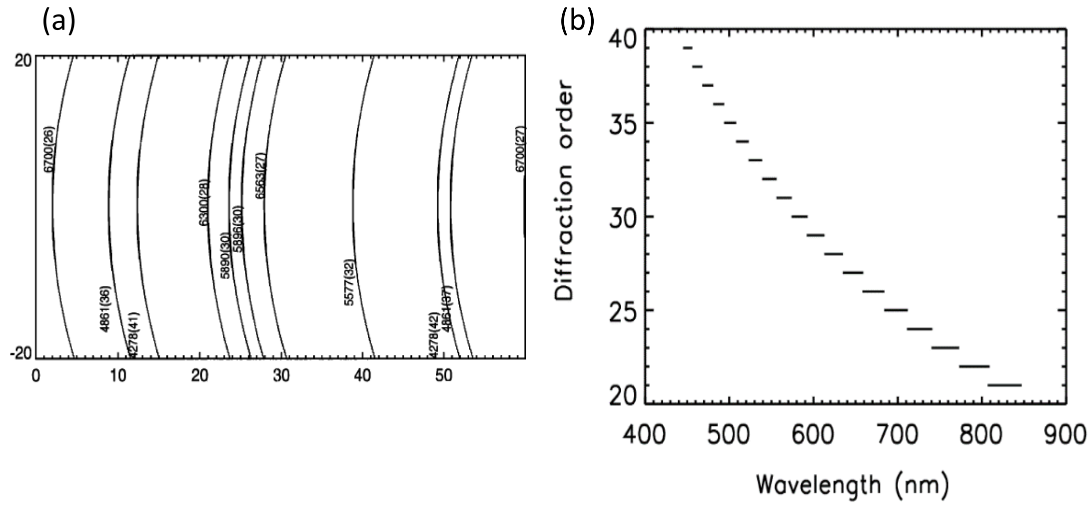

Figure 2.5: (a) The line spectrum simulated using the ray tracing method. Several prominent airglow emission lines and some test lines are used here. (b) The range of wavelengths diffracted for a given order is shown in each of the horizontal lines. All the wavelengths of different orders will appear simultaneously on the detector. As orders of diffraction increase, the regions of wavelength gaps decrease.

higher resolution, this dispersive element could not be used effectively in the past. In the past three decades, after the discovery and development of narrow bandwidth interference filters, the high-resolution capability of echelle grating has gained the importance (e.g., *Chakrabarti et al.*, 2001, 2012; *Pallamraju et al.*, 2000, 2002, 2013; *Galand et al.*, 2004; *Pallamraju and Chakrabarti*, 2006; *Marshall et al.*, 2011). Interference filters can have very narrow bandwidth, and therefore, light solely from the desired wavelength ranges is allowed to pass through it. Mosaic filters are made by joining interference filters of different central wavelengths and are essentially used to avoid order overlap. The diffracted rays cover multiple wavelengths corresponding to different orders in the same diffraction angle. While they pass through the mosaic filter, the wavelengths which are out of the filter's bandpass are filtered out and only the wavelength corresponding to the bandwidth of the filter is allowed to pass through in a given panel of the mosaic filter. Figure 2.6 shows a sample of a mosaic filter where three different interference filters are glued to one another. From left to right, 630.0, 777.4, and 557.7 nm interference filters are glued together, as shown in this figure.

Figure 2.7 shows the ray trace plot of figure 2.5a using a five-panel mosaic filter which had been designed during the calibration of HiTIES. Five filters having central wavelengths of 486.1, 630.0, 656.3, 557.7, 427.8 nm are used here. The emission lines are made to image in a distinct location in the detector. HiTIES uses a four-panel mosaic filter which allows the wavelengths of 486.1, 557.7, 656.3, and 630.0 nm and the full width at half maxima (FWHM) of around 10-20 nm. Two folding mirrors are used to direct the rays inside the instrument (figure 2.2).

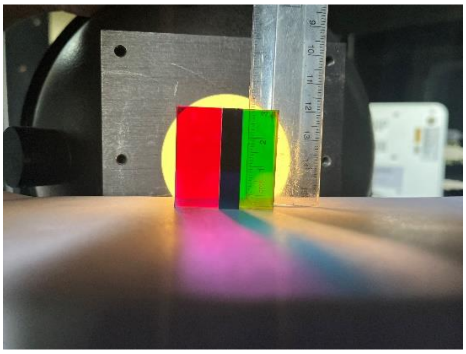

Figure 2.6: Sample picture of mosaic filter where 630.0, 777.4, and 557.7 nm interference filters (left to right) are stacked.

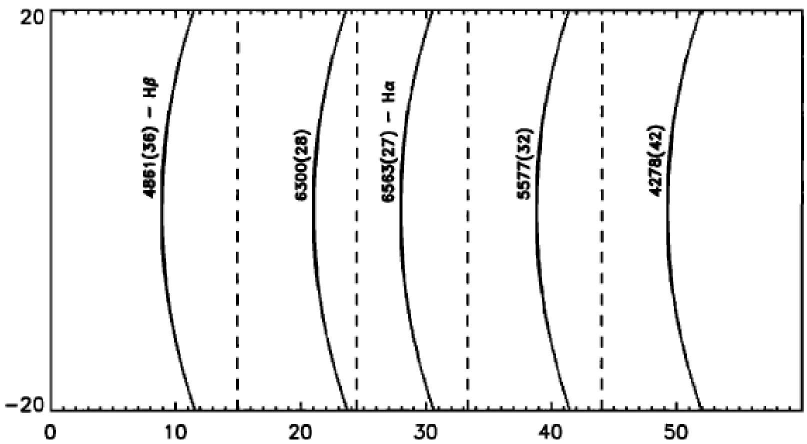

Figure 2.7: Using the five-panel mosaic filters, such as H_β (486.1 nm), 630.0, H_α (656.3 nm), 557.7, 427.8 nm, the wavelengths in the line spectra shown in the figure 2.5a are filtered.

CCD detector: Charge coupled device (CCD) is highly sensitive and effective tool for recording a spectral image. It consists of a large number of small sensitive areas, which are known as pixels. The major components of the CCD are silicon sensors and capacitors. The silicon sensor produces electrons as the photons of the visible light (or nearby the visible region) fall on it. The capacitor collects these electrons, and the voltage across the capacitor is noted, which is proportional to the charge collected. This information is sent to the computer. This combination of silicon sensor and capacitor is miniaturized into an integrated circuit that represents one pixel. HiTIES uses a 1024 × 1024 pixels Andor CCD detector where a given row and column provides the spectral and spatial information, respectively. It is binned (1×16) in the spatial direction to improve the signal-to-noise ratio (SNR). The CCD is operated at a temperature below -35°C to reduce the thermal noise. The dark signal and read noise values are around 0.05 electrons sec^{-1} $pixel^{-1}$ and 9 electrons RMS, respectively. The quantum efficiency of the detector is 90% for the spectral region at which HiTIES is designed to operate. The size of each pixel is 13 μm in the image plane of 13.3 mm × 13.3 mm which contains the 1024 × 1024 pixels. Further, the values of these CCD parameters are used in the calculation of intensity calibration and the uncertainty of the measurement, as mentioned in sections 2.3.1.3 and 2.3.1.5, respectively.

Data Acquisition System: HiTIES is operated in a fully automated mode. The scripts, which contain the information of date and time, exposure time, and desired CCD temperature written in visual basic language, enable the operation of CCD that is interfaced with MaximDL software.

2.3.1.2 Image Processing and extraction of nightglow

As discussed above, HiTIES is a multiwavelength spectrograph that is used to observe the thermospheric airglow emissions during nighttime. In this thesis work, we have studied the OI 630.0 nm nightglow emissions which emanate from the altitudinal region of 250 km in the nighttime. The generation mechanism of OI 630.0 nm is discussed in section 3.2 of chapter 3. The typical OI 630.0 nm spectral emission line as obtained from HiTIES is shown in figure 2.8a. The x-axis and y-axis correspond to the spectral and spatial information, respectively. From top to bottom, there are 64 pixels in the y-direction after the binning. The curvature seen in the image arises from the aberration due to the off-axis diffraction of the light passing through the long slit. Dark counts have been subtracted from every image, and the median filter is applied to remove the spurious counts (such as those occur due to cosmic ray hits or bad pixels). The median filter (3×3) replaces the center element with the median value of the given array. The spurious counts that appear

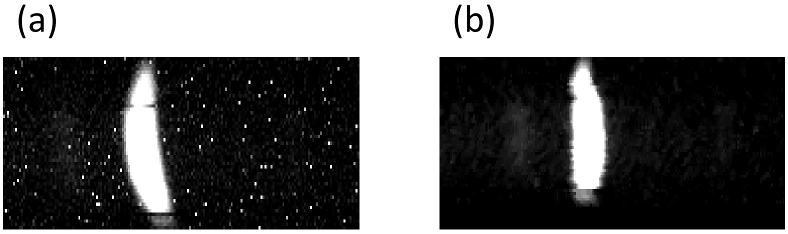

Figure 2.8: (a) Sample image as obtained from HiTIES. (b) The image was obtained after processing through dark subtraction, median filter, and straightening, as discussed in the above section.

in the image (figure 2.8a) are smoothed out after applying this correction, as shown in figure 2.8b. Then the curved image has also been made straight by shifting the rows, as also depicted in figure 2.8b. One can notice the two horizontal dark lines in the top and bottom part of the image 2.8a (on the top side, it appears at 15^{th} pixel, and in the bottom part, it appears at 46^{th} pixel), which occurs due to the obstruction of light by two side rods of the structure that hold the instrument. This blockage of light intensity has been removed through flat-fielding of the images, which is discussed next.

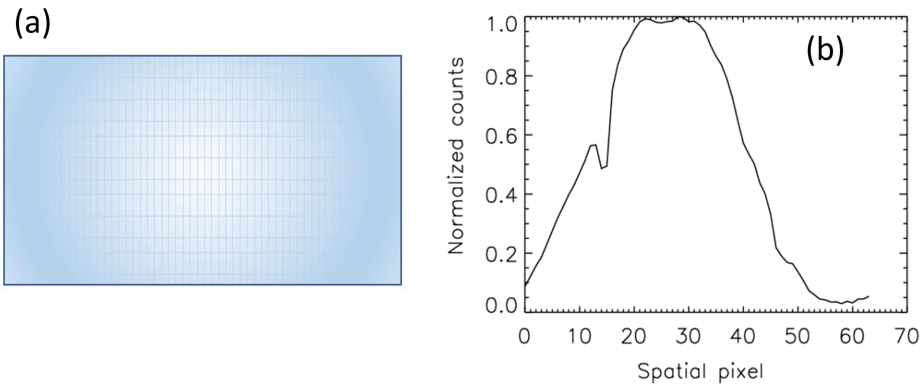

Figure 2.9: (a) A schematic which shows the non-uniform intensity distribution with respect to spatial direction that is caused due to the vignetting effect. The central part shows larger counts whereas, as one moves towards the edges the photon counts decrease. (b) The vignetting effect has been corrected through this normalized flat-field counts obtained from HiTIES.

The illumination per pixel decreases as the pixel number increases away from the centre, even when the light is uniform over the whole FOV of the instrument. It is due to the reduction in the light allowed by the off-axis rays passing through the system. This is called vignetting effect. Figure 2.9a shows a schematic of the non-uniform illumination of light over the different arrays. The central portion has larger illumination, whereas, one moves away from the centre, the intensity decreases. The normalized intensity counts of the spatial direction are shown in figure 2.9b as obtained from HiTIES. This is obtained during the twilight time in a month when the twilight brightness can be considered to be uniform. This is used as a flat-field image and has been taken when the solar zenith angle is about 90° and the Sun is situated in the same latitudinal plane of Mt. Abu (i.e., the azimuthal angle is almost zero). At such conditions, the light ray is expected to be of uniform intensity within the whole FOV of HiTIES as it is mostly scattered light. This reference flat-field image had been taken on 21 Apr and 22 Apr 2017 during the twilight time (figure 2.9b). The zenith shows maximum intensity, and as one moves away from the zenith, the intensity decreases. The vignetting effect that is present in the HiTIES images ($I_{image(x,y)}$) has been corrected by dividing this normalized flat-field counts as shown in equation 2.4.

$$I_{x,y} = \frac{I_{image(x,y)}}{I_{flat(x,y)}} \tag{2.4}$$

As airglow emissions obtained from the ground are column integrated, the emission brightness from the direction other than zenith is larger than those from the zenith (figure 2.10a) under the assumption that the emissions are uniform over a given spatial distance. This is called the Van Rhijn effect. This effect has been corrected by using the following relation given in *Roach and Gordon* (1973).

$$I_{zenith} = I_z\sqrt{1-(\frac{R}{R+h})^2\sin z^2} \tag{2.5}$$

Here, R is the radius of the Earth, h is the altitude from where the emissions are originating, and z is the zenith angle. The emission intensity coming from zenith direction and at a certain zenith angle, z, is noted as I_{zenith} and I_z, respectively. The effect of Van Rhijn effect with the variation in zenith angle and altitudes is shown in figure 2.10b. Although the Van Rhijn effect is very small for the given FOV of HiTIES, it is corrected for the present analysis.

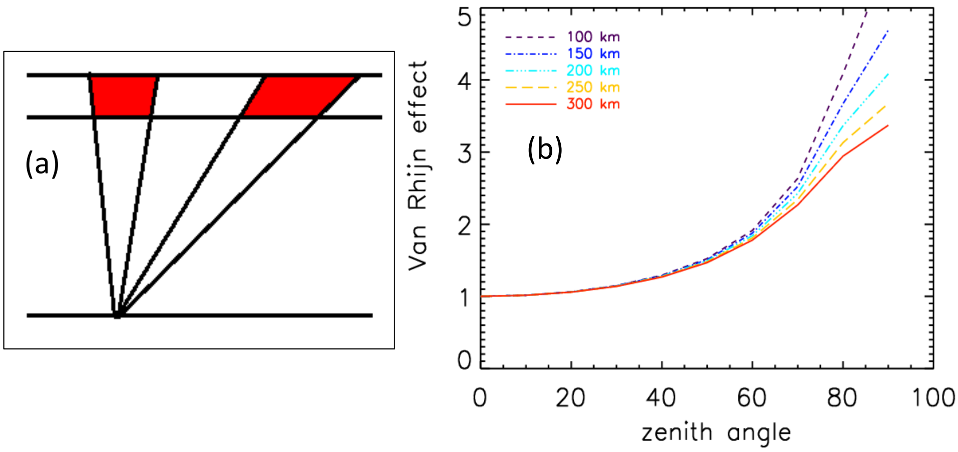

Figure 2.10: (a) The difference in column intensity when it is observed over the zenith and with some angle. This is called Van Rhijn effect which causes larger emissions as observed in the emissions far away from zenith. (b) The effect of Van Rhijn is shown with varying altitudes and zenith angles.

Thus, the images obtained from HiTIES have been processed following the dark count subtraction, smoothing with median filter, and straightening the curvature formed in line spectra. After that, the vignetting effect and the Van Rhijn effects have been corrected. The emission region is integrated to obtain the OI 630.0 nm nightglow emission rates as shown in figure 2.11. It can be noted that the emission intensity does not cover the whole spatial length. It has been observed that the image has been formed up to 52 pixels starting from pixel 01 in the spatial direction. Due to some obstacle in the south side, light could not enter through some parts of the slit in the southern side. A non-airglow spectral region away by 0.5 nm has been integrated and subtracted from the airglow count to remove the contribution of background scattering of the nighttime sky, which can arise from star light, zodiacal light etc. (figure 2.11). This background is typically around 1 Rayleigh Å^{-1} in the nighttime sky (*Broadfoot and Hunten*, 1966). In all these corrections, the counts corresponding to the same row have been considered, thereby, all conditions (new direction, slit width, vignetting, and Van Rhijn effects) are maintained to be equal.

2.3.1.3 Intensity Calibration

The extracted OI 630.0 nm nightglow emissions as discussed in the above subsection 2.3.1.2, are not the actual brightness of the source. The data numbers (DN) obtained

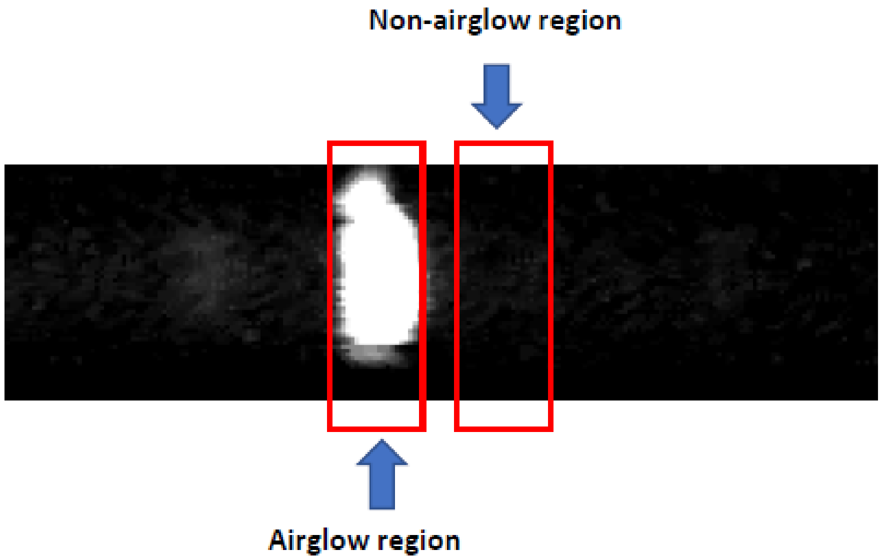

Figure 2.11: The OI 630.0 nm emission region as detected in CCD image. The non-airglow region is marked, which is subtracted from the airglow region to remove the contribution of background scattering in the measured emissions.

from the CCD are converted to the actual brightness of the source emission in Rayleighs using the known parameters of the optical instrument (*Chakrabarti et al.*, 2001). As explained in an earlier report for a daytime spectrograph (*Pallamraju et al.*, 2002), the brightness (B) of the source in Rayleighs (R) (1 Rayleigh= 10^6 photons cm^{-2} sec^{-1}) can be calculated as,

$$B = \frac{N}{S_{pix} \cdot t} \tag{2.6}$$

where, N is the number of photons passing through the instrument, S_{pix} is the sensitivity of the instrument in the unit of Data numbers per Rayleigh-second for the given pixel (pix), and t is the integration time.
S_{pix} can be calculated using the following formula:

$$S_{pix} = \frac{10^6}{4\pi} \cdot Q(\lambda) \cdot \tau \cdot A \cdot \Omega \cdot \frac{d}{n_{rows}} \tag{2.7}$$

As discussed earlier, the dimension of the slit is 60 mm × 0.47 mm. But, due to some obstacles, light does not enter through the whole length of the slit as mentioned earlier, but from around 43 mm which is calculated as =(52×16×13×4)/1000=43.26 mm.

wherein, the image formed on the detector is 1-52 pixels, as we have discussed earlier that each pixel is binned by 16 pixels in the spatial direction. The f-number of the field lens is of f/4 which means it reduces the image size by a factor of 4.

The throughput of the instrument, $A\Omega = (0.047 \times 4.326)/34^2 \times \pi \times 5^2 = 0.0138$ cm^2 sr, where, focal length and diameter of the collimator lens are 34 cm and 10 cm, respectively. Using the known values of different parameters of HiTIES as mentioned in table 2.1, we have calculated S_{pix}·t value, which is 5.8 DN Rayleigh^{-1} nm^{-1}, where t=300 sec. The data numbers obtained from HiTIES is divided by this factor to yield the information on the source brightness in Rayleigh (R).

Table 2.1: *Parameters of HiTIES used for brightness of observed 630.0 nm airglow*

Parameter	**Symbol**	**Value**
Overall efficiency of the CCD (quantum efficiency q(λ)/gain (g))	Q(λ)	(0.9/2.66=) 0.34
Optical efficiency	τ	0.135
Throughput (A= Area of the slit, Ω= solid angle formed by the slit)	$A\Omega$	0.0138 cm^2 sr
Dispersion	d	0.02 nm pix^{-1}
Number of rows co-added in the spatial direction along the slit	n_{rows}	52
Integration time	t	300 sec.

2.3.1.4 Angle Calibration

As we discussed earlier, HiTIES is a slit spectrograph oriented in the geomagnetic north-south direction. Light from different regions of the meridian direction contributes to the image formed on the detector. The view from the top of the hood is shown in figure 2.12a. The north-south direction is depicted here. The dashed line indicates the zenith position of HiTIES. The spatial information to which a given pixel corresponds, on-field experimental testing was carried out to calibrate the spatial information. Light is allowed to enter the instrument at different angular positions (θ) which is detected in different pixel numbers of the CCD. We have noted the different values of θ and the corresponding locations on the CCD. In this way, we have measured the FOV of HiTIES. A schematic of the FOV of the HiTIES that measures the OI 630.0 nm nightglow which is having peak emissions at around 250 km altitudes, is shown in figure 2.12b.

The calculated pixel numbers and the corresponding view angles are shown in figure 2.13. A linear fit has been carried out between the two, which resulted in the following equation: $y = -1.053x + 27.13$. The total FOV of HiTIES has been obtained around 54°; 27° on the either side of the zenith. Now, we have segregated the whole FOV region into five directions. The angular width and the corresponding pixel regions, taken for different directions, are shown in table 2.2.

Table 2.2: *View-angle of five directions and corresponding pixel numbers*

Direction	View Angle	Pixel numbers
Extreme north	15° to 27°	1-10
North	5° to 15°	11-20
Zenith	5° to -5°	21-30
South	-5 to -15°	31-40
Extreme south	-15° to -27°	41-52

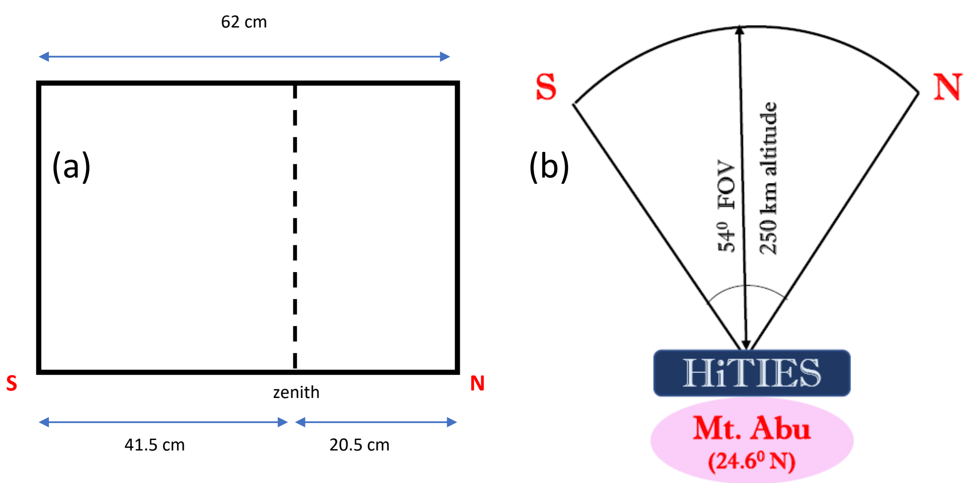

Figure 2.12: (a) The top view over the hood and the zenith position of HiTIES is marked. (b) The peak emission altitudes of OI 630.0 nm nightglow emissions and FOV of HiTIES.

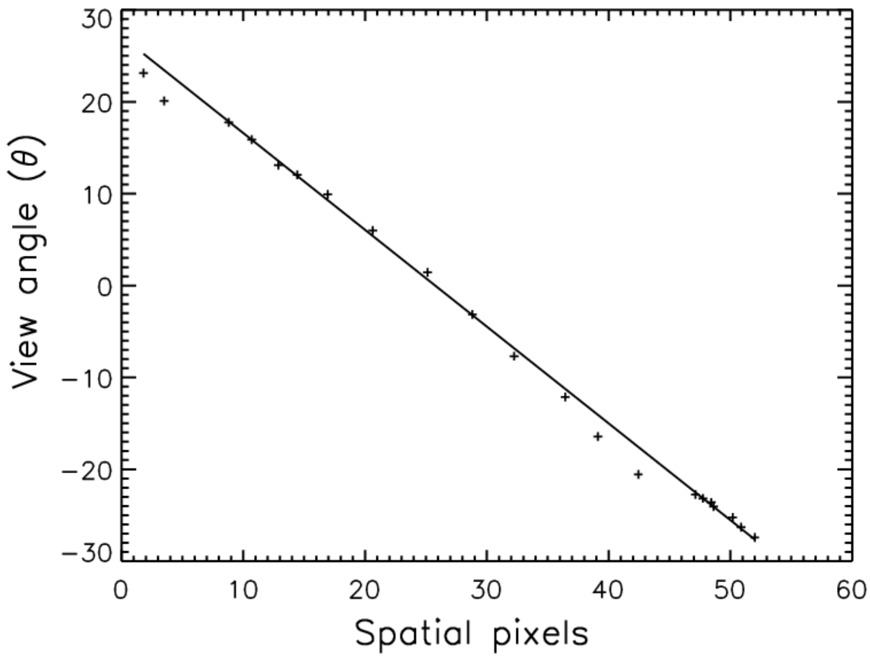

Figure 2.13: The lights coming from different angles are imaged at different pixel numbers.

2.3.1.5 Signal-to-noise ratio (SNR) and Uncertainty of measured nightglow

The signal-to-noise ratio (SNR) determines the strength of the signal over the noise generated by the instrument. The noise of the instrument originates due to various factors, such as the dark noise, readout noise, quantum efficiency of the CCD, etc. The dark noise (D) appears due to the thermal electron produced by the CCD temperature. For this reason, the CCD temperature is kept at around -35°C. The inhomogeneous performance of each detector array at the time of reading process and associated electronics causes the CCD readout noise (R). The SNR of the instrument is given by (*Roesler and Sica*, 1986; *Baumgardner et al.*, 1993; *Pallamraju*, 2003), $SNR = \frac{S}{\sqrt{S+B+D+R}}$, where, S=signal, B=background noise, D=dark noise/ thermal noise of the detector, R=readout noise of the detector.

The expression of these parameters depends upon several variables of the detector, such as quantum efficiency, readout and dark noise, pixel binning, and other components of the instrument, such as transmission coefficient of the optical components, exposure time, etc. The quantum efficiency describes the percentage of incoming photons which are detected by the CCD. Here, we have used the CCD with quantum efficiency (qe) value of 0.9 which means that 90% of the photons falling on the CCD are detected. The

Table 2.3: *CCD parameters and other variables used to calculate the SNR of HiTIES*

Parameter	**Values**
detector quantum efficiency (qe)	0.9
Filter transmission (ft)	0.7
Exposure time in seconds (t)	300
Background continuum in R/Å(bg)	1
Filter area/ bandwidth in Å(fa)	10
Dark noise in $e^{-1}pix^{-1}sec^{-1}$ (d)	0.05
Readout noise, e^{-1} (RMS) (ro)	9
No. of pixels binned before readout (be)	16
No. of pixels binned after readout (af)	1
Photons sec^{-1} R^{-1} incident on a pixel for a given f-number (k)	11.48×10^{-2}
System efficiency (se)	0.0135

dark noise (D) is thermally generated noise, whereas the readout noise (R) arises from the conversion of electrons detected at each pixel to the voltage in the CCD output. The charges collected from several adjacent pixels have been binned which results in reduction of readout noise and increase the SNR. The noises that arise in the instrument depend on the binning size, exposure time, number of pixels co-added after readout, etc. The transmission coefficient of the different optical components used in HiTIES determines the efficiency of the instrument. The expression of the parameters S, B, D, and R are shown below, and the values of various factors upon which these parameters are dependent are given in table 2.3.

$S = qe \cdot s \cdot ft \cdot t \cdot be \cdot af \cdot no \cdot k \cdot se$; $B = qe \cdot bg \cdot fa \cdot t \cdot be \cdot af \cdot no \cdot k \cdot se$

$D = d \cdot t \cdot be \cdot af \cdot no$; $R = no \cdot af \cdot (ro)^2$

The values of signal strength (s) and number of co-adds of the pixels after readout (no) depend upon the spatial region we are looking for. Using the values mentioned in table 2.3, we get,

$$SNR = \frac{4.69 \times s \times no}{\sqrt{no \times (4.69 \times s + 387.9)}}, \quad for\ no = 10 \tag{2.8}$$

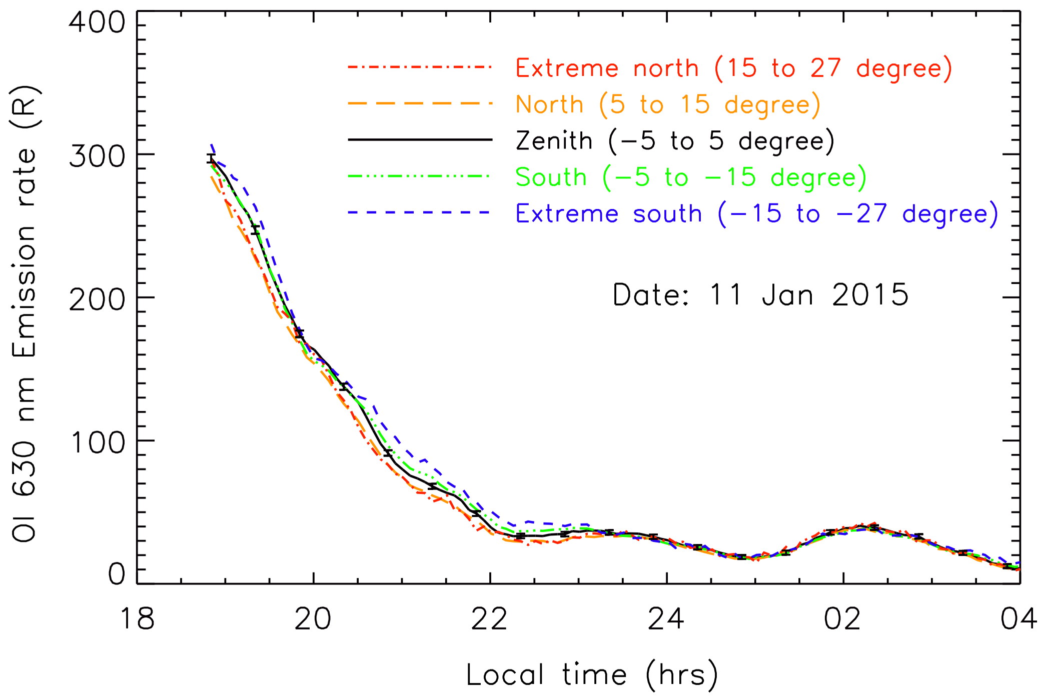

Figure 2.14: The nightglow variation of OI 630.0 nm emissions for different five view directions are shown for a sample night. It can be seen that the emission decreases monotonically after the sunset as the ionization stops after that time.

Using the above parameter values and the formula, we obtained the error in the measurement as follows:

For the signal value, s= 100 R, SNR= 50.6; s= 10 R, SNR= 7.1.

The uncertainty in the measurement is 1/ SNR. Therefore, for the SNR value 50.6, uncertainty=2%; SNR value 7.1, uncertainty=14%.

In section 2.3 of this chapter, we have discussed the instrumentation of HiTIES, the image processing, corrections for vignetting and Van Rhijn effects, and thereafter, the intensity calibration and uncertainty of measurements have been discussed. The OI 630.0 nm nightglow variations have been depicted in figure 2.14 for a given night on 11 January 2015 . The HiTIES starts the observation every night in a programmed manner at 18:45 LT and till early morning. The OI 630.0 nm nightglow emissions obtained from all five directions as discussed earlier are shown in the figure 2.14 in different colours and line styles. The uncertainty in the measurement is around 1-3 R and is shown in vertical bar in the emission variation over the zenith.

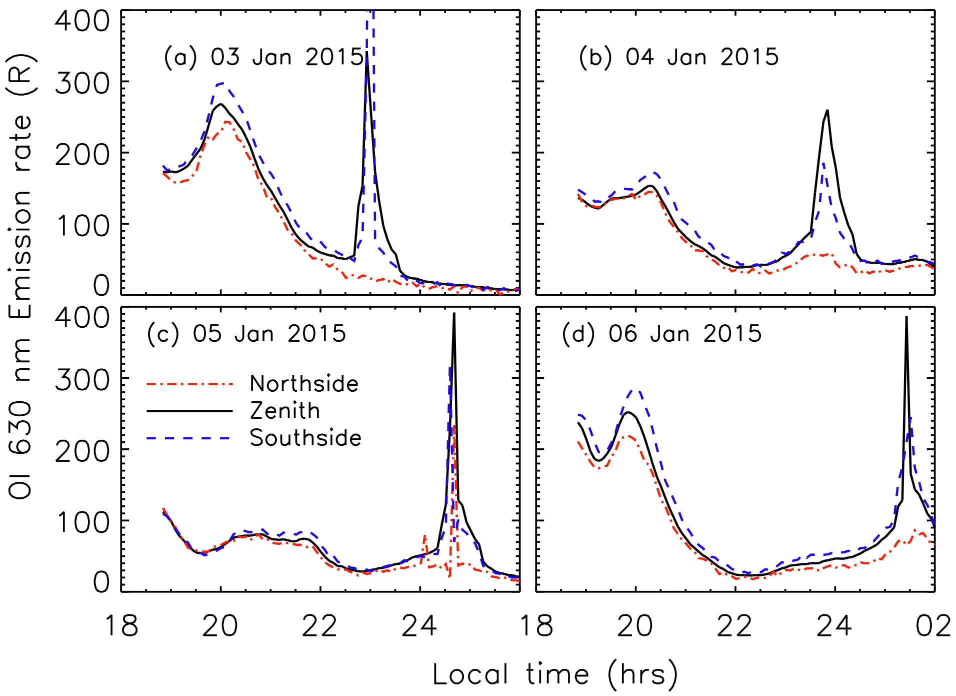

Figure 2.15: The variation in OI 630.0 nm emissions of four consecutive nights are shown. The sharp increase in emission manifests the presence of moonlight that came within the FOV of HiTIES.

2.3.1.6 Effect of moonlight and starlight present in the FOV of HiTIES

Moonlight and starlight are the main background light sources present in the night sky. When the moon passes through the FOV of HiTIES, a huge brightness can be detected on the detector which also gets saturated. Figure 2.15 shows the temporal variations of OI 630.0 nm nightglow emissions of four consecutive nights, where the large spikes in the emissions indicates the presence of moonlight in the FOV. The emissions are shown from three different directions and it can be noted that the intensity/ effect of moonlight is not equal in all the directions. As the phases of the moon and its orbital path change from night to night, the occurrence time of the spike in emissions due to the moonlight also shifts in consecutive nights.

Sometimes, a star might appear in the FOV of the instrument. As the starlight emits blackbody radiation, the brightness of the star is seen in all the spectral panels of HiTIES. Therefore, a straight horizontal line can be seen in the figure 2.16 which is a signature of starlight. Three consecutive images are shown for a particular night where the middle

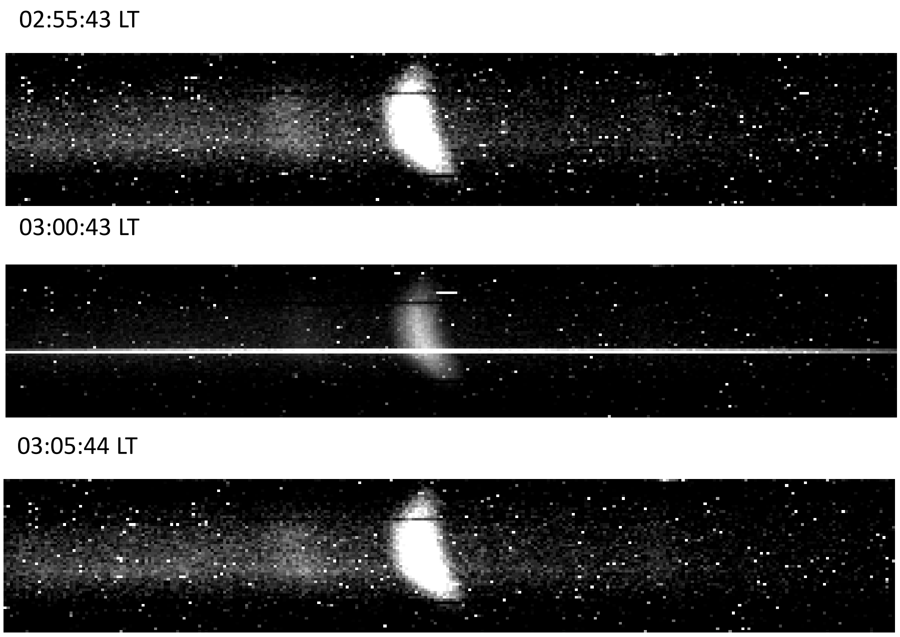

Figure 2.16: Presence of star light in the HiTIES image is shown of the night 11 Jan 2015. The local time is mentioned in hh:mm:ss format for each image. Three consecutive images are shown of which the middle shows the presence of a star in the FOV. The star emits light in the whole spectral region of the electromagnetic spectrum, so it is seen in all the wavelengths range in the 630.0 nm filter.

one shows the appearance of starlight. The local time information is shown above each image. It is clear that this starlight is not seen in the previous and later images as these two are separated by 5 minutes of the central image, and within this time duration, the star moved away from the FOV of HiTIES.

2.3.2 All-Sky Imager (ASI)

In this thesis work, we have also used the measurements of OI 630.0 nm nightglow emissions obtained from a CCD based (1024×1024 pixels) all-sky imager (ASI) operated from Kolhapur. The ASI measures different emissions (OI 630.0 nm, 555.7 nm, 840.0 nm, 846.0 nm, OH Meinel bands) that originate at different altitudes of the upper atmosphere. ASI operates over a large FOV of around 140°, covering around 1200 km spatial distance for OI 630.0 nm emissions in both zonal and meridional directions. We have used the OI 630.0 nm emissions obtained from ASI to investigate the plasma bubble features over

Kolhapur. Kolhapur is located in between the magnetic equator and the northern crest of EIA, almost at the same longitude of Mt. Abu and Ahmedabad, as shown in figure 2.1. The imager consists of front-end optics (fish-eye lens, field lens), collimator lens, filter panel, camera lens, and detector (*Mukherjee et al.*, 1998; *Narayanan et al.*, 2009; *Sharma et al.*, 2014). A detailed description of the instrumentation of the imager is available in the literature (*Sharma et al.*, 2014). The schematic of ASI is shown in figure 2.17.

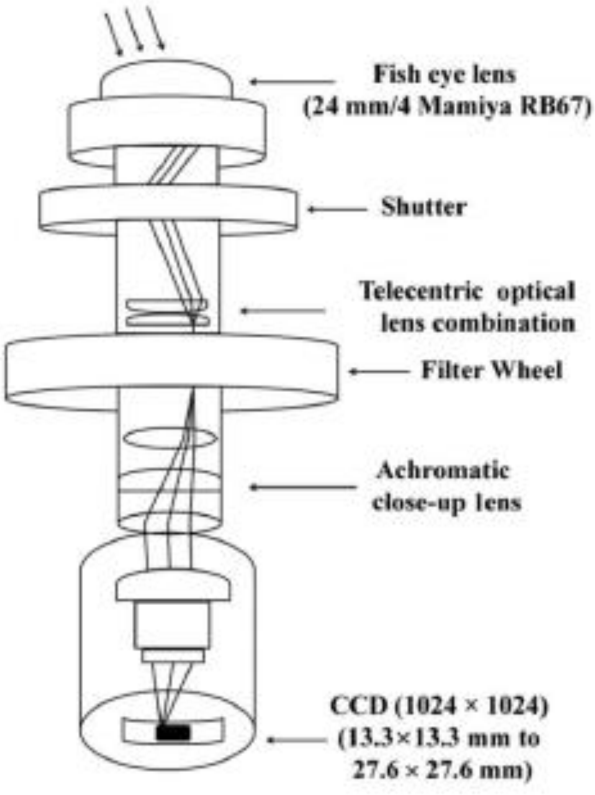

Figure 2.17: Typical schematic of the all-sky imager. (After *Sharma et al.*, 2014)

Figure 2.18 shows the sample image of a particular night after processing it for connection of dark subtraction and median filter. One image for OI 630.0 nm is obtained in each 7.5 mins. We have taken 100° FOV region, which covers a spatial range of around 600 km in both zonal and meridional directions, to avoid the curvature effect. Around 20 cloud-free and moonless nights during the period Feb-Mar in the year 2014 have been used to study the dynamics and scale sizes of the plasma bubble. The investigation has been discussed in detail in chapter 5.

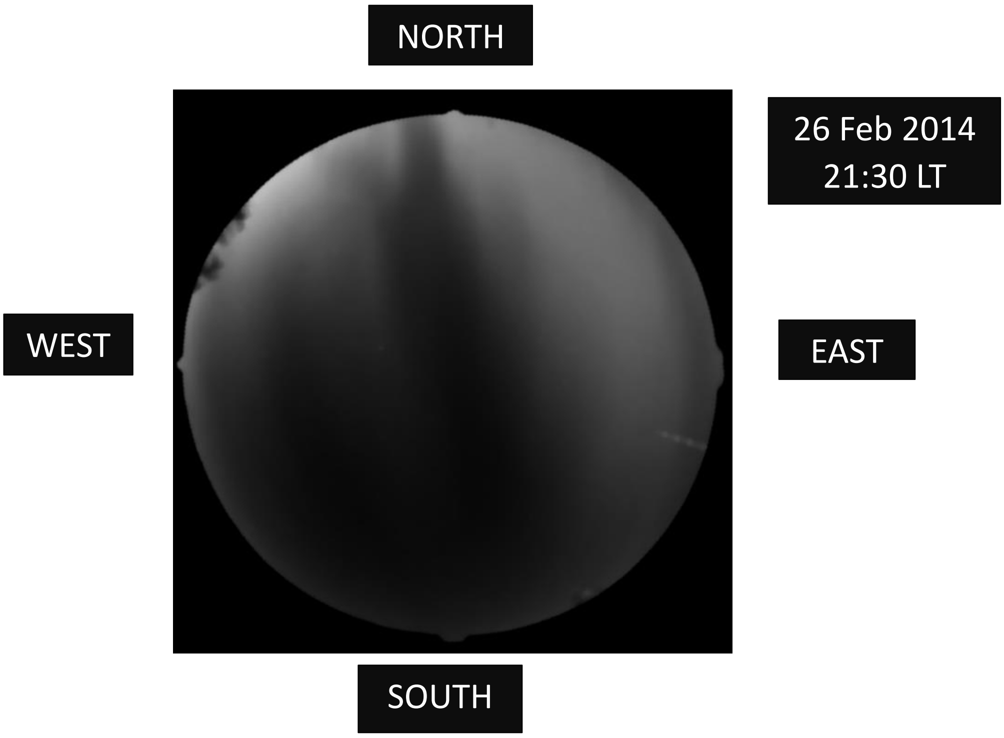

Figure 2.18: A sample image obtained from ASI where the signature of plasma bubbles observed over Kolhapur is shown. The four directions are also marked here.

2.4 Radio measurement

The information about ionospheric plasma density can be obtained using the radio sounding method. We have used digital ionosonde Portable Sounder (DPS-4D) (*Reinisch et al.*, 2009) data in this thesis work. The ionosonde works on the principle of reflection of radio waves from the ionospheric layer. The change in refractive index in the ionospheric medium when a radio wave propagates through that medium can be understood by magneto-ionic theory. The Appleton-Hartree equation provides crucial information about the magneto-ionic theory. After neglecting the factor of collision and magnetic field, the Appleton-Hartree equation becomes

$$n^2 = a - \frac{\omega_n^2}{\omega^2} \tag{2.9}$$

where, ω_n and ω are the frequency of ionospheric plasma and radio waves, respectively. The angular frequency of the electrons in the ionospheric medium is given by,

$$\omega_n = \sqrt{\frac{N_e e^2}{m\varepsilon_0}} \tag{2.10}$$

where, N_e is the electron density, e and m are the charge and mass of an electron, respectively, ε_0 is the permittivity of the free space.

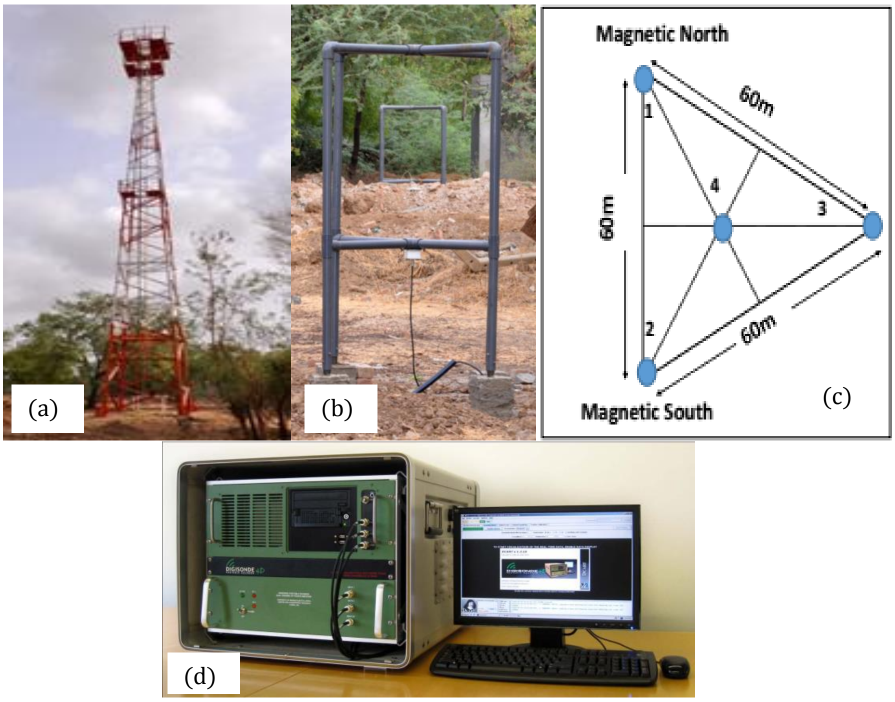

Figure 2.19: Different components of the digisonde such as transmitter, receiver, the array diagram of the four receivers, and an electronic unit are shown in the panels a, b, c, and d, respectively.

Digisonde consists of three major parts: transmitter, receiver, and electronics unit, as shown in figure 2.19. The transmitter transmits radio signals vertically upward in the frequency ranges from 1-30 MHz. The transmitted radio waves penetrate through the ionosphere of increasing electron density. It can be noted from equation 2.10 that the plasma frequency increases with an increase in electron density. Therefore, when the frequency of the radio signal matches with the critical frequency of plasma oscillations ($\omega = \omega_n$), it is reflected back towards the Earth. The frequency of the radio waves (f) at that critical frequency can be written as,

$$f = \sqrt{\frac{N_e e^2}{4\pi\varepsilon_0 m}} = \sqrt{80.5 N_e} \tag{2.11}$$

Here, the frequency of the transmitted signal (f) and electron density (N_e) are expressed in Hz and m^{-3}. Transmitted frequencies greater than the critical frequency are transmitted toward outer space. Thus, we can obtain the information on the bottom side of the ionosphere using the technique of ground-based digisondes.

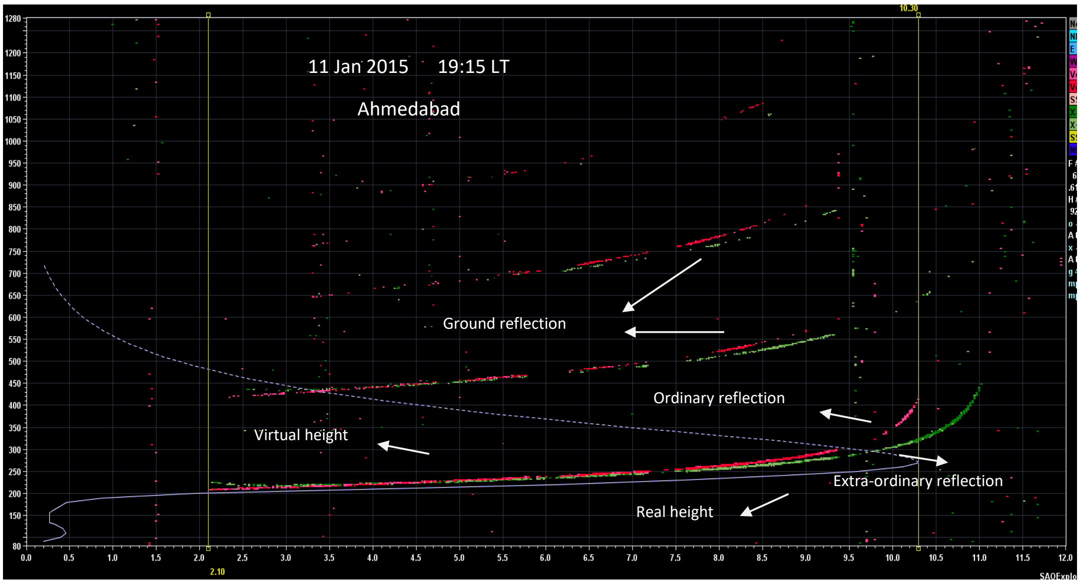

Figure 2.20: Snapshot of an ionogram image mentioning various features observed in the image.

Digisonde records the transmitted frequency and the time delay between the transmitted and received signals which can provide the information of altitudes from where the signals have been reflected. By considering that the speed of the radio waves is equal to the speed of light in free space, the virtual height at each frequency has been estimated. After the correction of the speed of radio waves through the ionospheric medium, we can get the real height as shown in figure 2.20. Using equation 2.11, the electron density present at that altitude can be calculated. All the ionograms are meticulously scaled manually and read by SAO Explorer software. A snapshot of an ionogram image is shown in the figure 2.20. Since, the ionospheric medium is birefringent in nature, the double reflection of the radio waves, ordinary and extra-ordinary (figure 2.20) is observed. In this thesis work, we have used digisonde data over Ahmedabad (a low-latitude location) and Trivandrum (a dip-equatorial location) which provide ionograms at a cadence of 7.5 minutes. The ionospheric electron density profiles have been used in a photo-chemical model calculations to estimate the nighttime OI 630.0 nm emission rates as discussed in section 3.3 of chapter 3. These are also compared with the measured emission rates obtained by the HiTIES. The vertical drift during the sunset time has been calculated using the ionosonde data over Trivandrum which is used in the investigation as discussed in chapters 4, 5, 6.

2.5 Magnetometer measurement

Ground-based magnetometer data have been used to calculate the strength of the EEJ over the dip-equator. As we have discussed earlier in chapter 1 (section 1.2.1) that there is the presence of a strong eastward current in the ionospheric E-region over the dip-equator during daytime which is called EEJ. This strong electrojet induces a magnetic field which is detected by the ground-based magnetometers those are installed in the equatorial region. The ground-based magnetometer data is used to calculate the strength of EEJ over the dip-equator. The daytime magnetic field over the dip-equator is contributed by geo-dynamo, magnetospheric currents, and the EEJ, whereas, over the off-equatorial locations, the contribution of the magnetic field comes from geo-dynamo and magnetospheric current. Therefore, to calculate the induced magnetic field generated due to the EEJ, we need horizontal component of the magnetic field (H) from dip-equator and off-equator (*Cohen and Bowles*, 1963; *Chandra and Rastogi*, 1974; *Rastogi and Iyer*, 1976; *Rastogi and Patil*, 1986). Here, we have calculated the strength of EEJ over Indian sector using the geomagnetic field data of Tirunelveli (TIR) (equatorial location) and Alibag (ABG) (off-equatorial location). Variations of corresponding night times base values of each location are subtracted to eliminate the geodynamo contributions at those latitudes.

$$\Delta H_{TIR} = H_{TIR} - H_{TIR,night}$$

$$\Delta H_{ABG} = H_{ABG} - H_{ABG,night}$$

Then, magnetic data of ABG are subtracted from that of TIR to remove the contribution of magnetospheric currents, if any, and thereby obtain the electrojet strength over the equator.

$$EEJ = H_{TIR} - H_{ABG}$$

Hourly geomagnetic data of TIR and ABG that have been used to calculate the EEJ strength, are obtained from http://wdciig.res.in/WebUI/Home.aspx. The locations of TIR and ABG have been depicted in figure 2.1.

The strength of EEJ over the American sector has been used in chapter 4. Magnetometer data of one minute resolution from Jicamarca and Piura have been obtained from http://lisn.igp.gob.pe, which have been used to calculate the daytime EEJ strengths in the American sector. The EEJ strength over Jicamarca is obtained by subtracting the magnetometer data of the off-equatorial location, Piura, in the same way as described for the estimation of the strength of EEJ over Indian longitudes.

$$EEJ_{American\,sector} = H_{Jicamarca} - H_{Piura}$$

2.6 Other datasets

In addition to the datasets described so far, we have also used other datasets to understand the ionosphere-thermosphere system as a part of the thesis objective. The temperature, plasma density of the ionosphere-thermosphere system varies depending on the strength of solar activity, which affects the dynamics over this region. The sunspot number, solar F10.7 cm flux are used as an indicator of the solar activity. The F10.7cm flux have been obtained from https://lasp.colorado.edu/lisird/data/noaa_radio_flux/ , whereas, the information on the sunspot numbers has been obtained from https://www.sidc.be/silso/datafiles. The quasi-dipole geomagnetic coordinates of different locations have been obtained from http://www.geomag.bgs.ac.uk/, which uses the quasi-dipole field approximation based on IGRF-13 model. The ISR data over Jicamarca have been obtained from http://millstonehill.haystack.mit.edu/list. Photo-chemical models, such as NRLMSISE-00 (*Picone et al.*, 2002) and IRI-16 (*Bilitza et al.*, 2017) have been used to obtain the information of number densities of neutrals and plasma, temperatures of the ionosphere-thermosphere system. Outputs from the Horizontal Wind Model (HWM-14) (*Drob et al.*, 2015) have also been used to understand the systematic behaviour of the zonal and meridional wind in the thermosphere. The geomagnetic disturbances have been characterized by the Ap indices and Dst values, which have been obtained from `http://isgi.unistra.fr/indices_kp.php` and `https://wdc.kugi.kyoto-u.ac.jp/dstae/index.html`, respectively.

2.7 Spectral analysis

The atmosphere of Earth is affected by solar heating and gravitational forces of the Moon and the Sun, etc. They are periodic in nature and therefore, these periodic fluctuations can be seen in the different parameters of the atmosphere, such as temperature, wind, and density. There are several other fluctuations of various time scales due to planetary and gravity waves. Time series analysis is an important tool which can provide useful information about the periodic fluctuations present in the medium. There are several time series analyses methods, such as Fourier transform, Lomb-Scargle periodogram, wavelet transform, curve fitting, multi-spectral analysis, Wigner distribution function, etc. which can be used. In this chapter, we have described the procedures of the analyses which have been used in the investigation of various scientific problems.

2.7.1 Fourier analysis

If a data series is evenly spaced in time, then Fourier transform is used to compute the periodicities present in the dataset. The Fourier transform $F(\omega)$ of a continuous time series $f(t)$ is given by,

$$F(\omega) = \int_{-\infty}^{+\infty} f(t)e^{-j\omega t}dt \tag{2.12}$$

where, $j = \sqrt{-1}$.

The above equation converts the time domain (t) of the dataset into frequency domain (ω) which provides the periodic information present in the dataset. The inverse Fourier transformation can bring back to the time domain of the dataset which can be expressed as,

$$f(t) = \frac{1}{2\pi}\int_{-\infty}^{+\infty} F(\omega)e^{j\omega t}d\omega \tag{2.13}$$

The squared amplitude of the $F(\omega)$ represents the power spectral density (PSD) for the given frequency ω of the time series and this represents the strength of each frequency. PSD is given by,

$$P(f) = |F(\omega)|^2 \tag{2.14}$$

The observational data is obtained in discrete format, $f(t_i)$, $i = 1,2,\ldots,N$. Therefore, the Fourier transform of such function will be given by,

$$F(\omega_k) = \frac{1}{N}\sum_{i=1}^{N} f(t_i)e^{-j\omega_k t_i} \tag{2.15}$$

For $k = 1,2,\ldots,N$. This is called discrete Fourier transform (DFT). In the similar way, reverse DFT can also be calculated.

$$f(t_i) = \sum_{k=1}^{N} F(\omega_k)e^{j\omega_k t_i} \tag{2.16}$$

It can be seen from equation 2.15, DFT takes N^2 number of multiplications and additions in the calculations. Fast Fourier transform (FFT) is such an algorithm which calculates the DFT in much faster way. The scale length of FFT is around N logN, which generates the output much faster.

The power spectral density (PSD) will be,

$$P(f) = \frac{1}{N}|\sum_{i=1}^{N} f(t_i)e^{-j\omega t_i}|^2 \tag{2.17}$$

where, $\frac{1}{N}$ is the normalization factor of the Fourier transformation.

At many times, the data points are not equally spaced with time due to some practical considerations. The presence of moonlight, or sometimes any artifacts, and clouds make the usable data unevenly spaced. As we know, Fourier transform can be done for continuous function/ evenly spaced function only. Therefore, the Fourier transform cannot be applied to estimate the oscillations present in the medium. In such cases, we use Lomb-Scargle Fourier transform (LSFT) which has been discussed next.

2.7.2 Lomb Scargle analysis

For a given dataset which is unevenly spaced, $Y(t_i)$, $i = 1,2,\ldots,N$, the periodogram is defined as (*Schuster*, 1898; *Deeming*, 1975),

$$\begin{aligned} P_Y(\omega) = |F(\omega)|^2 &= \frac{1}{N}|\sum_{i=1}^{N} Y(t_i)e^{-j\omega t_i}|^2 \\ &= \frac{1}{N}|(\sum_{i=1}^{N} Y(t_i)\cos\omega t_i)^2 + (\sum_{i=1}^{N} Y(t_i)\sin\omega t_i)^2| \end{aligned} \tag{2.18}$$

This function is called as classical periodogram. Y is periodic function having frequency ω_0. The product of $Y(t)$ and $e^{-j\omega t}$ are in phase when $\omega = \omega_0$. The summation of equation 2.18 produce large contribution at this condition. The statistical properties of the equation 2.18 can be modified as shown in equation 2.19 (*Scargle*, 1982).

$$P_Y(\omega) = \frac{1}{2}\{\frac{[\sum_i Y(t_i)\cos\omega(t_i-\tau)]^2}{\cos^2\omega(t_i-\tau)^2} + \frac{[\sum_i Y(t_i)\sin\omega(t_i-\tau)]^2}{\sin^2\omega(t_i-\tau)^2}\} \tag{2.19}$$

where, τ is the time offset which is defined as,

$$\tau = \frac{1}{2\omega}\tan^{-1}(\frac{\sum_i \sin(2\omega t_i)}{\sum_i \cos(2\omega t_i)}) \tag{2.20}$$

The periodogram as shown in the equation 2.19 which has been normalized with the total variance (σ) of the data (*Lomb*, 1976; *Scargle*, 1982; *Press and Rybicki*, 1989) is given by,

$$P_Y(\omega) = \frac{1}{2\sigma^2}\{\frac{[\sum_i (Y(t_i)-\bar{Y})\cos\omega(t_i-\tau)]^2}{\cos^2\omega(t_i-\tau)^2} + \frac{[\sum_i (Y(t_i)-\bar{Y})\sin\omega(t_i-\tau)]^2}{\sin^2\omega(t_i-\tau)^2}\} \tag{2.21}$$

The Scargle periodogram, as shown in equation 2.21, matches well with the frequencies constructed by least-square fitting as proposed by *Lomb* (1976). Therefore, it is called Lomb-Scargle Fourier Transform (LSFT).

The significance of the obtained frequency using this LSFT is characterized by false alarm probability (FAP), which is defined as,

$$FAP = 1-(1-e^{-z})^{N_i} \tag{2.22}$$

where, z is the spectral power. N_i, N_0 are the number of independent frequencies and number of data points in the observation (*Horne and Baliunas*, 1986) as given by,

$$N_i = -6.362 + 1.193N_0 + 0.00098N_0^2 \tag{2.23}$$

Therefore, FAP is determined by the data numbers of the given dataset. Any power less than FAP will be considered statistically insignificant. Therefore, the frequencies with spectral power greater than z will be significant for a given FAP (*Scargle*, 1982; *Horne and Baliunas*, 1986). From the equation 2.22, it can be derived that,

$$z = -\ln[1-(1-FAP)^{\frac{1}{N_i}}] \tag{2.24}$$

FAP with a value of 0.1 denotes the statistical significance is around 90%.

The uncertainty of the Lomb-Scargle periodogram is given by (*Horne and Baliunas*, 1986; *Bretthorst*, 1988),

$$\delta\omega = \frac{3\pi\sigma_N}{2\sqrt{N_0}TA} \tag{2.25}$$

where, A is the amplitude of the signal, σ_N is the standard deviation of the noise associated obtained after subtracting the signal, and T is the length of the data set. As an example, we have used a periodic function plotted in the figure 2.21a having time periods of 30, 10, and 20 units as given by,

$$y = 5\cos(\frac{\pi}{15}x) + 6\cos(\frac{\pi}{5}x) + 4\cos(\frac{\pi}{10}x) \tag{2.26}$$

The Fourier transform and Lomb-Scargle periodogram analysis have been carried out which provides the exact periodicities of the input signal (figures 2.21b, 2.21c). As we have discussed earlier in actual observations, the data sets become unevenly spaced in time usually. We have removed some data points from the input signal as shown in figure 2.21a to make the input data uneven as shown in figure 2.21d, and carried out the Fourier and Lomb-Scargle periodogram of them. The output of the analysis can be seen in figures 2.21e, 2.21f, where, Lomb-Scargle analysis shows many accurate periodicities for the uneven data set. The horizontal solid red line shows the 99% significance level which corresponds to the FAP value of 0.01.

2.7.3 Wavelet analysis

The temporal evolution of the periodicities cannot be obtained by the Fourier transform and the Lomb-Scargle periodogram. Wavelet transform is used to calculate the variation of periodicities with time. The use of wavelet transform was initiated since 1980s invented by Jean Morlet and others (*Morlet et al.*, 1982) and later developed by *Grossmann and Morlet* (1984); *Goupillaud et al.* (1984); *Daubechies* (1988); *Mallat* (1989).

Suppose, an input signal, $y = 5\cos(\frac{\pi}{15}x) + 6\cos(\frac{\pi}{5}x) + 4\cos(\frac{\pi}{10}x)$ has three different periodicities. The variation of signal y with time and corresponding Lomb-Scargle periodicities of the signal are shown in figures 2.22a and 2.22b, respectively. The periodicities

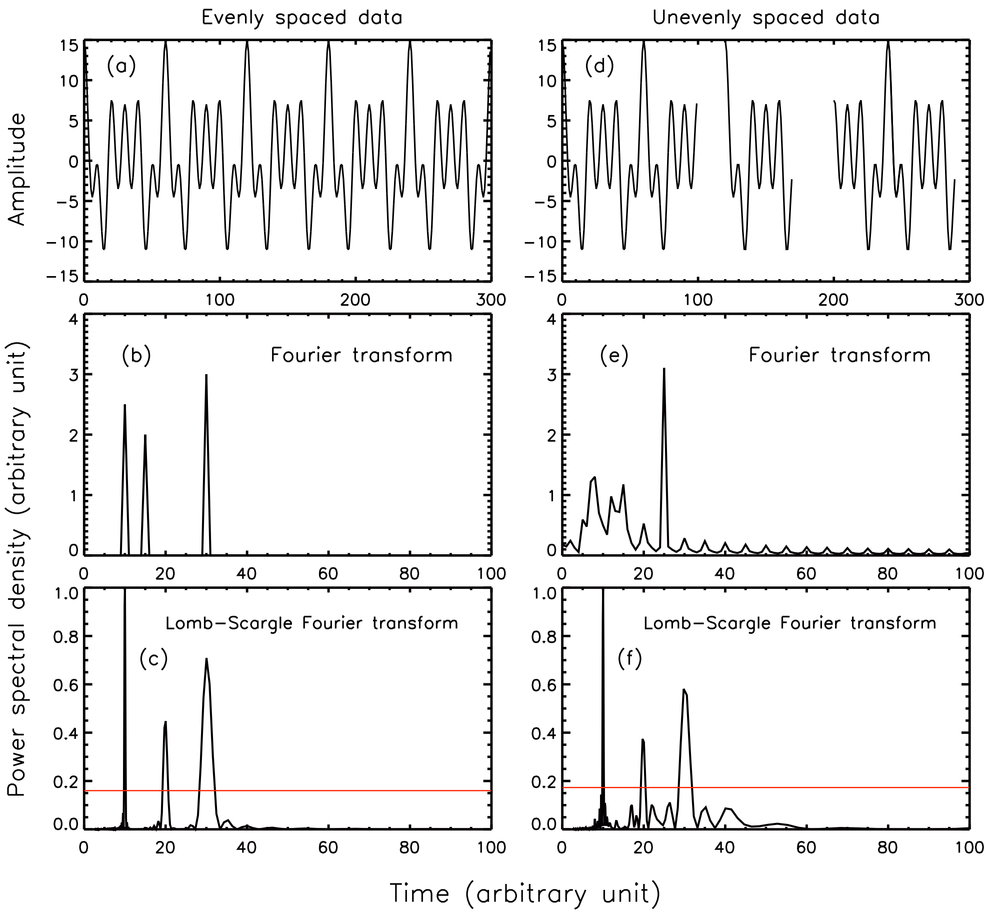

Figure 2.21: (a) A periodic signal has been plotted. The periodicities obtained using Fourier and Lomb-Scargle periodogram analysis are given in b and c. The horizontal solid red line indicates the 99% significance level. Both the analyses show same periodicities of around 10, 20, and 30 unit of time. Some data points have been removed from the signal as shown in panel a to make the data set uneven with time. The same periodogram analysis has been carried out which is shown in panels e and f. The Lomb-Scargle analysis shows much more accurate result as compared with the Fourier transform.

obtained are 10, 20, and 30 units of time. As we discussed earlier, it does not provide information about the existence of these periodicities with time. The wavelet analysis is shown in figure 2.22c. It can be seen that these three periodicities are present throughout the time. In the figure 2.22d, the input signals are generated in such a way that these three periodicities are present at different times. The Lomb-Scargle periodogram analysis provides the periodicities present in the dataset (figure 2.22e) where it cannot identify the difference between two signals shown in figures 2.22a and 2.22d. The wavelet analysis as shown in figure 2.22f can identify the value of the periodicities as well as the time

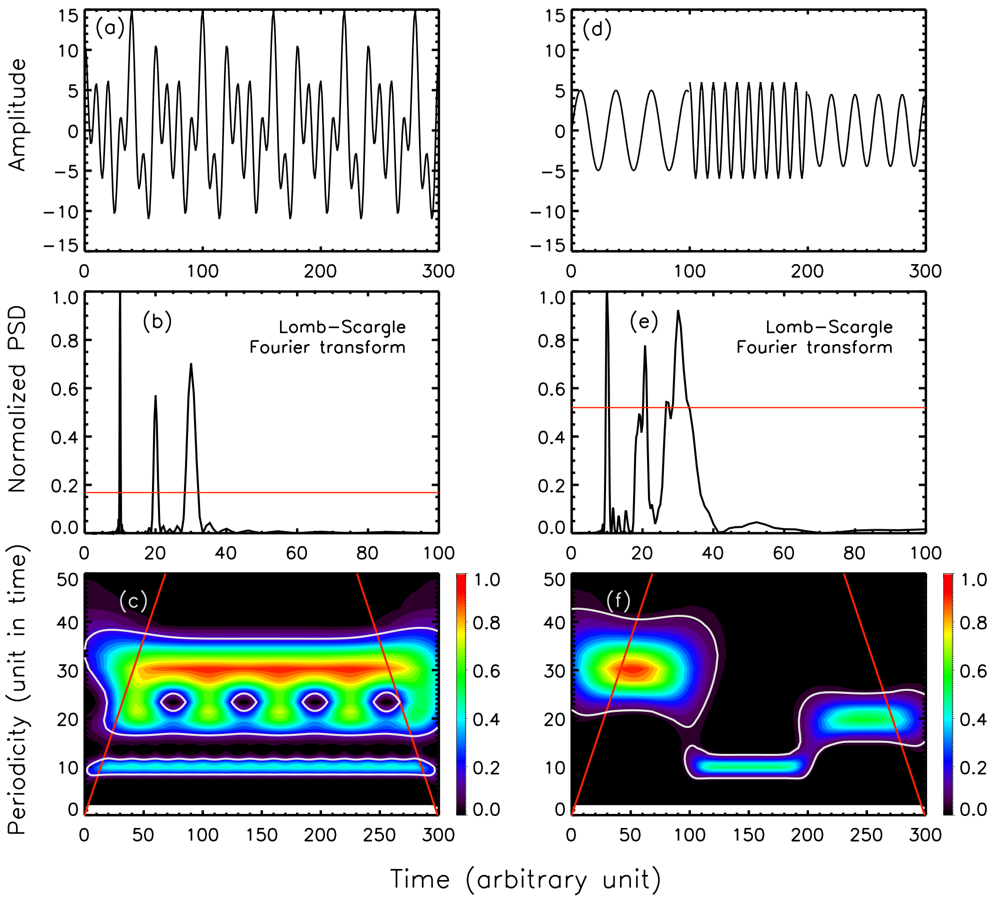

Figure 2.22: (a) A sample periodic function having three different periodicities. (d) Same as (a) but having those periodicities at different times. (b) and (e) are the Lomb-Scargle Fourier transform of the given signals (a) and (d), respectively. The wavelet analysis of the corresponding signals is shown in (c) and (f), respectively. The 95% significant values and cone of influence (COI) are shown in white and red coloured solid lines, respectively.

of presence of those periodicities. In this way, wavelet analysis becomes a useful tool to obtain the temporal evolution of the periodic variations present in a given dataset.

The time series data is finite in number. Therefore, the errors will arise at the extreme end of the data length in the wavelet power spectrum. The Fourier transform is used in the wavelet analysis which assumes the data as cyclic. The cone of influence (COI) is the region where the edge effect is minimum. In the wavelet analysis shown in Figures 2.22c and 2.22f, the COI is drawn in solid red line. The significant level decides the confidence value of the obtained periodicities. In figures 2.22c and 2.22f, the 95% confidence value is indicated using the white line boundary.

2.8 Summary

In this chapter we have discussed the various observational techniques which are used in this thesis work. HiTIES and ASI are the two optical instruments used to observe OI 630.0 nm nightglow emissions from two different locations, have been introduced. The detailed discussion about the optical design, extraction of nightglow, angle, and intensity calibration of HiTIES have been described. Datasets other than optical, such as digisonde, magnetometers have also been discussed. The estimation of the strength of EEJ over the equatorial region using the magnetometer data is described. The working principle of ionosonde and details of ionograms have been elucidated. Apart from that, various other datasets which are used in the study, such as solar flux, sunspot number, and model outputs are also discussed. The time series analysis provides useful information about the oscillations/ waves present in the upper atmosphere which can be associated with various geophysical activities.

Chapter 3

OI 630.0 nm nightglow emission processes and variability

3.1 Background

The upper atmosphere consists of different neutral and charged species at different altitudinal regions as discussed in chapter 1. The electrodynamics as well as neutral dynamics play important roles in driving various processes in the ionosphere-thermosphere system that makes the whole system highly coupled in nature. Airglow emissions of different wavelengths act as passive remote sensing sources of the altitudinal regions of the upper atmosphere from where they originate. A brief introduction of the airglow emissions is presented in chapter 1. It is also important to understand the mechanism processes of various airglow emissions. In this thesis work, we have used OI 630.0 nm nightglow emission (red line), primarily over a tropical region over Indian longitudes. The red line emission peaks at an altitude of around 250 km; therefore, it carries the information of the ionosphere-thermosphere system at those altitudinal regions. This chapter discusses the photo-chemical model developed to estimate the nighttime red line emissions, the various dependencies of the emissions. The temporal and broad variability of this emission are also discussed in this chapter.

3.2 Introduction

The observation of airglow emissions is being used for the investigation of the upper atmosphere since the beginning of the 20^{th} century. These mesospheric-thermospheric emissions act as tracer to the upper atmospheric regions from where they originate. The airglow emissions are very sensitive to the dynamics occurring in the upper atmosphere. The variations of these airglow emissions provide short-term as well as long-term behaviour of the upper atmosphere. Several important parameters, such as the concentration and composition of the ambient atmosphere, temperature, winds, plasma drifts, TEC, etc. can be elucidated using the measurement of airglow emission variability at different wavelengths.

The 630.0 nm airglow emissions originate at an altitude around 250 km with a full width at half maxima of around 50-70 km. The variability in the OI 630.0 nm nightglow emissions delineates the changes that happen in the thermospheric altitudes below the peak F-layer. The OI 630.0 nm photons emit by the transition of excited atomic oxygen O(^{1}D) to the ground state O(^{3}P). The radiative lifetime of this emission line is around 110 sec. and the excitation energy of the O(^{1}D) state is 1.96 eV. Because of its large radiative lifetime of the given state, it becomes difficult to measure in the laboratory experiments. Further, the transition of O(^{1}D) to O(^{3}P) is a forbidden state and is difficult to produce in the laboratory. This transition yields a triplet (figure 3.1). Of them, 630.0 nm and 636.4 nm are significantly intense and the third one (639.2 nm) is very weak. The emission probability of 630.0 nm emission is around 75% out of these triplet emissions.

The O(^{1}D) state is produced following two steps, charge exchange and dissociative recombination, which are discussed as follows:

Charge exchange: The ambient oxygen molecules get converted to molecular oxygen ions through the charge exchange with atomic oxygen ions.

$$O^+ + O_2 \rightarrow O_2^+ + O$$

Dissociative recombination of the molecular oxygen: The molecular oxygen ion produces O(^{1}D) state by interaction with the thermal electrons.

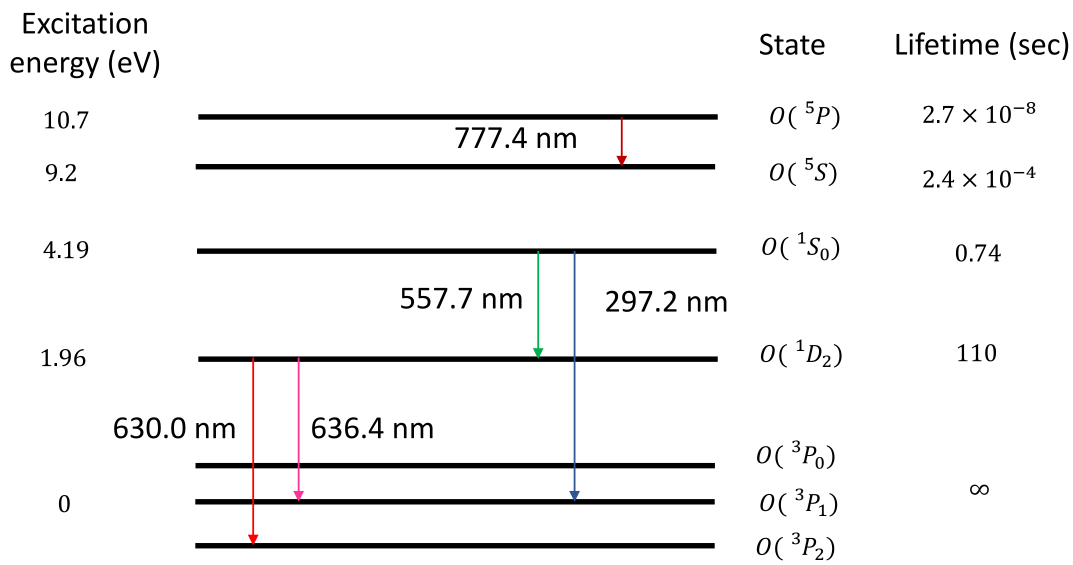

Figure 3.1: Schematic of OI energy level diagram.

$$O_2^+(X^2\Pi_g) + e_{th} \rightarrow O(^1D) + O(^3P) \tag{3.1}$$

The transition of the O(^{1}D) state to the O(^{3}P) state emits the triplet red lines as mentioned above,

$$O(^1D) \rightarrow O(^3P_2) + h\nu_{\lambda=630.0nm}$$
$$O(^1D) \rightarrow O(^3P_1) + h\nu_{\lambda=636.4nm}$$
$$O(^1D) \rightarrow O(^3P_0) + h\nu_{\lambda=639.2nm}$$

In the daytime, in addition to the dissociative recombination discussed above, there are other production mechanism, which are impact of photoelectrons on atomic oxygen and photo-dissociation of molecular oxygen that contribute to the emission of OI 630.0 nm photons (*Solomon and Abreu*, 1989). Apart from the OI 630.0 nm emissions, there are several other emissions at different wavelengths that originate at different altitudes in the upper atmosphere. Some of them are given below:

OH emissions:

Hydroxyl (OH) emissions originate in the mesospheric region. The OH emissions originate from around 87 km altitude having full width in half maxima around 8-10 km (*Baker and Stair Jr*, 1988). The emitted photons fall in the infrared range having the range of wavelengths from 700-4500 nm. The spectra observed in the rotational and vibrational bands of OH molecules were proposed by Herzberg and Meinel proved it experimentally. Therefore, these are called Meinel band (*Meinel*, 1950; *Meinel et al.*, 1950). The radiative lifetime of these Meinel band emission is around 6 sec. The mechanism of OH emissions can be found by *Meriwether Jr* (1989) and references therein, *Khomich et al.* (2008),

$$O + O_2 + M \rightarrow O_3 + M$$
$$H + O_3 \rightarrow OH^*(\nu' \leq 9) + O_2 + 3.3\ eV$$
$$OH^* \rightarrow OH + h\nu$$

NaD emission:

The sodium doublet (NaD) originates around the altitude of 92 km. The emission wavelengths are 589.0 and 589.6 nm. The generation of excited Na atoms from the neutral Na (*Chapman*, 1939) and the emission of the corresponding nightglow is given below:

$$Na + O_3 \rightarrow NaO^* + O_2$$
$$NaO^* + O \rightarrow Na^* + O_2$$
$$NaO^* + M \rightarrow NaO + M$$
$$NaO + O \rightarrow Na^*(^2P,\ ^2S) + O_2$$
$$Na^*(^2P_{\frac{3}{2},\frac{1}{2}}) \rightarrow Na^*(^2S_{\frac{1}{2}}) + h\nu(589.0,\ 589.6\ nm)$$

This is an allowed transition. Therefore, it has a very short lifetime of around 2×10^{-8} sec.

O_2 (0-1) emission:

Molecular oxygen emits spectral band having peak emission at 864.5 nm from around 94 km altitudinal region (*Chamberlain et al.*, 1958; *Sullivan*, 1971). The emission mechanism of O_2(0-1) emissions is as follows (*Chapman*, 1939):

$$O + O + M(O_2,\ N_2) \rightarrow O_2(c^1\Sigma_u^-) + M$$
$$O_2(c^1\Sigma_u^-) + O_2 \rightarrow O_2(b^1\Sigma_g^+) + O_2$$
$$O_2(b^1\Sigma_g^+) \rightarrow O_2(X^3\Sigma_g^-) + h\nu$$

The lifetime of $O_2(b^1\Sigma_g^+)$ is around 12 sec.

OI 557.7 nm emission:

The emission of OI 557.7 nm wavelength generates when the transition of atomic oxygen takes place from $O(^1S)$ to $O(^1D)$ state which appears as a green line emission. The mechanism of 557.7 nm airglow emission was first proposed by *Chapman* (1931). He suggested one-step process for this emission as follows:

$$O + O + O \rightarrow O_2 + O(^1S)$$
$$O(^1S) \rightarrow O(^1D) + h\nu_{\lambda=557.7\ nm}$$

This is known as Chapman Mechanism. *Barth and Hildebrandt* (1961) proposed a two-step process as modification to the Chapman's mechanism.

$$O + O + M \rightarrow O_2^* + M$$
$$O_2^* + O \rightarrow O_2 + O(^1S)$$
$$O(^1S) \rightarrow O(^1D) + h\nu_{\lambda=557.7\ nm}$$

This is known as Barth mechanism. M is a molecule (O_2 and N_2) acts as a third body catalyst. During nighttime, on occasions, especially if the F-region ionospheric densities are large, then dissociative recombination can also play a role in the emission of OI 557.7 nm nightglow.

$$O_2^+ + h\nu \rightarrow O + O(^1S)$$

The nighttime OI 557.7 nm emission originate from the altitude around 150 km. The lifetime of the atomic O(^{1}S) state is 0.74 sec.

OI 777.4 nm emission:

The OI 777.4 nm wavelength emission occurs due to the atomic transition of O(^{1}D) to O(^{5}S) state (figure 3.1). The radiative recombination of O$^+$ and e$_{th}$ produce the O(^{5}P) state.

$$O^+ + e_{ph} \rightarrow O(^5P)$$
$$O(^5P) \rightarrow O(^5S) + h\nu_{\lambda=777.4\ nm}$$

The 777.4 nm airglow emission rate is proportional to n$_e^2$ (n$_e$=number density of electron) as the emission depends on the densities of both O$^+$ and e. In the F region, the number density of O$^+$ is nearly equal to the electron density and, therefore, the emission of this wavelength depend on n$_e^2$, not on the height variation of the F region. The OI 777.4 nm emission mainly comes from the F layer peak. As the collision cross-section of O$^+$ and e is very small, the emission magnitudes of OI 777.4 nm are very small. The radiative lifetime of 777.4 nm emission is very small (2.7×10^{-8} sec).

3.3 OI 630.0 nm nightglow emission photo-chemical model

A photo-chemical model has been developed to estimate the OI 630.0 nm nightglow emissions using the measured electron density as obtained by digisonde and other models, such as NRLMSISE-00 and IRI-16. The red line oxygen emission is produced through the de-excitation of O(^{1}D) to the ground state as discussed in the previous section. The rate of production of O(^{1}D) depends on the concentration of the electrons and molecular oxygen ions present in that altitude. Because of the presence of collisions with the ambient oxygen, nitrogen molecules, electrons, etc., the quenching of the excited O(^{1}D) cannot be ignored. Volume emission rate (VER) is the number of photons emitted from the source per unit volume per unit time as a function of altitude. The VER, V$_{630.0}$(z) (Ph cm^{-3} s^{-1}) can be written as (*Abreu et al.*, 1982, 1986; *Link et al.*, 1981; *Link and Cogger*, 1988;

Cogger et al., 1980):

$$V_{630.0}(z) = \beta_1 K_1[O^+][O_2] \cdot \frac{A_{630.0}}{A_{1D} + K_2[N_2] + K_3[O_2] + K_4[e]}$$
$$V_{630.0}(z) = \frac{0.76\beta_1 K_1[O^+][O_2]}{1 + (K_2[N_2] + K_3[O_2] + K_4[e])/A_{1D}} \quad (3.2)$$

Where, K_1, K_2, K_3, K_4 are the rate coefficients of the different reactions. β_1 is the production efficiency and $A_{630.0}$ is the transition coefficient and A_{1D}=$A_{630.0}$+$A_{636.4}$. The values of the coefficients that have been used to estimate the VER are shown in table 3.1. These have been obtained from *Link and Cogger* (1988) and references therein.

Table 3.1: *Values of the parameters which have been used in the calculation of VER*

Parameter	**Rate coefficient (cm^3 sec^{-1})**
K_1	$3.23 \times 10^{-12} \times e^{\frac{3.72\times300}{T_i} - \frac{1.87\times300\times300}{T_i^2}}$
K_2	$2.0 \times 10^{-11} \times e^{\frac{111.8}{T_n}}$
K_3	$2.9 \times 10^{-11} \times e^{\frac{67.5}{T_n}}$
K_4	$1.6 \times 10^{-12} \times T_e^{0.91}$
Parameter	**Metastable yield**
β_1	1.1
Parameter	**Transition coefficient (sec^{-1})**
$A_{630.0}$	5.15×10^{-3}
$A_{636.4}$	1.66×10^{-3}
A_{1D}=$A_{630.0}$+$A_{636.4}$	6.81×10^{-3}

NRLMSISE-00 atmospheric model (*Picone et al.*, 2002) has been used to obtain neutral densities of the species, such as O, O_2, N_2, and neutral temperature. The electron densities are obtained by carrying out true height analysis of ionograms obtained from the digisonde located at Ahmedabad. We obtain the ion density values using the ratios given in IRI-16 model (*Bilitza et al.*, 2017). The peak altitude of the OI 630.0 nm nightglow varies typically from 240 km to 300 km, with an average full width half maximum in the range of 50-70 km. The VER for a given night is shown in figure 3.2 for three different times. As the night progresses, the VER decreases. The peak emission and the full width

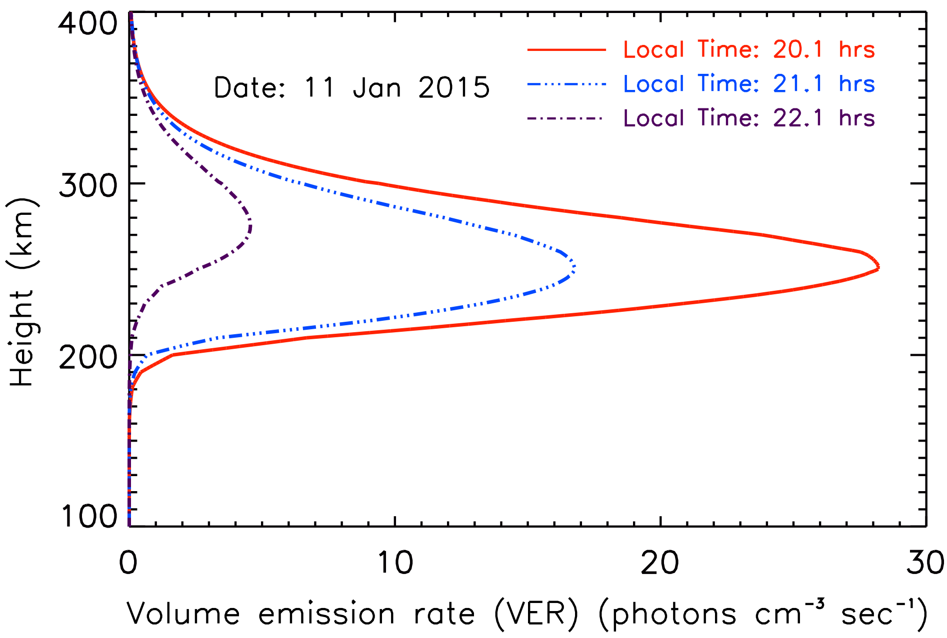

Figure 3.2: Volume emission rates with respect to altitudes measured over Ahmedabad are shown for three different times. The height of peak emissions can be found around 250 km with full width at half maximum in the range of 50-70 km.

at half maxima can be seen in the estimated VER for that given night which also vary over the course of time.

The OI 630.0 nm emissions have been estimated by integrating the VER over a height range of 100 to 700 km and has been compared with the measured nightglow emissions obtained from Mt. Abu. The emissions measured from different directions over Mt. Abu (figure 2.14) along with the estimated emissions over Ahmedabad are depicted in figure 3.3. Ahmedabad is around 170 km away from Mt. Abu in the equatorward direction. The difference in the magnitude between measured and estimated emissions are probably due to the difference in spatial distance. As Ahmedabad is located nearer the equator compared to Mt. Abu, the crest in EIA can be located closer to Ahmedabad which may contribute to the increase in electron density over there. Therefore, the emissions are found to be more over Ahmedabad at the post-sunset time, which later in the night, converge to similar values. Thus, the similar variations can be seen between the estimated (from Ahmedabad) and measured (over Mt. Abu) emissions and as a result, the correlation coefficient during 19-04 LT is extremely high (0.99) (figure 3.3). Such strong correlation is seen in many nights. Several nights of data are shown in subsequent chapters along

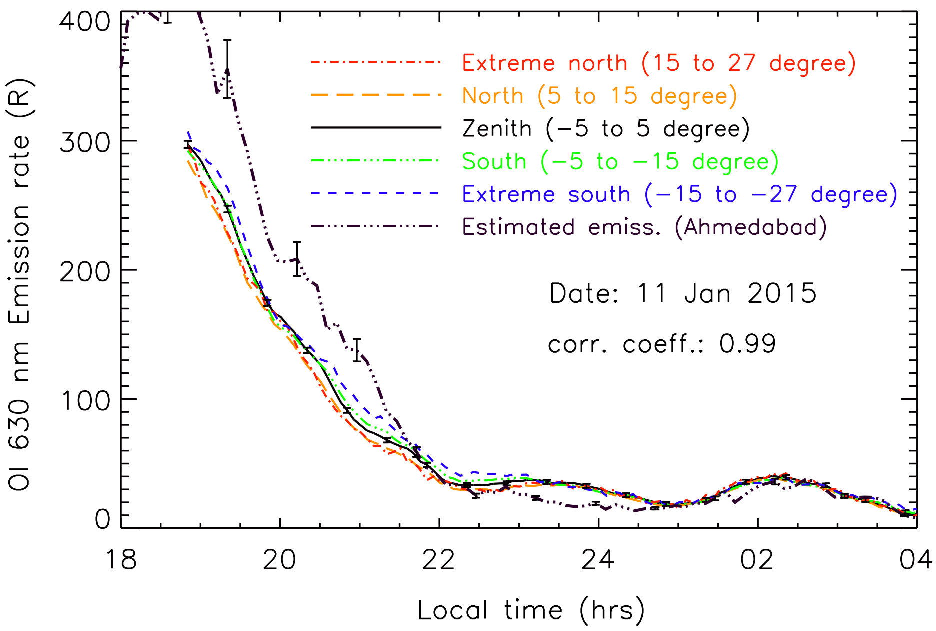

Figure 3.3: The OI 630.0 nm nightglow emissions estimated by using the measured electron density over Ahmedabad are shown along with the observed emission over Mt. Abu as shown in figure 2.14

with detailed discussions on their variations in a given night.

The production of O(^{1}D) through the dissociative recombination process (equation 3.1) is proportional to the electron density present at that altitude. In the figure 3.4, the variation in OI 630.0 nm estimated emissions is shown with electron density present at the peak emission altitude (250 km) and peak F-layer height for four given nights of different years which can be seen varying proportionately to each other. The fall in estimated emissions can be seen after sunset time due to decrease in electron density in the ionosphere. More importantly, the variation in the electron density at 250 km corresponds well with the estimated emission rates as compared to the electron densities at peak F-layer height. The variations in emission with the small changes in time can also be seen with those in electron density at 250 km altitude (figure 3.4), whereas those small-scale variations with time are not clearly visible in the variation in electron density at F-layer peak. In that way, the measurement of OI 630.0 nm nightglow emissions can provide very sensitive information of those altitudinal regions centered at 250 km.

We have seen in the figures 3.2 and 3.4 that the peak emissions originate at around 250 km altitude. In figure 3.5, the variation of base and peak F-layer heights with time

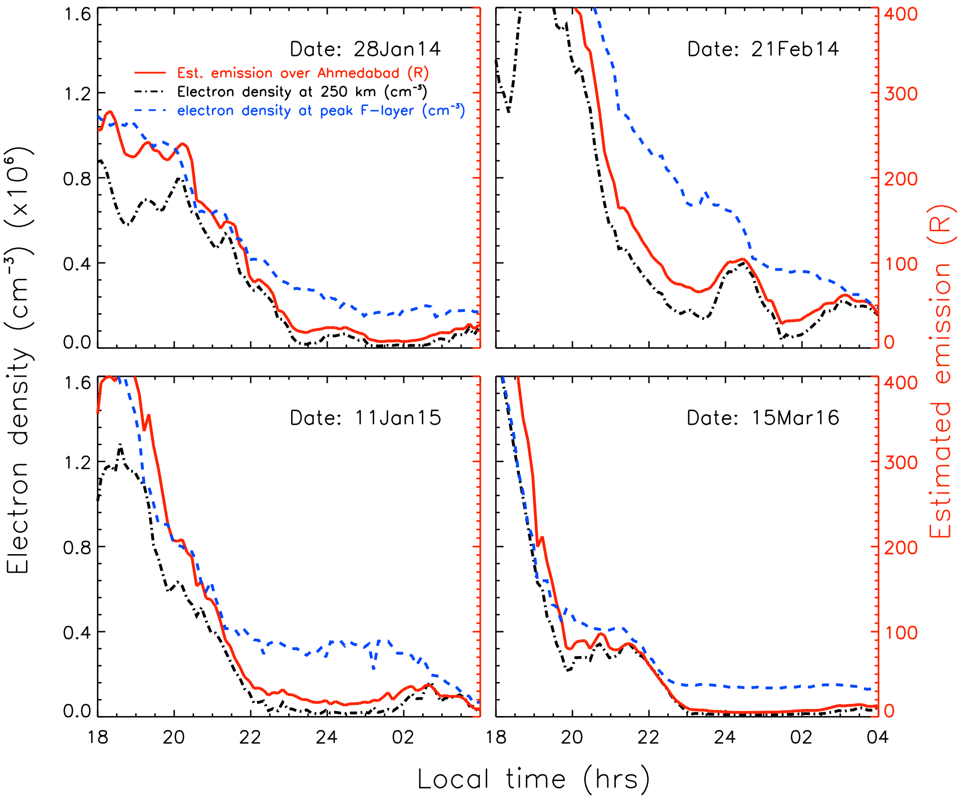

Figure 3.4: The OI 630.0 nm estimated emissions, electron density at the peak emissions altitude, and electron density at the peak F-layer are shown for four given nights.

are shown as obtained from digisonde located at Ahmedabad in black dash-dot and green coloured dashed lines, respectively. The variation in the altitudes of emissions is also shown at the corresponding time. The thick red line shows the altitude of the peak emissions as obtained from the estimated VER and the thin red lines show the altitudes at the half of peak emission values. It can be seen that the contribution of OI 630.0 nm emissions varies more closely with the bottomside of the F-layer. The magnitude of emissions varies depending on the movement of peak F-layer. For example, an increase in emission can be seen at 24.5 LT on 21 Feb 2014 (figure 3.4) which also corroborates with the increase in electron densities at 250 km altitudes. Although the electron density at the peak F-layer did not show such increase in value. In fact, as the emissions start increasing, the electron densities in the peak F-layer show a decreasing trend. This can be understood when we observe the height variation of the F-layer. The height of the peak F-layer show decrease at that time and it came closer to the emission altitude of OI 630.0 nm emission. Therefore, the emissions can be seen to increase in magnitude as the larger electron density from the peak F-layer descends to altitude of OI 630.0 nm emission.

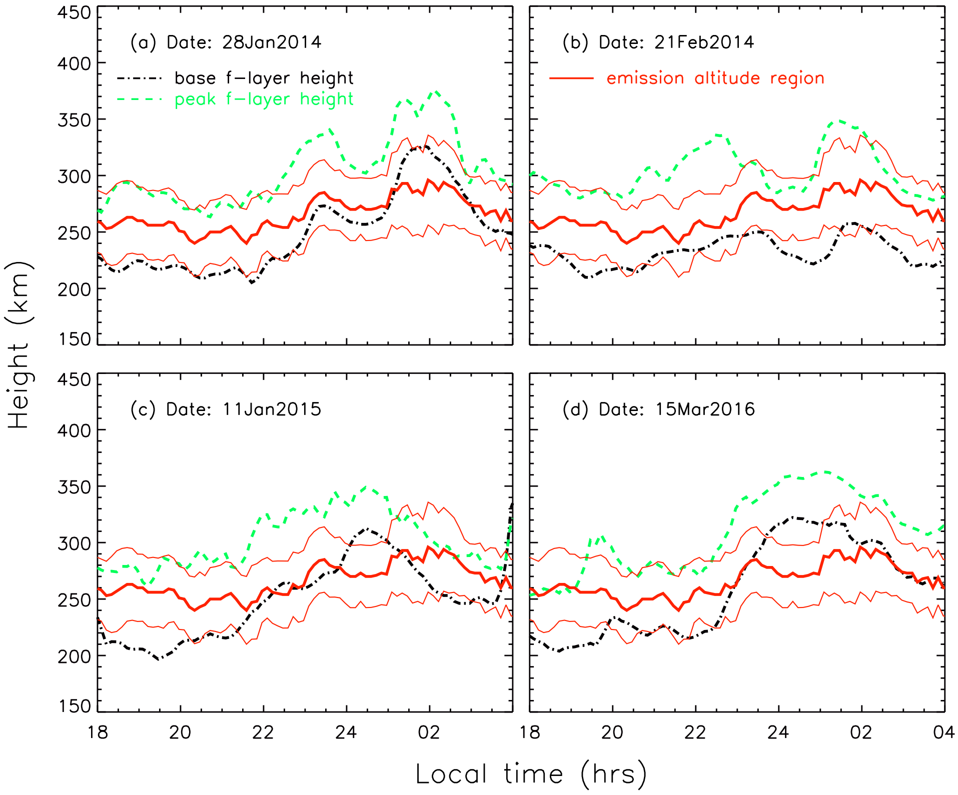

Figure 3.5: The peak and base F-layer height are shown along with the altitudinal regions of the OI 630.0 nm emissions. The OI red line emissions emanate from the bottomside of the peak F-layer.

In figure 3.6, the estimated OI 630.0 nm emissions and peak F-layer height is depicted for four given nights. It should be noted that the y-axis for top and bottom panels are different as they correspond to two different years having different solar activity conditions. The solar activity of the year 2016 is moderately low as compared to the year 2014, which can be seen reflected in their emission values also. All these nights show enhancement in emission within the period 20-22 LT. The simultaneous measurement of the peak F-layer shows descend to lower altitudes, closer to the peak emission altitude (around 250 km), whenever the emissions got enhanced. With the descend of peak F-layer height, the larger electron densities are brought down to the emission altitude which is around 250 km. Therefore, the variation of OI 630.0 nm nightglow emission shows better relationship with the electron density at 250 km rather than the electron density at peak F-layer (figure 3.4). As an effect of such kind of vertical movement in the ionospheric F-layer, we have seen significant changes in the magnitudes of OI 630.0 nm nightglow emissions that has been discussed in detail in chapter 5.

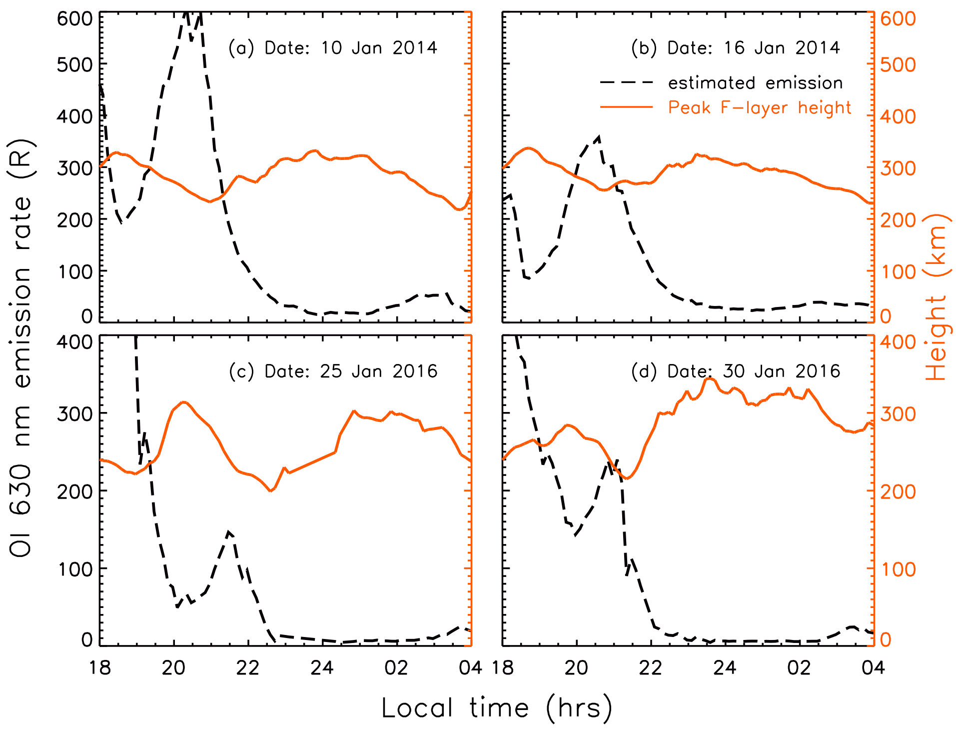

Figure 3.6: The OI 630.0 nm estimated emissions are shown for four given nights with the simultaneous variation of peak F-layer height. Whenever, the height of peak F-layer decreases, descends closer to the emission altitude of OI 630.0 nm emission, the emission increases.

3.4 OI 630.0 nm nightglow emission with varying solar flux activity

As discussed in chapter 2, The investigation of ionosphere-thermosphere system has been carried out in this thesis work using the measurement of OI 630.0 nm nocturnal emissions primarily over Mt. Abu, a low-latitudinal region. An optical spectrograph (HiTIES) has been used to measure the OI 630.0 nm nightglow emissions. A 5-years dataset (2013-2017) of HiTIES has been obtained during different months. The solar flux varied from high to moderately low during this period. The nightly averaged OI 630.0 nm emissions during 20-04 LT are compared with the corresponding daily sunspot numbers and are shown in figure 3.7. These broadly show a similar variation. As it is known that the electron density increases at high solar active period in the presence of larger EUV flux and so, expectedly, the OI 630.0 nm airglow emission also increases. However, the average nightglow emissions follow large day-to-day variation apart from the broad variation with the solar activity. These are essentially due to the equatorial and low-latitude electrodynamics, that show day-to-day variation. Several of such variabilities in the emissions as observed from Mt. Abu are discussed in this thesis.

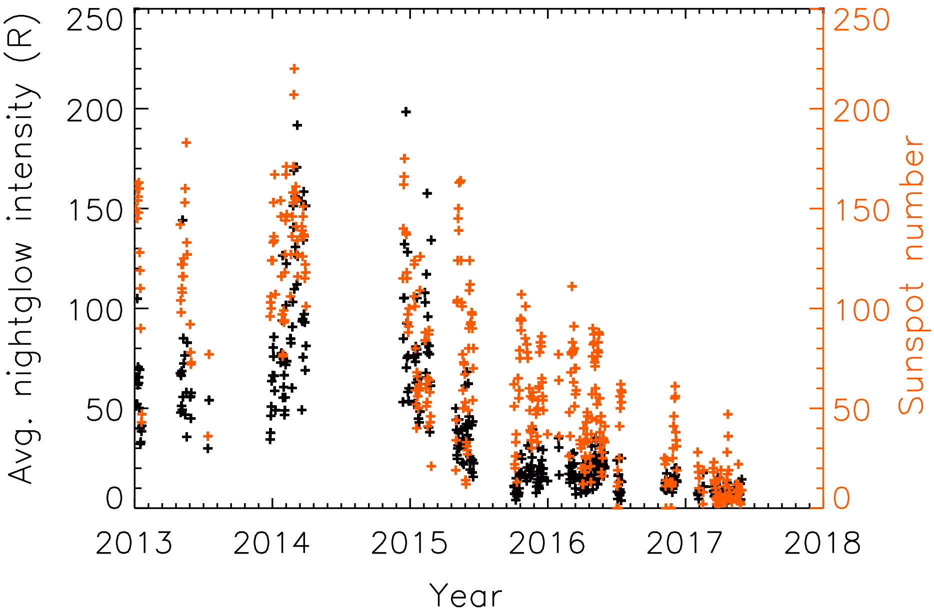

Figure 3.7: The OI 630.0 nm average nightglow emissions measured over Mt. Abu over a period of 2013-2017 at different solar activity period.

3.5 Variability in OI 630.0 nm nightglow emission as seen from tropical region

The details of the measurement and extraction of the nightglow emissions have been discussed in chapter 2. Various kinds of emission variability are seen in this red line emission measured over the tropical region. Each of the nocturnal variations in all the data have been carefully observed for all the geomagnetic quiet nights, in order to remove the effects of high latitudes and prompt penetration of electric fields, if any, the focus was to critically understand the quiet time nocturnal behaviour in the observed emissions. The detailed scrutiny leads to a categorization of four broad types in the OI 630.0 nm nocturnal emissions. These are depicted in figure 3.8.

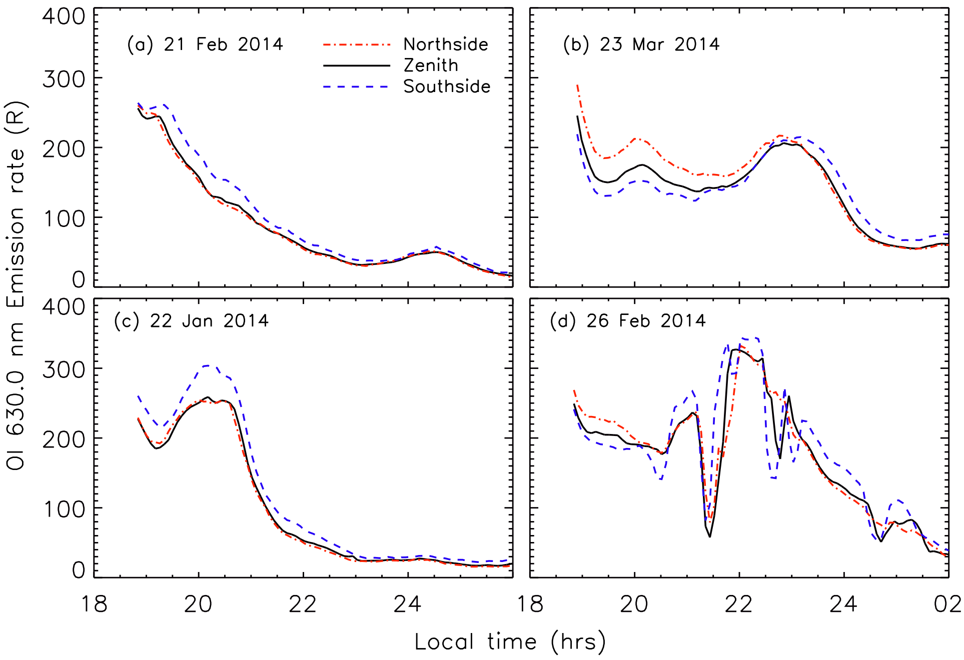

Figure 3.8: The broadly four types of variation in OI 630.0 nm emissions observed are shown. (a) The typical OI 630.0 nm nightglow variation which decreases monotonically after sunset. (b) Latitudinal movement of OI 630.0 nm emissions observed where the northern-side show larger emissions. (c) The enhancement in seen in the nightglow emission during post-sunset period. (d) Several excursions in nightglow emission have been observed.

It is found that the nocturnal variations seen in type (a) are most common and are due to a decrease in the electron density in the emission altitude. Type (b) shows both northward and southward gradients in emissions obtained over the FOV of the measurements. This northward gradient as seen after sunset time changes to the southward later in the night due to what is called as the reversal in the EIA. The observation in type (c) shows enhancement in OI 630.0 nm nightglow emissions during post-sunset time. These enhancements vary in consonance with the decrease in the ionospheric heights as measured by the digisonde at Ahmedabad and are considered to be due to the poleward meridional winds. It appears that the OI 630.0 nm nocturnal emissions are uniquely placed to capture the subtle changes that seem to be occurring in the bottomside of the ionosphere as captured in (b) and (c). The behaviour as seen in type (d) is a direct result of the development of plasma bubbles over the equator. This study also discussed the zonal scale sizes of gravity waves that exist when the plasma bubbles are present and or absent. These types of variations (b), (c), and (d) in the OI 630.0 nm nightglow emissions are discussed in detail in the chapters 4, 5, and 6.

3.6 Summary

In this chapter, we have discussed the production mechanism of various thermospheric airglow emissions along with the OI 630.0 nm nocturnal emissions. The OI 630.0 nm nightglow emissions have also been estimated using a photochemical model which uses measured electron density as input that is obtained from digisonde operating at Ahmedabad. The estimated emissions are compared with the measurements which are carried out from a nearby location Mt. Abu. The altitude region of this red line emission has been discussed using the estimated height profile of the OI 630.0 nm VER. The OI 630.0 nm nightglow emissions originate at the bottomside of the F-layer. Therefore, this nightglow emission shows one-to-one variation with the electron density at the emission altitudes (around 250 km) rather than the electron density at the peak F-layer. The variabilities seen in the emissions during geomagnetic quiet times are broadly classified into four types which are shown in figure 3.8. These are discussed in detail in the following chapters.

Chapter 4

Latitudinal movement of EIA crest during nighttime

4.1 Background

The low-latitude ionosphere-thermosphere system is greatly influenced by the electrodynamic processes that occur over the equatorial region as discussed in chapter 1. The distribution of plasma over the low-latitude region through the electrodynamic and neutral wind dynamic processes affects the airglow emission brightness. During nighttime, plasma density decreases monotonically after the sunset due to recombination. The effects of processes at the sunset time, like PRE in zonal electric field can persist until the midnight time over the low-latitudes. During high solar flux year 2014, the strength of PRE is quite large and so strong vertical drifts are generated over the dip-equator. As a consequence, the plasma can reach to latitudes as far as Mt. Abu (16°N Mag), thereby, poleward movement of EIA crest is obtained as a function of latitude in the OI 630.0 nm nightglow emissions. After the sunset, the zonal electric field reverses its direction. The nighttime motion of EIA crest, both in the poleward and equatorward direction, as seen in OI 630.0 nm nightglow emission as observed over a large field of view from Mt. Abu will be discussed in this chapter.

4.2 Introduction

The plasma distribution takes place over the low-latitudinal region through the transport processes governed by various electrodynamic and neutral processes as discussed in chapter 1. OI 630.0 nm emissions emanate from the altitudes centred around 250 km and with emission width of around 100 km, which provide information of the variabilities at that altitudinal region. During nighttime, the OI 630.0 nm emissions originate due to the dissociative recombination of molecular oxygen, as discussed in detail in chapter 2. Various types of emissions have been observed in the OI 630.0 nm nocturnal emission variations as shown in figure 3.8 of chapter 3. The strength of electrodynamic processes, such as the EIA, the PRE and the neutral winds, which govern the plasma distribution over low-latitudinal locations, vary from day-to-day (e.g., *Sridharan et al.*, 1993b; *Pallam Raju et al.*, 1996; *Rishbeth*, 2000; *Pallamraju et al.*, 2010; *Karan et al.*, 2016; *Parihar et al.*, 2018). It has been shown that the strength and the location of the EIA crest varies with the strength of the equatorial electric field. As the eastward EEJ is formed due to this primary eastward electric field (e.g., *Woodman and La Hoz*, 1976; *Raghavarao et al.*, 1988b, 1991; *Hysell and Burcham*, 2000), it has been considered to serve as a good proxy for the equatorial F-region electric field. Further, it has also been shown that the strength of the EEJ is directly proportional to the strength of the EIA (*Raghavarao et al.*, 1978). During sunset time, the upward vertical drift of plasma shows large increase in magnitude before reversing its direction which is known as PRE, as discussed in chapter 1 with greater detail. The PRE in electric field can reinitiate the EIA process, thereby, the redistribution of plasma over low-latitude regions occurs during the post-sunset time. The strength of PRE varies with season and solar activity (*Farley et al.*, 1986). Therefore, the latitudinal extent and magnitude of enhancement in electron densities at the EIA crest are also solar flux and season dependent.

During daytime, as the EEJ strength gradually build up, the E×B drift also gets stronger and it takes around 2-4 hours for the EIA crest to be developed (*Venkatesh et al.*, 2015). The plasma brought down to the low-latitude region is reflected in the OI 630.0 nm airglow emissions also. The EIA crest formed by this process can be seen moving away from the equator as the strength of the daytime electrodynamics increases towards noon (e.g., *Farley*, 1960; *Rastogi and Klobuchar*, 1990; *Pallam Raju et al.*, 1996; *Rishbeth*, 2000). As discussed earlier, EIA process can be reinitiated due to PRE, the poleward movement of EIA crest can be relaunched. The equatorward movement of the EIA in the nighttime using radio measurements has not been reported so far, presumably due to the decrease in plasma densities by an order of magnitude or greater as compared to the daytime. However, as the ground-based OI 630.0 nm emissions measurements are inherently integrated over a column, they capture the variations in plasma densities more readily, as demonstrated in some of the works reported in literature (e.g., *Pallamraju et al.*, 2001; *Saha et al.*, 2021) including those that reported the reversal in the movement of the EIA crest during nighttime (e.g., *Sridharan et al.*, 1993b; *Narayanan et al.*, 2013).

The investigations carried out using the OI 630.0 nm emissions over Mt. Abu, situated under the northern crest region of the EIA in the Indian longitudes are discussed. We report the latitudinal movement of the EIA crest during the nighttime - both poleward (in the evening) and equatorward (in the night) directions. During the high solar activity year of 2014, we have observed that the location of the EIA crest is within the FOV of the instrument for the three months of the observation period (Jan-Mar). Equatorward movement of the crest has been observed later in the night on many occasions. In this study we present the results obtained on the movement of the crest, both away from the equator and towards the equator as a direct result of the changes in the equatorial electrodynamics in the evening and night times. These results provide insights into the dynamical nature of the nocturnal variation in the OI 630.0 nm airglow emissions over a low-latitude location vis-à-vis its response to the equatorial ionospheric electrodynamics.

4.3 Data sets used

OI 630.0 nm (red line) nightglow emission over Mt. Abu obtained from a large FOV instrument High throughput Imaging Echelle Spectrograph (HiTIES) is used in this study. The whole spatial region has been segregated into five independent directions as discussed in chapter 2. These are: one along zenith, two regions along the northern direction and two along the southern direction. Data from the Digisonde Portable Sounder (DPS-4D) at Trivandrum (a dip-equatorial location) has been used in this study to assess the equatorial ionospheric condition on a given day/night. F-region ionospheric vertical drifts during the sunset time have been obtained using this data set at 7.5 minutes cadence. We have calculated the vertical drift of the ionospheric F-layer by monitoring the heights of the iso-electron density contours at 7 MHz. Hourly EEJ values have been obtained over Indian sector using the geomagnetic data from a dip-equatorial location, Tirunelveli (TIR), and an off-equatorial location, Alibag (ABG). The strength of EEJ over American sector has been calculated using the minute resolution magnetometer data from Jicamarca and Piura. The estimation of the strength of EEJ have been discussed in section 2.5 of chapter 2.

4.4 Observation and results

The nocturnal variations in OI 630.0 nm emissions of two sample nights are shown in figure 4.1 which depict the different types of variabilities observed during the nighttime over this low-latitudinal location. As discussed in the above section, the FOV of HiTIES is around 54°, the five segregated regions of the whole FOV are shown in different colours and line styles. The detailed description with regard to HiTIES and its image processing have been discussed in the chapter 2. The data cadence of HiTIES is 5 minutes and the uncertainty, σ, in each measurement varies typically from 1-3 R (as shown in figure 4.1a for emissions along two different directions). The estimation in uncertainty measurement of HiTIES has been discussed with greater detail in chapter 2. It can be noted that for most of the duration the emission rates along these view directions, and especially those along (i) the extreme south, (ii) extreme north, and (iii) the zenith, show magnitudes that are independent of each other as they are away by $\pm 1\sigma$ (uncertainty) values of each other during most of the post-sunset hours. The larger emissions along the southern direction as viewed from Mt. Abu can be seen in figure 4.1a, whereas, figure 4.1b shows larger emissions along the northern direction after the sunset time. These different features, as depicted in figure 4.1, indicate the dynamic nature of the thermospheric behaviour, as the red line emissions readily respond to such variations. We have investigated the variations in magnitudes of emissions between the northern and southern directions, which is considered to be a result of the latitudinal movement of the crest in the EIA after the sunset. The nights when the magnitude of emissions between the two view directions differ by at least 2σ values at a given time are considered to determine this movement. Under this criterion, there exists a total of 122 nights of clear sky data (excluding moonlit and cloudy nights) obtained during the months of Jan, Feb, and Mar in the year 2014 (72 nights) and Jan, Feb in 2015 (50 nights) which are used for analysis. Crests have been found in the northern side (similar to figure 4.1b) on around 47% nights out of these 122 nights during this period.

The different types of OI 630.0 nm nocturnal emission variations across latitudes as

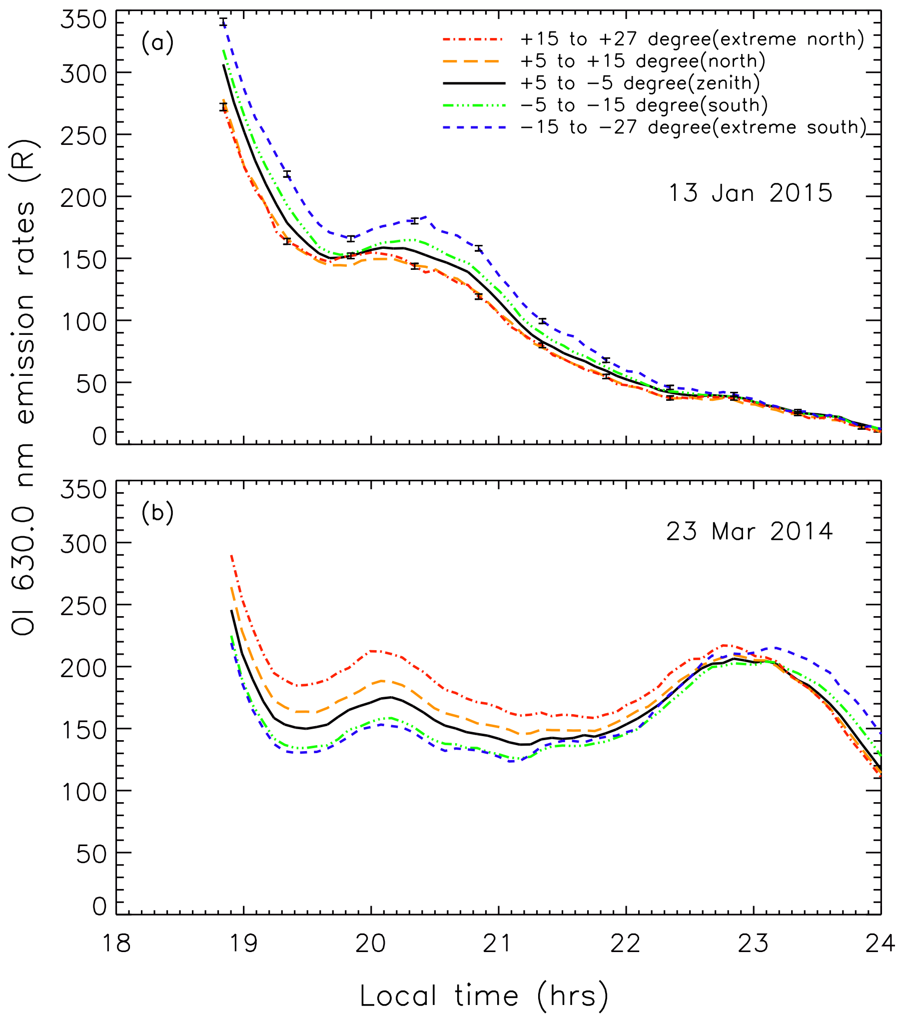

Figure 4.1: Panel (a, b) Emission variations over the whole field-of-view of observations which have been segregated into five spatially independent directions as shown by different line-styles and colours. Nocturnal variations in emissions on two sample nights are shown with different regions of enhancements corresponding to the enhanced electron densities due to the EIA crest.

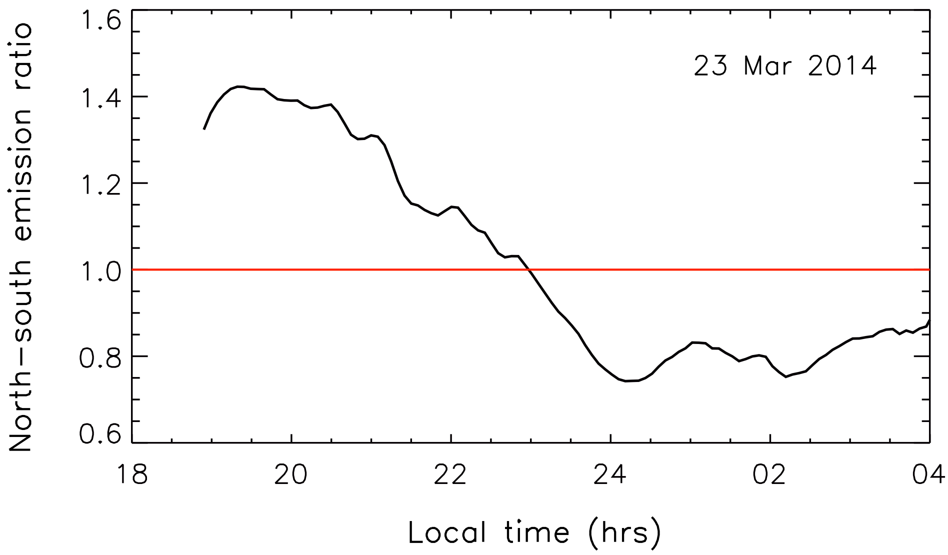

Figure 4.2: N-S emission ratio for the same night as shown in figure 4.1b, 23 Mar 2014, during whole course of the night. The increasing and decreasing trend in the N-S emission ratio indicates the poleward and equatorward motion of the EIA crest over Mt. Abu.

seen along different view directions in the given FOV of HiTIES are depicted in figure 4.1. Variations are seen during the course of the night as well. On some nights after the sunset, the emissions in the southern direction are larger as compared to those in the northern direction (e.g., figure 4.1a), and completely opposite on some other (e.g., figure 4.1b). This is most likely a consequence of transportation of electrons in terms of the movement of the EIA crest across latitudes, which is different on different nights. From the production mechanism of the OI 630.0 nm nightglow discussed above, it can be noted that almost all the variabilities in the emissions are essentially due to the changes in the electron densities in the regions of emissions (chapter 3). We have shown that the height of the F-layer and the OI 630.0 nm emission magnitudes are anti-correlated (figure 3.6 in the chapter 3). The variations in the F-layer height can bring-in/take-away the electrons to/from the peak altitude of OI 630.0 nm nightglow emissions, and thereby affecting the emission rates. Thus, these variabilities are essentially due to the varying strengths of equatorial electrodynamics from one night to the other. In order to quantify such latitudinal movement of OI 630.0 nm emission after the sunset, ratios between emissions along the north-most (from now on represented as N) to the south-most (henceforth, S) view directions with respect to Mt. Abu, have been considered. These two view directions correspond to a separation of about 2.3° in latitude. The variation in the N-S emission ratio throughout the night has been depicted in figure 4.2 for a given night as shown in figure 4.1b. The N-S emission ratio greater than 1 can be attributed to the presence of the EIA crest in the northward of Mt. Abu. As the value of ratio increases, it is an indication of an intensification of the strength of the EIA and of its location further away towards north from Mt. Abu. This is because the column along N would cut across a larger number densities of electron as compared to that towards S. We have investigated the various possible causes which determine the motion of the EIA crest away from the dip-equator towards the low-latitudes, such as the EEJ and PRE as discussed in the sections below.

4.4.1 Effect of the EEJ strength on the ratio of latitudinal emission rates

The strength of EIA corroborates with the strength of EEJ (*Rush and Richmond*, 1973; *Raghavarao et al.*, 1978). The integrated EEJ strength during the pre-noon period showed good correlation with the strengths of EIA, which, as a consequence, determines the latitudinal extent of plasma fountain and location of the EIA crest (*Sridharan et al.*, 1999). As we are investigating the movement of EIA crest during the post-sunset time, we have considered integrated EEJ values for the whole day (7–17 LT). The nightglow observations start in a programmed manner at 18.75 LT on every night. Therefore, these integrated EEJ values have been compared with the N-S emission ratios for a duration of about 15 minutes (18.75–19.00 LT) soon after the start of observations. The N-S emission ratios during this 15-minute period has been shown with day of year in the figure 4.3. The variation in the ratios shows increasing nature with DOY from January to March (winter solstice to equinox). The values of the ratios corresponding to different months are shown in different colours and different pointing symbols. As the integrated EEJ strength serves as a proxy to the equatorial electric fields (*Raghavarao et al.*, 1978; *Sridharan et al.*, 1999; *Hysell and Burcham*, 2000; *Kumar et al.*, 2022b), and thereby to the EIA strength, the variation in emission ratios has been compared with the integrated EEJ strengths for whole day which is shown in figure 4.3b. The nightglow emission ratios of initial period show a small increasing trend with the integrated EEJ variation showing a correlation coefficient of 0.45. As the observations are available starting only at 18.75

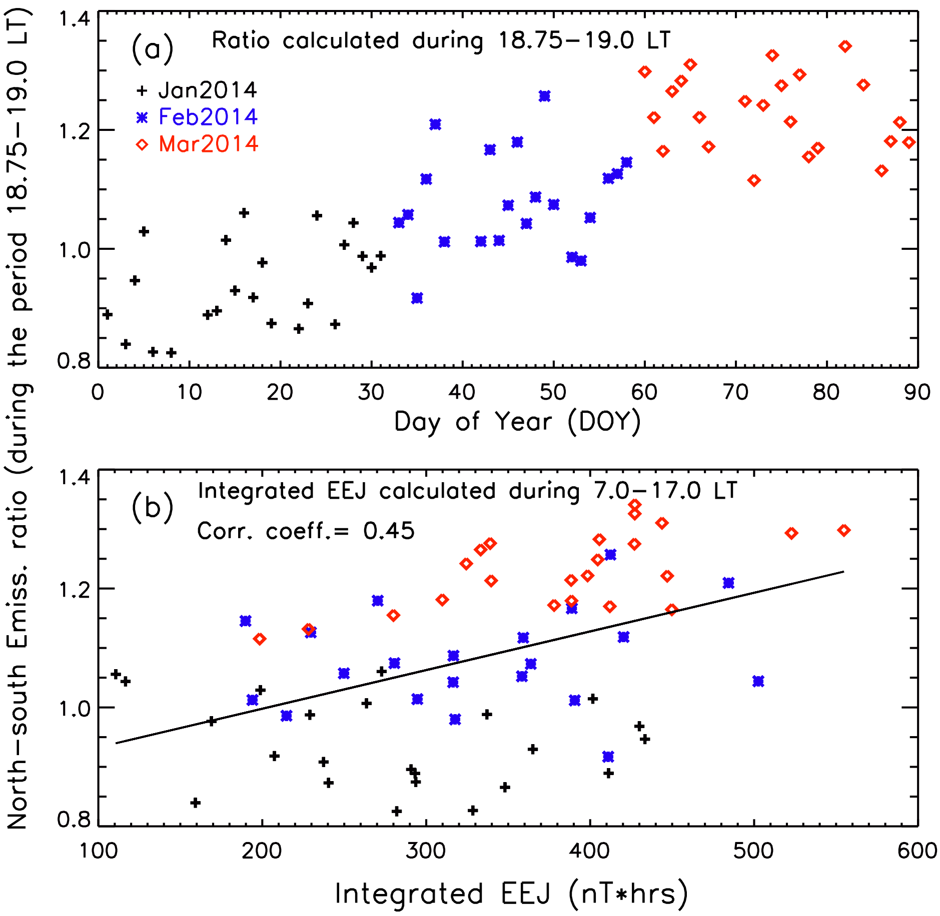

Figure 4.3: Panel a and b show the variation in ratios of emissions obtained along extreme-north (N) and extreme-south (S) as viewed from Mt. Abu during 18.75-19.0 LT with respect to the DOY and integrated EEJ, respectively.

LT, the ratio values can be calculated only from this time and not before. The airglow emission ratios were calculated for a constant time duration 18.75 to 19.00 LT for all the three months. As, the plasma diffusion time for the movement of ionization from equatorial to low-latitudes is of the order of around three hours during the daytime, and so, the electron densities corresponding to the EIA crest could have also been formed even before the starting time of the OI 630.0 nm nightglow emission observations. Further, for the sake of completeness, we have also compared the variation of these ratios with the EEJ data integrated for the pre-noon hours as well which has been carried out in some earlier studies (*Raghavarao et al.*, 1978). The integrated EEJ during the pre-noon time (7-12 LT) also show similar variation as seen for the whole day integrated EEJ values discussed here. Therefore, a clear role of the daytime integrated EEJ strength on the observed emission ratios might not be revealed when only a fixed time duration of 18.75–19.0 LT nighttime airglow measurements are considered. Nevertheless, as it is known that the plasma diffusion initiated in the day is assisted and sometimes rejuvenated by the effect of the PRE at the sunset time, those effects are considered as described below.

4.4.2 Effect of PRE on the variation in the ratio of latitudinal emission rates

PRE in electric field which generates larger vertical drift over the dip-equator during the sunset time can cause a resurgence of plasma fountain, similar to that caused in the daytime EIA by the F-region electric fields. The strength of the PRE in electric field has been determined from the vertical drift by calculating the rate of change of height variation in the iso-electron density at 7 MHz over Trivandrum, the echoes of which correspond to the altitudes above 300 km, and so the effect of recombination on them is negligible (*Bittencourt and Abdu*, 1981). The strength of the PRE on a given day has been characterized by taking the average of ±15 minutes centred at the peak value of PRE occurrence. After the observation starts at 18.75, the emission ratio can be seen increasing and reach a peak value of around 1.45 at 19.5 LT (figure 4.2). The 30-minute average value in emission ratio has been calculated taking the ratio value for the time duration 19.25-19.45 LT for this night. Now, depending upon the time of occurrence of PRE the peak value in N-S emission ratio can change. The time of occurrence of peak value in PRE is different in different months as the sunset times vary from January (18.3 LT) to March (18.6 LT). The peaks in the N-S emissions ratios have been found to occur over times varying from around 30-90 minutes from time of peak occurrence in the PRE. The N-S emission ratios have been compared with the DOY as shown in figure 4.4a. As the winter solstice progresses to equinox, the average emission ratios also show a gradual increase which illustrates that the crest of EIA is also moving in the poleward direction within this duration. The variation in N-S emission ratio indicates the position of EIA crest. Around 33 nights have been found wherein the EIA crest crossed the zenith, moved towards north, and a clear peak in the N-S emission ratios has been found (as shown in figure 4.5 for some of those nights). The data for around first seven nights in the months of January and few nights in each of the months have been excluded either due to unavailability of

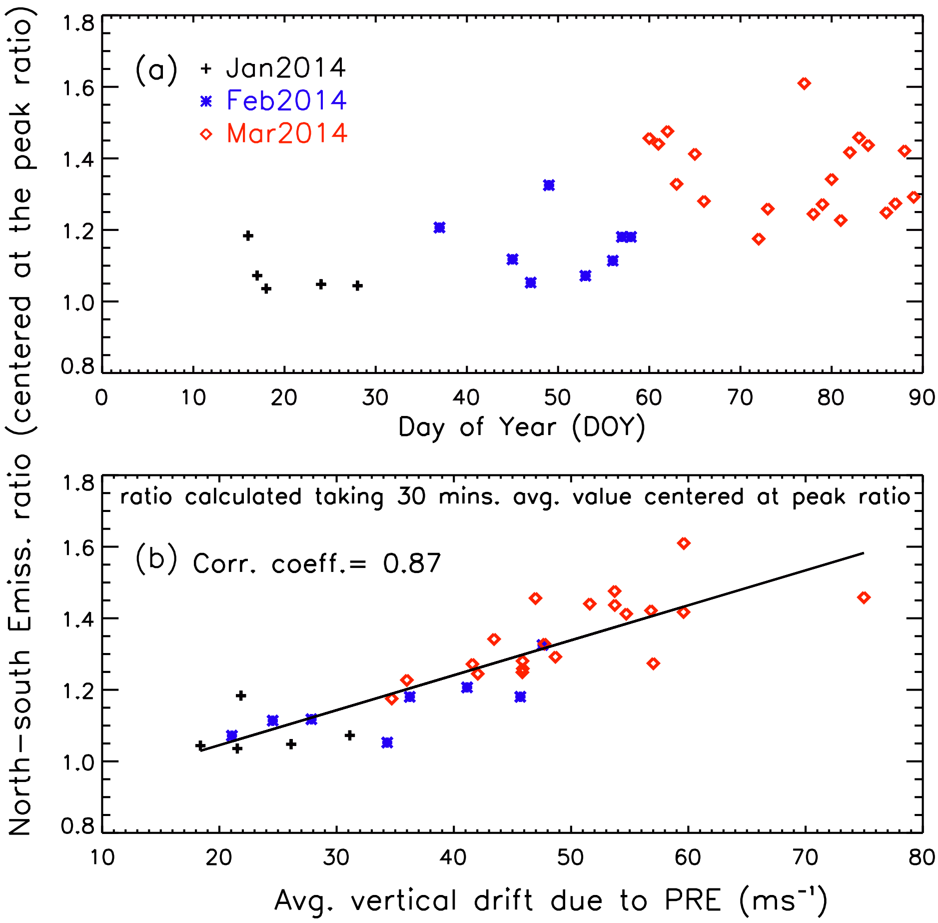

Figure 4.4: Panel a and b show the variation in N-S emission ratios with respect to the DOY and strength of PRE, respectively. The ratios have been calculated by taking ±15 min average centred at the peak emission ratio. The PRE values are averaged (±15 min) around the peak PRE.

equatorial ionosonde data or due to the presence of moonlight in the FOV. The relative effects vary from day-to-day which might explain this varying range of 30-90 minutes between the times of occurrences in the peak PRE and the peak ratios in the emissions. Figure 4.4b shows the integrated (for ±15 min centred at peak) PRE versus the peak ratio (integrated for ±15 min centred at peak) as obtained over different times, which are well correlated (correlation coefficient of 0.87). As we discussed earlier, the strength of PRE increases from solstice to equinox period, the average emission ratios also show a linearly increasing trend with DOY (figure 4.4). The strength of PRE rejuvenates the fountain process during the sunset time and causes the latitudinal movement in the EIA crest. The stronger the PRE, the further the extent of the EIA crest. So far, the northward movement of the crest under the influence of PRE has been described, in the following, the reason for the reverse movement of the crest will be discussed.

4.4.3 Reversal in the EIA crest and estimation of the reversal speed

We have discussed the poleward movement of the EIA crest by considering the ratios between the emissions from northern and southern directions. During the month of March, the values of the N-S emission ratios are higher, which indicates that the likely position of the EIA crest is towards the latitudes further away in the northern direction as compared to other months (January and February). This is most likely due to the effect of a stronger PRE in March as compared to that in January (*Fejer et al.*, 1991). In figure 4.5, the airglow emission variations for 12 nights, four nights for each of the three months in the year 2014, are shown. Higher emissions along N have been observed on all these nights. Interestingly, as we move from January to March, the differences in magnitudes of emission rates between those obtained in the north and the south increase, with larger values towards North. In this context, it may be noted that the emission rates for February and March are larger, the values are depicted on the right-side y-axis. This is understood to be due to larger amount of plasma being brought over to the low-latitudes from the equatorial locations during sunset time, displaying a clear effect of plasma transport that is varying from month to month. After sunset, the rate of decrease in the magnitude of emissions becomes smaller along N compared to that of S. In contrast to this, the emission magnitudes that were larger along N decrease at a rate faster as compared to those at S at a later time. This is inferred to be due to the process of initiation in the reverse movement of the EIA crest as a function of time. The vertical drift measured by incoherent scatter radar (ISR) and satellite data (*Fejer et al.*, 1991, 2008) over the dip-equator show an upward plasma vertical drift during daytime which corresponds to the eastward electric field over the equatorial F-region. During nighttime, the electric field reverses and becomes westward and so the vertical drift becomes downward (*Fejer et al.*, 1991). It is known from earlier studies, including our own (*Saha et al.*, 2021), that an F-layer movement to lower altitudes causes an increase in OI 630.0 nm emissions by the process of dissociative recombination as a downward movement of the F-region brings-in greater number of electron densities into the peak emission altitudes (250 km

$\pm$ 50 km) of the OI 630.0 nm. This downward movement of the ionospheric height can be caused by the equatorial westward electric field. Thus, this reversal in the EIA crest is inferred to be due to this nightly equatorial westward electric field. Further, in order to explore if meridional winds can contribute to the increase in emissions as observed in the southern direction, we have looked at their typical nightly variation. The increase in emissions in the southern direction is observed during 21-24 LT, wherein, the meridional winds are typically equatorward (*Drob et al.*, 2015; *Saha et al.*, 2021). It is known that the equatorward meridional winds cause uplift of plasma along the field lines, and consequently, will result in decrease of OI 630.0 nm emissions (*Saha et al.*, 2021), and not an increase. Therefore, it can be inferred that the meridional winds at this time cannot contribute to the observed increase in emissions in the southern direction.

To investigate the reverse movement of the EIA crest from one night to the other, ratios in emissions from N to S have been estimated for all the times (figure 4.6), unlike only around peak values as shown in figure 4.4. The variation in the N-S ratios on the nights are depicted in figure 4.6 for the nights as shown in figure 4.5. On a given night, the maximum value in ratios suggests that the crest is located in the northern region and the time corresponding to the maximum ratio is considered to indicate the time when the EIA crest has reached to that location. As the crest moves in the southward direction it crosses the value of one, which indicates that emissions over the northern and southern sides of the view direction are almost equal. The minimum values in the ratio indicate that the EIA crest is located in the southern-most view direction of HiTIES on a given night. To identify the times of maximum or minimum values in the ratios, we have considered those times only when the differences between the emissions along N and S are greater than 10 R, which is at least 3 to 4 times greater than the value of the measurement uncertainty (σ). After the time of occurrence in the minimum value, the ratios trace back to around a value of one with time as the poleward side of the EIA crest moves further southward and away from the HiTIES FOV and so, the airglow emissions at both N and S decrease to the nightly 'background' values. On some nights, e.g., 22 Feb and 25 Feb 2014, after the maximum values in emission ratios were observed, there were one or more excursions in emissions before the ratios reached to one. Such observations are possibly due to the latitudinal structures that may be existing in the EIA on a given night. In the present work, during the high solar activity year 2014, we have noted reverse movement of the

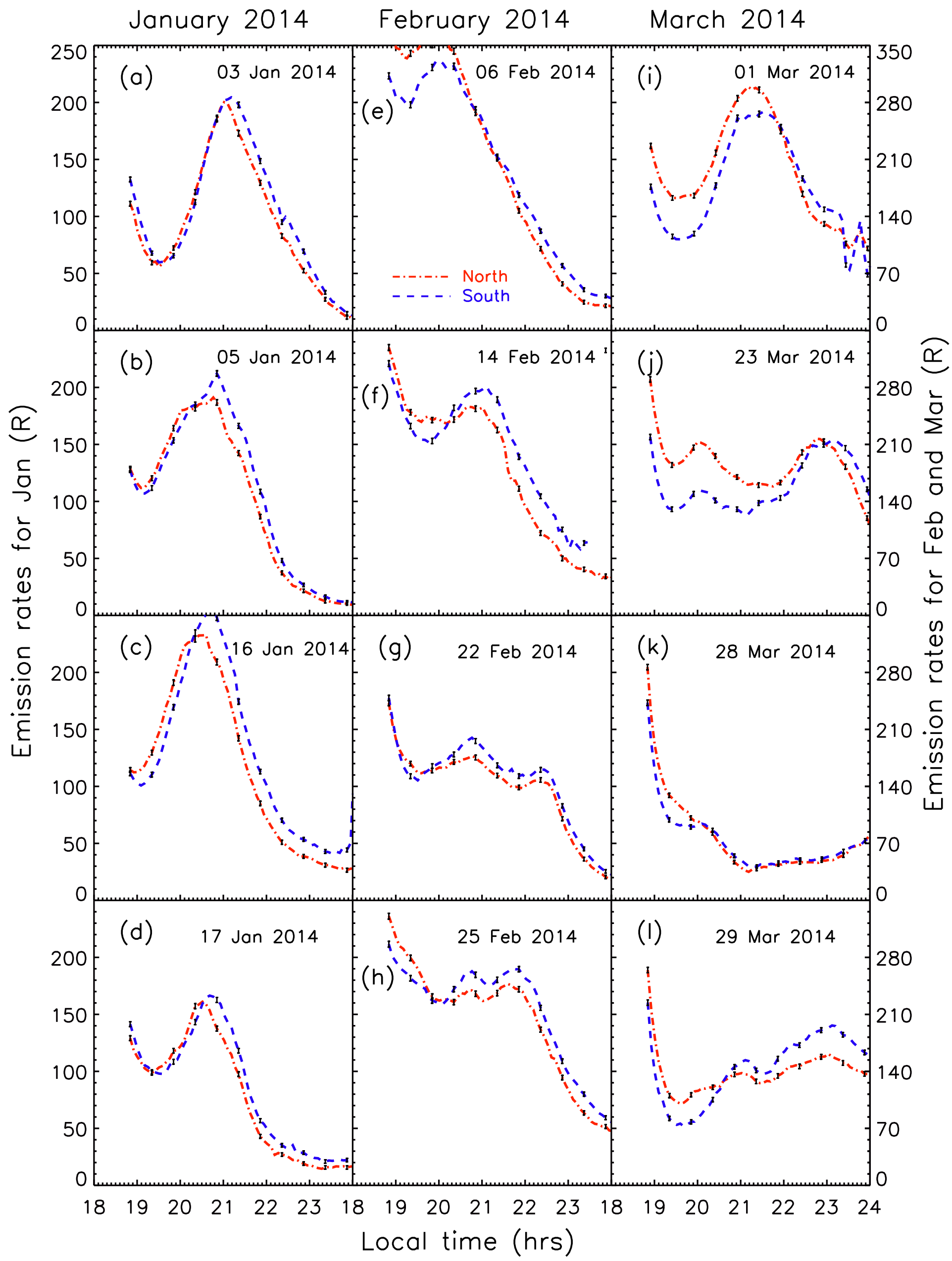

Figure 4.5: Emission variations along the two directions (N and S) for 12 nights, 4 nights for each of the months, are shown in a column. The left side y-axis corresponds to the month of Jan and the right one corresponds to those for Feb and Mar. Uncertainty in the measurements are small (± 1.4 – ± 2.4 R), shown in each of the figures.

EIA crest on many nights. On some nights there are data gaps due to the presence of moonlight in the FOV. Also, there are other nights, wherein, equatorial spread-F had occurred. These two effects, when present over large spatial extents in the given FOV, prevent unambiguous determination of the reversal in the EIA all through the FOV. Therefore, for these nights, a portion of the distance, either from north to zenith or zenith

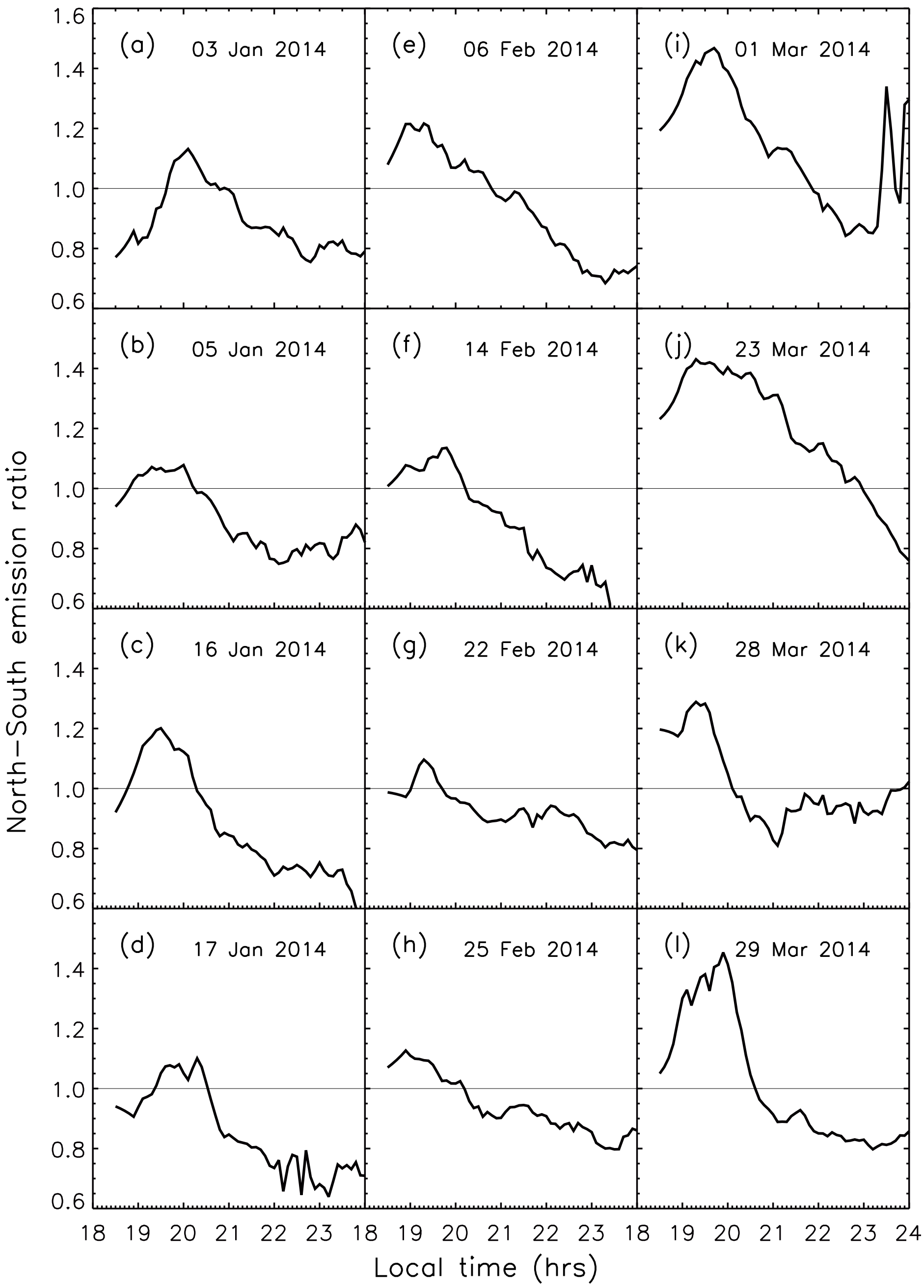

Figure 4.6: The N to S ratios obtained in the OI 630.0 nm emission rates are shown for the 12 nights whose nocturnal emission rates along N and S are depicted in figure 4.5

to south is considered for the estimation of reversal speeds.

A nice pictorial sense of reverse equatorial ionization had been presented in figure 4.7 which has been reproduced from the work of *Sridharan et al.* (1993b). By using All-sky Imaging Fabry-Perot Spectrometer measurements of OI 630.0 nm nocturnal emissions, images of Fabry-Perot interferometric rings were reported in that work which serve as

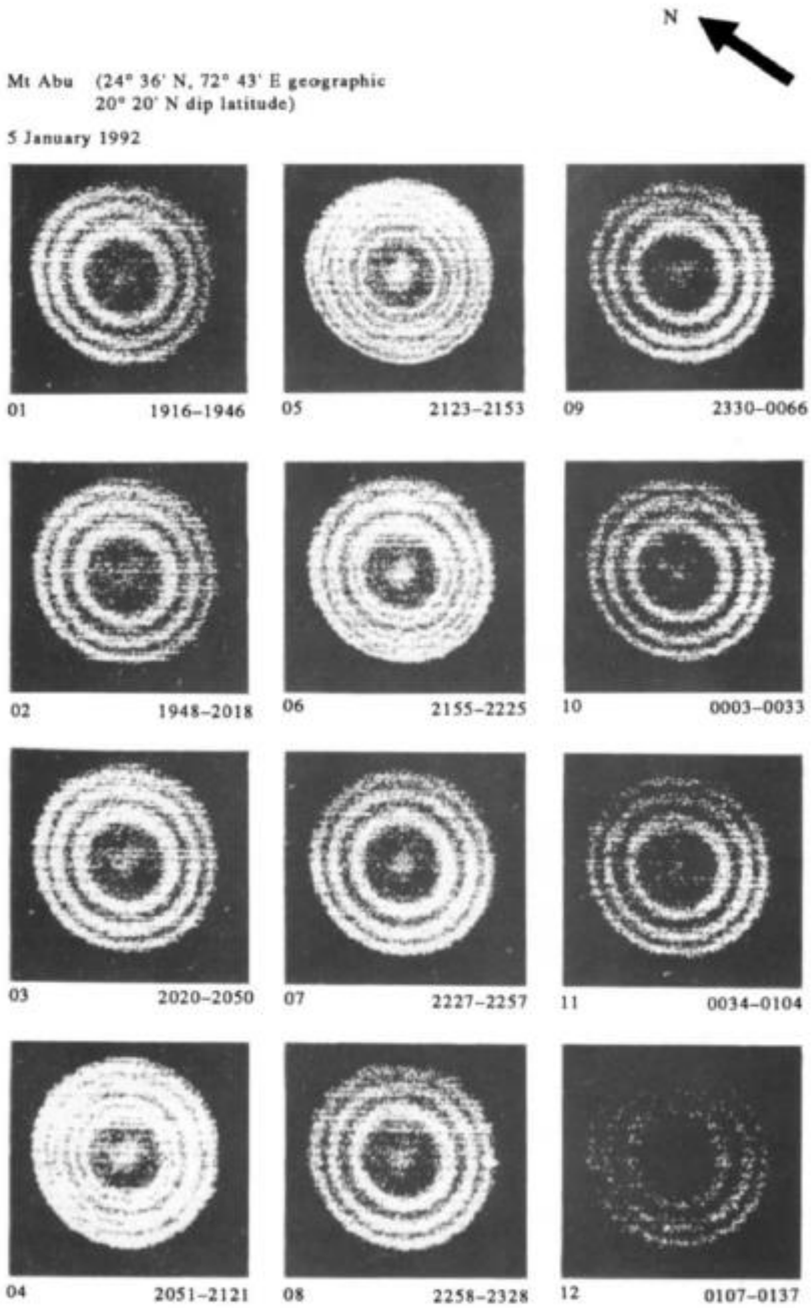

Figure 4.7: Equatorward movement of EIA crest obtained from Mt. Abu on 05 Jan 1992 using the all-sky imaging Fabry-Perot spectrometer. (After *Sridharan et al.*, 1993b).

a clear observation of the equatorward movement of the EIA crest as observed on the night of 05 Jan 1992 from Mt. Abu. Each image of this figure shows Fabry-Perot fringes corresponding to data obtained for half an hour over a 140° FOV. The fiducial shows the orientation of the magnetic north. From the sequence of images, it is clear that during 1916-1946 LT the emission rates are higher towards north, indicating that the crest of the EIA is northward of Mt. Abu on that night in the duration of high solar activity period (the solar flux was 257.7 solar flux units on this day, 1 sfu=10^{-22} $Wm^{-2}Hz^{-1}$). As time progresses, it can be seen that the brightness in emission sequentially shows a southward movement. In the images obtained during 2051–2153 LT, the emission intensity in all the fringes seem to be equal in all the directions. Later, this enhancement in emission rates move further southwards and by 0137 hours of 06 January 1992, the EIA crest had moved away from the FOV of the instrument. Based on these measurements, the speed of the movement was reported to be 1.4° lat.hrs^{-1} or 42 ms^{-1}.

In the present study, we have estimated the speeds of the equatorward movement of the EIA by taking the time differences of the crests at north and south. The distance between the centre of northern and southern directions is considered for the estimation of the speed of the reversals. A schematic has been shown in figure 4.8 which helps in visualizing the calculation of reversal speed. The uncertainties in the location arise due to the spatial extent considered for each directional segment (north and south) and we have taken centre-to-centre distance between two segments while calculating the speeds. We have also checked the available optical data in January and February in the year 2015 and calculated the speed of the movement of the EIA crest. Total of 40 nights, 25 in 2014 and 15 in 2015, have been considered for estimation of the speeds of the EIA crest. The speeds obtained from the present data fall in the range of 10–55 ms^{-1} with an uncertainty in them of around 6-30 ms^{-1} as shown in figure 4.9.

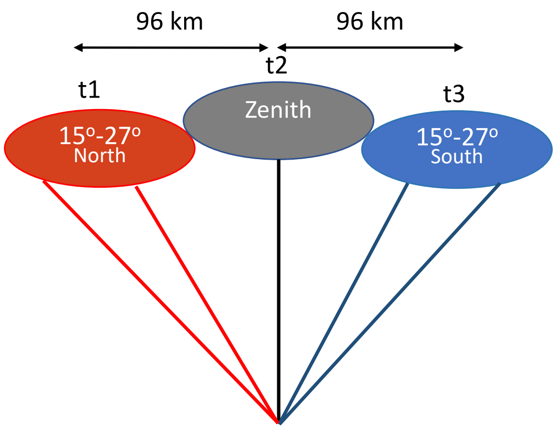

Figure 4.8: Schematic of the reversal speed calculation. The extreme north and extreme south correspond to the angular separation 15°-27° out of whole FOV of HiTIES (54°).

In an earlier work that was based on optical imager measurements from Kolhapur (11.1°N Mag), the reversal speeds in EIA were reported to be in the range of 25-90 ms^{-1}

for nights during January-March in the year 2008 (*Narayanan et al.*, 2013). We have also included those values reported in that work in figure 4.9.

4.4.4 Variation of reversal speeds with solar flux, season and PRE

As discussed so far, the upward vertical drift during sunset time causes the poleward movement of EIA and then, in the night time, as the zonal electric field reverses its direction towards westward, the vertical drift becomes downward. Thus, the base of the F-layer height is pushed down, and as a consequence it gives rise to larger emissions in the southern direction. To explore the relationships of the speeds of reversal with the background plasma density, meridional neutral winds, and evening time equatorial electrodynamics, if any, we have plotted them with respect to the solar flux, day of the year (seasons), and PRE strength in figures 4.9 and 4.10.

The variation in the speeds of EIA crest movement with solar flux values is depicted in figure 4.9a corresponding to the years 2014 and 2015. As mentioned above, the reversal speeds reported earlier in studies in 1992 (*Sridharan et al.*, 1993b) and 2008 (*Narayanan et al.*, 2013) are also included in this figure. Estimated speeds from *Narayanan et al.* (2013) show large excursions within a small variation in solar flux which was calculated during the year 2008 from another location, Kolhapur, that is located around 8° away in latitude towards equator from Mt. Abu. In the year 2014 and 2015, the solar flux values are comparatively higher than those in 2008. The average speed of the crest decreased during the high solar activity year 2014-2015 compared to that calculated over Kolhapur in 2008. We do recognize that there could probably be differences in the reversal speeds with respect to magnetic latitudes as Mt. Abu and Kolhapur are far apart. Nevertheless, a decrease is seen in the values of the reversal speeds of EIA with solar flux, although the nature of its variation does not indicate any conclusive result in the given extent of the data.

Figure 4.9b depicts the variation in the reversal speeds with respect to the DOY, wherein, all the available data are plotted as shown in figure 4.9a. Even though it may appear that the envelope of higher values in reversal speeds shows a decreasing trend with DOY (season), however, as the data are biased with larger number of nights during the months of January and February as compared to that during March, therefore, unambigu-

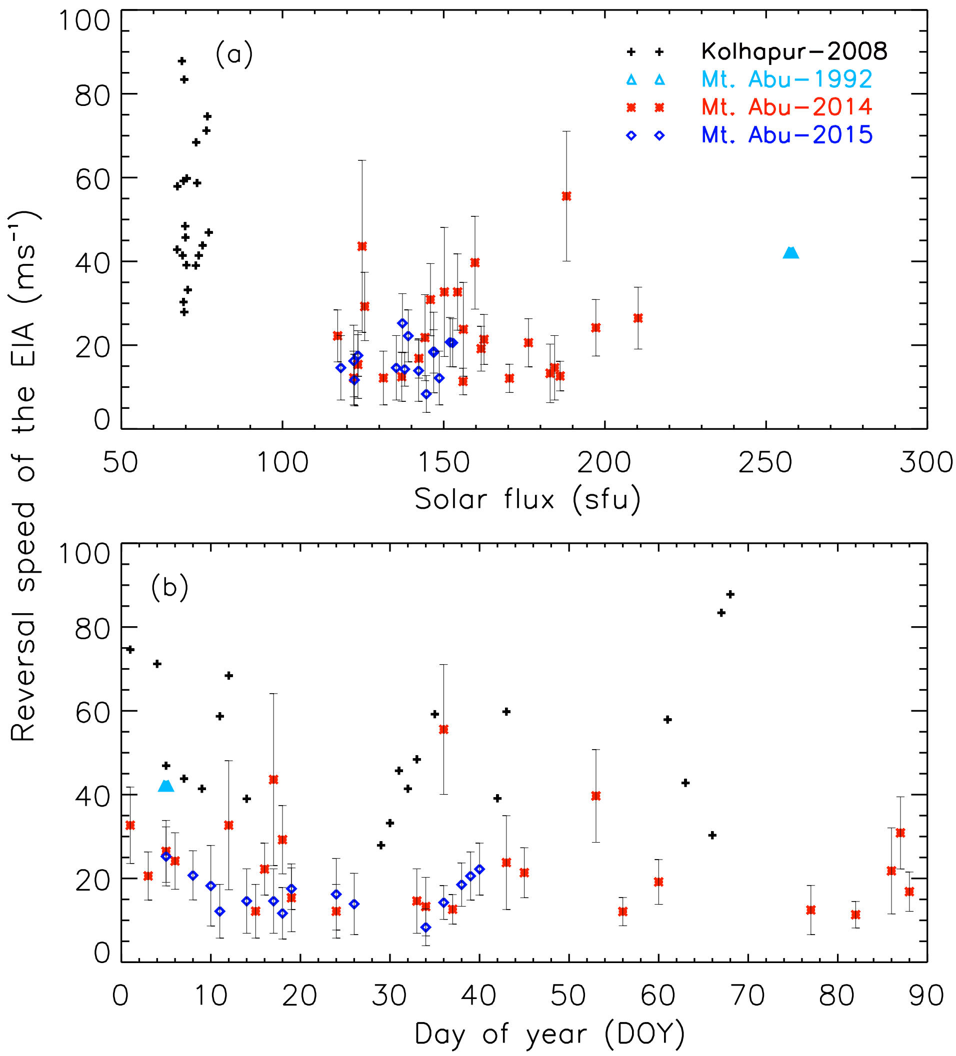

Figure 4.9: (a) The speeds of the EIA crest movement with solar flux variation are depicted for a total of 61 nights. Result from earlier published results from different studies is also included. The speeds calculated for the emissions obtained from Mt. Abu for two different years 2014 and 2015 are shown in red and blue colour, respectively. (b) Reversal speeds of the EIA crest for the same nights have been depicted with the day of year (DOY).

ous inferences cannot be made. Although the seasonal trends of vertical drift over the dip-equator show an increasing nature, and the poleward meridional wind a decreasing behaviour from January to March, the variation in reversal speeds, however, do not show any relation whatsoever with model meridional winds or solar flux.

From the previous discussions presented in this study, it is quite clear that the latitudinal extent of the EIA crest in the poleward direction is solely dependent upon the strength of the vertical drifts generated by PRE in electric fields. Therefore, we have

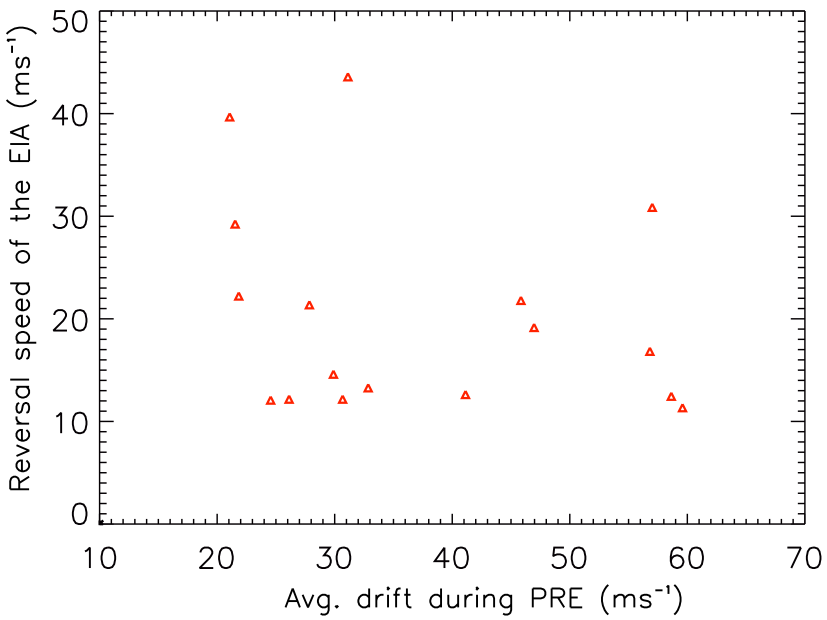

Figure 4.10: The reversal speed of the EIA crest is shown along with the available average vertical drifts obtained during PRE in the year of 2014.

explored if the variation in the reversal speeds observed in the EIA movement has any relation with the strength of the PRE. On the basis of the available data on equatorial vertical drift, reversal speeds for seventeen nights during 2014 have been obtained and are depicted in figure 4.10. It can be readily noted that the PRE strengths do not show any relation with the reversal speeds of the crest location EIA. Therefore, it seems that the nighttime electrodynamics is independent of the strength of the PRE that occurs during sunset time.

4.5 Discussion

From the measurement of vertical plasma drifts over the magnetic equator as shown in figure 4.11, it is known that the drifts are vertically downward in the nighttime indicating a westward electric field. It can also be seen in the figure 4.11, that the magnitude and the variability of the downward plasma drift undergo significant changes, both during the course of a night and from night-to-night. Therefore, it can be expected that the equatorward movement of the crest of the EIA is due to such westward electric field over the equator. This, however, has not been demonstrated in any of the studies so

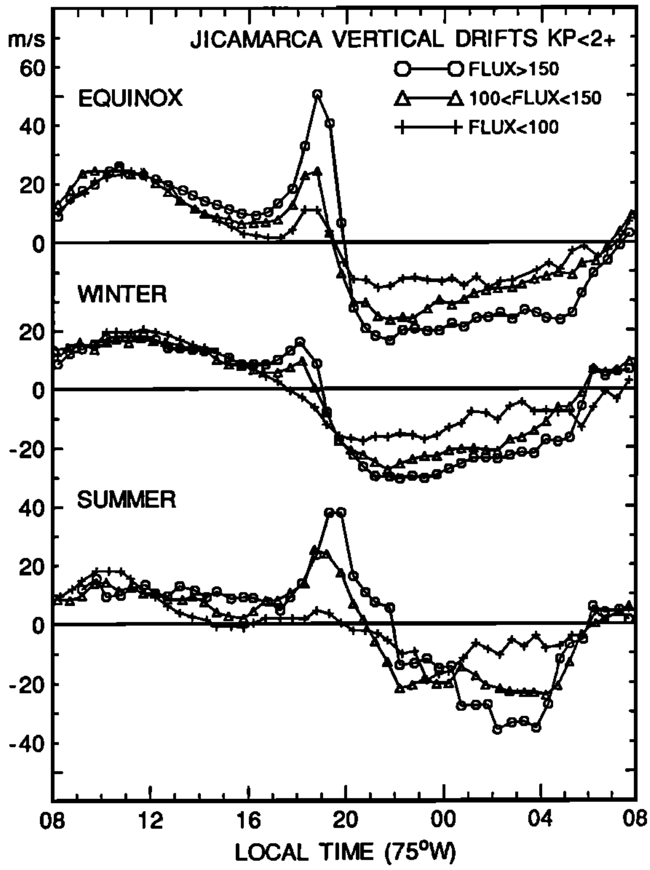

Figure 4.11: Vertical drift of plasma over the dip-equatorial location Jicamarca. The nighttime vertical drift shows quite variability in terms of solar flux and season. The day-to-day variability in the vertical drift is also expected. (After *Fejer et al.*, 1991).

far. This is because, the direct measurement of the westward equatorial electric fields has been mainly restricted to the American longitudes where an ISR exists. Due to the recombination between neutrals and ions, electrons in the nighttime upper atmosphere, it is difficult to obtain unambiguous information of the nighttime electric field from the digisonde. Besides, on several occasions, the presence of equatorial spread-F also hinders the measurement of ionospheric electron density using digisonde. Further, satellite measurements of ion-drifts or electric fields over the magnetic equator are not available over the Indian longitudes during the night time. Few passes of C/NOFS over Indian longitudes during our observational period, whenever available, were above 500 km altitude and so, the electron densities were low. Presumably, due to these low electron densities at these altitudes, the vertical drift measurements on-board C/NOFS, whenever present showed large fluctuations.

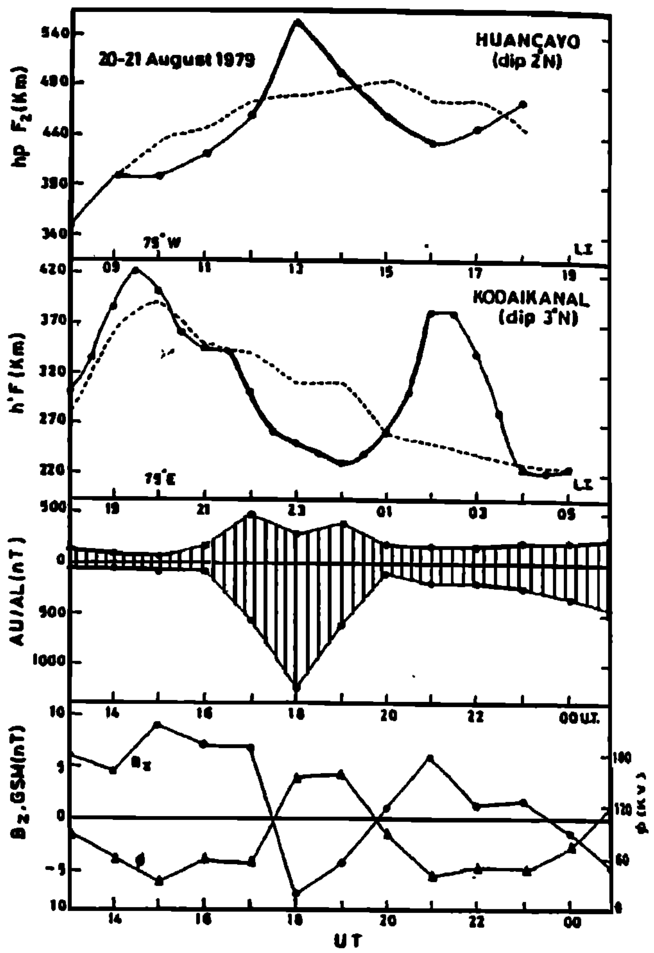

Figure 4.12: The top panels show the ionospheric height variation at Huancayo and Kodaikanal on 20-21 Aug 1979. The bottom panels indicate the presence of strong geomagnetic disturbance on that day. (After *Sastri et al.*, 1992)

Therefore, in the absence of any direct measurement(s), we ascertain the veracity of our interpretation on the westward electric field being the cause for the equatorward movement of the EIA by taking recourse to the fact that the equatorial electric fields are global in nature. The ionospheric electric fields are governed by $\oint \mathbf{E} \cdot d\mathbf{l} = 0$, where $\mathbf{E}$ is the electric field at a given location and d$\mathbf{l}$ is the element of length along the dip-latitude. Therefore, it is imperative that larger eastward electric field in a longitude sector will be compensated by a simultaneous westward electric field in the opposite sector (*Fejer et al.*, 1991). In this background, we consider the findings of an earlier study as a beacon to go forward, in which *Sastri et al.* (1992) showed that the effects of prompt-penetration during substorm event over two equatorial locations which are situated in the opposite longitudes, Kodaikanal in the Indian sector and Huancayo in the South American sector,

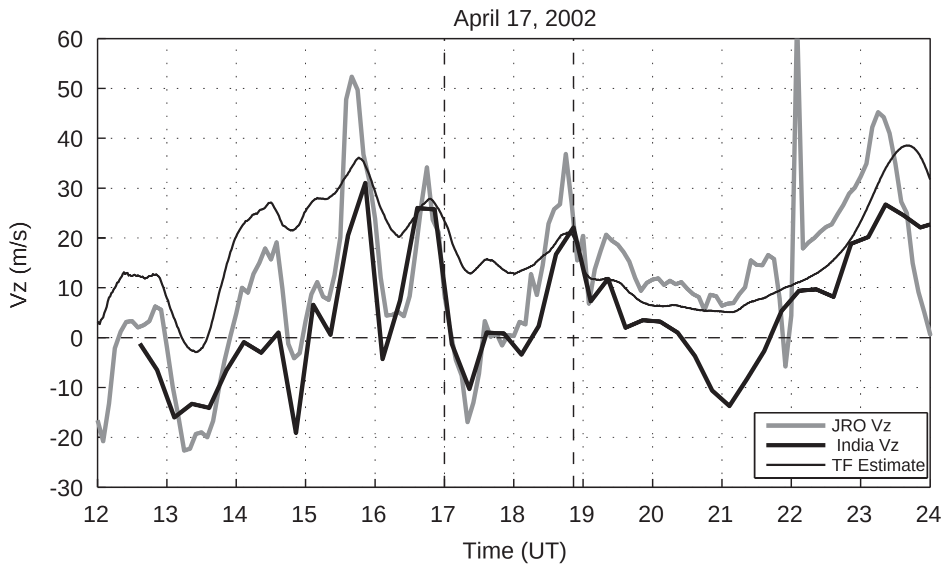

Figure 4.13: The vertical drifts from Peru and India are overplotted here. The negative magnitude of vertical drift is shown for Indian data. The vertical dashed line at 17 UT indicates the local noon at Jicamarca, whereas, the vertical dashed line at 19 UT corresponds to local midnight in India. (After *Kelley et al.*, 2007)

were greatly related. In that study, it was shown that an increase in polar cap potential decreases the F-layer height over Kodaikanal which was in simultaneity with an increase in height of the F-layer over Huancayo. Subsequently, the decrease in polar cap potential causes an increase in the F-layer height over Kodaikanal and a decrease over Huancayo (figure 4.12). Another example in which the daytime vertical drifts over Jicamarca were observed to be perfectly anti-correlated with the night time vertical drift over India was reported during the geomagnetic storm event of 17 Apr 2002 (*Kelley et al.*, 2007). The equatorial electric field has been observed varied similar with the interplanetary electric field on this day with 86% correlation coefficient. The negative magnitude of vertical drift measured over Indian longitudes is overplotted with the vertical drift over Jicamarca (figure 4.13). The magnitudes of the vertical drifts at these two sectors are quite similar which are understandable as the magnitude of the penetrated electric field in comparable in these both day and night sector. The results reported in these two studies are a clear demonstration of the irrotational nature of the global ionospheric equatorial electric field. These events were during geomagnetic disturbed conditions, wherein the effects are known to get accentuated. Such results, motivated us to explore whether this effect can be established during geomagnetic quite conditions also, to which our present experimental results correspond. To the best of our knowledge, there has been no experimental evidence of irrotational nature of global ionospheric electric field that has been reported in the literatures for geomagnetic quiet times, presumably as the changes are expected to be subtle. However, this irrotational nature of the equatorial electric field which satisfies the relation $\oint \mathbf{E} \cdot d\mathbf{l} = \oint B\mathbf{v} \cdot d\mathbf{l} = 0$, is used in the process of generation of the global empirical ionospheric vertical plasma drift model by *Scherliess and Fejer* (1999).

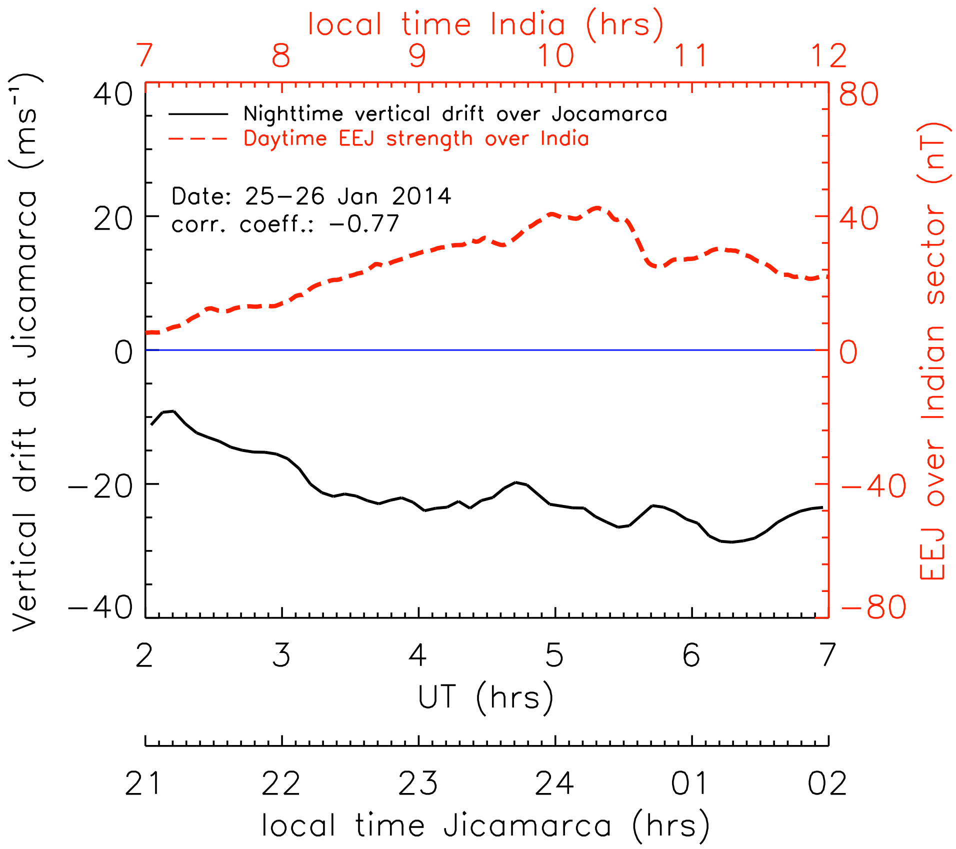

Figure 4.14: The variation of nighttime vertical drift over Jicamarca is shown with the variation of EEJ over Indian sector at simultaneous time of a given day which is a non-ESF night over Jicamarca. The universal time and corresponding local times at Jicamarca and Indian sector are shown in different x-axes. The variation shows clear anti-correlation behaviour between these two.

Here, we have tried to show simultaneous variation in the day and nighttime electric field variations using nighttime vertical drifts and daytime EEJ strengths from two opposite longitude sectors during geomagnetic quiet time periods. The vertical drifts measured from ISR over Jicamarca are used to serve as a proxy for nighttime ionospheric electric field. The daytime EEJ variation measured from Indian sector is used to serve as a proxy of daytime electric field. Such simultaneous variation of the nighttime vertical drifts and daytime EEJ strengths for one night is shown in figure 4.14 for a non-ESF night over Jicamarca. The temporal variation of the vertical drift on the nightside shows a clear anti-correlation with the EEJ variation on the dayside. Similarly, in reciprocity, the variation in the EEJ over Jicamarca sector indicates the variation in the nighttime electric fields over Indian sector.

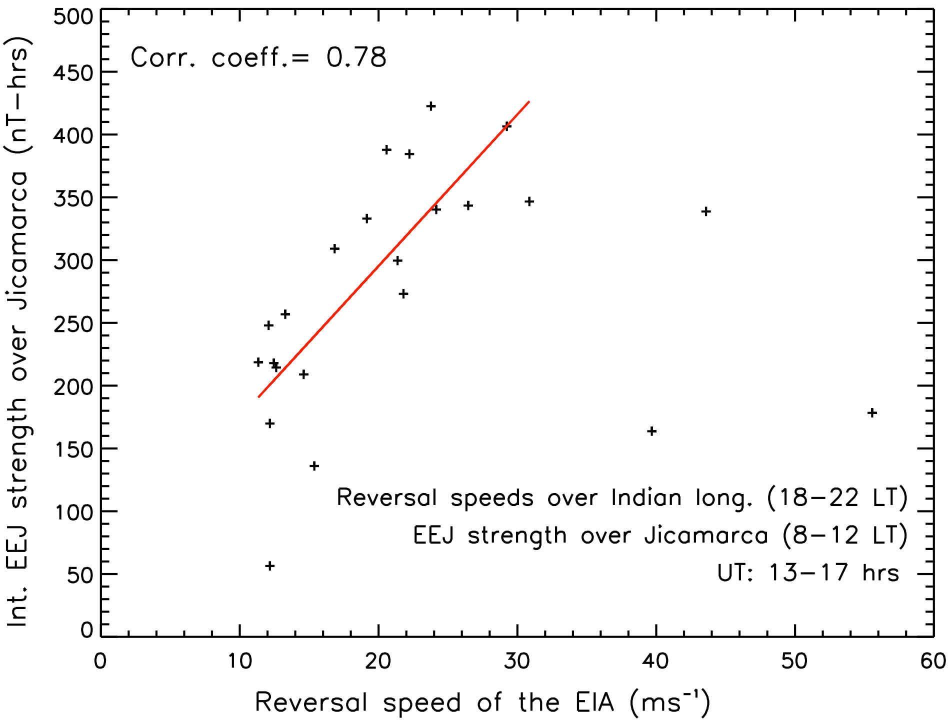

Figure 4.15: Integrated EEJ variation for the duration 8-12 LT over Jicamarca is compared with the reversal speed of EIA over Indian sector for the year 2014. The three nights when the speeds are > 40 ms^{-1} are not considered in obtaining the linear fit and the correlation coefficient.

In this background, we have attempted to explore the equatorial electrodynamic behaviour at opposite longitudes in simultaneity with those of our measurements over Indian longitudes. In order to do that, we have considered the daytime EEJ strength integrated for pre-noon (duration 8-12 LT for Jicamarca) as a proxy of the daytime equatorial F-region over the American longitudes (*Raghavarao et al.*, 1978; *Hysell and Burcham*, 2000). We have compared this with the nighttime reversal speeds of the EIA crest obtained in simultaneity using the optical measurements over the Indian sector as shown in figure 4.15.

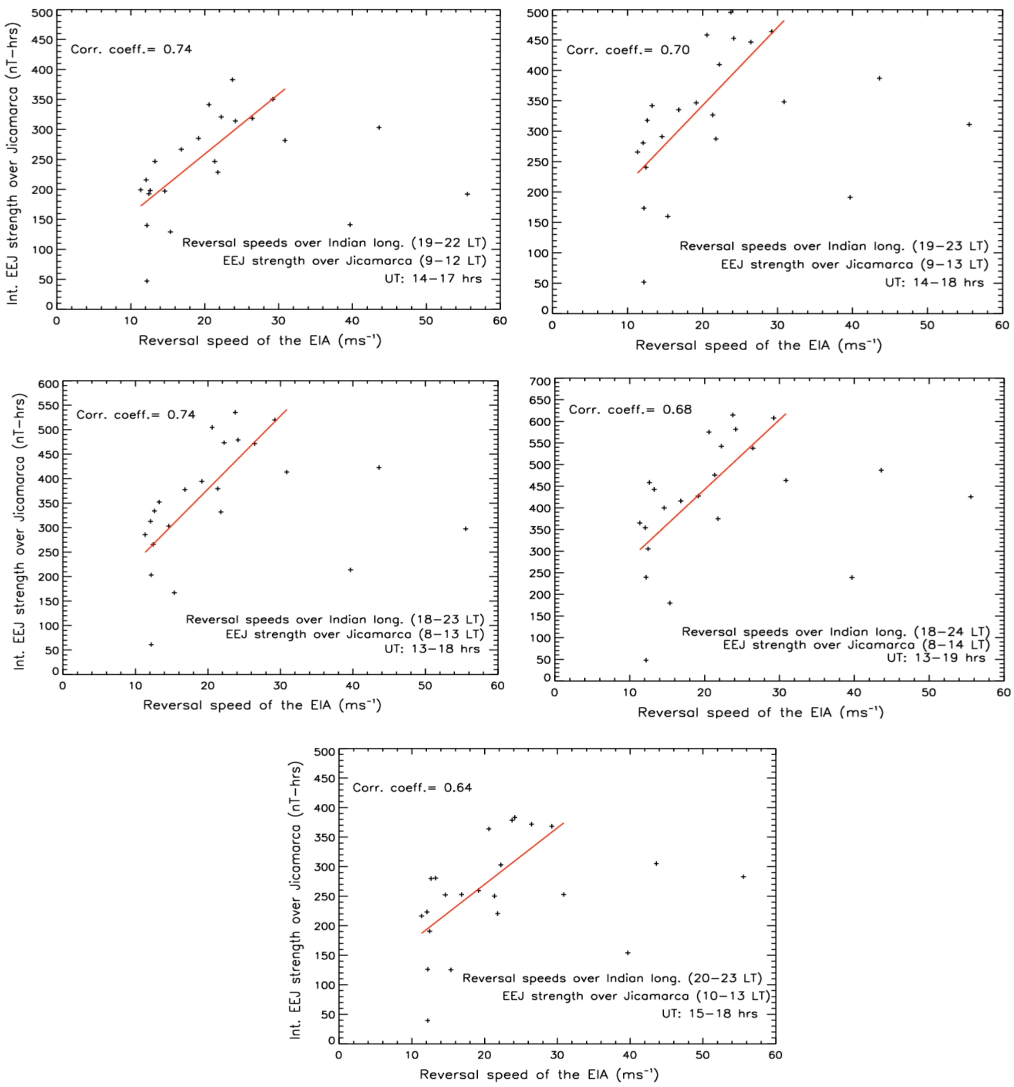

Figure 4.16: Same as figure 4.15 with different time duration.

As discussed earlier, the reversal of EIA depends on the variation of the nighttime westward electric field, therefore, the speeds of the reversal of EIA have been compared with the strength of the daytime EEJ at Jicamarca. It is remarkable that these two proxies correlate very well (correlation coefficient of 0.78) (*Saha and Pallamraju*, 2022). Here, the nights in the year 2014 when the EIA crest had reached the latitude of Mt. Abu as seen in the emissions have been considered. On many nights in the year 2015, the EIA crest did not reach Mt. Abu, most likely due to the decreased solar activity in 2015 compared with 2014, and hence has not been included in this analysis. It should be mentioned here that the three points with speeds greater than 40 ms^{-1} have not been considered for the calculation of the correlation coefficient. The large deviation in the speeds on these three nights could not be understood, at present, especially as these were geophysically quiet days and also as the rest of the values are around 30 ms^{-1} or less. For the sake of completeness, we have compared and calculated the correlations between the integrated EEJ over American longitudes with the reversal speeds for other time durations also, such as 8-13 LT (corr. coeff. 0.74), 8-14 LT (corr. coeff. 0.68), 9-12 LT (corr. coeff. 0.74), 9-13 LT (corr. coeff. 0.7), and 10-13 LT (corr. coeff. 0.64) and it can be noted that they all are positively correlated, which are shown in figure 4.16. It can be noted that they all are positively correlated.

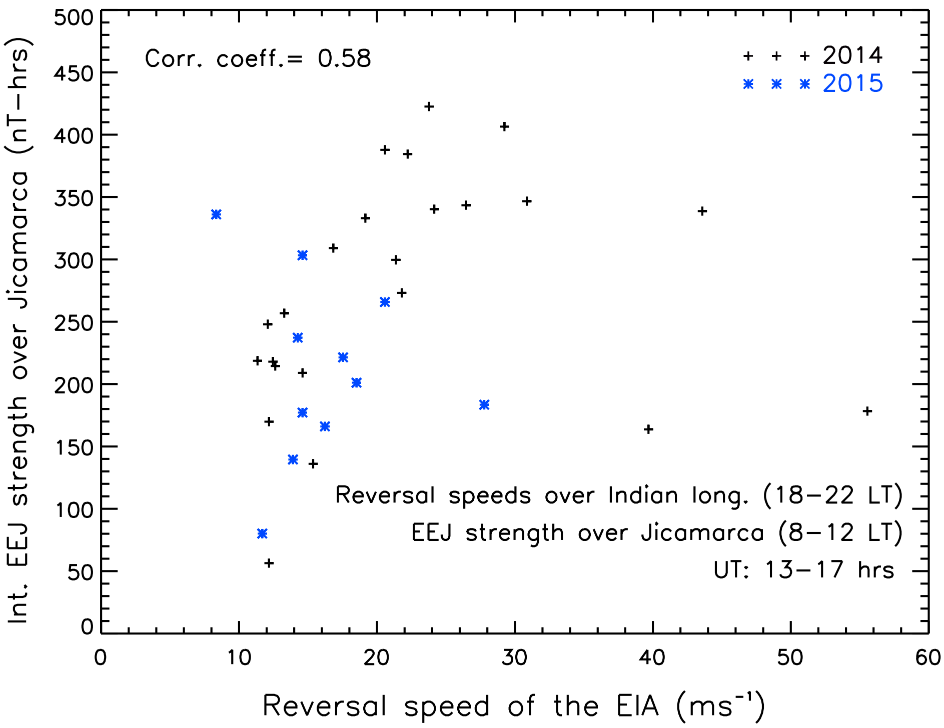

Figure 4.17: Same as figure 4.15 with including the data points of the year 2015 also. Most of the data points show quite good linear relationship between the nighttime reversal speed over Indian longitudes and the integrated EEJ strength over Jicamarca.

In figure 4.17, we have compared the reversal speed with the integrated EEJ strength over Jicamarca including the nights in the year 2015. The correlation value between the integrated EEJ and reversal speed is found of around 0.58 after including the nights of 2015 along with the nights mentioned in figure 4.15 for the year 2014. On many nights in the year 2015, the EIA crest did not reach Mt. Abu, most likely due to the decreased solar activity in 2015 as compared with that in 2014 which can be understood to may result in the reduced correlation value as depicted in figure 4.17. It can be seen that most of the data points depict nice linear relationship. As these are all geomagnetic quiet periods, therefore, geomagnetic disturbance effect cannot be cause for such deviation. Probably, the contribution of electric field variation from other sectors (afternoon, midnight) is different as well to maintain the $\oint \mathbf{E} \cdot d\mathbf{l} = 0$ condition. This possibility could not be verified and would be explored in future.

The present results are particularly interesting as they show the experimental evidence of the global nature of equatorial electric fields during the geomagnetic quiet time periods. In doing so, two proxies for electric fields, integrated EEJ strength in the daytime, and reversal speeds of EIA in the nighttime as seen in OI 630.0 nm airglow emissions have also been characterized. The electric fields are extremely difficult to measure during nighttime. Only measurements from an ISR located over the magnetic equator can yield accurate information on the equatorial electric fields. However, it is practically impossible to install an ISR over several longitudes around the globe. In contrast, it is more viable to obtain the OI 630.0 nm nightglow measurements over a large FOV at different longitudinal sectors, which could give information on relative variations in the electric field. It is expected that simultaneous measurements of westward electric fields from ISR, Jicamarca and estimation of reversal speeds in EIA as measured from optical emissions from the same longitude sector will enable a direct comparison and enable quantification of the EIA reversal speeds with the equatorial electric fields. Models and simulations studies will also help in quantifying the extent of correspondence between the reversal speed and nighttime electric field variations, which will be carried out in the future.

4.6 Summary

OI 630.0 nm emission data from a large FOV optical instrument, HiTIES, is used to investigate the latitudinal movement of the EIA crest during the post-sunset time for geomagnetic quiet conditions. During March (and towards the end of February), it has been observed that the airglow emissions along the northern direction are larger after sunset time as compared to those along the southern direction when viewed from Mt. Abu. The ratios in emissions towards north and south directions have been investigated as a consequence of equatorial electrodynamical phenomena, such as daytime integrated EEJ, and the PRE strength of electric field. A good relationship between the vertical drift due to PRE in electric field at sunset time and N-S emission ratios in the nightglow has been obtained. As the strength of the PRE increases, plasma rises to higher altitudes over the dip-equator, and following the plasma fountain process, the plasma moves to latitudes farther away and thereby the peak in EIA crest location is decided. As the night progresses, the existing plasma is continually lost due to recombination resulting in a decrease of emissions. The crest formed at the northern direction traces back towards the equator, which, in turn, shows larger airglow emission values in the southern region later in the night. The speeds of the reverse movement of the crest have been estimated for different nights and are found to be varying in the range of 10–55 ms^{-1} with more number of nights having values closer to the lower range. These were compared with the variations in the equatorial PRE, solar flux, and seasons, but except for a weak trend in decrease in speeds with the increase in solar flux, no clear correspondence was noted. The primary reason for the variation in the speeds of reversal is interpreted to be the nocturnal equatorial westward electric fields. Considering the data from other longitude sectors and given the fact that the equatorial electric fields are global in nature ($\oint \mathbf{E} \cdot d\mathbf{l} = 0$), we have compared the reversal speeds in the EIA crest obtained from Indian longitude sectors using optical emissions with the daytime integrated EEJ strength from Jicamarca in American longitudes which is located in opposite sector. The pre-noon time EEJ strength over Jicamarca shows good relationship with the observed reversal speed, which establishes an empirical evidence to show that the observed variation in the equatorward movement of the EIA crest is indeed due to the nighttime westward electric field. The present results are particularly interesting as they show the experimental evidence of the global nature of equatorial electric fields during the geomagnetic quiet time periods. In doing so, through this work, the speeds of equatorward movement of the EIA emerge as a viable proxy to determine the temporal behaviour of the nightly westward electric fields – which are otherwise extremely difficult to obtain, and can have far reaching implications.

Chapter 5

Enhancement in OI 630.0 nm Nocturnal Emissions during Post-sunset hours

5.1 Background

Different kinds of variability have been observed in the OI 630.0 nm nightglow emissions as shown in figure 3.8 of chapter 3. After the sunset, due to the absence of ionization, the emission rates decrease monotonically due to the recombination. In chapter 4, we have discussed the variation in the latitudinal gradient of emissions in response to the PRE. In this work, we found that the change in the north-south emission gradient from increasing at the beginning of observation due to PRE strengths to decreasing with time after around 21 LT in response to the nighttime westward electric field. We have established that the reversal speeds of EIA crest observed in the OI 630.0 nm nightglow measurements can be used to infer the strength of nighttime (westward) electric field, which is otherwise difficult to obtain. In the present chapter, we have discussed a different kind of behaviour of the post-sunset enhancement as seen in OI 630.0 nm nightglow emissions. On several occasions, we have observed an enhancement in the emissions which occurred typically around 20-21 LT following the monotonic decrease in emission after the sunset. A total of 142 nights of data corresponding to January, February, and March in the years 2013, 2014, and 2016, obtained from Mt. Abu are investigated for this study. The plasma can be brought over the low-latitudes by the electrodynamic processes and meridional winds. This chapter presents a detailed investigation on the role of equatorial electrodynamics and meridional winds in the nightglow emission variability as observed over low-latitudes. This work has helped us to understand the cause of such behaviour in the emissions. Variations in the magnitudes of such enhancement as a function of the solar flux and seasonal variation are also discussed here.

5.2 Introduction

As discussed in chapter 1, the thermospheric-ionospheric system is coupled with each other through various neutral and electrodynamic processes and shows intriguing behaviour. Over the years upper atmospheric phenomena and their variability have been studied using the observation of airglow emissions, which act as a passive remote sensor. Vertical coupling in the atmosphere (e.g., *Laskar et al.*, 2013, 2014), wave activity in the upper atmosphere (e.g., *Chakrabarti et al.*, 2001; *Pallamraju et al.*, 2010, 2014, 2016; *Laskar et al.*, 2015; *Karan and Pallamraju*, 2017), mesospheric temperature and wave dynamics (e.g., *Vineeth et al.*, 2007; *Lakshmi Narayanan et al.*, 2010; *Singh and Pallamraju*, 2015, 2017; *Narayanan and Gurubaran*, 2013; *Parihar and Taori*, 2015), and plasma irregularities in the ionosphere (e.g., *Mendillo and Baumgardner*, 1982; *Shiokawa et al.*, 2004; *Martinis et al.*, 2009; *Krall et al.*, 2010) have been investigated using such optical emissions originating in the upper atmosphere.

The off-equatorial low-latitude regions are connected to the equatorial region through the geomagnetic field lines. As discussed in the chapters 1 and 4, the equatorial electrodynamics, such as the EIA and PRE in the zonal electric field over the dip-equator can influence the plasma distribution over the low-latitude regions (*Raghavarao et al.*, 1978). The EIA refers to the formation of two crests in ionization on either side of the magnetic equator brought-in essentially due to the plasma fountain effect which results in a trough in the electron densities over the magnetic equator in the daytime. This plasma distribution affects the airglow emissions as well over the low-latitudes (*Karan et al.*, 2016). At the time of sunset, on occasions, enhanced vertical drifts over the magnetic equator due to the PRE in the electric field can cause a resurgence of the plasma fountain effect which brings in additional ionization to latitudes further away from the equator in the evening and night times (e.g., *Klobuchar et al.*, 1991; *Sridharan et al.*, 1993b). Latitudinal movement in OI 630.0 nm emissions have been observed (*Sridharan et al.*, 1993b; *Narayanan et al.*, 2013) during nighttime due to the changes in such plasma distribution.

Meridional winds also play an important role in the distribution of plasma in the low-latitude region, as a result the airglow emission rates vary. Conventionally, the thermospheric winds have been calculated from the Doppler shifts in the night time OI 630.0 nm emissions (e.g., *Meriwether Jr et al.*, 1985; *Sridharan et al.*, 1991; *Gurubaran and Sridharan*, 1993) and incoherent scatter radar (e.g., *Salah and Holt*, 1974). Alternatively, estimation of meridional winds using ionograms from latitudinally separated locations have also been reported in the literature (*Miller et al.*, 1986; *Krishna Murthy et al.*, 1990; *De Medeiros et al.*, 1997). The strengths of the daytime electric field, the EIA, the PRE, and the neutral winds vary from day-to-day, with seasons, and solar activity during geomagnetic quiet times. During geomagnetic disturbances, these phenomena can further get modified by the changes equatorial electric fields due to both prompt-penetration and disturbance dynamo processes, affect the background wind structures and electron densities globally (e.g., *Salah and Holt*, 1974; *Mayr et al.*, 1978; *Karan and Pallamraju*, 2018; *Mandal and Pallamraju*, 2020).

During daytime, photoelectron, photodissociation, and dissociative recombination are the major mechanisms associated with the OI 630.0 nm airglow emissions, whereas, in the nighttime, in the absence of solar photons, the emissions originated only due to the dissociative recombination process. Therefore, the OI 630.0 nm emission rates decrease monotonically after sunset. But, on several occasions enhancement in OI 630 nm emissions have been reported during the midnight time. An increase in brightness of OI 630.0 nm emissions has been observed during midnight temperature maximum events (*Sastri et al.*, 1994; *Colerico et al.*, 1996; *Colerico and Mendillo*, 2002; *Otsuka et al.*, 2003). But, there are only a very few reports of observations on the enhancement in emissions during the post-sunset time (*Rao and Kulkarni*, 1973). Conventionally, based on radio measurements the strength of sunset time PRE in the electric field was thought to be responsible for such post-sunset enhancement in TEC. However, except for a few case studies, there has been no concrete experimental datasets in this regard. In this study, we present such enhancements in OI 630.0 nm nightglow emissions on many occasions corresponding to several months spread over different years from a low-latitudinal region. The behaviour in airflow emission intensity variations could be different than those correspond to TEC, as these mainly correspond to the base of the F-region and typically of around 100 km in width. The effects of both equatorial electrodynamics and meridional winds have been investigated during geomagnetic quiet time to understand the observed variations in the OI 630.0 nm nightglow emissions during post-sunset hours over the low-latitude location, Mt. Abu.

5.3 Data sets used

The nighttime OI 630.0 nm airglow emissions have been observed using High Throughput Imaging Echelle Spectrograph (HiTIES). The image processing and airglow extraction methodology have been discussed in chapter 2. The typical nightglow variation in the OI 630.0 nm nightglow emissions has been shown in figure 5.1 for one sample night of 27 January 2016. The solid red line shows the emission variation over the zenith of Mt. Abu. The x-axis and y-axis show local time (LT) in hours and OI 630.0 nm emission rates in Rayleigh, respectively. The SNR of the instrument varies in the range of 50.6 to 7.1 for a signal brightness of 100 to 10 R, which has been discussed in section 2.3.1.5 of chapter 2. Therefore, the uncertainty in the measurement typically varies in the range of 1-3 R as shown in figure 5.1. Emission variations from the other two directions, north and south, are depicted in orange dotted and blue dash-dotted lines, respectively, which can be seen varying quite similarly with the emissions along the zenith.

OI 630.0 nm nightglow emissions have been estimated over Ahmedabad using a photo-chemical model as described in chapter 3. The estimated nightglow emissions are compared with the measured emissions over Mt. Abu, a location around 180 km away in the northern direction from Ahmedabad. The dashed black line in figure 5.1 shows the variation of the estimated OI 630.0 nm emissions over Ahmedabad. The uncertainties in the estimated emission rates over Ahmedabad is calculated by incorporating the uncertainties in the measured electron densities (around 2-6%) obtained from digisonde and the models (around 15%) used are shown in figure 5.1. Since these two locations, Mt. Abu and Ahmedabad, are situated close to one another, the variations in the measured and estimated nightglow emissions from these two locations are compared with each other. The measured and estimated emissions show quite a good correlation for all the other nights also.

Digisonde Portable Sounder (DPS4D) located at Ahmedabad (low-latitude location) and Trivandrum (dip-equatorial location), has been used in this study. The digisonde data from Trivandrum are used to calculate the strength of the PRE on all the days under consideration during January, February, and March of 2013, 2014, and 2016. Further, digisonde data of the non-ESF nights have been used to estimate meridional winds. Geomagnetic data over Indian sector are used to calculate the strength of EEJ. The strength of EEJ over Indian longitudes has been calculated using the method described in section 2.5 of chapter 2.

5.4 Observation and results

In this study, we have used the OI 630.0 nm nightglow emission observation from a low-latitude location over the Indian sector. Figure 5.1 shows the typical nightglow variation. After sunset, as the ionization stops, the emissions decrease monotonically due to the recombination processes. The monotonic decrease both in measured and estimated emissions indicates the decrease in electron density after the local sunset at both these locations. The differences between the measured (over Mt. Abu) and the estimated (over Ahmedabad) emission rates are most likely due to the location of the EIA crest region closer to Ahmedabad. This can also be ascertained by the difference in emissions as obtained by HiTIES, as the emissions towards the southern (dash-dotted line) side of Mt. Abu (towards the EIA crest) are greater in magnitude than those measured towards the northern (dotted line) side (away from the EIA crest), with intermediary values over the zenith. Such discussion on the latitudinal gradient in the emissions and its variation over the course of the night in terms of movement of the EIA crest has been presented in the previous chapter 4. Further, it is seen on almost all the nights that the measured and estimated emissions become nearly equal as the night progresses (as can be seen in Figures 5.2 and 5.4). A total of 142 clear nights of data during geomagnetic quiet time periods in the months of January to March of the years 2013, 2014, and 2016 are considered for the investigation of the ionosphere-thermosphere system.

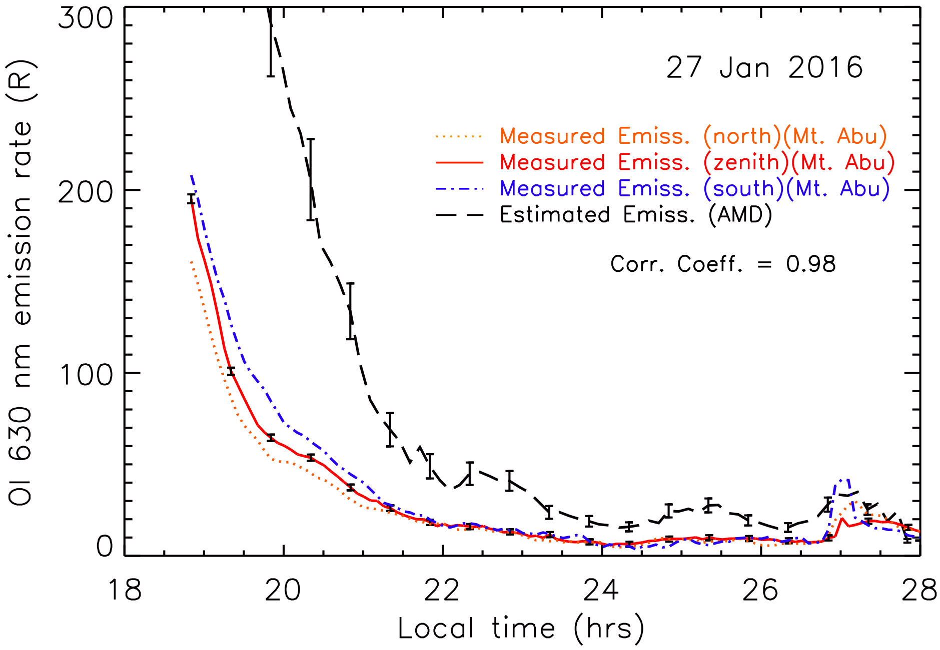

Figure 5.1: The variation of OI 630.0 nm emissions measured from Mt. Abu (solid red line) and those estimated over Ahmedabad (dashed black line) are shown for a given night. The distance between the southern and northern directions as viewed from Mt. Abu is around 250 km.

In the present study, we have considered the zenith measurements of OI 630.0 nm nightglow emissions as obtained from Mt. Abu. It has been observed that the emission enhancement exists on 85 nights (around 60%) out of these 142 nights. The enhancement in emissions during the post-sunset time are shown in figures 5.2a and 5.2b) for two given nights, each in the years 2013 and 2014, respectively. Figure 5.2c shows a night without having any post-sunset enhancement and figure 5.2d depicts variations in the nightglow emissions on 51 clear nights, which shows enhancements in the post-sunset hours. The variations have been shown for the duration of 18-24 LT. In figures 5.2a-c, the left-side y-axis shows the OI 630.0 nm nightglow emissions in Rayleighs, whereas, the right-side y-axis shows the base height of the F-layer in km over Ahmedabad. An enhancement in the emission rates observed around 20 LT over Mt. Abu on 05 Jan 2013 is shown in figure 5.2a (solid red line). The estimated emission rates over Ahmedabad (dashed black line) also show an enhancement around this time. The correlation coefficients is calculated between the measured and estimated emissions during 19-24 LT for each night and is shown in each of the panels of figures 5.2a-c. The variation in the base F-layer height

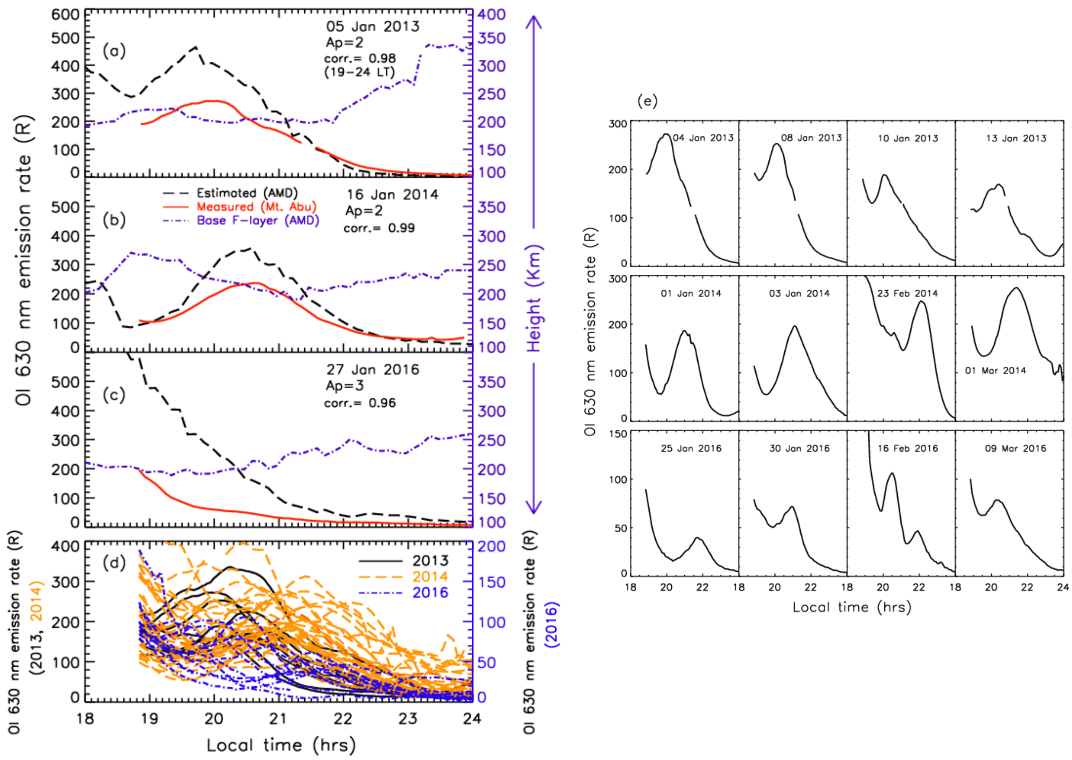

Figure 5.2: Panels (a, b, c) show the measured (solid red line) and estimated (dashed black line) emissions from the zenith of Mt. Abu and Ahmedabad, respectively along with the base F-layer height (dash-dot blue line) over Ahmedabad for three given nights of different years. Both Panels (a, b) show the presence of enhancement in emissions during post-sunset hours, whereas, Panel (c) shows no such enhancement after sunset. The correlation coefficients between the measured emissions at Mt. Abu and estimated emissions at Ahmedabad during 19-24 LT are also shown. The variation in OI 630.0 nm nightglow emissions for around thirty-eight nights with significant post-sunset enhancements is depicted in panel (d).

(estimated from h'F) over Ahmedabad obtained from the digisonde is depicted in blue dash-dot line. It may be noted that the height of the base F-layer is anti-correlated with the variations in the emissions. As the base F-layer height increases (in the duration of 18.5-19.5 LT and after 21.5 LT in figure 5.2a), the electrons in the ionosphere are lifted above the altitudinal region from where the OI 630.0 nm emissions peak, which results in a decrease in the emission rates. Figure 5.2b shows enhancement in emission during the post-sunset time for another night, 16 Jan 2014. The OI 630.0 nm emission rate shows anti-correlation with the variation of the base F-layer height over Ahmedabad due to the same reason as discussed earlier. Figure 5.2c shows a monotonic decrease in emissions from twilight time and the post-sunset emission enhancement cannot be observed. The base height of the F-layer too did not show any significant changes on this night. All the 51 nights of the year 2013, 2014, and 2016 which show enhancement in post-sunset emissions are overplotted in figure 5.2d. The black solid lines, orange dashed lines and the blue dash-dotted lines show the emission rates corresponding to the nights of the years of 2013, 2014, and 2016, respectively (figure 5.2d). The enhancements in emissions are observed mostly around 19-21 LT having a Gaussian-like shape. The emissions peak typically 2-3 hours after sunset following the monotonic decrement in emissions. Emissions in the year 2016 were faint (magnitudes are given on the right-side y-axis) as compared to the other years, which can be understood to be due to a decrease in solar flux. The magnitudes of emission enhancement have been observed to range between 270 to 15 R depending on the solar activity. A few more examples (12 nights) for the nights which show enhancement in emissions during the post-sunset time, are presented by taking four nights for each of the years 2013, 2014, and 2016 in the figure 5.2e. The small data gaps in the emission variation for the nights in the year 2013 are due to the presence of star light within the FOV of HiTIES. The objective of this study is to understand the possible cause behind this enhancement in emission as seen over Mt. Abu. We have investigated the role of the equatorial electrodynamics and meridional winds to understand the cause of such enhancement in emissions in the low-latitude region during the post-sunset hours which have been discussed in the following.

5.4.1 The Role of daytime electric fields

The E-region electric field over the off-equatorial region is mapped over the equatorial F-region through the geomagnetic field lines. In this section, we have studied the effect of the daytime electric field on the nighttime emission at the time of enhancement in emissions. The strength of the daytime electric field in the equatorial E-region ionosphere is measured using the strength of EEJ as a proxy. The strength of EIA has been shown to be proportional to the strength of daytime EEJ (*Raghavarao et al.*, 1978; *Karan et al.*, 2016). In earlier works (*Raghavarao et al.*, 1978), it has been shown that the strength of integrated EEJ during the prenoon time correlates well with the daytime EIA strength.

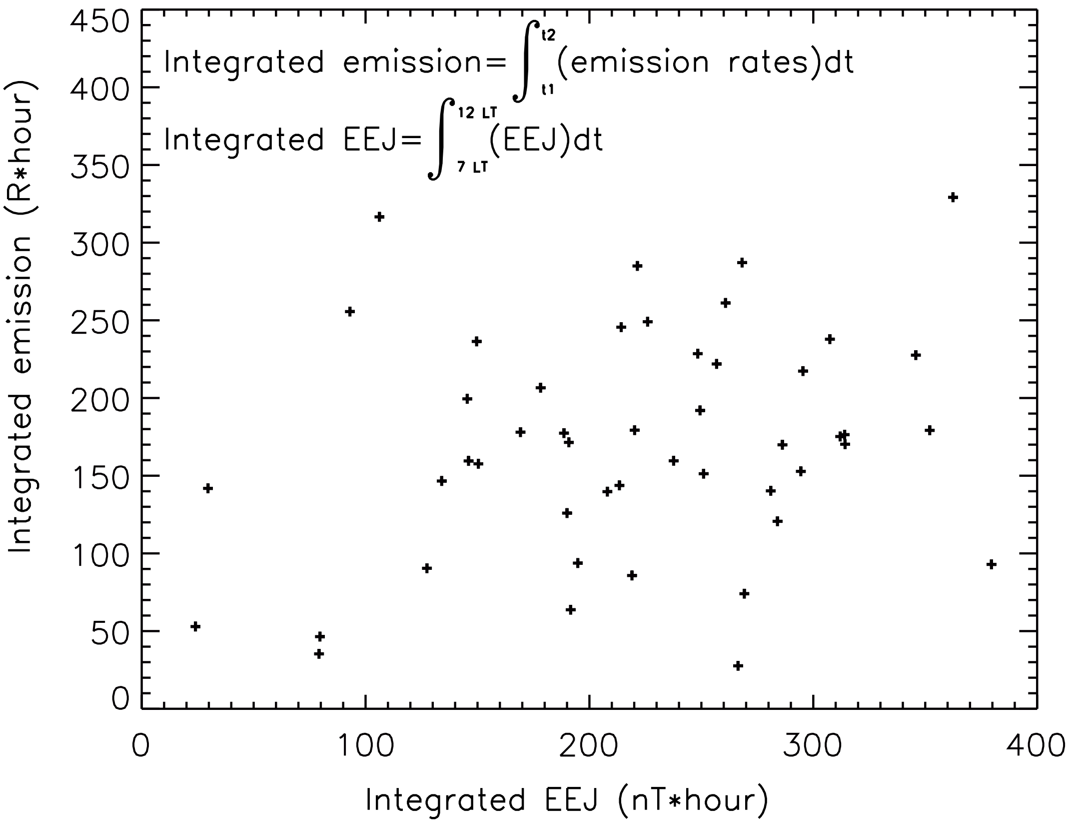

Figure 5.3: The Integrated EEJ values during 7-12 LT are compared with the integrated nightglow emission rates for one hour duration centred at the time of peak emissions (t1=Peak Time-30 min; t2 = Peak Time+30 min). The strength of EEJ do not show good correlation with the integrated OI 630.0 nm emissions during the time of post-sunset enhancements.

Such variations in equatorial electrodynamics cause the distribution of plasma over the low-latitudinal region. Therefore, to explore if this is the cause, we have taken the area under the curve of the OI 630.0 nm measured nightglow emissions during an hour keeping the time of peak emission in the centre and compared with the integrated daytime EEJ strength (as depicted in figure 5.3). The same nights mentioned in figure 5.2d are included in this investigation. Figure 5.3 shows this comparison where in it can be clearly noted that these two parameters are not correlated (the values of the correlation coefficient are -0.68, 0.28, and 0.23 in the years 2013, 2014, and 2016, respectively). The enhancement in electron density due to the development of EIA over the low-latitudes can take around 3 hours and it is quite understandable that the daytime electric field will have very little effect on the nighttime emission rates. Still, for the sake of a complete understanding of the effects of daytime electrodynamics on nighttime emissions, we have investigated the variations in the EEJ strength and compared them with the nighttime emissions. Therefore, the effects due to EEJ, if any, would be observed by the sunset time over Mt. Abu location, and not beyond that time.

5.4.2 Role of Pre-reversal enhancement in electric field

The sunset time PRE in the electric field can restrengthen the EIA process. As a consequence, plasma gets redistributed over the low-latitudes. These electrons can produce significant airglow emissions through dissociative recombination in the nighttime. Therefore, PRE is the possible factor for the enhancement seen in the post-sunset emissions over the low-latitudes.

To investigate the effect of equatorial electrodynamics over a low-latitudinal location, the variations in the base and peak of the F-layer heights and the time rate of change of F-layer height over Trivandrum are considered. Figure 5.4 shows the OI 630.0 nm measured and estimated emissions with varying magnitudes of post-sunset emissions (top panel), F-layer height variation over Trivandrum (middle panel) and the time rate of change of F-layer height $\frac{d(h'f)}{dt}$ at 5 MHz iso-electron density over Trivandrum (bottom panel), which is proportional to the PRE in electric field (*Goel et al.*, 1990; *Woodman et al.*, 2006) on a few sample nights. These nights are corresponding to the same months in the year 2014 under quiet-time geomagnetic conditions. Therefore, it is expected that the background condition will remain similar. The vertical solid yellow lines in the middle and bottom panels indicate the local sunset time (at Trivandrum). The estimated OI 630.0 nm emission rates over Trivandrum are also shown in the middle panel of figure 5.4, wherein a monotonic decrease in emissions is observed after the sunset, which is a clear consequence of the upward movement of the F-layer after the sunset time. However, larger emission enhancements are seen during the post-sunset time in the first three nights (10, 16, and 22 January 2014) over low-latitudes, wherein emissions as large as 400 to 240 R have been observed at Mt. Abu. The data gap shown in the figure 5.4j, during 22-23.5 LT is due to the presence of moonlight in the FOV of the instrument, and the estimated emission (dashed black line) confirms that there is no enhancement in emission during that time. It is pertinent to note that the PRE is, conventionally, considered as the most likely cause of such enhancements in nightglow over the low-latitudes. To investigate the

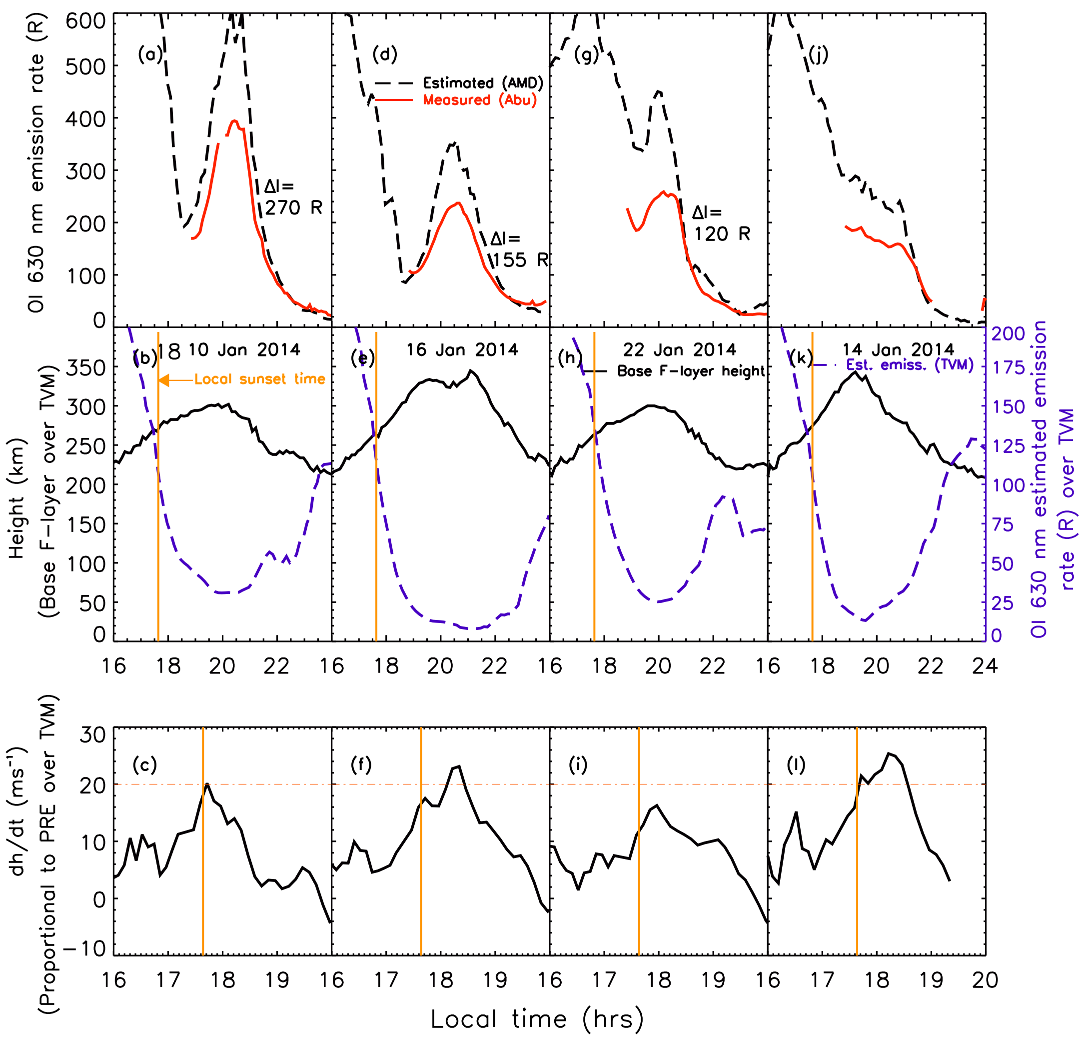

Figure 5.4: Top row shows the measured (solid red line) and estimated (dashed black line) OI 630.0 nm emission variations on four sample nights in the year 2014. The middle row shows the base F-layer height ($h'F$) (solid black line) over Trivandrum, the dip-equatorial location, for the same nights. The dashed blue line of the middle row shows the red line emission rates estimated over Trivandrum. The bottom row shows the time rate of change of the F-layer height (dh/dt) over the magnetic equator Trivandrum, which is proportional to the strength of PRE in equatorial electric field. The x-axis of the bottom panel is restricted to 16-20 LT as we are focused on the vertical drift during sunset time only. The vertical lines in the middle and bottom rows show the time of ground sunset over Trivandrum. To aid the eye, a horizontal dash-dot line is drawn for the plots in the bottom row at 20 ms^{-1}.

effect of equatorial electrodynamics in the nightglow emissions observed over the low-latitudinal location, the variations in the F-layer heights and, more importantly, the PRE in electric field over Trivandrum has been calculated on these nights. As expected, the base height of the ionospheric F-layer moves up (middle row) in the higher altitudes due to both recombination of ionization in the bottom side and vertical drift due to the PRE in electric field. To assess the extent of contribution of the PRE in electric field on each of the nights the values of rate of change of F-layer heights (dh/dt) are shown in the bottom panel. We have used 5 MHz iso-electron density contour in the estimation of variation in PRE as this corresponds to the altitudes above 300 km over Trivandrum in this duration, and therefore, the effect of recombination can be considered to be negligible. To aid the eye a horizontal line is drawn at the value of 20 ms^{-1}. It can be noted that the PRE is the smaller on the nights 10, 16 and 22 Jan 2014 but shows enhancement in OI 630.0 nm emissions whereas, the value of PRE is the largest on 14 Jan 2014 (the rightmost column) among all the days in consideration but no enhancement in emissions over Mt. Abu are observed. We have compared the dh/dt values with the magnitude of enhancements (ΔI), which is calculated by taking differences between the peak value and the interpolated emission value at that time if the peak is not present (see top panel of figure 5.4). ΔI values 270 R, 155 R, and 120 R, are obtained on 10 Jan, 16 Jan, and 22 Jan 2014, respectively. The dh/dt value for 16 Jan (23 ms^{-1}) is higher compared to 10 Jan (20 ms^{-1}), however, the ΔI is smaller on 16 Jan (155 R) compared to 10 Jan (270 R). As can be seen the PRE data on 14 January, in fact, showed the highest values (25 ms^{-1}) of dh/dt among all the four nights, but did not show any presence of post-sunset enhancement in emissions. The magnitudes of the drifts fall off sharply on all the days after the sunset over the equator.

While these results are intriguing, in order to gain a greater understanding of the systemic nature of nocturnal emissions, these investigations are extended to several nights. In the year of 2014, we have found around 25 nights out of 34 clear nights during the period January to March which showed post-sunset enhancement in emissions. The F-layer vertical drift has been depicted for these nights in figure 5.5a. The red coloured lines indicate the nights having enhancement in emissions, whereas the black coloured lines indicate the nights where the enhancement in emission was absent. The vertical drift values during the PRE do not show any contrasting picture for the cases with and without post-sunset enhancements in emissions. There are several occasions where PRE values are small though enhancements have been seen and several cases when no enhancements

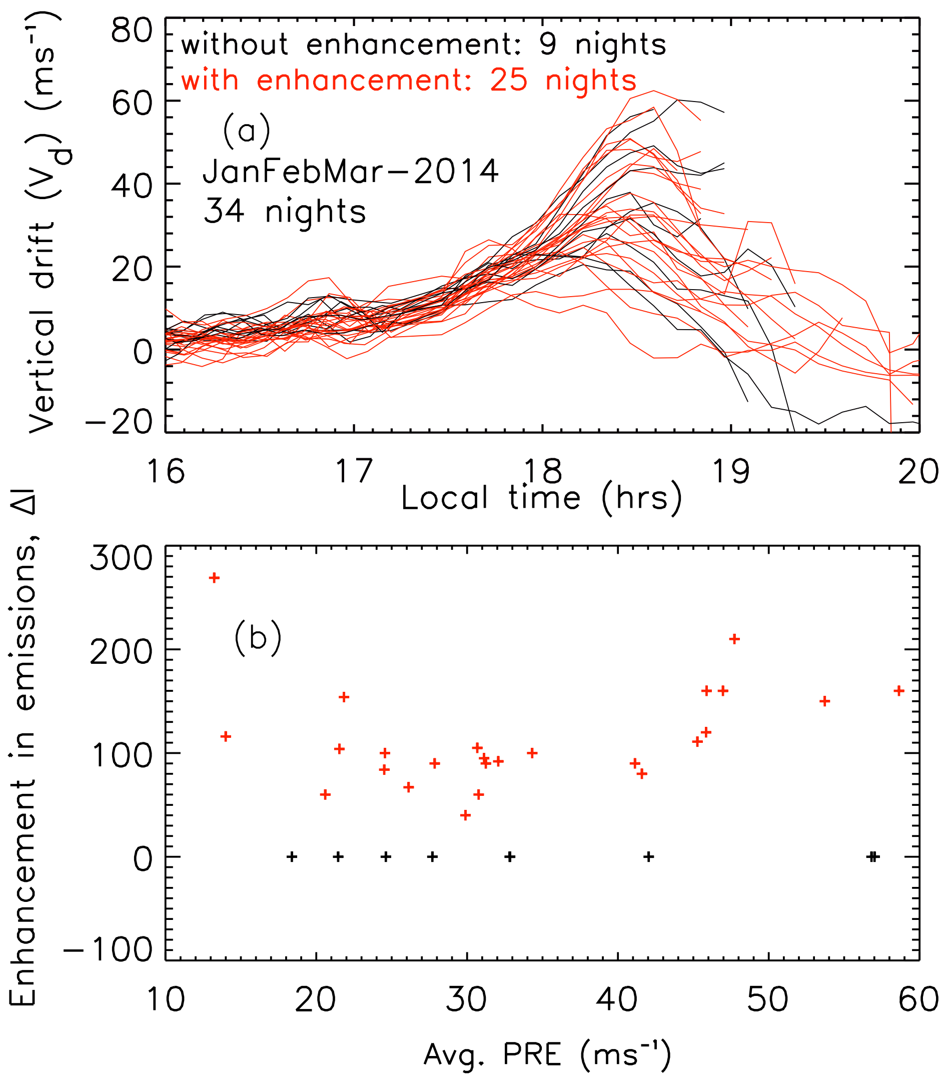

Figure 5.5: (a) F-layer vertical drift for total 34 nights during the period Jan-Mar in the year 2014. The red and black solid lines indicate the nights with and without having enhancement in emissions, respectively. (b) The magnitude of enhancement (ΔI) is depicted with the strength of PRE, which has been calculated by taking $\pm$15 minutes average around the peak PRE. ΔI values are put to zero for the nights when there is no enhancement in emissions observed.

in post-sunset emissions are seen even though there are presence of large magnitude of vertical drift in PRE. The magnitude of emission enhancement (ΔI) and the average vertical drift during the PRE is shown in figure 5.5b. It can be noted that ΔI does not show a viable relationship with the strength of PRE. The ΔI values have been marked as zero for the nights which did not show enhancement in emissions. A similar kind of exercise has been carried out for the nights from 2013 and 2016 also (figure 5.6). Total

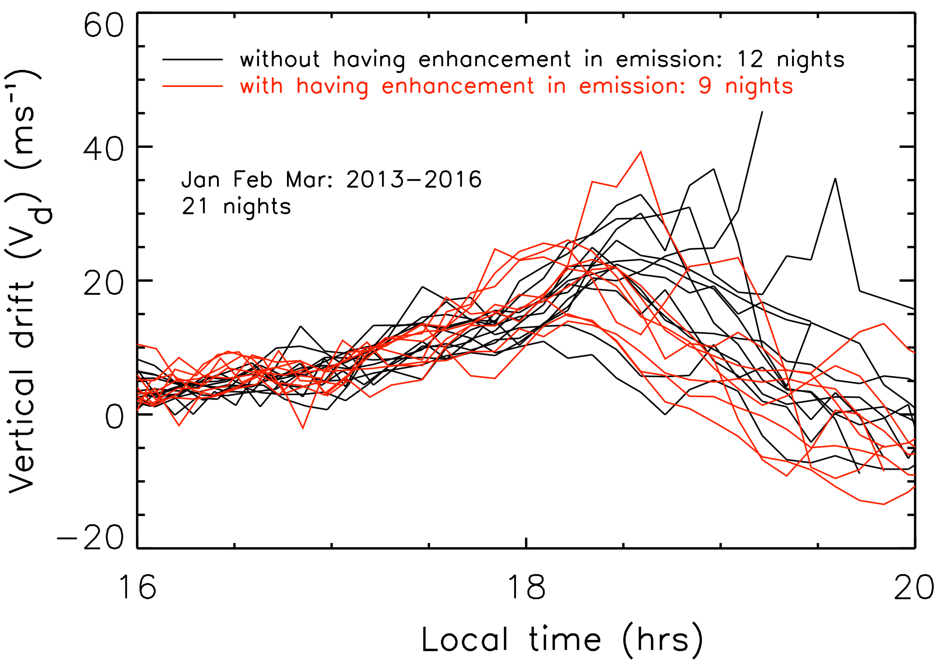

Figure 5.6: Same as plotted in figure 5.5a but for the years 2013, 2016.

21 nights have been plotted based on the clear sky conditions and data availability from ionosonde at Trivandrum for the years 2013 and 2016. Similar to the year 2014, no contrasting picture can be seen with the strength of PRE for these nights also. The observation of enhancement in emissions, the magnitude of enhancement, and the vertical drift over the dip-equator bring out a clear indication that the vertical drift during the sunset time, which is equivalent to the PRE in electric field is not the main factor which is responsible for such post-sunset enhancement in the OI 630.0 nm emission observed over low-latitudes, as has been considered conventionally.

5.4.3 Role of Meridional winds

The sence and magnitude of the meridional winds can also cause plasma distribution over the low-latitude regions. The effect of the equatorward and the poleward meridional winds (either transequatorial or otherwise) is depicted in figure 5.7 which can be seen effective on the movement of plasma at different latitudes. In the presence of meridional wind of speed U, plasma drifts along the geomagnetic field lines with an effect of $U \cos I$, where, I is the dip angle at that location. Therefore, the plasma moves vertically upward/downward direction depending on either equatorward/poleward meridional wind (*Rishbeth*, 1977).

As seen in the observation (figure 5.2) and described above, upward movement of the F-layer causes a decrease in OI 630.0 nm emissions over Mt. Abu as the available electron density in the altitude region of airglow emissions are reduced. Similarly, a downward movement of the plasma causes an enhancement in the emissions as it brings in more electrons in the altitude region of emissions. As described above and shown in figure 5.7, this upward/downward motion in the F-region can be caused by equatorial/poleward meridional winds. Hence, the change in meridional wind is an extremely potential factor to cause the enhancements in the 630.0 nm nightglow emissions. As there is no measurement of neutral wind from this location during this period, we have estimated the relative variation in the meridional winds using the ionospheric data from two locations. They are Ahmedabad, a low-latitude location, where we want to estimate the meridional winds, and Trivandrum, a dip-equatorial location. From figure 5.7 we note that meridional winds do not contribute to a change in the F-region height over the magnetic equator owing to the horizontal nature of the magnetic field lines, whereas, for any latitude away from the equatorial latitudes ($> \pm 3°$), the ionospheric heights do get affected by the presence of a meridional wind.

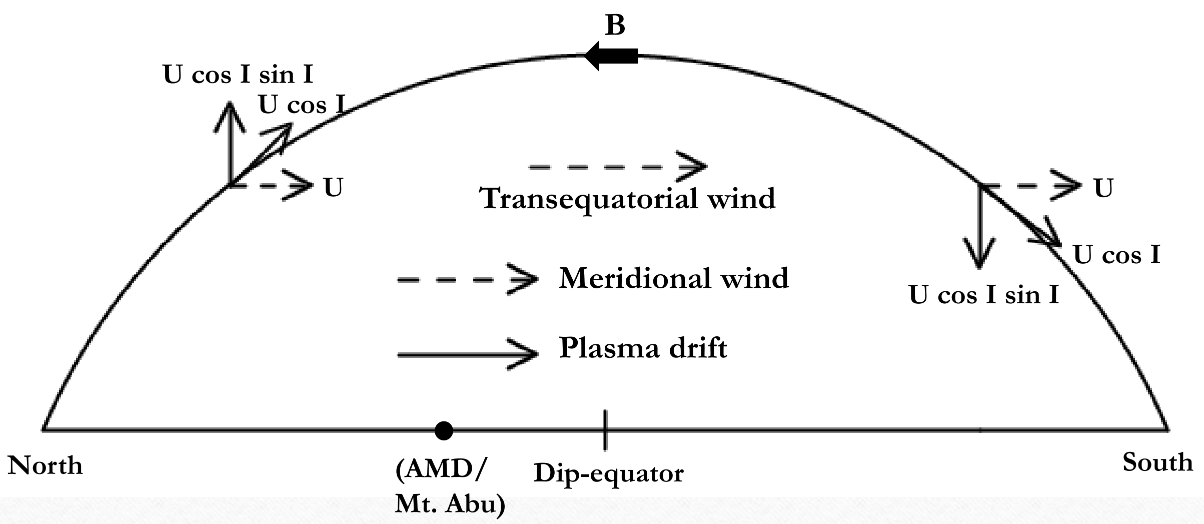

Figure 5.7: Schematic showing the movement of ionospheric plasma in response to meridional winds (Adapted from *Rishbeth* (1977)).

The vertical movements of the F-layer at any location are caused due to three factors, the $\mathbf{E}\times\mathbf{B}$ drift, meridional winds, and plasma diffusion, and they are expressed as,

$$V = V_d \cos I - U \cos I \sin I - W_d \sin^2 I \tag{5.1}$$

where, V_d is the vertical $\mathbf{E}\times\mathbf{B}$ drift over the dip-equator, U is the meridional wind taken as positive in the poleward direction, W_d is the plasma diffusion, and I is the dip angle. The dip angle is zero at the magnetic equatorial location, therefore, to the first order, the measured vertical drift of the F-layer corresponds to only $\mathbf{E}\times\mathbf{B}$ drift (V_d).
By rearranging the terms in equation 5.1, the meridional wind (U) at a given location can be written as,

$$U = \frac{2V_d \cos I - V}{\sin 2I} - W_d \tan I \tag{5.2}$$

However, the measured vertical drift is the sum of true vertical (E×B) drift (V_{true}) and apparent vertical drift ($V_{apparent}$). $V_{apparent}$ results due to the recombination of charges at lower altitudes of the ionosphere, as also discussed above, and can be estimated as a product of the rate of recombination coefficient β and scale height H. If, $(V_T)_{meas}$, $\beta_T H_T$, and $(V_A)_{meas}$, $\beta_A H_A$ represent the measured and apparent vertical drifts at Trivandrum and Ahmedabad, respectively, then, $(V_T)_{meas}$, $(V_A)_{meas}$, can be written as,

$$(V_T)_{meas} = (V_T)_{true} + (V_T)_{apparent} \tag{5.3a}$$

$$(V_T)_{meas} = (V_T)_{true} + \beta_T H_T \tag{5.3b}$$

$$(V_A)_{meas} = (V_A)_{true} + (V_A)_{apparent} \tag{5.3c}$$

$$(V_A)_{meas} = (V_A)_{true} + \beta_A H_A \tag{5.3d}$$

Therefore,

$$(V_T)_{true} = (V_T)_{meas} - \beta_T H_T \tag{5.4a}$$

$$(V_A)_{true} = (V_A)_{meas} - \beta_A H_A \tag{5.4b}$$

Now, $(V_T)_{true}$ is equal to the E×B drift over the equator (V_d). Therefore, using equations

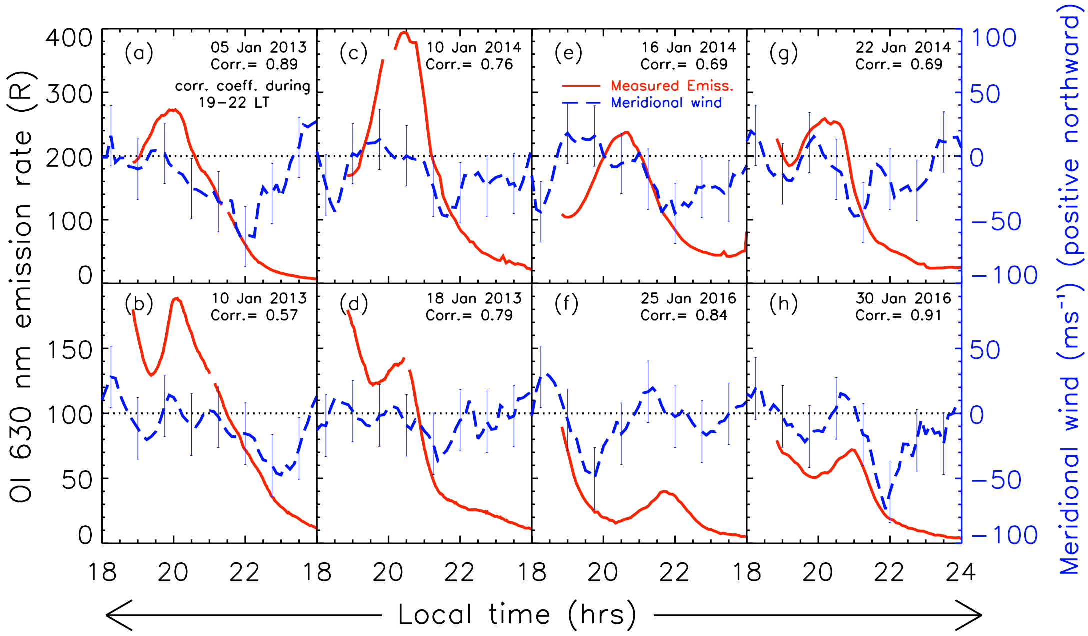

Figure 5.8: Variations in the measured 630.0 nm emissions (solid red lines) over Mt. Abu and the relative variations of meridional winds (dashed blue lines) calculated over Ahmedabad (positive poleward) are shown. The horizontal dotted lines indicate the zero value of the meridional wind. The correlation coefficient between variations in the measured emissions and estimated meridional winds are also shown in each of the panels.

5.4a and 5.4b, and V for $(V_A)_{true}$, in equation 5.2, the expression becomes,

$$U = \frac{2((V_T)_{meas}\cos I)}{\sin 2I} - \frac{2(\beta_T H_T \cos I - \beta_A H_A)}{\sin 2I} - W_d \tan I \tag{5.5}$$

H is calculated as N $\frac{dH}{dN}$ (*Subbarao and Murthy*, 1983), wherein, we have used two frequencies 2.0 MHz and 2.5 MHz in the calculation of meridional wind over Ahmedabad. The ionospheric altitudes of these frequencies represent the ionospheric altitudes of around 250 km, the typical nightglow emission altitudes of OI 630.0 nm emissions. The value of dip angle (I) corresponding to the years under consideration is taken from IGRF model (`http://wdc.kugi.kyoto-u.ac.jp/igrf/point/index.html`). The uncertainty in the calculation of meridional wind has been computed to be ±23.7 ms^{-1} considering the uncertainty in the measurement of height from the digisonde to be of 5 km and a data cadence around 7.5 min, mentioned in the figure 5.8 at 45 minutes interval.

This approach had been demonstrated earlier using the digisondes at Trivandrum and SHAR (*Krishna Murthy et al.*, 1990) over Indian longitudes. In the present work as the geomagnetic quiet times are considered (Ap < 20), we assume that there are no inter-locational changes in the neutral temperature and that the electric field variation until the EIA crest location that changes little or to be a $\cos I$ factor of that of the equatorial region. Under these assumptions, we obtain the relative variations in meridional winds at the thermospheric altitudes using this method (*Saha et al.*, 2021). Incidentally, one of the recent results on the influence of equatorial electric field on the OI 630.0 nm dayglow variation in the range of 5°-18° magnetic latitude showed that there was a small variation in the electric field (as seen with the EEJ as a proxy) at least until the EIA crest latitude of EIA (*Kumar et al.*, 2022b). The results reinforce the assumption made earlier to obtain the information on the meridional wind by this indirect method in the present study. Considering the lack of true information on the magnitudes of other parameters such as the thermospheric temperature and electric field, the present method can only yield information on the relative variations in winds and not their absolute magnitudes. With this understanding, let us now explore as to how these relative variations in meridional winds compare with those of the measured airglow emissions.

As discussed earlier, Mt. Abu and Ahmedabad are two nearby locations, and the variability in estimated emission rates over Ahmedabad show an excellent relationship (correlation coefficient > 0.9) with the measured emission rates over Mt. Abu. With this background, one can compare the variations in the meridional wind over Ahmedabad with that of the measured OI 630.0 nm emissions over Mt. Abu. These are shown in figure 5.8 for several nights in the years 2013, 2014, and 2016 including those depicted in figure 5.4. The x-axis shows the local time, and the left side y-axis shows the emission rates in Rayleighs. Please note the differences in the ranges of left side y-axes between the top and the bottom panels. The right-side y-axis depicts the derived relative meridional wind values. The small gaps in the measured emissions on some nights refer to the removal of data due to the presence of star light (in figures 5.8a, 5.8b) and moon light (in figures 5.8c, 5.8d) in the FOV. The daytime poleward meridional winds turn equatorward after the sunset. Qualitatively, these plots show that there is an association of enhancement in the emission in the post-sunset time with the turning of meridional wind from equatorward to poleward or cessation of equatorward directed winds. In the similar way, when the meridional winds again turn in the equatorward direction, the nightglow emission rates start decreasing (figures 5.8). As discussed earlier, the poleward wind brings down the

F-layer height, causing the peak of the F-layer to move down, thereby bringing larger densities in electrons to the emission altitudes of the OI 630.0 nm emissions resulting in an enhancement in emissions as measured in our data. It may be noted that the correlation coefficients calculated between the measured emission rates and estimated meridional winds are high (in the duration of 19-22 LT) as shown in these plots. In some cases, time differences between the measured airglow emissions in response to the meridional wind variations have been observed to be varying from around 15 to 45 minutes, which could be due to the small spatial distance between Mt. Abu and Ahmedabad. Also, physical parameters, such as plasma lifetime, diffusion constant, ion-drag, and viscous-drag can create time delays in the response of the ionosphere with the imposed meridional wind. Beyond 22 LT, the electron density becomes so small that meridional wind does not have any perceptible effect on the airglow emission variabilities, especially during the geomagnetic quiet and non-ESF nights that are considered here.

In spite of the independent nature of these two datasets, namely, one being measurements of optical OI 630.0 nm airglow emission variability over Mt. Abu and the other being relative meridional wind variations obtained by digisondes at two locations, the high correlation (many of the cases, the correlation coefficient values are more than 0.75) between them is remarkable and reinforces the proposition that the cause of the variability in the measured OI 630.0 nm emission brightness over low-latitudes in the post-sunset time during geomagnetic quiet times is most likely due to the variation in the meridional winds.

5.5 Discussion

In this study, we have investigated the plausible cause of the enhancements as seen in the measured airglow emissions during the post-sunset time over the low-latitude location, Mt. Abu. The first possible cause that we pursued to explain the emission enhancement is the PRE in electric field over the magnetic equator which did not show any contrasting behaviour between the nights with and without post-sunset emission enhancements. It is interesting to note the contrast between the ratio in N-S nightglow emissions being larger for higher PRE values as discussed in chapter 4 and the post-sunset emission enhancement over Mt. Abu not showing any clear relation with PRE as described in this chapter. However, it is seen that the emission enhancements were sensitive to the variations in the meridional winds. While discussing about the meridional winds, there are two aspects that are implicit in it, one is the sense of winds and the other is the electron densities that are present at that given time. From figure 5.8, it can be readily noted that the changes in the magnitude of meridional winds from equatorward to poleward portray almost good relationship with the emission enhancements as seen by the correlation coefficient values. 'Almost', because the electron density is also involved. Sufficient electron number density is required for significant changes to be seen in the nocturnal emissions. This is the reason why near or after midnight, the emission variations do not correlate with the variations in the calculated meridional winds, as the electron number density is very low. The values of the electron densities are proportional to the solar flux. The solar flux values in the present study were such that they can be considered to represent moderate, high, and low solar activity periods in the years 2013, 2014, and 2016, respectively. Thus, the results obtained in this study are independent of the variation in solar flux. Nevertheless, the changes in the meridional winds correlate well with the variation in the measured airglow emission enhancements during the post-sunset time. For example, in figures 5.8c and 5.8e, during the post-sunset time, relative changes in meridional winds from equatorward to poleward are quite similar, however, the magnitude of emissions are different (400 R and 230 R). This is explained to be due to the higher solar flux on 10 Jan 2014 (solar flux unit, sfu, of 170; sunspot number: 137) (1 sfu= 10^{-22} W m^{-2} Hz^{-1}) compared to 16 Jan 2014 (sfu of 117; sunspot number: 80). The digisonde measured electron densities at 250 km at the time of peak emissions were 2.34×10^6 and 1.3×10^6 cm^{-3} on these two nights. It is striking to note that all these parameters, namely, sunspot number and electron densities are scaled by a value of around 1.7, which is also similar to the observed emission brightness.

The electric field variation over low-latitudes is considered to be proportional to the equatorial electric field. Any small deviation from this proportional behaviour in the equatorial electric field may contribute to the small additional ionospheric height variation over the low-latitudes. As the geomagnetic quiet time is considered in the present study, the equatorial electric fields are not expected to change irregularly. In any case, there is no way to ascertain such variations, if any, in the electric field at such high temporal cadence,

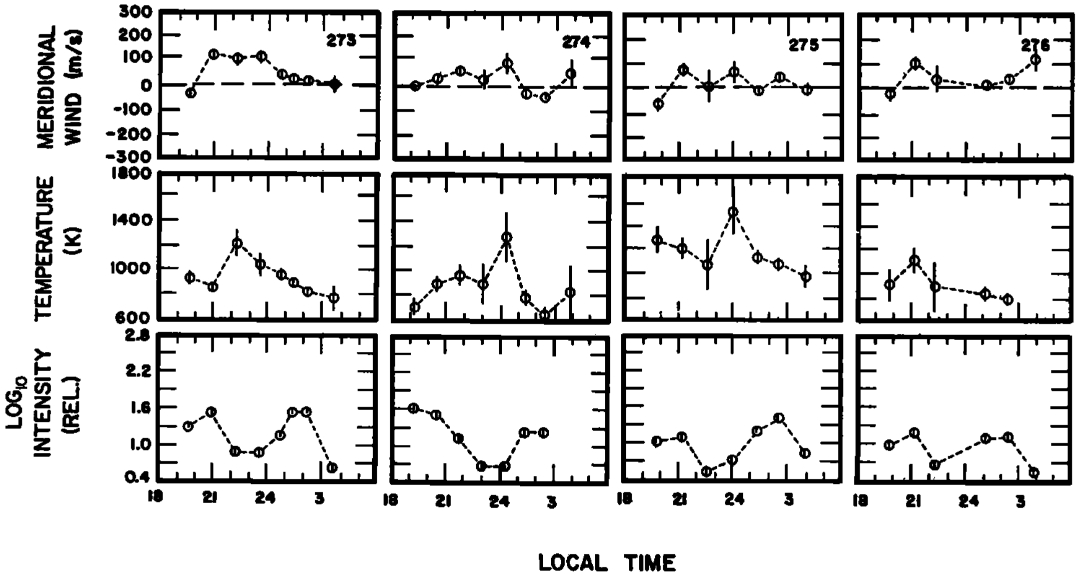

Figure 5.9: : Meridional wind (northward positive), kinetic temperature, and OI 630.0 nm relative intensity for four nights in the year of 1984 over south side of Arequipa, 7°S Mag, are shown (*Meriwether Jr et al.*, 1985). The days of year of these observations are mentioned in the top panel.

as no studies exist on these aspects so far over low-latitudes. However, there are several numbers of evidence in the literature that showed the meridional winds do change over short timescales of an hour using ground-based measurements (e.g., *Meriwether Jr et al.*, 1985). Figure 5.9 shows the interferometric measurements of thermospheric winds, neutral temperature, and OI 630.0 nm nightglow intensities over the south side (7° dip latitude) of an equatorial station Arequipa, Peru (16.2°S, 71.4°W, 3.2°S Mag) (*Meriwether Jr et al.*, 1985). The numbers shown in the top panel correspond to the DOY of the year 1984. The observation shows the presence of northward (equatorward) wind around 21 LT over this southern hemispheric location. Simultaneous measurement of OI 630.0 nm emission intensity shows depletion in emission during that time. The lack of emission intensity caused due to the uplift of ionospheric height near the dip-equator is consistent with the model studies. But, in this report, the rise of ionospheric height caused by the equatorward wind as the vertical drift due to PRE will not be significant during this low solar active year (*Fejer et al.*, 1979). The similar observation during the winter solstice (April-June) over there showed the presence of poleward wind and the OI 630.0 nm emissions showed an increase in nature during the post-sunset hours (*Meriwether et al.*, 1986). The measurements from Mt. Abu carried out during Feb 1991, using a

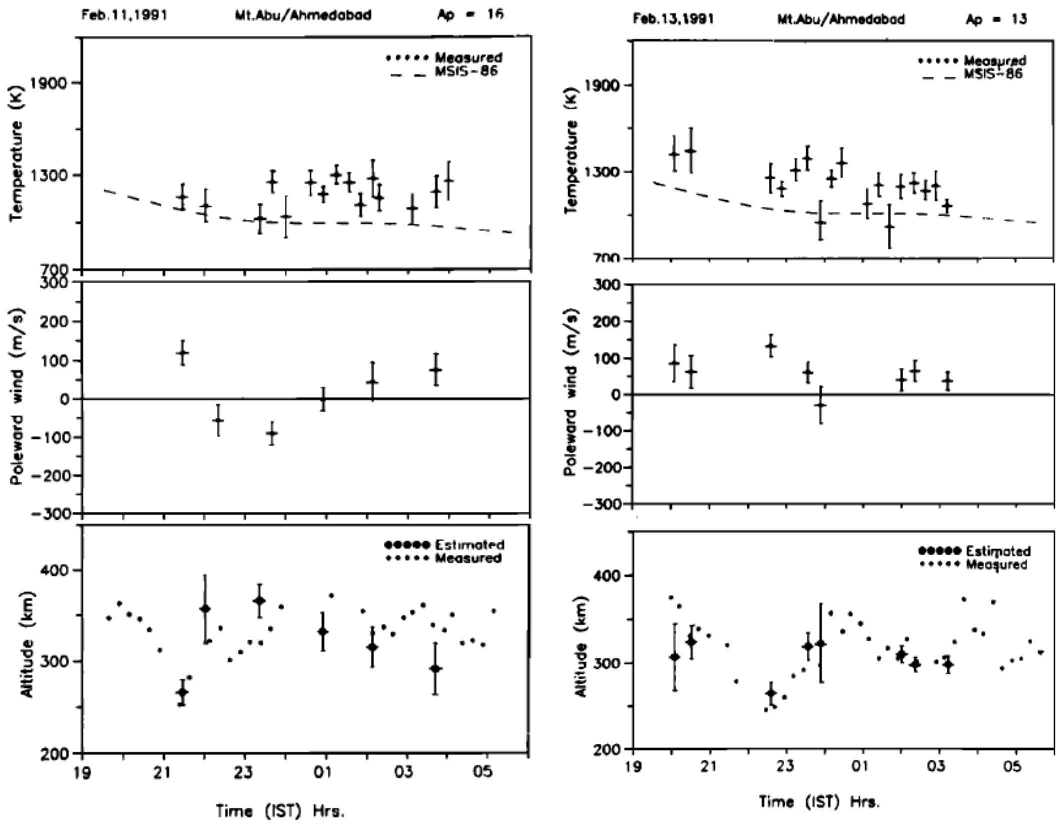

Figure 5.10: The measured thermospheric parameters, like, temperatures, wind and peak F-layer height have been depicted for two nights, 11 Feb and 13 Feb 1991. The thermospheric temperature is shown in the top panel. The measured meridional wind using the Doppler shift of OI 630.0 nm emission in Fabry-Perot interferometer is shown in middle panel. The bottom panel shows the height variation of peak F-layer. (After *Gurubaran and Sridharan*, 1993)

Fabry-Perot spectrometer (*Sridharan et al.*, 1991), showed the presence of poleward wind in the post-sunset time with a magnitude of around 100-150 ms^{-1} that varied within 1-2 hours duration (*Gurubaran and Sridharan*, 1993). The variation of thermospheric temperature, meridional wind, and F-layer height for the nights 11 Feb and 13 Feb 1991 are shown in figure 5.10 (*Gurubaran and Sridharan*, 1993). It is interesting to note that the measured wind values are poleward in nature during the post-sunset period, around 21-23 LT. Whenever the wind is in the poleward direction, the peak F-layer height comes down to the peak emission altitudes of OI 630.0 nm emissions. As we discussed earlier, more number of electrons that are brought down in this way cause the enhancement in emission. Simultaneous decent of F-layer and the enhancement in emission are observed in the present study (figure 5.2). After midnight, as the electron density becomes low, the emission rate cannot increase due to lack of sufficient electron density. Even, the observation of these two nights as shown in figure 5.2 shows that although there is presence of poleward wind in the post-midnight time, the peak F-layer height did not reach down to the peak emission altitudes. These can be the possible reasons for the absence of emission enhancement in the post-midnight time. Many other ground-based observations from different locations also showed variations of meridional wind in short time scales ranging from a fraction of an hour to a couple of hours (*Meriwether Jr et al.*, 1985; *Harper*, 1973; *Biondi and Sipler*, 1985).

The magnitude of enhancements in emissions have been compared with the solar flux variations which are depicted in figure 5.11 including a total of 51 nights those mentioned in the figure 5.2d. We have plotted the enhancement in emissions (ΔI) as a function of solar flux variations in figure 5.11a. It is interesting to note from figure 5.11a that the enhancement in emissions is reasonably correlated with solar flux. As we have seen above in Figure 5.8 that the enhancement in electron densities is related to the increase in solar flux, which varied from 90 to 210 sfu. As the average background emission also increases with increasing solar flux, we have calculated the percentage enhancements in emissions [(ΔI/I) $\times$100] which remain independent of the variation in solar flux as shown in figure 5.11b. As this percentage variation in ΔI/I is reasonably free from the background solar flux, these variations for three different years have been compared as a function of the day of year (DOY) in figure 5.11c to investigate the seasonal variations in them, if any. Here we have considered January 1 of each year as the DOY = 1. It is seen that, in general, there is a decrease in the percentage enhancement in emissions from Jan 1 to Mar 30. Poleward winds over Ahmedabad at 20 LT, a representative time of the observations in emission enhancements, obtained using the HWM-14 (*Drob et al.*, 2015) are also plotted (solid red line). Being a climatological model, a night-to-night comparison is not possible from HWM-14 derived wind values, however, the broad seasonal trend in them as a function of the DOY (season) can be readily noted. This decrease in poleward winds is consistent with the decrease in ΔI/I in post-sunset emissions as measured over a low-latitude location. We further compare these variations with the model values of vertical drifts at the post-sunset time as presented by the vertical drift model (*Fejer et al.*, 2008). The sunset time vertical drift values for the winter solstice and equinox times are considered and are overplotted in Figure 5.11c (dashed line). As it is known, the PRE values are larger in the equinoxes

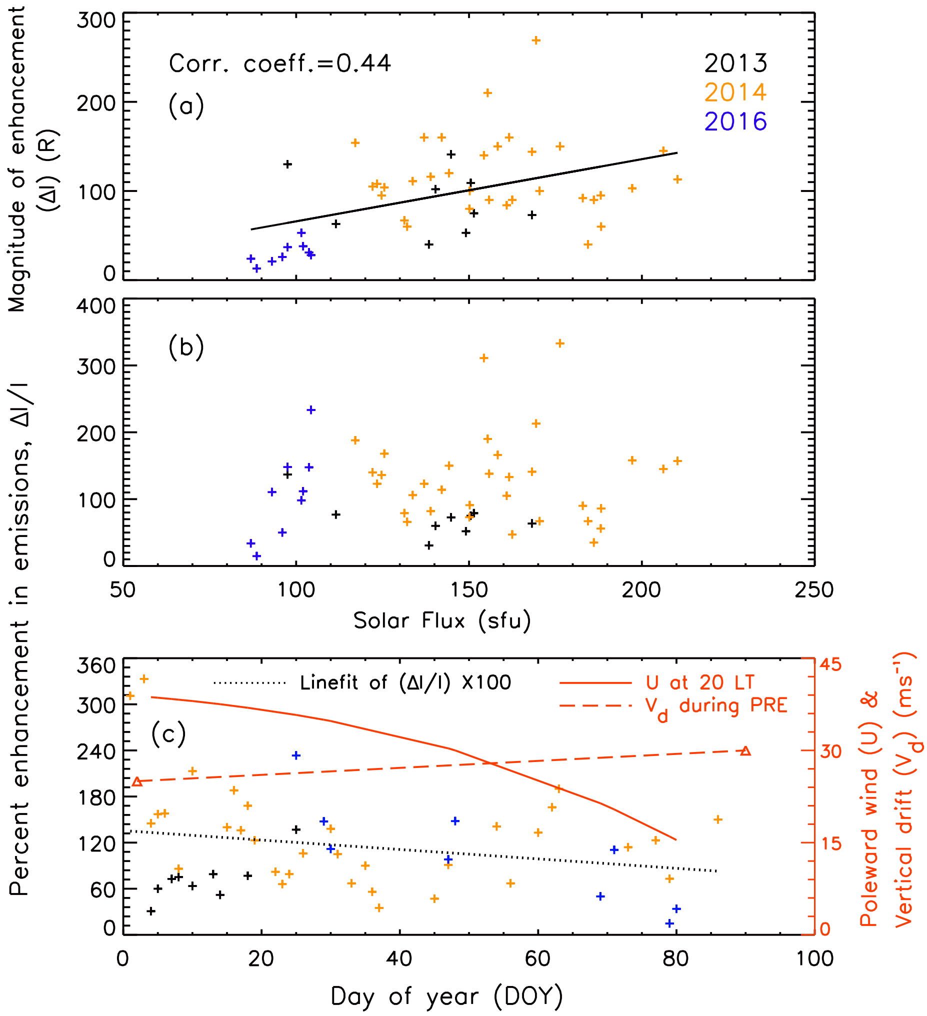

Figure 5.11: The variation of magnitude of enhancement (ΔI) and percentage enhancement in emissions [(ΔI/I) ×100] with solar fluxes are shown in top two panels for the nights as depicted in figure 5.2d. Panel c shows the percentage variation in (ΔI/I) with day of year for three different years.

as compared to the winters, which is in stark contrast with the observed values of ΔI/I.

There have been reports with observations of enhancements in thermospheric airglow emission intensities during post-midnight time. An increase in temperature was also observed simultaneously at that time (midnight temperature maximum, MTM) (*Herrero et al.*, 1983; *Herrero and Spencer*, 1982; *Otsuka et al.*, 2003; *Sastri and Rao*, 1994; *Colerico et al.*, 1996). The upward propagating semidiurnal tides was shown to be causing the MTM in TIEGCM model simulation (*Fesen*, 1996). The MTM amplitudes obtained from the model output estimated much smaller values as compared to the observed values. The absence of terdiurnal component of the tidal forcing in the TIEGCM model is probably hindering to obtain more accurate result. The passage of a brightness wave was observed in association of MTM, turning of meridional winds from equator to poleward direction, and local minima of zonal neutral winds (*Colerico et al.*, 1996; *Colerico and Mendillo*, 2002). As a consequence, the peak height of the ionospheric F-layer falls below to 300 km which is known as post-midnight collapse. Coordinate measurement of two nights found great correlation with the thermospheric winds and F-layer height variation over India longitudes. FPI measurement over Kavalur (9.5°N Mag) observed the MTM phenomena and at the same time, midnight collapse was observed over Ahmedabad (26.3°N Mag) (*Sastri and Rao*, 1994). The estimated meridional wind using the ionosonde data of Trivanrum (0.6°N Mag) and Sriharikota (10.5°N Mag) observed presence of significant poleward meridional wind during that period (*Sastri et al.*, 1994). The enhancement in emission during post-sunset hours as observed in our study is also supported by the poleward meridional wind. Therefore, it is probably similar to such midnight phenomena. Further detailed study will be required to understand the cause for the increase in temperature and generation of the poleward wind.

In conclusion, considering all the observational datasets, namely, (i) ionospheric F-region height variations over Trivandrum and Ahmedabad, (ii) PRE in electric field over the magnetic equatorial location (Trivandrum) in Indian longitudes, (iii) measured column integrated OI 630.0 nm emissions variations over Mt. Abu, a low-latitude location, (iv) the column integrated emission rates estimated using digisonde measured electron density over Ahmedabad and Trivandrum, and (v) the relative meridional wind variations derived from the measured values of electron densities at separate latitudes during the geomagnetic quiet time periods, it seems that the observed enhancements in nighttime OI 630.0 nm nocturnal airglow emissions over Mt. Abu in the post-sunset period are due to the variations in those of meridional winds for all solar flux conditions. Typically the meridional winds are equatorward after the sunset. On occasions of enhancements in emission, the presence of poleward meridional wind has been noted. This reversal in meridional winds could be due to a pressure bulge in the equatorial thermosphere induced by the increase in local temperature. The poleward winds bring down the height of the F-layer to lower altitudes and as a consequence enhancements in OI 630.0 nm nightglow emissions are seen. The decrease in the observed percentage enhancement in emissions as a function of DOY (from Jan to Mar) further reinforces the role of meridional winds in the post-sunset emission enhancement as the nature of variation in the model meridional winds is similar (representing the changing seasons from winter to equinox).

What is presented here is the circumstantial evidence of the significant role played by the meridional winds in causing the observed OI 630.0 nm emission enhancements in the post-sunset hours. Measurements of neutral winds from the same location at an earlier time and also from other longitudes do show that the meridional winds do change in their magnitudes (and direction) in short times scales (half an hour to a couple of hours' duration). Simultaneous Fabry-Perot interferometric measurements of neutral winds and temperatures are planned in the future from Ahmedabad/ Mt. Abu, which will enable quantification of the calculated meridional winds from the digisonde measurements as described in this study. Such a study will also enable the assessment of the relative contribution of winds and the PRE in governing the OI 630.0 nm emission variability in such low-latitude locations on a night-to-night basis.

5.6 Summary

The enhancement in OI 630.0 nm nocturnal emissions during the post-sunset hours were observed on several nights from Mt. Abu as well as in the estimated OI 630.0 nm emissions over Ahmedabad. The day-to-day variation in the equatorial electrodynamics and the meridional wind have been investigated to understand the possible causes for the observed post-sunset enhancement in the OI 630.0 nm nightglow emissions over a period of three years during geomagnetic quiet time period. The strength of the daytime EEJ do not show any relationship with the integrated nightglow emissions during the interval of time when enhancements are seen. Variations in the base of F-layer height and the PRE in electric field over an dip-equatorial location, Trivandrum, have been studied around the sunset time, and they too do not show any contrast in their behaviour between the nights with and without post-sunset enhancement in the OI 630.0 nm nightglow emissions. In this background, it is proposed that the poleward meridional winds can suitably explain the post-sunset enhancement in OI 630.0 nm emissions over Mt. Abu. Whenever the meridional wind turns poleward from the equatorward direction or cessation in the equatorward wind occurs, a clear enhancement has been noticed in the measured OI 630.0 nm nightglow emissions during post-sunset hours over the low-latitude location. The magnitudes of the enhanced emission depend on the number density of electrons present at those altitudes from where the emissions originate. The variabilities in the OI 630.0 nm emissions correlate well with the estimated relative variation in meridional wind on all of the nights on which radio data were available over Trivandrum during non-ESF and geomagnetic quiet times. These variations in emission enhancements are also consistent with those in the model meridional winds, which add strength to the conclusion arrived at in this study. The observations of emissions spanned over the years 2013, 2014, and 2016 with varying solar activity, which asserts that the results are independent of the solar flux variation.

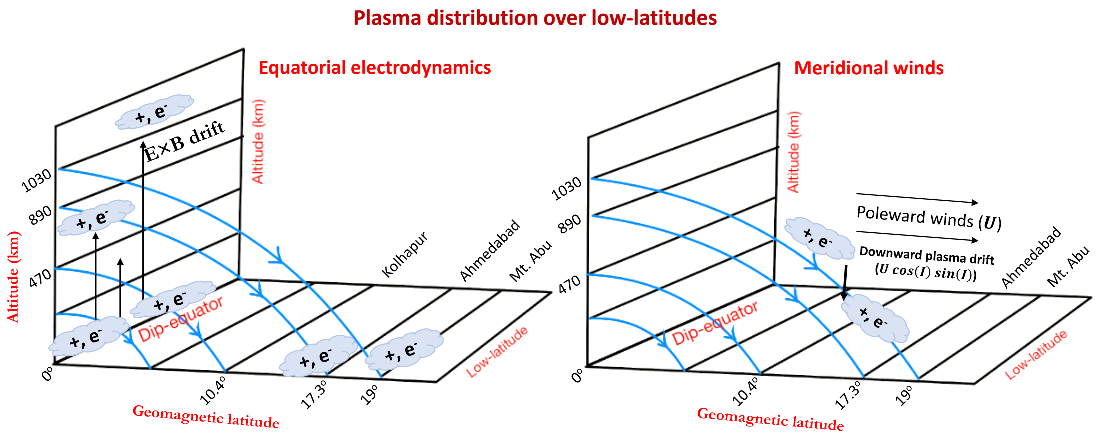

Figure 5.12: Plasma distribution over the low-latitudes is shown in this schematic. The equatorial electrodynamics and the ambipolar diffusion bring the plasma over the low-latitudes from the dip-equator through the geomagnetic field lines. Whereas, the poleward winds push down the plasma at the lower altitudes. Such dynamics are used in the understanding of the variabilities observed in the OI 630.0 nm nightglow emissions over the low-latitudes as discussed in chapters 4, 5, and 6

.

Figure 5.12 shows the effect of plasma distribution over the low-latitudes caused by the equatorial electrodynamics and meridional winds is seen in the OI 630.0 nm nightglow emissions measured over there. The northward geomagnetic field lines are shown in blue lines. The plasma lifts up by the $\mathbf{E} \times \mathbf{B}$ drift in the equatorial plane at higher altitudes and mapped over the low-latitudes through the geomagnetic field lines following the ambipolar plasma diffusion. The increase in emissions at different latitudinal locations over the low-latitudes depends upon the strength of PRE which decides the altitudes up to which the plasma can be uplifted over the dip-equator and the location of the crest of EIA after the sunset time as discussed in chapter 4. The downward movement of the plasma brings downs due to the poleward meridional winds enhances the electron density at the emission altitude of OI 630.0 nm emissions. As a consequence, the enhancement is seen in the nightglow emissions during the post-sunset time which is discussed in this chapter.

Chapter 6

Investigation of Equatorial Plasma Bubbles as seen over low-latitudes

6.1 Background

Different kinds of variabilities have been observed in OI 630.0 nm nightglow emissions as shown in figure 3.8 in chapter 3. The poleward and equatorward movements of the EIA crest for which sunset and night time electric fields are found to be responsible, respectively are shown in chapter 4. Chapter 5 presents the enhancements observed in OI 630.0 nm emissions during the post-sunset time over several years and suggests the poleward meridional winds as the cause for such enhancements. In this chapter, we will discuss the excursions in emissions as observed over Mt. Abu as shown in figure 6.1. These fluctuations in emissions are caused by the equatorial plasma bubbles (EPBs) as they appear within the FOV of HiTIES. The EPBs are generated over the dip-equator during the sunset time, get mapped over to the low-latitudes through the geomagnetic field lines and contribute to the nightglow emissions over low-latitudes. Simultaneously, the irregularity in ionosphere as seen in the abrupt variation of the electron densities also spotted. Such fluctuations in the plasma densities/ plasma density gradients pose practical difficulties in satellite-based communication and navigation. Due to far-reaching consequences that the plasma fluctuations have on societal applications, this motivates the scientific community working in the ionospheric studies to understand these phenomena in greater detail. The uplift of the plasma bubbles over the dip-equator depends upon the strength of vertical drift during sunset time. The heights to which the plasma bubbles reach, govern the latitudinal extent of these plasma depletions over low-latitudes (*Abadi et al.*, 2015; *Tulasi Ram et al.*, 2006). The occurrence of EPBs and their movement varies with respect to solar flux and seasons. Although many of the aspects of the EPBs are well understood, still, the day-to-day variability is a subject of critical investigation. Gravity waves are thought to be one of the major factors that are responsible for the seeding of Rayleigh-Taylor instability. The inter-bubble separations as observed over the low latitudes have been shown to be the horizontal scale sizes of the gravity waves (*Makela et al.*, 2010; *Das et al.*, 2020). In this context, we have studied the zonal scale sizes as obtained from OI 630.0 nm nightglow emissions over an off-equatorial location in addition to other dynamical phenomena, such as latitudinal extent, zonal speed of EPBs and the zonal scale sizes of the gravity waves present on the EPB nights.

6.2 Introduction

Equatorial ionospheric spread-F can extend to large spatial distances in latitudes which causes significant difficulties for trans-ionospheric radio wave propagation. Some of the manifestations of these irregularities are: the spread in reflected echoes (spread-F) of radio frequency as seen in ionograms (ESF), plasma bubbles as seen in optical imagers, plasma plumes as observed using radars, and plasma scintillations as seen in VHF and GPS measurements among others (e.g., *Farley et al.*, 1970; *Woodman and La Hoz*, 1976; *Basu and Kelley*, 1977; *Abdu et al.*, 1983; *Kelley*, 1985; *Takahashi et al.*, 2001, 2021; *Sekar et al.*, 2007, 2008; *Huang et al.*, 2013; *Patra et al.*, 2014; *Abadi et al.*, 2015; *Huang and Roddy*, 2016; *Sivakandan et al.*, 2019). In chapter 1, we have discussed the generation of bubble-like structures through the generalised Rayleigh-Taylor instability (RTI) which, to the first order, is understood to be responsible for the generation of such plasma irregularities over the magnetic equator (*Balsley et al.*, 1972; *Kelley*, 1985). The development and the growth rate of those EPBs depends upon the ambient electric field, neutral winds, ion-neutral collisions, etc. ESF shows large seasonal, solar flux, and day-to-day variabilities (e.g., *Abdu et al.*, 1981; *Tsunoda*, 1985; *Maruyama and Matuura*, 1984; *Sridharan et al.*, 1994; *Pimenta et al.*, 2003; *Jyoti et al.*, 2004; *Makela et al.*, 2004; *Huang and Roddy*, 2016; *Sivakandan et al.*, 2019). Detailed studies on the conditions of precursors in the ionosphere-thermosphere regions are needed for a greater understanding on the generation of ESF. Gravity waves are observed in many cases to be dominant seed perturbation in the bottomside F-layer and generates plasma irregularities which can evolve with a scale of several hundreds of km (e.g., *Röttger*, 1981; *Kelley et al.*, 1981; *Hysell et al.*, 1990, 2014; *Huang and Kelley*, 1996; *Fritts and Vadas*, 2008; *Takahashi et al.*, 2009; *Abdu et al.*, 2009; *Makela et al.*, 2010; *Narayanan et al.*, 2012; *Patra et al.*, 2013; *Aa et al.*, 2020; *Das et al.*, 2020, 2021; *Mandal et al.*). Both, large-scale wave structures (LSWS) (*Tsunoda*, 2005; *Thampi et al.*, 2009; *Tsunoda et al.*, 2010) and small-scale wave structures (SSWS) (*Narayanan et al.*, 2012; *Sekar et al.*, 2001) have been observed to be present in the scale sizes of the EPBs. However, a comprehensive understanding of the seed perturbation of the EPBs is not yet understood comprehensively. The study of the required scale sizes, the origins of such gravity waves, etc. are still the subjects of investigation for better understanding of the generation and variability in ESF occurrence. The inter-bubble separations have been observed to be similar to the horizontal scale sizes of the gravity waves that are responsible for the initiation of plasma instability (*Makela et al.*, 2010; *Das et al.*, 2020).

The equatorial plasma instabilities have been investigated using various techniques, like, radar, ionosonde, optical photometers, spectrographs, interferometers, and imagers from both ground and space-based platform. Optical emissions have been used extensively in the investigations of equatorial plasma bubbles. OI 630.0 nm and 777.4 nm emissions originating from around 250 km and peak F-layer, respectively, are more commonly used for the EPB investigations (*Mendillo and Baumgardner*, 1982; *Kelley et al.*, 2002; *Makela and Kelley*, 2003; *Mukherjee*, 2003; *Rajesh et al.*, 2010; *Sekar et al.*, 2012a; *Ghodpage et al.*, 2014) as the electron densities play an important role in the production of these emissions.

The temporal variation of the plasma bubbles as seen in large field-of-view observation shows their eastward zonal movement (*Mendillo and Baumgardner*, 1982; *Pimenta et al.*, 2003). The zonal speed of the EPBs becomes maximum during 21-22 LT and it decreases towards and after midnight time. Although the EPBs move in the eastward direction, the structure is observed to be tilted in the westward direction increasing in the poleward direction (*Zalesak et al.*, 1982; *Mendillo and Tyler*, 1983; *Sekar and Kelley*, 1998; *Abalde et al.*, 2001; *Mukherjee*, 2003). In the radar data, C-shaped structure observed from different locations, like Jicamarca (*Woodman and La Hoz*, 1976), ALTAIR (*Tsunoda et al.*, 1982), and Indian sector (*Sekar et al.*, 2012b). Further, this backward C-shaped structures were observed in many other satellite observations (*Kelley et al.*, 2003; *Kil*, 2015; *Karan et al.*, 2020; *Aa et al.*, 2020). The difference in flux-integrated conductivities between the E and F region generates the plasma shear in the zonal direction, and as a consequence, such kind of structure is formed in the EPBs (*Sekar et al.*, 2012b; *Tsunoda and White*, 1981; *Kudeki et al.*, 1981; *Fejer et al.*, 1985; *Kelley et al.*, 1986; *Kil et al.*, 2009a).

The seasonal and solar flux variation have been investigated using such long-term data which presented interesting information about the characteristics of EPBs (*Maruyama and Matuura*, 1984; *Tsunoda*, 1985; *Makela et al.*, 2004; *Sobral et al.*, 2002; *Sobral and Abdu*, 1991; *Agyei-Yeboah et al.*, 2019). Using the airglow imager data and GPS data during the period January 2002 to August 2003, seasonal variation of EPBs occurrence has been investigated (*Makela et al.*, 2004). Around 300 clear nights have been used from Hawaii to understand the seasonal variation during this period. The equinox period of April and September showed a larger occurrence probability 45% and 83%, respectively. For the months of June to August, EPBs were mostly observed in the midnight time rather than post-sunset time which suggests that the development of EPBs happened in the westside of the observation location and as these bubbles did not show vertical movement, therefore, it can be considered as fossil bubbles. Larger occurrence in ESF has been observed during the high solar activity period (55%) using the data obtained during high solar active years 1988-1991 and low solar active years 1994-1998 (*Sahai et al.*, 2000). Even the EPBs reach at higher altitudes ($>$ 1500 km) during the high solar activity period (66%) as compared to a low solar active period (34%). Around 934 days of data were studied using OI 630.0 nm nightglow emissions during the years 1977 to 1998 (*Sobral et al.*, 2002). During the high solar active period, the occurrence of EPBs is larger in the months September to April, whereas, in the low solar active period, this becomes October to March.

In this study, we observed OI 630.0 nm emission during the nighttime over the period of January to March in the year of 2014 from two different locations, namely, Mt. Abu (16°N Mag) and Kolhapur (8.2°N Mag). Mt. Abu is located at the northern edge of the EIA crest, whereas, Kolhapur is located between the magnetic equator and the northern crest of the EIA. Signatures of the EPBs have been observed in the OI 630.0 nm emissions from these two locations using two different optical instruments, High throughput Imaging Echelle Spectrograph (HiTIES) over Mt. Abu and All-sky Imager (ASI) over Kolhapur. This passive remote sensing of the upper atmosphere has resulted in improving our understanding of the signatures of nighttime gravity wave behaviour both in zonal and meridional directions. The plasma bubbles are clearly seen as depletions in emissions in the imager and the spectrograph. The zonal plasma drift, horizontal scale sizes as obtained from the imager data, and the plasma bubble periodicity obtained from two locations will be discussed in this chapter.

6.3 Data sets used

OI 630.0 nm nightglow data have been obtained from HiTIES and ASI as mentioned earlier. The detailed discussion about these instruments and data calibration have been carried out in chapter 2. In this study, we have mainly used the zenith observation of HiTIES. The 1024×1024 pixels CCD-based ASI gives 140° FOV which covers 1200 km distance (*Sharma et al.*, 2014). To avoid the image curvature introduced at lower elevation angles, we have restricted the data usage to 100° FOV which corresponds to a range of around 600 km both in zonal and meridional directions in our analysis. Radio sounding data using Digisonde Portable Sounder (DPS-4D), from two locations Trivandrum (dip-equatorial location) and Ahmedabad (low-latitudinal location) have been used in this study. We have used 7 MHz iso-electron density to calculate the sunset time F-layer vertical drift over the dip-equator. The different instruments which are commissioned at different locations over Indian longitudes are shown in figure 2.1 of chapter 2 which gives a pictorial view of different locations and the significance of those locations.

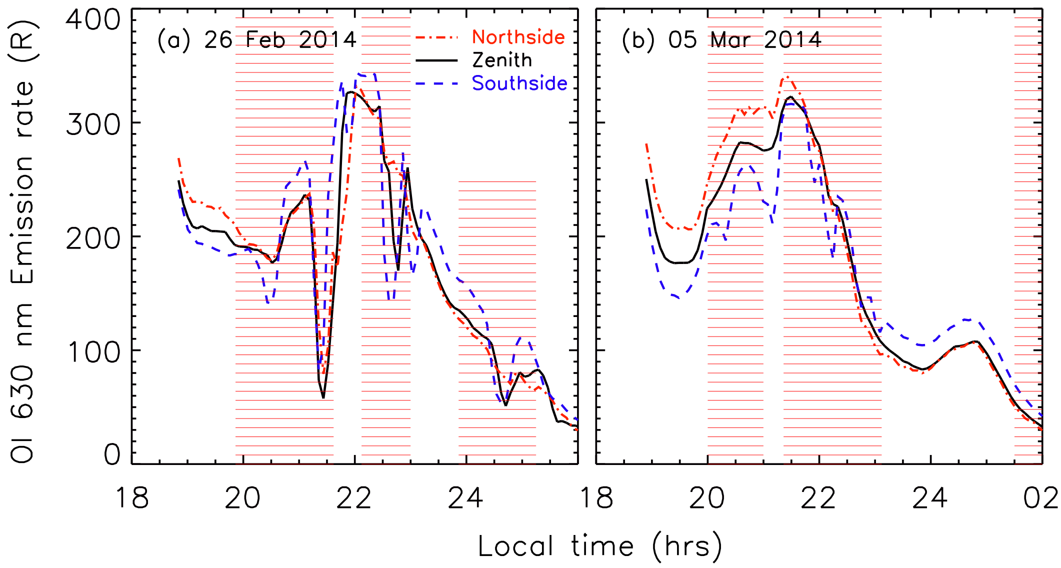

Figure 6.1: Typical nightglow variations of OI 630.0 nm emissions are depicted here. The total FOV of HiTIES is segmented in three sections, one towards North, one South, and Zenith as indicated in these different colour and line styles. Panels (a) and (b) show multiple excursions in emissions. The shaded regions in the panels (a) and (b) indicate the time of spread-F observed in digisonde which is situated about 1.5° southward of Mt. Abu.

6.4 Observation and results

Different kinds of variabilities in OI 630.0 nm nightglow emissions have been shown in figure 3.8 of chapter 3. The effect of equatorial electrodynamics, such as PRE, and meridional winds have been discussed in chapters 4 and 5. On several nights, we have observed excursions in emissions (as shown in figures 6.1a, 6.1b). There are four depletions in emissions that have been observed on 26 Feb 2014 at 20.5, 21.4, 22.7, and 24.6 LT (figure 6.1a). A close inspection indicates that the emissions decrease at the same time and with the same magnitudes in all directions, north, zenith and south at 21.4 LT. Whereas, for the other depletions, the southern side emissions (blue dashed line) show a much sharper and deeper decrease than that in the northern side. Similarly, the depletions in emissions seen on the other night, 05 Mar 2014, have different rates of decrease in different directions. All these differences are the tell-tale signature of the plasma bubbles, their latitudinal and longitudinal extents, etc., as will be clear once the data from other datasets are presented and discussed as given below. Out of 68 moonless clear sky nights during Jan-Mar of the year 2014, 26 nights showed such excursions in emissions.

6.4.1 Simultaneous observation from different datasets

The simultaneous digisonde measurement from a nearby location Ahmedabad indicated a presence of spread-F during the times of depletions in the nightglow emissions observed from Mt. Abu. The durations of spread-F are indicated with the shaded region (pink coloured horizontal lines) in the figure 6.1a and 6.1b. The presence of spread-F at the time of depletions in emissions admits the presence of plasma irregularities having scale sizes of several hundred km over this region. The presence of depletions in emissions over Mt. Abu and spread-F over Ahmedabad coincides on all (100%) of the occasions out of those 26 EPB nights when excursions in emission observed over Mt. Abu, as mentioned above. However, the presence of spread-F was observed in digisonde (around 1.5° southward of Mt. Abu) on around 36 nights out of those 68 moonless clear sky nights. Among which, plasma depletions are present on around 69% of occasions (26 nights) indicating that on such other nights the plasma depletions did not extend to latitudes beyond Ahmedabad.

To ascertain that such sharp fluctuations as obtained in our measurements over Mt. Abu are due to plasma depletions, we have investigated the all-sky imaging measurements of OI 630.0 nm nightglow emissions from Kolhapur, which is situated between the magnetic equator (Trivandrum) and low-latitude region (Mt. Abu/ Ahmedabad). We have around 20 clear nights of data from the imager during the same period of Jan-Mar in the year of 2014. Figure 6.2 shows variations in OI 630.0 nm nightglow from both the places, Mt. Abu and Kolhapur. The meridional segment (12 km over zenith x 600 km along North-South) from each of the images obtained from Kolhapur is arranged with time to form a keogram, and are shown in the bottom panels of figure 6.2. The OI 630.0 nm nightglow variations obtained from Mt. Abu are shown in the top panels. The gap in the bottom panels is due to the non-availability of the data at that time. Interestingly, for four nights, 24 Feb, 26 Feb, 04 Mar, 05 Mar (Figures 6.2a-h), all the depletions in emissions observed over Mt. Abu have a clear concurrence with plasma bubbles seen in all-sky images obtained over Kolhapur in simultaneity, which confirms that the depletion signatures observed over Mt. Abu are due to the plasma bubbles present over latitudes

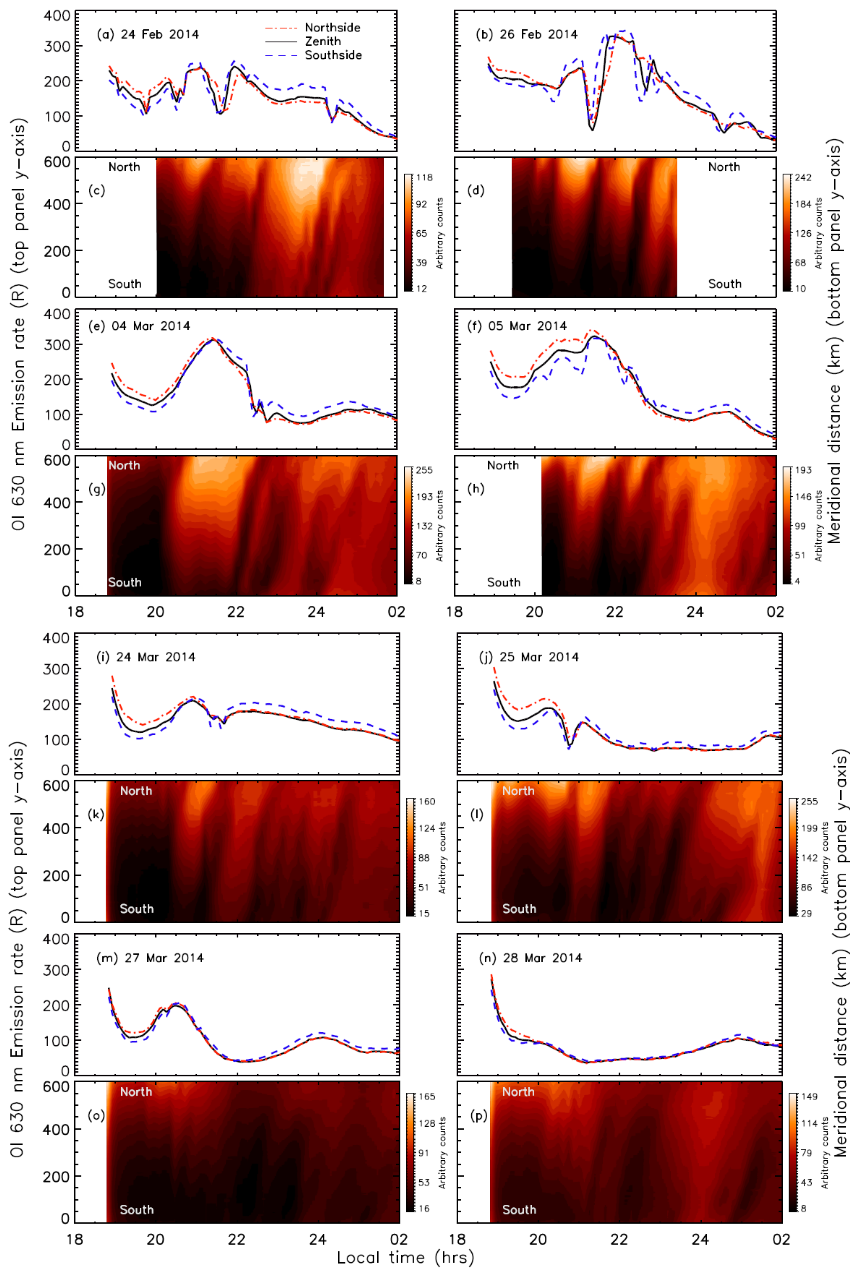

Figure 6.2: OI 630.0 nm emission variations for eight nights as observed over Mt. Abu are shown in top panels a, b, e, f, I, j, m, and n, whereas, the keograms in the bottom panels c, d, g, h, k, l, o, and p show OI 630.0 nm emission variations in the north-south direction over Kolhapur. The y-axis of the top panels indicates the OI 630.0 nm emission rates as observed over Mt. Abu whereas, the y-axis for the bottom panels indicates the North-South distance with Kolhapur as the zenith. Whenever the plasma depletions are observed over Mt. Abu, plasma bubbles are also observed over Kolhapur simultaneously, but the converse is not true.

corresponding to that of Mt. Abu. There are several examples of nights when the plasma bubbles did not reach over to Mt. Abu although they have been observed over Kolhapur. For example, on the nights of 24 and 25 Mar (Figures 6.2i-l), only one or two bubbles have reached over Mt. Abu, although many more are seen over Kolhapur. It is important to take into cognisance that the distance between the northernmost location presented in the ASI data and the southernmost view direction as presented in figure 6.2 is around 400 km. Thus, it is understandable that not all plasma bubbles seen in the ASI data from Kolhapur will be present in the HiTIES data over Mt. Abu. Another important aspect that can be noticed is that the depletions in emissions are not equal at all the three different directions (north, zenith, and south) as observed from Mt. Abu. The plasma bubbles are aligned along the magnetic field lines and as the different latitudes are mapped to different apex altitudes over the dip-equator, it can be inferred that the electron density depletion is greater at lower altitudes as compared to those higher above.

Although, visually the depletions in the images from both the HiTIES and ASI data seem similar, to make a quantitative assessment, we have carried out spectral analysis of the data, wherein, the emissions obtained from the southern-most direction from HiTIES are compared with the emissions obtained in the northern-most segment of the ASI imager. The result from the Lomb-Scargle periodogram analysis (*Lomb*, 1976; *Scargle*, 1982) for these two datasets is shown in figure 6.3 for four sample nights with 90% false alarm limit (FAL) (shown as horizontal line). The solid black line indicates the normalized power spectral density (PSD) for different periodicities over southernside of Mt. Abu, whereas, the dashed blue line indicates normalized PSD over northernside of Kolhapur. A detailed discussion on Lomb-Scargle analysis has been made in section 2.7.2 of chapter 2. The periodicities obtained in these analyses indicate the occurrence rate of the plasma bubble for a given night. Figure 6.3 shows the presence of periodic fluctuations of 1-3 hrs at both locations. The similar periodicities as observed in plasma bubble depletions from the analysis as discussed above and depicted in figure 6.3 suggest that these are consistently present at both locations. As already mentioned above, the spatial separation between these two viewing orientations in these two datasets is around 400 km, and therefore, it is expected that not all the periodicities are present with similar strengths at both locations. A case in point can be seen on 24 Feb 2014 (figure 6.2a), wherein, all the periodicities

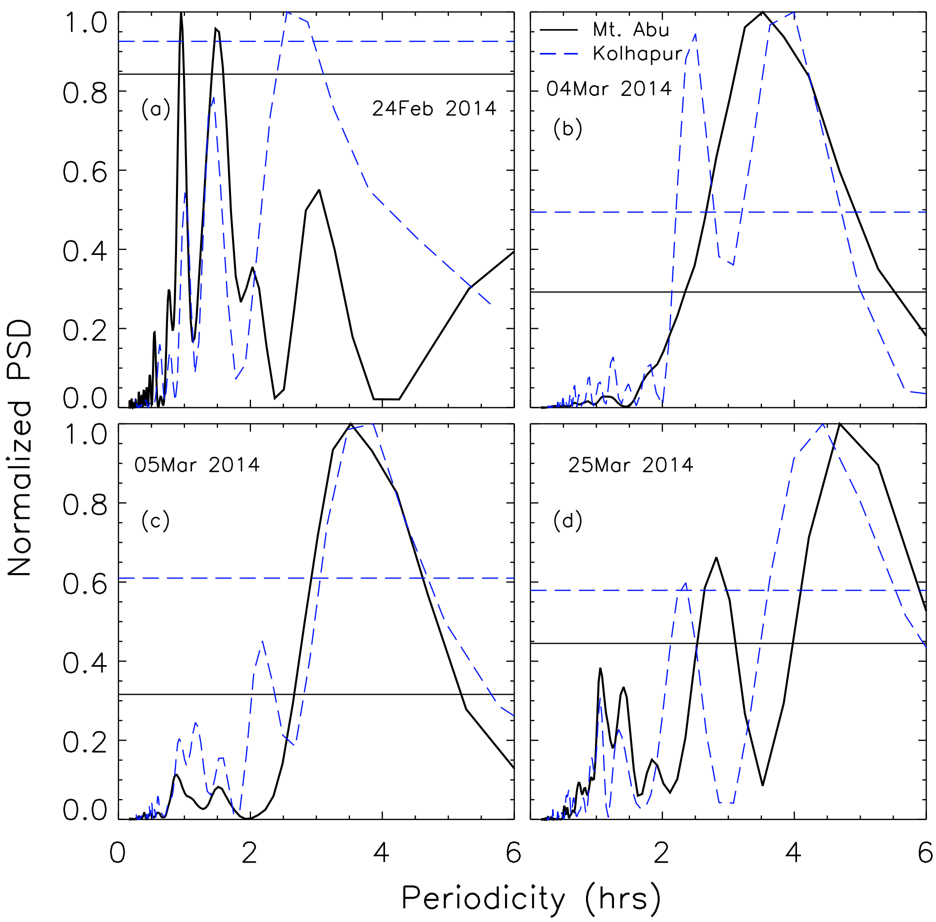

Figure 6.3: The Lomb-Scargle periodicities obtained for four sample nights as observed over both the places, Mt. Abu and Kolhapur are presented. Emissions obtained from the Southern-most view direction from Mt. Abu and northern-most as viewed from Kolhapur, which are separated by around 400 km are used in these analyses.

around 1.0, 1.5, and 2.5 hr are present in both the datasets, but the relative strengths are different in each of them.

6.4.2 Effect of PRE in the generation of ESF and latitudinal extent of the plasma bubbles

The apex altitude to which these bubbles are required to be raised over the magnetic equator is around 1000 km in order to reach over the latitudes of Mt. Abu. The vertical uplift of the plasma during the sunset time depends upon the strength of the electric field during that time. In our study, we have investigated the presence of plasma bubbles over Mt. Abu in terms of observed plasma depletion as seen in the nightglow images. As we

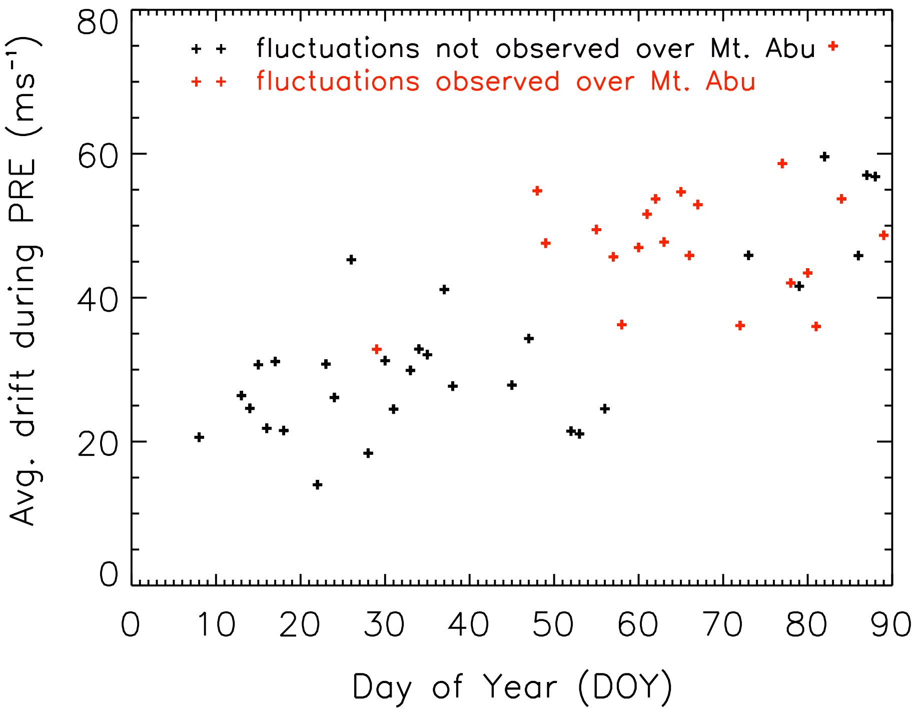

Figure 6.4: Avg. PRE strength with day of year (DOY) during Jan-Mar in the year of 2014 is shown. The points in red colour indicate the presence of plasma depletions as observed in the OI 630.0 nm emission data over Mt. Abu.

have discussed earlier, Mt. Abu is located in the low latitudinal region under the northern crest. Therefore, the strength of PRE should be sufficient so that the plasma bubbles can be uplifted to the higher altitudes over the dip-equator and can be mapped over to Mt. Abu. We have used the rate of change of the height corresponding to the returned echo of 7 MHz iso-electron density to calculate the F-layer vertical drift over Trivandrum during the sunset time. The strength of the PRE has been characterized by taking 30 minutes average centred at the time of occurrence of peak value in PRE. Out of the 51 nights of PRE data available over Trivandrum, we have found that around 21 nights showed sharp depletions in the optical emissions over Mt. Abu. Figure 6.4 depicts the variation of PRE strength with the day of year (DOY). The red points indicate the values of the PRE on the nights when the plasma depletions extended until the latitudes of Mt. Abu. On all these nights spread-F had occurred as observed over Trivandrum (except for two; DOY 22 and 52). Due to the high strength of PRE, the plasma bubbles were lifted up to high altitudes (> 1000 km) which enabled them to reach over to Mt. Abu. The plasma

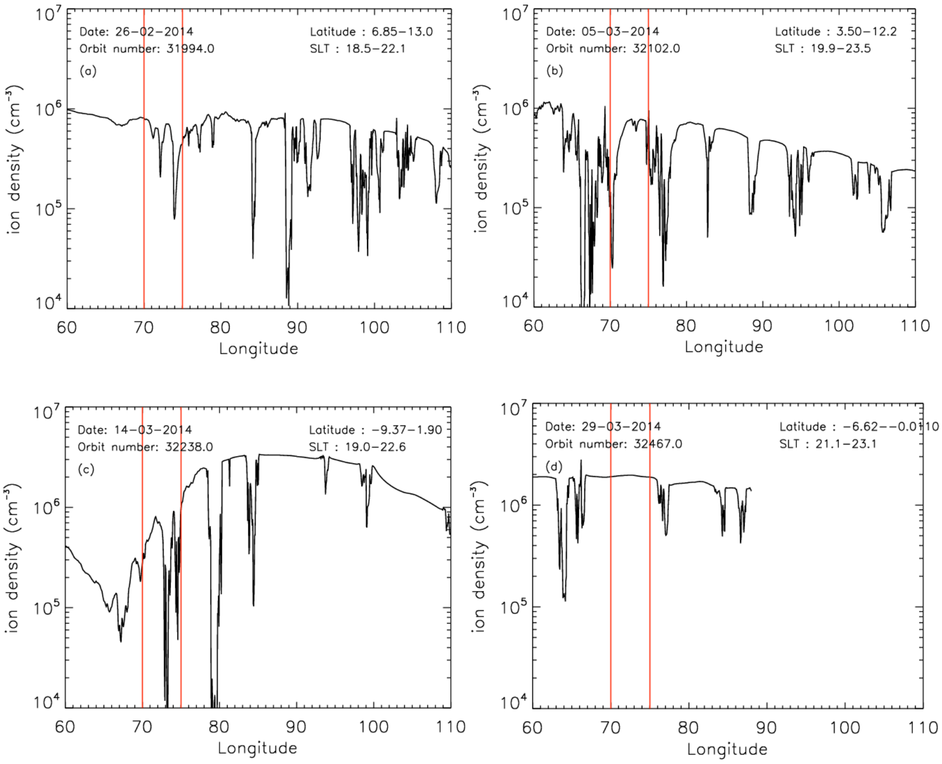

Figure 6.5: Ion density for four different nights is shown which are observed from C/NOFS satellite over the Indian longitudes. The ion density variation for one orbit is shown for each night. The latitudinal and temporal coverage during that orbit is mentioned by vertical red lines in each panel.

depletions over Mt. Abu were observed on most of the occasions when the PRE values are in the range of 40-60 ms^{-1}. Here, it is emphasised that PRE plays an important role in extending the depletion of electron densities to be mapped over to the latitudes further away along the geomagnetic field lines rather than PRE as the seeding factor (as the discussion corresponds to the developments after the bubble generation). On some occasions, the plasma bubble was absent over Mt. Abu although large values of PRE were present (for example DOY: 73, 79, 82, 86, 87, 88). However, among these nights, plasma bubbles were seen in the ASI data over Kolhapur on the two nights of available data (DOY: 86 87) as also shown in figures 6.2o, and 6.2p (27, 28 Mar). On the night of DOY 87, spread-F was not observed in the digisonde data at Ahmedabad (although equatorward location of Mt. Abu) indicating the bubble had not reached the latitude of Ahmedabad.

To ascertain if the bubbles had reached further north of the observational location of Kolhapur we have also looked into the concurrent observation of the C/NOFS satellite data which had an orbit at an inclination angle of 13°. This is also done to serve the purpose of explaining the electron density variation near the equatorial region during these nights when the all-sky imager data were unavailable. As per the availability of C/NOFS data, the electron densities exhibit sharp decrease on all nights not only when the depletions were observed over Mt. Abu, but also when the depletions were not observed over Mt. Abu on the days mentioned above (DOY: 73, 86, 87, 88). Variations in electron density over the Indian longitudes as observed from C/NOFS are shown in figure 6.5 for four nights. C/NOFS provides the ion density values for the altitudes ranging from around 400-600 km. The vertical bars shown in the figures indicate the longitudinal location from where our optical observations are carried out. The depletion in the plasma density can be seen in the satellite data over this region which confirms the presence of plasma bubble over this region in simultaneity. We have shown the plasma density variation for a single orbit of four given nights. The latitudinal coverage and the solar local time are given in each of the nightly plot. For a given night on 29 Mar 2014 (figure 6.5d), plasma depletion is not found within the ground-based observational location. As we can notice that plasma bubble is present in the nearby longitudes, surely those will reach over that location. The plasma bubbles were not present over there only when the satellite was passing over the region at a particular time. Now, several factors, such as electric fields, and neutral winds, could have prevented the plasma bubbles from reaching to Mt. Abu later in the night in spite of large magnitudes of PRE earlier on those nights.

The importance of EIA and PRE in the seeding of the EPBs are reported in many of the earlier studies (*Raghavarao et al.*, 1987, 1988a; *Sridharan et al.*, 1994; *Prakash et al.*, 2009). Apart from that, the role of PRE in the latitudinal extent of the plasma bubbles has been investigated using ionosonde and scintillation data (*Abadi et al.*, 2015; *Valladares et al.*, 2004; *Tulasi Ram et al.*, 2006). The observation of plasma depletion at different latitudinal regions validates the field line mapping of the plasma bubbles over the low latitudes. Presence of plasma bubbles at various locations of different longitudinal sectors situated over dip-equator and low latitudes, such as Christmas Island (3.1°N Mag), Brazil (16°S Mag), and Hawaii (21.3°N Mag) are reported in earlier studies (*Sahai et al.*, 1994; *Kelley et al.*, 2002; *Makela*, 2006). Simultaneous observations of EPBs from two geomagnetic conjugate locations over Japan (24°N Mag) and Australia (24°S Mag) are also reported (*Otsuka et al.*, 2002; *Shiokawa et al.*, 2004). In figure 6.6, the maximum

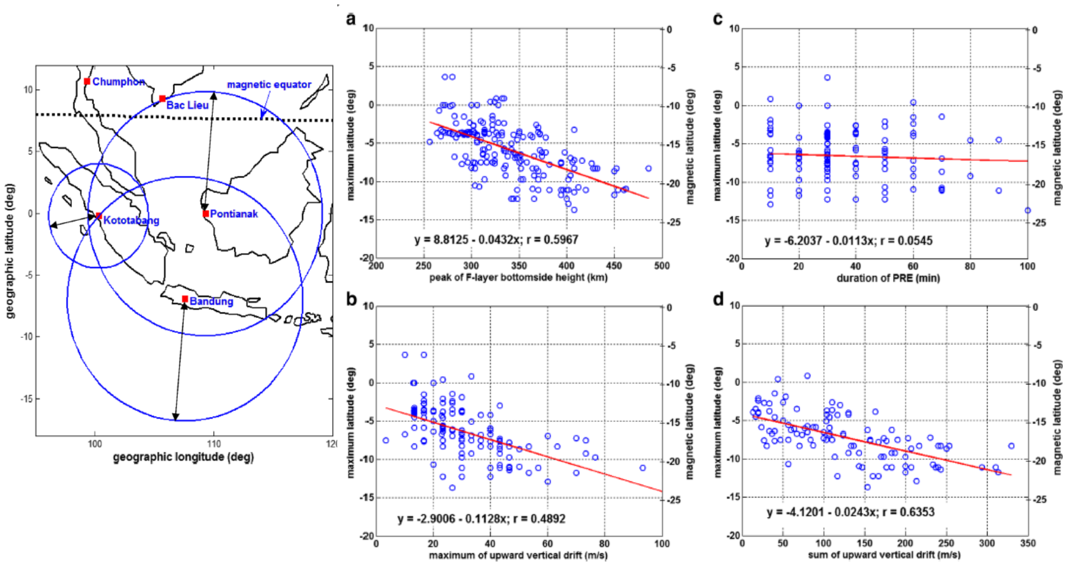

Figure 6.6: The left side figure shows the FOV of the different instruments located at nearby locations. The peak F-layer height, duration of PRE, peak PRE value and the integrated PRE values are compared with the latitudinal extent of plasma irregularities which are measured by the GPS scintillation of S4 index are shown in the right-side a, b, c, d panels. Ionosonde data from Chumphon and GPS data from Pontianak and Bandung are used here. (After *Abadi et al.*, 2015)

extent of the GPS scintillation has been depicted as a function of F-layer height, peak magnitude of PRE, duration of PRE, and the integrated PRE strength. The magnitude of amplitude scintillation (S4 index) as obtained from GPS data over Pontianak (9.8°S mag), and Bandung (16.7°S mag) and the ionospheric height, vertical drifts obtained from Ionosonde data over Chumphon (0.86°N mag) are used in this figure (*Abadi et al.*, 2015). The nights of equinoctial months (March, April, September, and October) in the year 2010-2012 have been included in this study. The GPS scintillation S4 index has been observed to be distributed in the 0°-10° latitudes which corresponds to 10°-20° geomagnetic latitudes in this Southeast-Asian sector. The peak h'F height have been observed to be varying in the range of 250-450 km, maximum drift during PRE ranged from 10-70 ms^{-1}, and integrated PRE strength ranged from 20-250 ms^{-1}. The linear fits have been calculated for each plot as shown in figure 6.6 and the cross-correlation coefficient values have been noted. The latitudinal extent of equatorial plasma instability which has been observed in terms of GPS scintillation shows a good correlation with the ionospheric F-layer height and also the strength of the sunset time electrodynamics.

Depending upon the strength of PRE in electric field, the plasma gets uplifted to higher altitudes, which is essentially reflected as an increase in the height of the F-layer. The plasma depletion generated over the equator during the sunset time, then diffuses to the latitudes further away through the geomagnetic field lines.

6.4.3 Eastward movement of the EPBs

After the generation of plasma bubbles over the equator, these grow vertically upward and move in the eastward direction. Airglow emissions observed in all-sky imagers provide two-dimensional picture of the night sky. The plasma bubbles generated over the equator aligned along the geomagnetic field lines and mapped over the low-latitudes. These north-south aligned plasma depletion structures can be seen moving in the eastward direction (*Mendillo and Baumgardner*, 1982; *Pimenta et al.*, 2003; *Nade et al.*, 2013; *Gurav et al.*, 2019). Plasma bubbles observed in OI 630.0 nm emissions over Paulista are shown in figure 6.7a (*Pimenta et al.*, 2001). The intensity variation in the zonal direction is shown figure 6.7b taking an east-west cross-section along the zenith. Calculating the zonal distances moved by the plasma bubbles as seen in successive images over time, the zonal speeds of the plasma bubbles have been estimated (*Pimenta et al.*, 2001, 2003). The typical zonal drifts of the plasma bubbles range from 100-200 ms^{-1} before the midnight time having peak values around 21-22 LT and 50 ms^{-1} after the local midnight (*Mendillo and Baumgardner*, 1982; *Mendillo et al.*, 1997; *Taylor et al.*, 1997; *Pimenta et al.*, 2003; *Nade et al.*, 2013; *Gurav et al.*, 2019; *Ghodpage et al.*, 2018, 2021). The values of the zonal plasma drift during nighttime as measured from incoherent scatter radar, Jicamarca (*Fejer et al.*, 1991) matches well with the zonal speed of the EPBs. Differences in zonal speed have been observed when observed at different latitudes (*Pimenta et al.*, 2003; *Martinis et al.*, 2003; *Eccles*, 1998a,b; *Kil et al.*, 2009a). The change in direction of the EPBs from eastward to westward was observed during the geomagnetic disturbed condition in the presence of penetrated electric field due to over-shielding and under-shielding effects over low-latitudes (*Gurav et al.*, 2021; *Li et al.*, 2018). The motion of the plasma bubble showed differences in zonal speeds between those at the central part of depletion, and in the eastern and western walls of the depletion. It was reported in that work that the eastern wall showed an increase in speed of around 40% as compared with the western

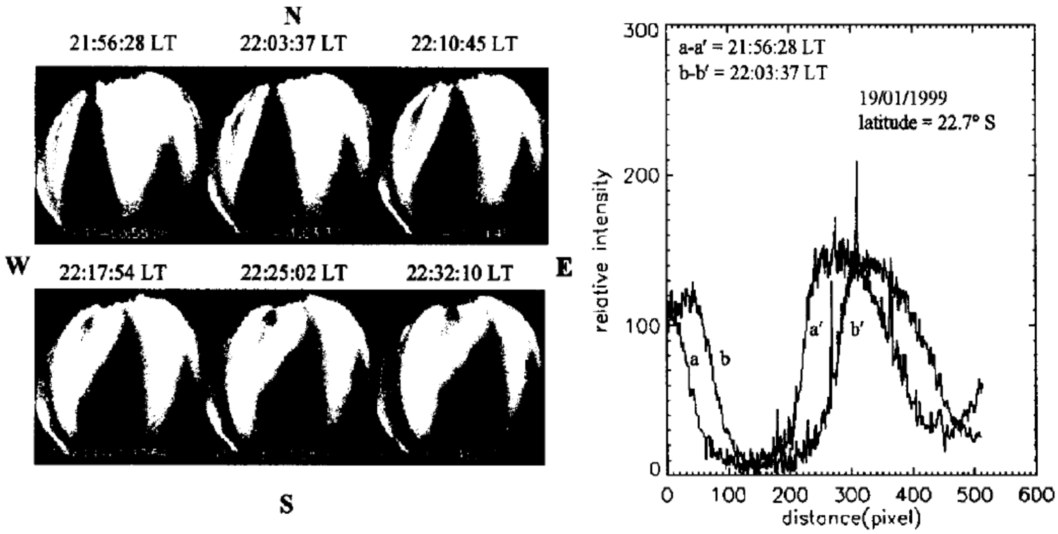

Figure 6.7: Plasma bubble structures as seen in OI 630.0 nm nightglow emissions over Paulista, Brazil on 19 Jan 1999 in the left side panel. The right-side panel shows the OI 630.0 nm emission variation in the zonal direction. Using the variation of two consecutive images, the zonal speed can be calculated. (After *Pimenta et al.*, 2001)

wall, whereas, the central depletion showed an increase by 10-20%. The internal space-time dynamics of the plasma bubble structure probably lead to this asymmetry in zonal speed in different depletion walls.

In our study, we have calculated the zonal drifts in the plasma depletions using the nightly images obtained from all-sky imagers commissioned at Kolhapur. The zonal segment (12 km over zenith $\times$ 600 km along East-West) in each image is considered and they are stacked one above the other as shown in figures 6.8a and 6.8b. By observing the spatial movement of depletions in emissions with time, we have calculated the zonal drift of a plasma bubble. As can be seen from figures 6.8a and 6.8b for 04 and 05 Mar 2014, different bubbles keep appearing as time progresses (shown in y-axis) beginning from the western most location of the FOV, moving eastwards, and disappearing. The times corresponding to the appearance and disappearance of the bubbles are noted along with the spatial distances to calculate the average zonal drift of each plasma bubble. Four plasma bubbles have been marked on these nights in the figures 6.8a and 6.8b. It can be noted that the bubble 01 is present over the whole 600 km in the east-west direction for a long duration on both the nights, whereas, the other bubbles dis not last that long. Also, the first bubble is the deepest and widest of all the bubbles. The variability in the

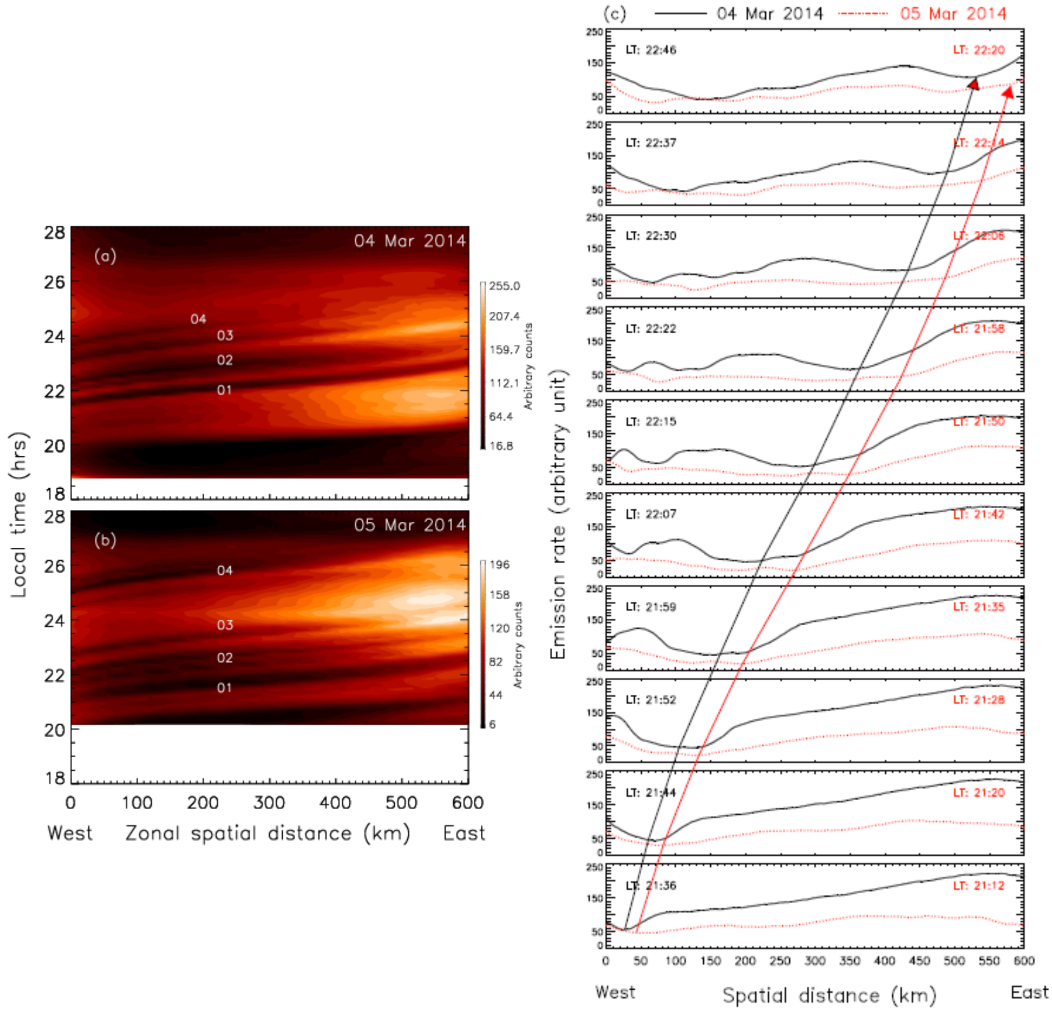

Figure 6.8: Zonal variations in OI 630.0 nm emissions have been depicted with time for two neighbouring nights in panels (a) and (b). A zonal strip for each image (12 km centred over zenith × 600 km) is considered. The zonal movement of the plasma bubble marked as '01' for the nights 04 Mar and 05 Mar 2014 has been shown over the time in panel (c).

zonal extent has been seen on the other nights as well. There is another bubble that can be seen on 05 Mar around 20 LT seen earlier than the one marked by 01. However, as this was present even before the first image was obtained on that night, in order to avoid any ambiguity, it is not used for the estimation of the drift speed. The spatial movements of the plasma bubble 01 for the nights of 04 Mar and 05 Mar 2014 are depicted in solid black and dotted red lines, respectively (Figure 6.8c). The time evolution of each frame of the figure 6.8c is mentioned in the left and right sides for the nights 04 Mar and 05 Mar 2014, respectively. From the time evolution of the depletions seen in the frames as shown

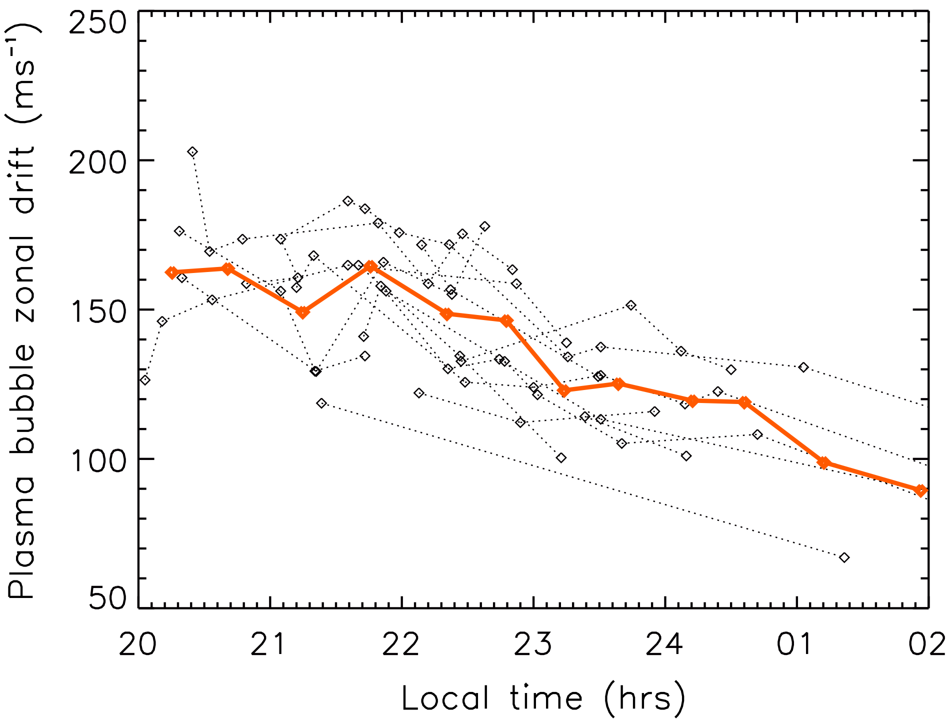

Figure 6.9: Zonal drift of the plasma bubbles depicted for 14 nights. The orange line shows the average zonal drifts where all the values in a given 30 minutes duration are averaged.

in Figure 6.8c, it can be noted that they have travelled around 510 km and 540 km with zonal speeds of around 121.4 and 132.4 ms^{-1} for 04 Mar and 05 Mar 2014, respectively. Now, these two bubbles passed over the zenith location at around 22.25 and 21.7 LT. The average zonal speeds at the corresponding time when the bubbles passed over the zenith have been plotted to understand its temporal variation. In the similar way, the zonal drift values for the other plasma bubbles for different nights have been calculated and are shown in figure 6.9.

Figure 6.9 shows the zonal drift values of the plasma bubbles for a total of 14 nights which include those plasma bubbles that have crossed the zenith location as seen in the images. It can be seen that the zonal speeds are higher during the post-sunset time and they decrease as the night progresses. The zonal drifts reach around 190 ms^{-1} at 21-22 LT and after midnight they reduce to around or below 100 ms^{-1}. The orange line in figure 6.9 shows the temporal variation of average zonal drift where all the values in a given 30 minutes duration are averaged. The temporal variation of plasma bubble zonal drift obtained from this study is found to be consistent with the earlier findings from different

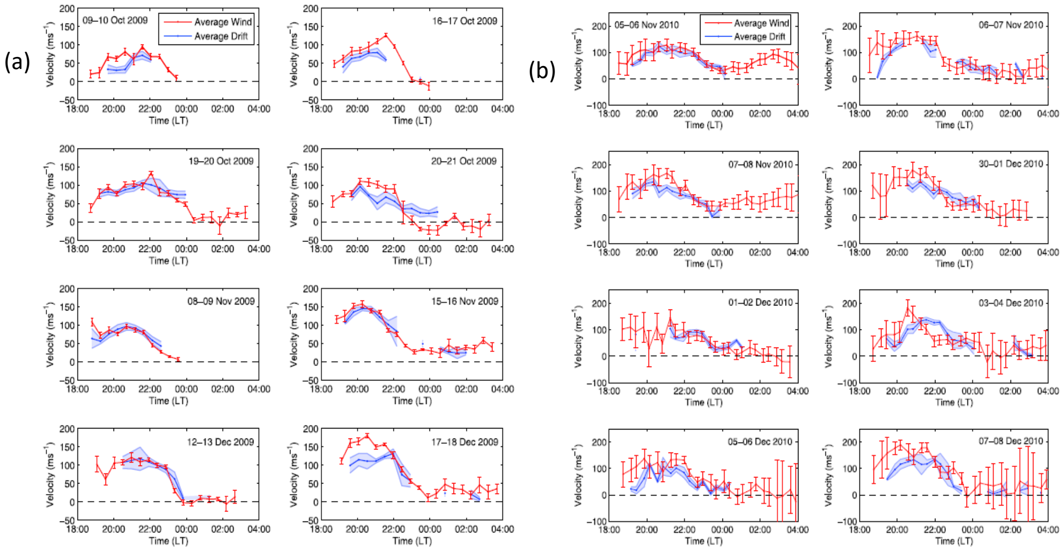

Figure 6.10: (a) the variation of zonal drift of the plasma bubbles and zonal wind are shown over Brazilian sector. (b) Same as (a) but over Peru, South-American sector. (After *Chapagain et al.*, 2012, 2013)

sectors around the globe (*Mendillo and Baumgardner*, 1982; *Martinis et al.*, 2003; *Nade et al.*, 2013). The result shows good agreement with the zonal drift of the plasma measured from incoherent scatter radar over Jicamarca (*Fejer et al.*, 1991), showing no longitudinal differences between these two sectors, whereas, vertical drifts are found to be larger over American longitudes, owing to the smaller magnitude of magnetic field (B) compared to that over Indian longitudes.

Concurrent measurements of neutral wind and zonal drift of EPBs show similar variations between these two as reported in some earlier studies. The measured neutral wind over the Brazilian sector and South-American sector have been observed to be varying in accordance with the drift of the plasma bubbles (*Chapagain et al.*, 2012, 2013). In figure 6.10, the comparison of the zonal wind and the zonal plasma drift is shown for several nights during the period Oct-Dec in the years of 2009 and 2010 (*Chapagain et al.*, 2012). The zonal drifts of the EPBs have been calculated over Cajazeiras (6.9°S, 38.56°W) using the Fabry Perot interferometer, a wide-angle imaging system PICASSO (Portable Ionospheric Camera and Small-Scale Observatory) (*Makela and Miller*, 2008). Using the Doppler shift in the observed OI 630.0 nm emissions obtained from the Fabry-Perot interferometer over two locations Cajazeiras and Cariri (7.11°S, 36.53°W) which are located in the north-eastern region of Brazil the zonal winds have been measured. The zonal winds and zonal movement of the EPBs showed good correlation in the variation as well as in magnitudes. A similar observation from Peru which is located in the South-American sector also showed similar behaviour (*Chapagain et al.*, 2013).

6.4.4 Scale size variation in the observed plasma bubbles structures

So far, we have discussed the dynamics of the plasma depletions observed over two low-latitudinal regions, Mt. Abu and Kolhapur. As discussed, the 100° FOV of the all-sky imager data provides spatial coverage with a range of 300 km radius centred over Kolhapur. We have calculated the zonal scale sizes from the OI 630.0 nm images using the Lomb-Scargle periodogram analysis. Figure 6.11 shows the variation in scale sizes with time for four nights. A contrasting behaviour of zonal scale size has been noticed between the nights when the plasma bubbles are present (03 Feb and 24 Feb 2014) and when they are not (04 Feb and 25 Feb 2014). Figures 6.11a, 6.11b, and 6.11c, 6.11d show the data from two neighbouring nights with such contrasting information. The 99% FAL value for various frequencies has been estimated and it is 0.2 or smaller in terms of the normalized PSD. Therefore, it can be seen from the bottom panels of the Figure 6.11 that the zonal scale sizes of 50 km and greater are significant for all the nights. It can also be noted that for all the nights the scale sizes in the range of 250-300 km are present with larger power in comparison to those of 150-200 km range. On the nights that showed the presence of EPBs, several smaller scale sizes were noticed (Figure 6.11b, 6.11d) which is in stark contrast with the nights that did not show any presence of EPBs (figure 6.11a, 6.11c).

Different scale sizes are significant with varying strengths (as seen in the PSD values) at different times. Therefore, the percentage occurrence and the averaged PSD value of a given range of scale size are obtained for a given night. The estimated scale sizes have been binned in 50 km grids as shown in figure 6.12 with the number of occurrences for a given range of scale size, whereas, the figure 6.13 shows the average PSD value for that particular range of scale size. Suppose for different scale size bins, λ_i (i=1, 2, 3, 4, ...) etc., the number of occurrences found are n_i, the percentage of occurrences in a given scale size bin has been calculated as, $(n_i/\sum n_i)\times 100\%$. Now, for a given scale size bin, λ_i, if the number of occurrences of that bin are n_i and normalized PSD values of each

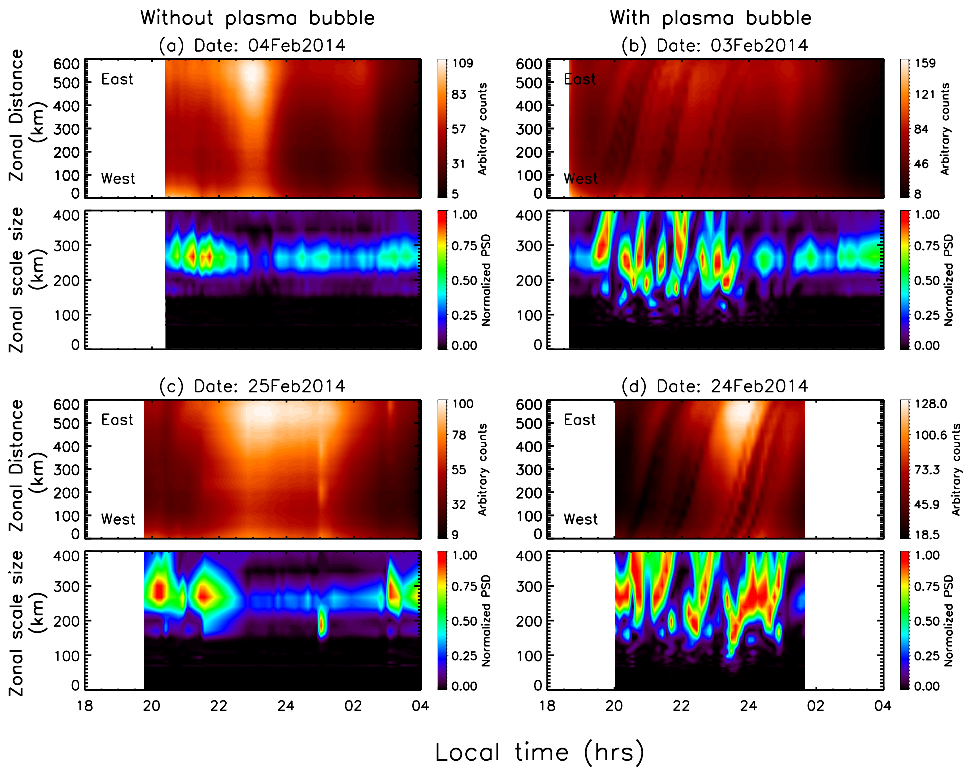

Figure 6.11: The east-west spatial variation and scale sizes are shown in OI 630.0 nm emissions as observed over Kolhapur for four different nights. The values of scale sizes show contrasting behaviour between the nights with the occurrence of EPB and those with the absence of the EPBs.

occurrence are p_k (k=1, 2, ..., n_i), then the average PSD value has been calculated as, $\sum p_k/n_i$ for that given scale size bin. The data corresponding to the nights as shown in Figure 6.11 are depicted in figures 6.12 and 6.13. Scale sizes above the 99% FAL have been considered in this representation. A clear contrast is seen in terms of the percentage occurrences of different scale sizes between those nights with and without the presence of EPBs. The dominant 150-200 km and 250-300 km zonal scale sizes on the nights without EPBs (figures 6.12a, 6.12c) are interpreted to be the typical scale sizes of the gravity waves present in the ionosphere-thermosphere region as these are also present on the nights with the EPB occurrences (figures 6.12b, 6.12d). However, the shorter scale sizes can be seen only on the nights with the EPB occurrence (figures 6.12b, 6.12d). Moreover, not only does the percentage occurrence of shorter scale sizes, but also their average PSD values show an increase during the nights with the occurrence of EPBs (figure 6.13). This clearly shows the significance of shorter scale sizes during the nights with EPB occurrence. This type of contrast in scale sizes is seen for the other nights as well. Thus, the plasma bubble

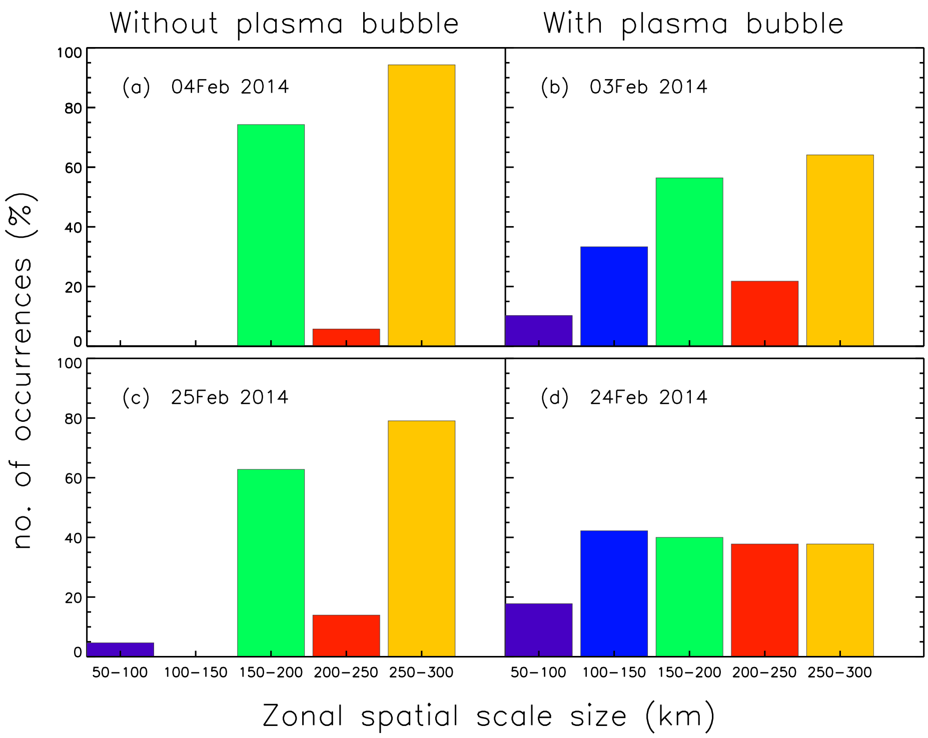

Figure 6.12: The scale sizes are put in 50 km grid which are shown in x-axis. The y-axis depicts the percentage occurrence of a given scale size.

characteristics associated with it, such as the inter-bubble separation(s), bifurcation of bubbles, widths of the bubble, etc., change with time. The contrast in scale sizes as observed between EPB and non-EPB nights provides important information on the state of nighttime ionosphere thermosphere regions during the presence of plasma bubbles. To the best of our knowledge, such characterization in the zonal gravity wave behaviour as obtained from OI 630.0 nm airglow emissions over a large FOV has not been presented in the literature so far.

The gravity waves are one of the potential factors in the seeding of the plasma bubbles that triggers the Rayleigh-Taylor instability as we discussed earlier (e.g., *Kelley et al.*, 1981; *Huang and Kelley*, 1996; *Makela et al.*, 2010). The instability grows non-linearly as it evolves in the higher altitudes. The non-linear simulation also showed that the zonal scale size of the plasma bubbles depends on the zonal scale sizes of the initial perturbation (*Zalesak and Ossakow*, 1980). From the literature reported earlier, the observed inter-bubble spacing shows good correlation with the horizontal gravity wave scale size (*Takahashi et al.*, 2009; *Makela et al.*, 2010; *Das et al.*, 2020). The gravity waves observed in bottomside electron density structure mostly originated in the tropospheric

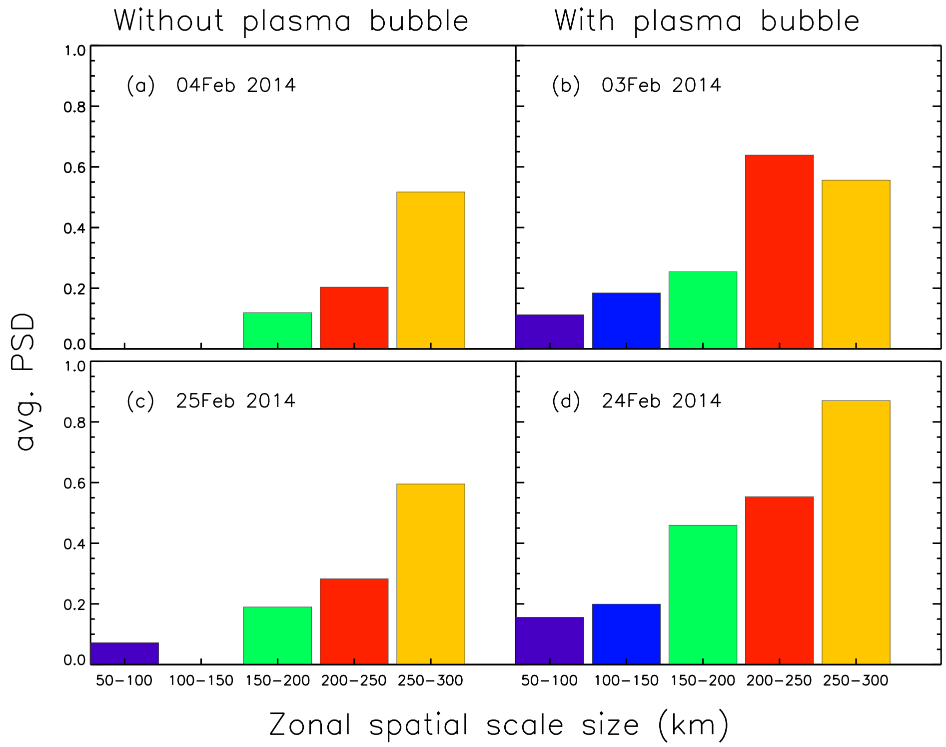

Figure 6.13: The scale sizes are considered in 50 km grids which are shown in x-axis same as figure 6.12. The y-axis depicts the average PSD values of the corresponding scale sizes.

convective sources (*Vadas and Liu*, 2009; *Vadas and Fritts*, 2009; *Vadas and Crowley*, 2010; *Ajith et al.*, 2020). It shows day-to-day variability which reflects in the F-layer density variation as well as the vertical drift of plasma during PRE. The idea of collisional shear instability had been shown to seed large-scale waves (*Hysell and Kudeki*, 2004). The inter-bubble spacing measured from radar data over Gadanki in Indian longitudes has been shown to be following a linear relationship with the horizontal wavelengths of gravity waves as estimated from the collocated data from ionosonde (*Das et al.*, 2020). Figure 6.14 shows the periodic spacing between the consecutive plasma bubbles as seen over Chile, a low-latitude location using the 3-years of data during 2006-2009 (*Makela et al.*, 2010). The plasma bubble spacings for each night have been put in a 100 km wide bin and the average spacing has been found to be lying in the range of 200-300 km. With the support of the ray tracing method as discussed by (*Vadas and Crowley*, 2010), these bubble spacings are argued as evidence of horizontal wavelength of gravity waves, which are mostly secondary gravity waves present at these thermospheric altitudes. The distribution of periodic spacing decreases from 2006 to 2009 due to the transition to a lower solar activity period. As the thermospheric temperature (T_n) decreases, the gravity

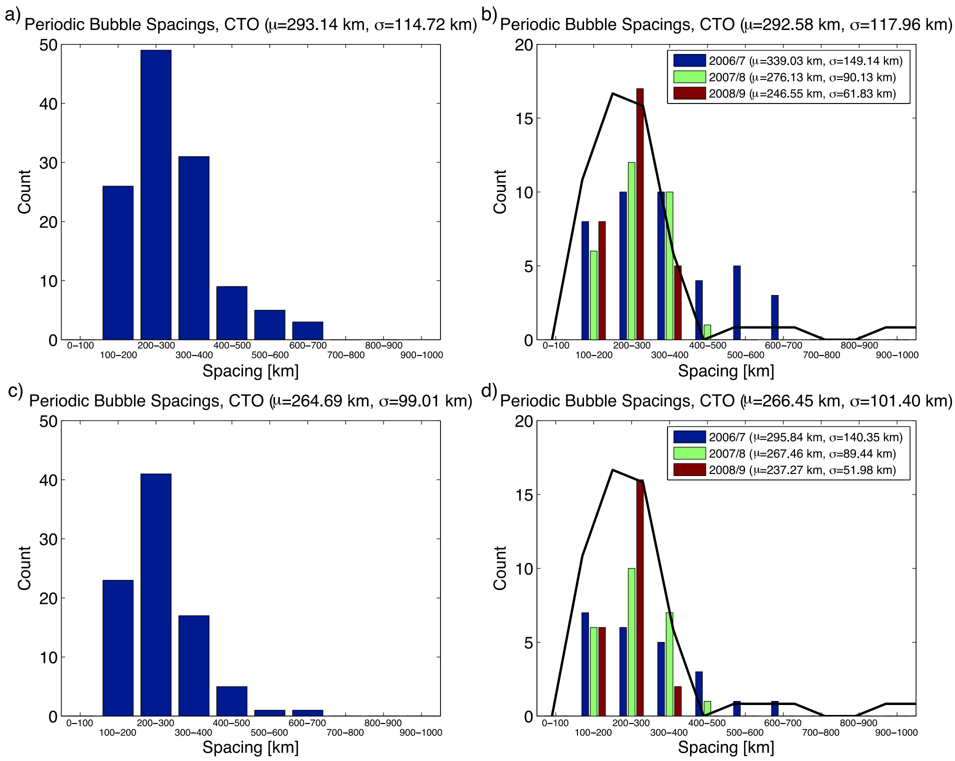

Figure 6.14: (a) The inter-bubble separations are put in histogram plot. The range of data shown here is during the years 2006-2009. (b) The same is plotted when broken out in different years. The dark lines show the distribution of horizontal wavelengths associated with secondary gravity waves as measured by (*Vadas and Crowley*, 2010). The panels c, d are same as panels a, b but considering three or more bubbles when observed. (After *Makela et al.*, 2010)

waves having larger wavelengths with shorter amplitudes appear to be dissipating before reaching to the altitudes where plasma bubbles are seeded. In our study, the 250-300 km scale sizes have been found to be omnipresent irrespective of the presence/absence of plasma bubbles indicating that this scale size of the gravity wave exists at all times in the upper atmosphere. Further, smaller length scales are found to be present during the nights when EPBs were observed. The gravity waves with smaller scale sizes seem to be playing an effective role in the generation of plasma bubbles. These scale sizes on the nights with EPB occurrence also coincide with the inter-bubble distance. Thus, it is postulated that these smaller scale size gravity waves in the zonal direction < 250 km are potential seeds that trigger the occurrence of plasma bubbles.

We have calculated the scale sizes for each of the images that are present at 7-8 minute

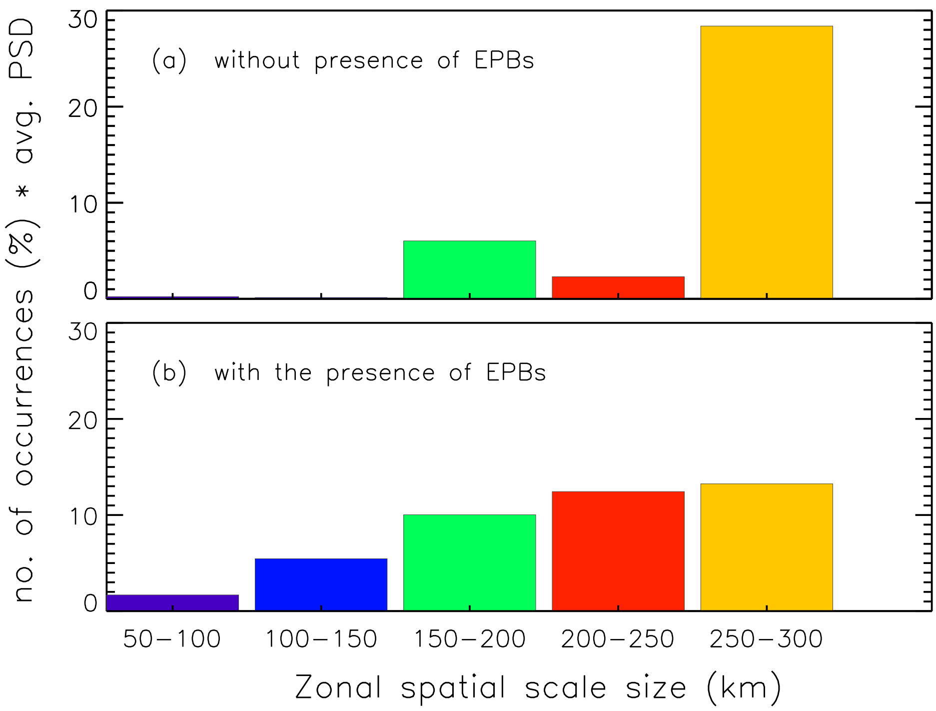

Figure 6.15: The scale sizes which are segregated in 50 km grids are compared between the cases when the bubbles appeared in the image and when they did not. In the y-axis the collective effect of number of occurrence and PSD value for a given scale size has been shown by calculating the product of these two. The top panel includes all the images when the bubbles were not observed and the bottom panel shows the distribution of scale sizes when the plasma bubbles were observed in the images.

cadence. Figure 6.15 shows the distribution of scale sizes between the two categories of the presence of EPBs and absence of EPBs. Therefore, a product of the average PSD value of a given scale size with the percentage of occurrences of that scale size is obtained for a given night to take into account, both, their strength and number of occurrences. This product, in a sense, qualitatively indicates the influence of that scale size on the thermosphere. This product is akin to the intensity of light in optical analogy, wherein the number of photons (n) are multiplied with a given photon of energy hν(I=nhν). Around 1290 images have been analysed for 20 nights among which 688 images showed the presence of plasma bubble signatures ($\sim$ 53%), thereby yields a fair comparison between the zonal gravity wave characteristics in both the categories of existence / absence of EPBs. There is a strong occurrence of 250-300 km scale size during non-EPB images (similar to that seen on 04 and 25 Feb 2014 in figure 6.12), whereas, when the EPBs are present, the power corresponding to zonal scale sizes shorter than 250 km is also seen to be increasing. The power in the 250-300 km scale sizes seems to be redistributed among the shorter scale sizes like 200-250 km, 150-200 km, and 100-150 km. As also stated above, these scale sizes give a fair indication of the inter-bubble spacings. The presence of the small-scale wave-like structure (SSWS) as seen in the inter-bubble depletion is discussed in some earlier reports with some numerical simulation (*Sekar et al.*, 2001) and a case study (*Narayanan et al.*, 2012). As the crests of the gravity waves in the zonal direction are likely to give rise to density depletion as the low-density plasma from lower altitudes is lifted upwards over the equator forming a plasma bubble, as seen in optical all-sky images over Kolhapur, it is proposed that the zonal scale sizes of gravity waves smaller than 250 km are the likely seeds for the plasma bubble generation on a given night (*Saha et al.*, 2022).

6.5 Summary

OI 630.0 nm nighttime airglow emissions have been investigated over Mt. Abu, a low-latitude location. Multiple excursions have been found in the OI 630.0 nm emissions on several nights during the observation period Jan-Mar in the year of 2014. Simultaneous radio observations using ionosonde from a nearby location, Ahmedabad, exhibited spread in the reflected echoes from the F-region exactly at the times when depletions were observed in the nightglow emissions. We have also analysed the OI 630.0 nm emissions obtained using an all-sky imager from Kolhapur, which is situated between the low-latitude and the dip-equatorial locations. The depletions in the OI 630.0 nm nightglow are seen at both the places, Mt. Abu and Kolhapur, in simultaneity. The strength of the PRE was found to be larger on the nights when the depletions in emissions were observed in the OI 630.0 nm emission over Mt. Abu, indicating that the bubbles rose over 1000 km over the magnetic equator on those occasions. The plasma bubbles generated due to Rayleigh-Taylor instability over the magnetic equator move eastwards as the night progresses along with the zonal wind. The zonal speeds of the plasma bubbles estimated from all-sky imager data over Kolhapur have been found to be varying in range from around 190 to 90 ms^{-1} decreasing in magnitudes from post-sunset to midnight. Further, we have also carried out wave number analyses for the emissions in the zonal direction for around 1300 images with nearly equal number of images of occurrence and absence of EPBs. It is found that typically during nighttime the zonal scale sizes are in the range of 150-200 km and 250-300 km (with greater strength in the latter scale-size) on geomagnetic quiet nights without the presence of any plasma bubbles. The zonal scale sizes show contrasting behaviour between the nights with and the occurrence of EPBs. The scale sizes of gravity waves smaller than 250 km have been observed on almost all the times whenever the plasma bubbles were present, which correspond to the inter-bubble separation separation. As the bubble depletions over the magnetic equator most likely occur at the crest region of the gravity wave, the zonal distances between the bubbles, as seen in a location close to the magnetic equator can be assumed to be the zonal scale size of gravity waves over the equator. Therefore, it is proposed that the gravity wave in the zonal direction of scale size smaller than 250 km, if present in the evening, could potentially act as the triggers for the generation of plasma bubbles.

Figure 6.16 shows the schematic how the EPBs, generated over the dip-equator, rise up in higher altitudes and then, mapped over the low-latitudes through the geomagnetic field lines. The inter-bubble separations developed over the dip-equator can also be seen in the zonal scale sizes of the EPBs observed over the low-latitudinal regions.

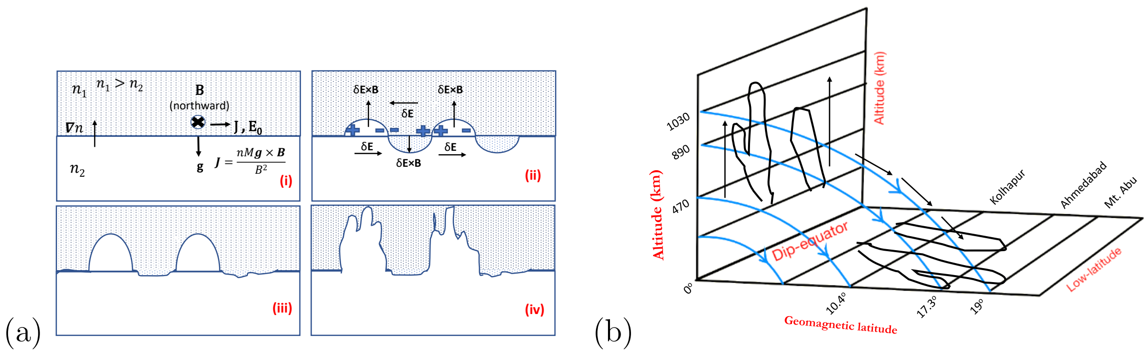

Figure 6.16: Generation of plasma bubbles over the dip-equator is shown in the left-side schematic. Those plasma bubbles are mapped over the off-equatorial and low-latitudes through the geomagnetic field lines as depicted in the right-side schematic.

Chapter 7

Summary and Future scope

7.1 Summary

The ionosphere-thermosphere system (ITS) over the low-latitudes has been investigated in this thesis work. OI 630.0 nm nightglow emissions have been observed from a tropical region which are used as passive remote sensing sources to investigate and understand the processes those are prevalent in the ITS. The equatorial and low-latitudinal region is coupled through various dynamical processes over the upper atmosphere which plays an important role in the distribution of plasma over these regions and as a consequence, the emissions also vary. OI 630.0 nm nightglow emissions originate from an altitudinal region centered at 250 km. These emissions are very sensitive to the changes in the electron density. Therefore, they act as very useful tracers to investigate the upper atmospheric dynamics and infer possible causes for the observed variations in the emissions.

The essential background information about the ITS is given in chapter 1 of the thesis. The neutral and plasma structure of the ITS, their composition, and chemistry have been discussed here. The neutral (thermosphere) and charged particles (ionosphere) co-exist in this region and form a coupled (ionosphere-thermosphere) system. Several phenomena, such as EEJ, EIA, PRE, and ESF play an important role in the redistribution of plasma over the low- and off-equatorial regions over the course of the day and night. Various techniques have been developed over the years to probe this region which are used in both ground- and space-based platforms which are also discussed.

The measurement of OI 630.0 nm nightglow (red line) emissions over Mt. Abu, a low-latitudinal location, has been used as primary dataset in this thesis work. The optical instrument, High Throughput Imaging Echelle Spectrograph (HiTIES), which has been used to measure these red line emissions is discussed in detail. The method used for image processing, extraction of the nightglow emission brightness, angle and intensity calibration have been discussed. Further, the digisonde and magnetometer data of different locations that have been used in this work are summarized. These supplementary data have been used to understand the cause of variabilities seen in the OI 630.0 nm nightglow data. There are discussed in chapter 2.

The mechanisms of the various nightglow emissions, especially the OI 630.0 nm nocturnal airglow are discussed in chapter 3. The measured emissions are compared with the estimated emission which show excellent similarity. The impact of electron density, base and peak height of the F-layer in the red line emissions are discussed. The nightglow emission rates also show variation with the changes in solar activity. Using the long-term database of HiTIES (2013-2017), we have observed such variability in the average nightglow emissions. Apart from that, the OI 630.0 nm nightglow emissions measured over the low-latitudinal regions show large day-to-day variability, but it was found that they all fall into one of the four categories. They are (a) monotonic decrease in brightness after sunset, (b) presence of latitudinal gradients in emissions that vary over the course of the night, (c) presence of post-sunset enhancements in emissions, and (d) multiple excursions in emissions.

We briefly summarize the results of this thesis work which answers the questions put forth in section 1.5 of chapter 1 in view of the understanding of those variabilities seen in the OI 630.0 nm nightglow emissions.

I. The latitudinal movement of the OI 630.0 nm nightglow emissions is observed in both, poleward and equatorward directions. What are the factors/ dynamics associated with such observations in emissions?

Chapter 4 discusses such observations and addresses the possible dynamics associated with this latitudinal movement of the OI 630.0 nm nightglow emissions. It has been found that the airglow emissions along the northern direction as observed from Mt. Abu are larger after sunset time as compared to those along the southern direction on several nights. The gradient in emissions towards north is understood to be dependent on the strengths

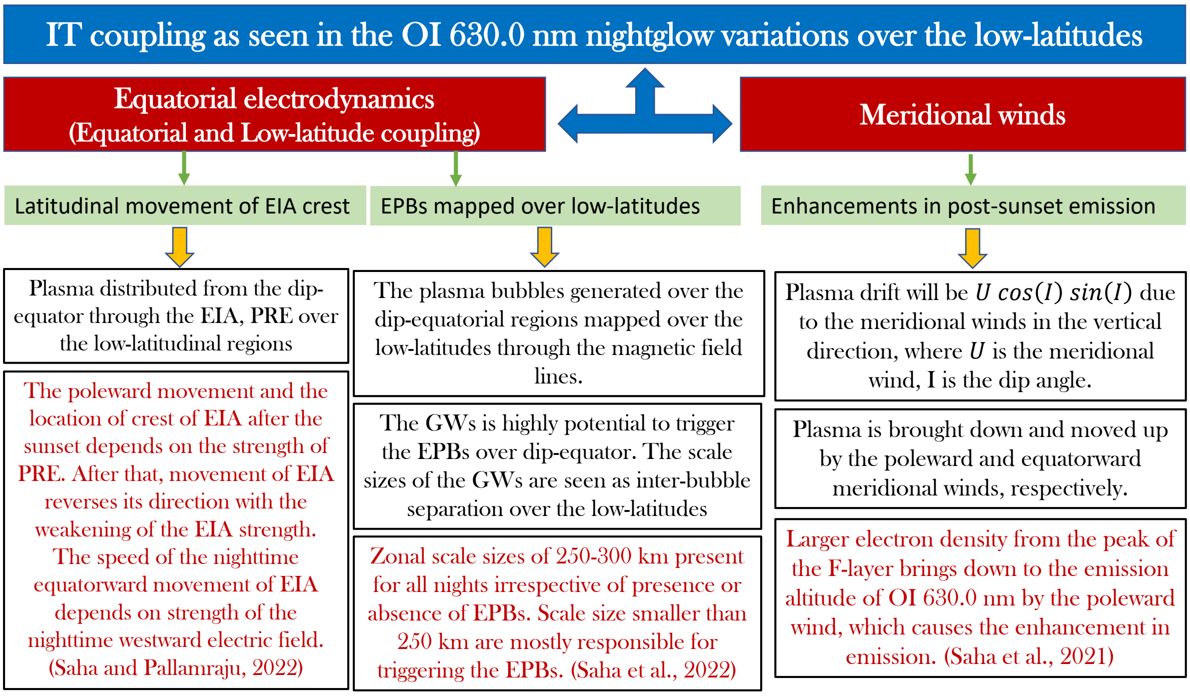

Figure 7.1: The results obtained in this thesis work as discussed in the chapters 4, 5, and 6.

of PRE at sunset time. As the night progresses, the larger emissions move towards the equator, which is known as reversal of EIA. Some earlier studies observed reversal of EIA and calculated the speed of the reversal movement (*Sridharan et al.*, 1993b; *Narayanan et al.*, 2013). In this thesis work, we have studied such reversal of EIA for several nights, calculated the speeds, and found them to be varying in the range of 10-55 ms^{-1}.The nighttime westward electric field is shown to be responsible for such reversal motion of EIA. The present results are particularly interesting as they show the experimental evidence of the global nature of equatorial electric fields during the geomagnetic quiet time periods. We also propose that this equatorward movement of EIA as seen in the nighttime airglow emissions can form a proxy to the westward nocturnal electric field over the equator (*Saha and Pallamraju*, 2022).

II. After sunset, the airglow decreases due to the absence of ionization. But, on several occasions, we have observed enhancement in emission after sunset. What is the reason behind such enhancement in emissions?

Chapter 5 describes in detail such behaviour. The equatorial electrodynamics and the meridional wind variations have been investigated to understand the plausible causes for the observed post-sunset enhancement in the OI 630.0 nm nightglow emissions. There are several reports on the midnight brightness wave and associated midnight temperature maxima. However, there are not many reports on post-sunset enhancement in emission. Based on the conventional understanding, we started investigating the role of PRE in causing such emission enhancements, but a consistent picture did not emerge. Then, the role of other potential parameter, namely, the meridional wind, has been investigated. The meridional winds have been estimated over Ahmedabad using the digisonde data obtained from two locations, Trivandrum and Ahmedabad. It is found that the existence of poleward meridional winds or cessation of the equatorward winds at that time over the low-latitudes can effectively explain the post-sunset enhancement in the observed OI 630.0 nm nightglow emissions (*Saha et al.*, 2021). The poleward winds bring down the plasma to the emission altitude of OI 630.0 nm nightglow emissions from the peak F-layer and as a result emission increases.

III. What are the characteristics of the equatorial plasma bubbles in terms of latitudinal and longitudinal extent, the effect of gravity wave scale sizes in the generation of equatorial plasma bubbles as seen from low-latitudes?

The observation of the equatorial plasma bubbles (EPBs) over the low-latitudinal region and the results of investigation are discussed on chapter 6. On several nights, especially, in the month of February and March of 2014, multiple excursions in OI 630.0 nm nightglow emissions are observed over Mt. Abu. Simultaneous measurements using digisonde and all-sky imager at different locations in the similar longitudinal region confirm the presence of EPBs in the FOV of HiTIES which caused such excursions in emissions observed over the low-latitudes. The zonal speeds of the plasma bubbles have been estimated from all-sky imager data over Kolhapur and which are found to be in the range of 190 to 90 ms^{-1}. Further, we have also carried out wave number spectral analyses for the emissions in the zonal direction using data from around 1300 images with nearly equal number with presence and absence of EPBs. The scale sizes of gravity waves in the range of 250-300 km have been observed to be present on almost all the occasions irrespective of the presence or absence of EPBs. In contrast, the scale sizes of gravity waves smaller than 250 km have been only observed on the occasions when the plasma bubbles were present. Therefore, it is proposed that the gravity wave scale sizes in the zonal direction smaller than 250 km, if present in the evening, could potentially act as the triggers for the generation of plasma bubbles (*Saha et al.*, 2022).

7.2 Future scope

An effort has been made to understand the ionospheric-thermospheric system in this thesis work in connection with the coupling between equatorial and low-latitudinal regions. Several insightful results have been obtained which provide significant advancement in our knowledge and understanding of equatorial electrodynamics, neutral dynamics over the low-latitudinal ITS both in a qualitative and quantitative way. With this new understanding, a significant scope for the future has emerged at the end of this work, which are listed as follows:

i. The nightglow observation carried out from an off-equatorial region (equatorward of Mt. Abu) will provide reversal movement of EIA with larger number of nights irrespective of solar activity conditions which can be useful for the long-term study of EIA reversal phenomena. The measurement using a larger field-of-view can also provide the temporal variation in reversal speeds.

ii. The variation in reversal speeds of the EIA crest is characterized with the nighttime electric field considering into account the daytime EEJ strength at the opposite longitude sector as proxy. Simulation/modeling studies can be carried out using the measured reversal speeds to estimate the nighttime vertical drifts over the equator.

iii. The optical measurements have been obtained from a low-latitudinal location over the Indian longitude from where we have calculated the reversal speeds of the EIA in the nighttime. Ideally, such optical experiments in the South-American sector will enable direct comparison with nighttime westward electric field measured over Jicamarca since the ISR measurements over an equatorial location are only available from Jicamarca.

iv. We have estimated the relative variation of meridional winds using digisonde data. The simultaneous measurement of the neutral winds using FPI will enable to quantify the estimated winds.

v. The relative variation of the meridional winds has been estimated from a given location over the low-latitudinal regions comparing the plasma vertical drift between equatorial and low-latitudinal region measured by digisonde. Using the chain of digisonde data spread over different latitudes at a given longitude sector over the low-latitudinal region can be explored.

vi. The factors which ceases or reverses the direction of equatorward wind after sunset need to be identified.

vii. In this work, the enhancement in emission is investigated during the period of Jan-Mar in the years 2013, 2014, and 2016. Depending on the availability of the digisonde data over the equatorial region, these periods of data were selected. The enhancements in the post-sunset emissions have been observed on the other solstice months during the low solar active periods also. The long-term study of the post-sunset emission enhancement can be carried out in future.

viii. The enhancements in emissions are observed in the OI 630.0 nm nightglow emissions, which originate in the bottomside of the peak F-layer. Simultaneous nightglow observation of the OI 777.4 nm emissions which emanate from the peak F-layer can provide some more insightful information about this post-sunset thermospheric phenomena. The vertical coupling associated with the enhancements in emissions can be understood.

ix. Simultaneous operation of the digisonde and a Fabry-Perot interferometer can provide information on neutral wind and temperature, which along with the vertical phase speeds and scale sizes can be considered as inputs into the gravity wave dispersion relation to estimating the horizontal scale sizes.

x. Spaced-based airglow data obtained from various satellite data, such as SWARM, C/NOFS, DMSP, ICON, GOLD can be used to understand global behaviour of the ionospheric-thermospheric processes in connections with the aspects addressed in this thesis.

References

Aa, E., S. Zou, R. Eastes, D. K. Karan, S.-R. Zhang, P. J. Erickson, and A. J. Coster, Coordinated ground-based and space-based observations of equatorial plasma bubbles, *Journal of Geophysical Research: Space Physics*, *125*, e2019JA027,569, 2020. [Cited on pages 147 and 148.]

Abadi, P., Y. Otsuka, and T. Tsugawa, Effects of pre-reversal enhancement of e× b drift on the latitudinal extension of plasma bubble in southeast asia, *Earth, Planets and Space*, *67*, 1–7, 2015. [Cited on pages xxii, 21, 146, 157, and 158.]

Abalde, J., P. Fagundes, J. Bittencourt, and Y. Sahai, Observations of equatorial f region plasma bubbles using simultaneous oi 777.4 nm and oi 630.0 nm imaging: New results, *Journal of Geophysical Research: Space Physics*, *106*, 30,331–30,336, 2001. [Cited on pages 22 and 148.]

Abalde, J., P. Fagundes, Y. Sahai, V. Pillat, A. Pimenta, and J. Bittencourt, Height-resolved ionospheric drifts at low latitudes from simultaneous oi 777.4 nm and OI 630.0 nm imaging observations, *Journal of Geophysical Research: Space Physics*, *109*, 2004. [Cited on page 22.]

Abdu, M., R. De Medeiros, J. Bittencourt, and I. Batista, Vertical ionization drift velocities and range type spread f in the evening equatorial ionosphere, *Journal of Geophysical Research: Space Physics*, *88*, 399–402, 1983. [Cited on pages 24 and 146.]

Abdu, M., C. Brum, I. Batista, J. Sobral, E. de Paula, and J. Souza, Solar flux effects on equatorial ionization anomaly and total electron content over brazil: Observational results versus iri representations, *Advances in Space Research*, *42*, 617–625, 2008. [Cited on page 31.]

Abdu, M., E. A. Kherani, I. Batista, E. De Paula, D. Fritts, J. Sobral, et al., Gravity wave initiation of equatorial spread f/plasma bubble irregularities based on observational data from the spreadfex campaign, *Ann. Geophys*, *27*, 2607–2622, 2009. [Cited on page 147.]

Abdu, M. A., J. A. Bittencourt, and I. S. Batista, Magnetic declination control of the equatorial F region dynamo electric field development and spread F, *J. Geophys. Res.*, *86*, 11,443–11,446, 1981. [Cited on page 146.]

Abreu, V., G. Schmitt, P. Hays, and T. Dachev, Volume emission rate profiles of the 6300-å tropical nightglow obtained from the ae-e satellite: Latitudinal and seasonal variations, *Journal of Geophysical Research: Space Physics*, *87*, 6346–6352, 1982. [Cited on page 78.]

Abreu, V. J., J.-H. Yee, S. C. Solomon, and A. Dalgarno, The quenching rate of o (1d) by o (3p), *Planetary and space science*, *34*, 1143–1145, 1986. [Cited on page 78.]

Agyei-Yeboah, E., I. Paulino, A. F. Medeiros, R. A. Buriti, A. R. Paulino, P. Essien, S. O. Lomotey, H. Takahashi, and C. M. Wrasse, Seasonal variation of plasma bubbles during solar cycle 23–24 over the brazilian equatorial region, *Advances in Space Research*, *64*, 1365–1374, 2019. [Cited on page 148.]

Ajith, K., G. Li, S. Tulasi Ram, M. Yamamoto, K. Hozumi, P. Abadi, and H. Xie, On the seeding of periodic equatorial plasma bubbles by gravity waves associated with tropical cyclone: A case study, *Journal of Geophysical Research: Space Physics*, *125*, e2020JA028,003, 2020. [Cited on page 167.]

Alken, P., S. Maus, A. Chulliat, P. Vigneron, O. Sirol, and G. Hulot, Swarm equatorial electric field chain: First results, *Geophysical Research Letters*, *42*, 673–680, 2015. [Cited on page 7.]

Amory-Mazaudier, C., O. Bolaji, and V. Doumbia, On the historical origins of the CEJ, DP2, and Ddyn current systems and their roles in the predictions of ionospheric responses to geomagnetic storms at equatorial latitudes, *Journal of Geophysical Research: Space Physics*, *122*, 7827–7833, 2017. [Cited on page 32.]

Anandarao, B. G., Effects of gravity wave winds and wind shears on equatorial electrojet, *Geophys. Res. Lett.*, *3*, 545–548, 1976. [Cited on page 10.]

Anandarao, B. G., and R. Raghavarao, Structural changes in the currents and fields of the equatorial electrojet due to zonal and meridional winds, *J. Geophys. Res.*, *92*, 2514–2526, 1987. [Cited on page 9.]

Anderson, D., A. Anghel, J. Chau, and O. Veliz, Daytime vertical E×B drift velocities inferred from ground-based magnetometer observations at low latitudes, *Space Weather*, *2*, 2004, http://dx.doi.org/10.1029/2004SW000095. [Cited on pages 21 and 32.]

Anderson, D. N., A theoretical study of the ionospheric F region equatorial anomaly—I. Theory, *Planet. Space Sci.*, *21*, 409–419, 1973. [Cited on page 13.]

Appleton, E. V., Two anomalies in the ionosphere, *Nature*, *691*, 2003–2004, 1946. [Cited on page 12.]

Baker, D. J., and A. Stair Jr, Rocket measurements of the altitude distributions of the hydroxyl airglow, *Physica scripta*, *37*, 611, 1988. [Cited on page 76.]

Balan, N., G. J. Bailey, M. A. Abdu, K. I. Oyama, P. G. Richards, J. MacDougall, and I. S. Batista, Equatorial plasma fountain and its effects over three locations: Evidence for an additional layer, the F3 layer, *J. Geophys. Res.*, *102*, 2047–2056, 1997. [Cited on pages 14 and 16.]

Balsley, B., G. Haerendel, and R. Greenwald, Equatorial spread f: Recent observations and a new interpretation, *Journal of Geophysical Research*, *77*, 5625–5628, 1972. [Cited on page 146.]

Barth, C. A., Nitric oxide in the upper atmosphere., *International Assn. of Geomagnetism and Aeronomy*, 1966. [Cited on page 4.]

Barth, C. A., and A. F. Hildebrandt, The 5577 airglow emission mechanism, *J. Geophys. Res.*, *66*, 985–986, 1961. [Cited on page 77.]

Basu, S., and M. Kelley, Review of equatorial scintillation phenomena in light of recent developments in the theory and measurement of equatorial irregularities, *Journal of Atmospheric and Terrestrial Physics*, *39*, 1229–1242, 1977. [Cited on pages 19 and 146.]

Basu, S., S. Basu, J. Huba, J. Krall, S. McDonald, J. Makela, E. Miller, S. Ray, and K. Groves, Day-to-day variability of the equatorial ionization anomaly and scintillations at dusk observed by guvi and modeling by sami3, *Journal of Geophysical Research: Space Physics*, *114*, 2009. [Cited on page 14.]

Bates, D. R., and H. S. W. Massey, The basic reactions in the upper atmosphere. I, *Proceedings of the Royal Society of London. Series A. Mathematical and Physical Sciences*, *187*, 261–296, 1946. [Cited on page 5.]

Bates, D. R., and H. S. W. Massey, The basic reactions in the upper atmosphere II. the theory of recombination in the ionized layers, *Proceedings of the Royal Society of London. Series A. Mathematical and Physical Sciences*, *192*, 1–16, 1947. [Cited on page 5.]

Baumgardner, J. L., B. Flynn, and M. J. Mendillo, Monochromatic imaging instrumentation for applications in aeronomy of the earth and planets, *Optical Engineering*, *32*, 3028–3032, 1993. [Cited on page 53.]

Bilitza, D., D. Altadill, V. Truhlik, V. Shubin, I. Galkin, B. Reinisch, and X. Huang, International reference ionosphere 2016: From ionospheric climate to real-time weather predictions, *Space weather*, *15*, 418–429, 2017. [Cited on pages 64 and 79.]

Biondi, M. A., Electron-ion and ion-ion recombination, *Tech. rep.*, Pittsburgh Univ PA, 1963. [Cited on page 5.]

Biondi, M. A., and D. P. Sipler, Horizontal and vertical winds and temperatures in the equatorial thermosphere: Measurements from Natal, Brazil during August-September, *Planet. Space Sci.*, *33*, 817–823, 1985. [Cited on page 139.]

Bittencourt, J., and M. Abdu, A theoretical comparison between apparent and real vertical ionization drift velocities in the equatorial f region, *Journal of Geophysical Research: Space Physics*, *86*, 2451–2454, 1981. [Cited on pages 29 and 97.]

Booker, H., and H. Wells, Scattering of radio waves by the F-region of the ionosphere, *Terrestrial Magnetism and Atmospheric Electricity*, *43*, 249–256, 1938. [Cited on pages xii, 19, and 20.]

Bretthorst, G., Bayesian spectrum analysis and parameter estimation,'lecture notes in statistics 48, springer-verlag, berlin, 1988. [Cited on page 68.]

Broadfoot, A., and D. Hunten, N_2^+ emission in the twilight, *Planetary and Space Science*, *14*, 1303–1319, 1966. [Cited on page 49.]

Burke, W., L. Gentile, C. Huang, C. Valladares, and S. Su, Longitudinal variability of equatorial plasma bubbles observed by DMSP and ROCSAT-1, *Journal of Geophysical Research: Space Physics*, *109*, 2004. [Cited on page 31.]

Burns, G., The light of the sky, *J. Brit. Astron. Assoc.*, *16*, 308–309, 1906. [Cited on page 25.]

Campbell, W. H., An introduction to quiet daily geomagnetic fields, in *Quiet Daily Geomagnetic Fields*, pp. 315–331, Springer, 1989. [Cited on page 7.]

Chakrabarti, S., Ground based spectroscopic studies of sunlit airglow and aurora, *J. Atmos. Sol. Terr. Phys.*, *60*, 1403 – 1423, 1998. [Cited on page 28.]

Chakrabarti, S., D. Pallamraju, and J. Baumgardner, HiTIES: A High Throughput Imaging Echelle Spectrogragh for ground-based visible airglow and auroral studies, *J. Geophys. Res.*, *106*, 30,337–30,348, 2001. [Cited on pages 26, 27, 39, 44, 50, and 118.]

Chakrabarti, S., O.-P. Jokiaho, J. L. Baumgardner, T. A. Cook, J. Martel, and M. Galand, High-throughput and multislit imaging spectrograph for extended sources, *Optical Engineering*, *51*, 013,003, 2012. [Cited on page 44.]

Chakrabarty, D., M. S. Bagiya, S. V. Thampi, and K. Iyer, Solar EUV flux (0.1-50 nm), F10.7 cm flux, sunspot number and the total electron content in the crest region of equatorial ionization anomaly during the deep minimum between solar cycle 23 and 24, *Indian Journal of Radio and Space Physics*, 2012. [Cited on page 31.]

Chamberlain, J., D. Hunten, and J. Mack, Resonance scattering by atmospheric sodium—IV abundance of sodium in twilight, *Journal of Atmospheric and Terrestrial Physics*, *12*, 153–165, 1958. [Cited on page 76.]

Chamberlain, J. W., *Physics of the Aurora and Airglow*, Academic Press, 1961. [Cited on page 25.]

Chandra, H., and R. Rastogi, Geomagnetic storm effects on ionospheric drifts & the equatorial E_s over the magnetic equator, 1974. [Cited on page 62.]

Chandra, H., and R. RG, Equatorial electrojet studies from rocket and ground measurements, *Earth, planets and space*, *52*, 111–120, 2000. [Cited on page 11.]

Chapagain, N. P., J. J. Makela, J. W. Meriwether, D. J. Fisher, R. A. Buriti, and A. F. Medeiros, Comparison of nighttime zonal neutral winds and equatorial plasma bubble drift velocities over brazil, *Journal of Geophysical Research: Space Physics*, *117*, 2012. [Cited on pages xxii and 163.]

Chapagain, N. P., D. J. Fisher, J. W. Meriwether, J. L. Chau, and J. J. Makela, Comparison of zonal neutral winds with equatorial plasma bubble and plasma drift velocities, *Journal of Geophysical Research: Space Physics*, *118*, 1802–1812, 2013. [Cited on pages xxii, 163, and 164.]

Chapman, S., Bakerian lecture. Some phenomena of the upper atmosphere, *Proc. R. Soc. London. Ser. A*, *132*, 353–374, 1931. [Cited on page 77.]

Chapman, S., Notes on atmospheric sodium., *The Astrophysical Journal*, *90*, 309, 1939. [Cited on pages 76 and 77.]

Chapman, S., The equatorial electrojet as detected from the abnormal electric current distribution above Huancayo, Peru, and elsewhere, *Archiv für Meteorologie, Geophysik und Bioklimatologie, Serie A*, *4*, 368–390, 1951, https://doi.org/10.1007/BF02246814. [Cited on page 9.]

Cogger, L., J. Walker, J. Meriwether Jr, and R. Burnside, F region airglow: Are ground-based observations consistent with recent satellite results?, *Journal of Geophysical Research: Space Physics*, *85*, 3013–3020, 1980. [Cited on page 79.]

Cohen, R., and K. L. Bowles, The association of plane-wave electron density irregularities with the equatorial electrojet, *Journal of Geophysical Research*, *68*, 2503–2525, 1963, http://dx.doi.org/10.1029/JZ068i009p02503. [Cited on page 62.]

Colerico, M., and M. Mendillo, The current state of investigations regarding the thermospheric midnight temperature maximum (mtm), *Journal of atmospheric and solar-terrestrial physics*, *64*, 1361–1369, 2002. [Cited on pages 119 and 141.]

Colerico, M., et al., Coordinated measurements of f region dynamics related to the thermospheric midnight temperature maximum, *Journal of Geophysical Research: Space Physics*, *101*, 26,783–26,793, 1996. [Cited on pages 119, 140, and 141.]

Croom, S., A. Robbins, and J. Thomas, Two anomalies in the behaviour of the F2 layer of the ionosphere, *Nature*, *184*, 2003–2004, 1959. [Cited on page 12.]

Das, S., A. Patra, E. Kherani, P. P. Chaitanya, and K. Niranjan, Relationship between presunset wave structures and interbubble spacing: the seeding perspective of equatorial plasma bubble, *Journal of Geophysical Research: Space Physics*, *125*, e2020JA028,122, 2020. [Cited on pages 146, 147, 166, and 167.]

Das, S., A. Patra, and K. Niranjan, On the assessment of day-to-day occurrence of equatorial plasma bubble, *Journal of Geophysical Research: Space Physics*, *126*, e2021JA029,129, 2021. [Cited on pages 21 and 147.]

Daubechies, I., Orthonormal bases of compactly supported wavelets, *Commun. Pure Appl. Math.*, *41*, 909–996, 1988. [Cited on page 68.]

Davis, T. N., K. Burrows, and J. D. Stolarik, A latitude survey of the equatorial electrojet with rocket-borne magnetometers, *Journal of Geophysical Research*, *72*, 1845–1861, 1967, http://dx.doi.org/10.1029/JZ072i007p01845. [Cited on pages 11 and 31.]

de La Beaujardiere, O., et al., C/NOFS observations of deep plasma depletions at dawn, *Geophysical Research Letters*, *36*, 2009. [Cited on page 31.]

De Medeiros, R., M. Abdu, and I. Batista, Thermospheric meridional wind at low latitude from measurements of f layer peak height, *Journal of Geophysical Research: Space Physics*, *102*, 14,531–14,540, 1997. [Cited on pages 29 and 119.]

Deeming, T. J., Fourier analysis with unequally-spaced data, *Astrophys. Space Sci.*, *36*, 137–158, 1975. [Cited on page 66.]

Drob, D. P., et al., An update to the Horizontal Wind Model (HWM): The quiet time thermosphere, *Earth and Space Science*, *2*, 301–319, 2015. [Cited on pages 64, 100, and 139.]

Dungey, J., Convective diffusion in the equatorial f region, *Journal of Atmospheric and Terrestrial Physics*, *9*, 304–310, 1956. [Cited on page 20.]

Eastes, R., S. Solomon, R. Daniell, D. Anderson, A. Burns, S. England, C. Martinis, and W. McClintock, Global-scale observations of the equatorial ionization anomaly, *Geophysical Research Letters*, *46*, 9318–9326, 2019. [Cited on pages xii, 12, 13, and 28.]

Eastes, R., et al., Initial observations by the GOLD mission, *Journal of Geophysical Research: Space Physics*, *125*, e2020JA027,823, 2020. [Cited on page 28.]

Eastes, R. W., D. K. Karan, C. R. Martinis, R. E. Daniell, Q. Gan, A. G. Burns, and W. E. McClintock, GOLD observations of longitudinal variations in the nighttime equatorial ionization anomaly (EIA) crests latitudes, 2021. [Cited on page 14.]

Eccles, J. V., Modeling investigation of the evening prereversal enhancement of the zonal electric field in the equatorial ionosphere, *Journal of Geophysical Research: Space Physics*, *103*, 26,709–26,719, 1998a. [Cited on page 159.]

Eccles, J. V., A simple model of low-latitude electric fields, *Journal of Geophysical Research: Space Physics*, *103*, 26,699–26,708, 1998b. [Cited on page 159.]

England, S. L., S. Maus, T. J. Immel, and S. B. Mende, Longitudinal variation of the E-region electric fields caused by atmospheric tides, *Geophys. Res. Lett.*, *33*, 2006. [Cited on page 14.]

Englert, C. R., et al., Michelson interferometer for global high-resolution thermospheric imaging (MIGHTI): instrument design and calibration, *Space science reviews*, *212*, 553–584, 2017. [Cited on pages 28 and 31.]

Fagundes, P., Y. Sahai, I. Batista, M. Abdu, J. Bittencourt, and H. Takahashi, Observations of day-to-day variability in precursor signatures to equatorial f-region plasma depletions, in *Annales Geophysicae*, vol. 17, pp. 1053–1063, Copernicus GmbH, 1999. [Cited on page 21.]

Faivre, M., J. Meriwether, C. Fesen, and M. Biondi, Climatology of the midnight temperature maximum phenomenon at Arequipa, Peru, *Journal of Geophysical Research: Space Physics*, *111*, 2006. [Cited on page 27.]

Farley, D., B. Balsey, R. Woodman, and J. McClure, Equatorial spread f: Implications of VHF radar observations, *Journal of Geophysical Research*, *75*, 7199–7216, 1970. [Cited on pages 20 and 146.]

Farley, D., E. Bonelli, B. G. Fejer, and M. Larsen, The prereversal enhancement of the zonal electric field in the equatorial ionosphere, *Journal of Geophysical Research: Space Physics*, *91*, 13,723–13,728, 1986. [Cited on pages xii, 17, and 90.]

Farley, D. T., A theory of electrostatic fields in the ionosphere at nonpolar geomagnetic latitudes, *J. Geophys. Res.*, *65*, 869–877, 1960. [Cited on page 91.]

Fejer, B., D. Farley, R. Woodman, and C. Calderon, Dependence of equatorial f region vertical drifts on season and solar cycle, *Journal of Geophysical Research: Space Physics*, *84*, 5792–5796, 1979. [Cited on page 137.]

Fejer, B., E. Kudeki, and D. Farley, Equatorial f region zonal plasma drifts, *Journal of Geophysical Research: Space Physics*, *90*, 12,249–12,255, 1985. [Cited on page 148.]

Fejer, B. G., The equatorial ionospheric electric fields, A review, *Journal of Atmospheric and Terrestrial Physics*, *43*, 377–386, 1981, https://doi.org/10.1016/0021-9169(81)90101-X. [Cited on pages 17 and 30.]

Fejer, B. G., and M. C. Kelley, Ionospheric irregularities, *Reviews of Geophysics*, *18*, 401–454, 1980, http://dx.doi.org/10.1029/RG018i002p00401. [Cited on pages 19 and 30.]

Fejer, B. G., and L. Scherliess, Empirical models of storm time equatorial zonal electric fields, *J. Geophys. Res.*, *102*, 24,047–24,056, 1997. [Cited on page 17.]

Fejer, B. G., E. R. Paula, S. A. Gonzáez, and R. F. Woodman, Average vertical and zonal F region plasma drifts over Jicamarca, *Journal of Geophysical Research: Space Physics*, *96*, 13,901–13,906, 1991, https://doi.org/10.1029/91JA01171. [Cited on pages xvii, 17, 30, 99, 108, 109, 159, and 163.]

Fejer, B. G., L. Scherliess, and E. De Paula, Effects of the vertical plasma drift velocity on the generation and evolution of equatorial spread F, *Journal of Geophysical Research: Space Physics*, *104*, 19,859–19,869, 1999. [Cited on page 21.]

Fejer, B. G., J. W. Jensen, and S.-Y. Su, Quiet time equatorial F region vertical plasma drift model derived from ROCSAT-1 observations, *Journal of Geophysical Research*, *113*, 2008, http://dx.doi.org/10.1029/2007JA012801. [Cited on pages 17, 99, and 139.]

Fesen, C., Simulations of the low-latitude midnight temperature maximum, *Journal of Geophysical Research: Space Physics*, *101*, 26,863–26,874, 1996. [Cited on page 140.]

Fesen, C., G. Crowley, R. Roble, A. Richmond, and B. G. Fejer, Simulation of the pre-reversal enhancement in the low latitude vertical ion drifts, *Geophysical Research Letters*, *27*, 1851–1854, 2000. [Cited on page 19.]

Forbes, J. M., The equatorial electrojet, *Rev. Geophys.*, *19*, 469–504, 1981. [Cited on page 9.]

Frerichs, R., The singlet system of the oxygen arc spectrum and the origin of the green auroral line, *Physical Review*, *36*, 398, 1930. [Cited on page 25.]

Friis-Christensen, E., H. Lühr, and G. Hulot, Swarm: A constellation to study the Earth's magnetic field, *Earth, planets and space*, *58*, 351–358, 2006. [Cited on page 31.]

Fritts, D., and S. Vadas, Gravity wave penetration into the thermosphere: sensitivity to solar cycle variations and mean winds, in *Annales Geophysicae*, vol. 26, pp. 3841–3861, Copernicus GmbH, 2008. [Cited on page 147.]

Galand, M., J. Baumgardner, D. Pallamraju, S. Chakrabarti, U. Løvhaug, D. Lummerzheim, B. Lanchester, and M. Rees, Spectral imaging of proton aurora and twilight at tromsø, norway, *Journal of Geophysical Research: Space Physics*, *109*, 2004. [Cited on page 44.]

Garcia, F., M. J. Taylor, and M. Kelley, Two-dimensional spectral analysis of mesospheric airglow image data, *Applied optics*, *36*, 7374–7385, 1997. [Cited on page 27.]

Ghodpage, R., A. Taori, P. Patil, S. Gurubaran, S. Sripathi, S. Banola, and A. Sharma, Simultaneous optical measurements of equatorial plasma bubble (EPB) from kolhapur (16.8 N, 74.2 E) and gadanki (13.5 N, 79.2 E), *Journal of Atmospheric and Solar-Terrestrial Physics*, *121*, 196–205, 2014. [Cited on pages 27 and 147.]

Ghodpage, R., P. Patil, O. Gurav, S. Gurubaran, and A. Sharma, Ionospheric response to major storm of 17th March 2015 using multi-instrument data over low latitude station kolhapur (16.8 N, 74.2 E, 10.6 dip. lat.), *Advances in Space Research*, *62*, 624–637, 2018. [Cited on page 159.]

Ghodpage, R., O. Gurav, A. Taori, S. Sau, P. Patil, V. Erram, and S. Sripathi, Observation of an intriguing equatorial plasma bubble event over indian sector, *Journal of Geophysical Research: Space Physics*, *126*, e2020JA028,308, 2021. [Cited on page 159.]

Goel, M., S. Singh, and B. Rao, Postsunset rise of f layer height in the equatorial region and its relation to the f layer dynamo polarization fields, *Journal of Geophysical Research: Space Physics*, *95*, 6237–6246, 1990. [Cited on page 126.]

Gouin, P., Reversal of the magnetic daily variation at Addis Ababa, *Nature*, *193*, 1145–1146, 1962. [Cited on page 11.]

Goupillaud, P., A. Grossmann, and J. Morlet, Cycle-octave and related transforms in seismic signal analysis, *Geoexploration*, *23*, 85–102, 1984. [Cited on page 68.]

Grossmann, A., and J. Morlet, Decomposition of Hardy functions into square integrable wavelets of constant shape, *SIAM J. Math. Anal.*, *15*, 723–736, 1984. [Cited on page 68.]

Gurav, O., V. Narayanan, A. Sharma, R. Ghodpage, H. Gaikwad, and P. Patil, Airglow imaging observations of some evolutionary aspects of equatorial plasma bubbles from indian sector, *Advances in Space Research*, *64*, 385–399, 2019. [Cited on page 159.]

Gurav, O., S. Sripathi, and R. Ghodpage, Radio and optical investigations of storm time evolution of post-midnight equatorial plasma bubbles (EPBs) and their drifts over indian sector, *Advances in Space Research*, *67*, 87–101, 2021. [Cited on page 159.]

Gurubaran, S., The equatorial counter electrojet: Part of a worldwide current system?, *Geophys. Res. Lett.*, *29*, 511–514, 2002. [Cited on page 32.]

Gurubaran, S., and R. Sridharan, Effect of meridional winds and neutral temperatures on the f layer heights over low latitudes, *Journal of Geophysical Research: Space Physics*, *98*, 11,629–11,635, 1993. [Cited on pages xx, 26, 27, 119, and 138.]

Gurubaran, S., R. Sridharan, R. Suhasisni, and K. G. Jani, Variabilities in the thermospheric temperatures in the region of the crest of the equatorial ionization anomaly - A case study, *J. Atmos. Sol. Terr. Phys.*, *57*, 695–703, 1995. [Cited on page 26.]

Hanson, W. B., and R. J. Moffett, Ionization transport effects in the equatorial F region, *J. Geophys. Res.*, *71*, 5559–5572, 1966. [Cited on page 13.]

Hargreaves, J. K., *The Solar-Terrestrial Environment*, Cambridge University Press, 1992. [Cited on pages xi, 2, and 4.]

Hari, S., and B. K. Murthy, Seasonal variations of equatorial night-time thermospheric meridional winds, *Journal of Atmospheric and Terrestrial Physics*, *57*, 1241–1246, 1995. [Cited on page 29.]

Harper, R., Nighttime meridional neutral winds near 350 km at low to mid-latitudes, *Journal of Atmospheric and Terrestrial Physics*, *35*, 2023–2034, 1973. [Cited on page 139.]

Hays, P. B., G. Carignan, B. C. Kennedy, G. G. Shepherd, and J. C. G. Walker, The visible-airglow experiment on Atmosphere Explorer, *Radio Science*, *8*, 369–377, 1973. [Cited on page 28.]

Hays, P. B., D. W. Rusch, R. G. Roble, and J. C. G. Walker, The O-I (6300 $\AA$) airglow, *Rev. Geophys.*, *16*, 225–232, 1978. [Cited on page 31.]

Hecht, J., S. Kovalam, P. May, G. Mills, R. Vincent, R. Walterscheid, and J. Woithe, Airglow imager observations of atmospheric gravity waves at alice springs and adelaide, australia during the darwin area wave experiment (dawex), *Journal of Geophysical Research: Atmospheres*, *109*, 2004. [Cited on page 27.]

Hedin, A. E., and H. G. Mayr, Magnetic control of the near equatorial neutral thermosphere, *J. Geophys. Res.*, *78*, 1688–1691, 1973. [Cited on pages xii and 14.]

Heelis, R., and A. Maute, Challenges to understanding the earth's ionosphere and thermosphere, *Journal of Geophysical Research: Space Physics*, *125*, e2019JA027,497, 2020. [Cited on page 15.]

Heelis, R. A., P. C. Kendall, R. J. Moffett, D. W. Windle, and H. Rishbeth, Electrical coupling of the E- and F-regions and its effect on F-region drifts and winds, *Planet. Space Sci.*, *22*, 743–756, 1974. [Cited on page 17.]

Henderson, S., C. Swenson, A. Christensen, and L. Paxton, Morphology of the equatorial anomaly and equatorial plasma bubbles using image subspace analysis of global ultraviolet imager data, *Journal of Geophysical Research: Space Physics*, *110*, 2005a. [Cited on page 28.]

Henderson, S., C. Swenson, J. Gunther, A. Christensen, and L. Paxton, Method for characterization of the equatorial anomaly using image subspace analysis of global ultraviolet imager data, *Journal of Geophysical Research: Space Physics*, *110*, 2005b. [Cited on page 28.]

Herrero, F., and N. Spencer, On the horizontal distribution of the equatorial thermospheric midnight temperature maximum and its seasonal variation, *Geophysical Research Letters*, *9*, 1179–1182, 1982. [Cited on page 140.]

Herrero, F., H. Mayr, and N. Spencer, Latitudinal (seasonal) variations in the thermospheric midnight temperature maximum: A tidal analysis, *Journal of Geophysical Research: Space Physics*, *88*, 7225–7235, 1983. [Cited on page 140.]

Holt, J., D. Rhoda, D. Tetenbaum, and A. Van Eyken, Optimal analysis of incoherent scatter radar data, *Radio science*, *27*, 435–447, 1992. [Cited on page 30.]

Horne, J. H., and S. L. Baliunas, A prescription for period analysis of unevenly sampled time series, *Astrophys. J.*, *302*, 757–763, 1986. [Cited on pages 67 and 68.]

Huang, C.-S., and M. C. Kelley, Nonlinear evolution of equatorial spread f: 2. gravity wave seeding of rayleigh-taylor instability, *Journal of Geophysical Research: Space Physics*, *101*, 293–302, 1996. [Cited on pages 147 and 166.]

Huang, C.-S., and P. A. Roddy, Effects of solar and geomagnetic activities on the zonal drift of equatorial plasma bubbles, *Journal of Geophysical Research: Space Physics*, *121*, 628–637, 2016. [Cited on pages 24 and 146.]

Huang, C.-S., O. de La Beaujardiere, P. Roddy, D. Hunton, J. Ballenthin, and M. Hairston, Long-lasting daytime equatorial plasma bubbles observed by the c/nofs satellite, *Journal of Geophysical Research: Space Physics*, *118*, 2398–2408, 2013. [Cited on pages 24, 31, and 146.]

Hysell, D., and J. Burcham, Ionospheric electric field estimates from radar observations of the equatorial electrojet, *Journal of Geophysical Research: Space Physics*, *105*, 2443–2460, 2000. [Cited on pages 90, 95, and 112.]

Hysell, D., and E. Kudeki, Collisional shear instability in the equatorial f region ionosphere, *Journal of Geophysical Research: Space Physics*, *109*, 2004. [Cited on page 167.]

Hysell, D., M. Kelley, W. Swartz, and R. Woodman, Seeding and layering of equatorial spread f by gravity waves, *Journal of Geophysical Research: Space Physics*, *95*, 17,253–17,260, 1990. [Cited on page 147.]

Hysell, D., R. Jafari, D. Fritts, and B. Laughman, Gravity wave effects on postsunset equatorial f region stability, *Journal of Geophysical Research: Space Physics*, *119*, 5847–5860, 2014. [Cited on page 147.]

Immel, T. J., E. Sagawa, S. L. England, S. B. Henderson, M. E. Hagan, S. B. Mende, H. U. Frey, C. M. Swenson, and L. J. Paxton, Control of equatorial ionospheric morphology by atmospheric tides, *Geophys. Res. Lett.*, *33*, 2006. [Cited on pages 12, 14, and 28.]

Immel, T. J., et al., The ionospheric connection explorer mission: Mission goals and design, *Space Science Reviews*, *214*, 1–36, 2018. [Cited on page 31.]

Ivers, D., R. Stening, J. Turner, and D. Winch, Equatorial electrojet from ørsted scalar magnetic field observations, *Journal of Geophysical Research: Space Physics*, *108*, 2003. [Cited on page 32.]

Jadhav, G., M. Rajaram, and R. Rajaram, A detailed study of equatorial electrojet phenomenon using ørsted satellite observations, *Journal of Geophysical Research: Space Physics*, *107*, SIA–12, 2002. [Cited on page 7.]

Jin, S., E. Cardellach, and F. Xie, *GNSS remote sensing*, vol. 16, Springer, 2014. [Cited on page 31.]

Jones, A. V., and A. Harrison, Rotational temperatures of the auroral N_2^+ bands, *Journal of Atmospheric and Terrestrial Physics*, *6*, 336–343, 1955. [Cited on page 25.]

Jyoti, N., C. Devasia, R. Sridharan, and D. Tiwari, Threshold height $(h'f)_c$ for the meridional wind to play a deterministic role in the bottom side equatorial spread f and its dependence on solar activity, *Geophysical research letters*, *31*, 2004. [Cited on page 146.]

Karan, D. K., and D. Pallamraju, Small-scale longitudinal variations in the daytime equatorial thermospheric wave dynamics as inferred from oxygen dayglow emissions, *J. Geophys. Res.*, pp. 6528–6542, 2017. [Cited on pages 28 and 118.]

Karan, D. K., and D. Pallamraju, Effect of geomagnetic storms on the daytime low-latitude thermospheric wave dynamics, *Journal of Atmospheric and Solar-Terrestrial Physics*, *170*, 35–47, 2018. [Cited on page 119.]

Karan, D. K., D. Pallamraju, K. A. Phadke, T. Vijayalakshmi, T. K. Pant, and S. Mukherjee, Electrodynamic influence on the diurnal behaviour of neutral daytime airglow emissions, *Ann. Geophys.*, *34*, 1019–1030, 2016. [Cited on pages 28, 90, 118, and 124.]

Karan, D. K., R. E. Daniell, S. L. England, C. R. Martinis, R. W. Eastes, A. G. Burns, and W. E. McClintock, First zonal drift velocity measurement of equatorial plasma bubbles (EPBs) from a geostationary orbit using gold data, *Journal of Geophysical Research: Space Physics*, *125*, e2020JA028,173, 2020. [Cited on pages 28 and 148.]

Kelley, M., Equatorial spread-f: recent results and outstanding problems, *Journal of atmospheric and terrestrial physics*, *47*, 745–752, 1985. [Cited on page 146.]

Kelley, M., M. Larsen, C. LaHoz, and J. McClure, Gravity wave initiation of equatorial spread f: A case study, *Journal of Geophysical Research: Space Physics*, *86*, 9087–9100, 1981. [Cited on pages xii, 20, 30, 147, and 166.]

Kelley, M., M. Nicolls, D. Anderson, A. Anghel, J. Chau, R. Sekar, K. Subbarao, and A. Bhattacharyya, Multi-longitude case studies comparing the interplanetary and equatorial ionospheric electric fields using an empirical model, *Journal of atmospheric and solar-terrestrial physics*, *69*, 1174–1181, 2007. [Cited on pages xviii and 110.]

Kelley, M., et al., The condor equatorial spread f campaign: Overview and results of the large-scale measurements, *Journal of Geophysical Research: Space Physics*, *91*, 5487–5503, 1986. [Cited on page 148.]

Kelley, M. C., *The Earth's Ionosphere: Plasma Physics and Electrodynamics*, vol. 96, Academic press, 2009. [Cited on pages xii and 22.]

Kelley, M. C., and J. McClure, Equatorial spread-f: a review of recent experimental results, *Journal of Atmospheric and Terrestrial Physics*, *43*, 427–435, 1981. [Cited on page 20.]

Kelley, M. C., J. J. Makela, B. M. Ledvina, and P. M. Kintner, Observations of equatorial spread-f from haleakala, hawaii, *Geophysical Research Letters*, *29*, 64–1, 2002. [Cited on pages 21, 147, and 157.]

Kelley, M. C., J. J. Makela, L. J. Paxton, F. Kamalabadi, J. M. Comberiate, and H. Kil, The first coordinated ground-and space-based optical observations of equatorial plasma bubbles, *Geophysical Research Letters*, *30*, 2003. [Cited on page 148.]

Kelley, M. C., J. J. Makela, O. de La Beaujardière, and J. Retterer, Convective ionospheric storms: A review, *Reviews of Geophysics*, *49*, 2011. [Cited on page 19.]

Khadka, S. M., C. E. Valladares, R. Sheehan, and A. J. Gerrard, Effects of electric field and neutral wind on the asymmetry of equatorial ionization anomaly, *Radio Science*, *53*, 683–697, 2018. [Cited on page 13.]

Khomich, V. Y., A. I. Semenov, and N. N. Shefov, *Airglow as an indicator of upper atmospheric structure and dynamics*, Springer Science & Business Media, 2008. [Cited on page 76.]

Kil, H., The morphology of equatorial plasma bubbles-a review, *Journal of Astronomy and Space Sciences*, *32*, 13–19, 2015. [Cited on pages xiii, 23, 24, and 148.]

Kil, H., R. A. Heelis, L. J. Paxton, and S.-J. Oh, Formation of a plasma depletion shell in the equatorial ionosphere, *Journal of Geophysical Research: Space Physics*, *114*, 2009a. [Cited on pages 148 and 159.]

Kil, H., S.-J. Oh, L. J. Paxton, and T.-W. Fang, High-resolution vertical E×B drift model derived from ROCSAT-1 data, *Journal of Geophysical Research: Space Physics*, *114*, 2009b. [Cited on page 21.]

Kil, H., W. K. Lee, and L. J. Paxton, Origin and distribution of daytime electron density irregularities in the low-latitude f region, *Journal of Geophysical Research: Space Physics*, *125*, e2020JA028,343, 2020. [Cited on page 31.]

Klobuchar, J., D. Anderson, and P. Doherty, Model studies of the latitudinal extent of the equatorial anomaly during equinoctial conditions, *Radio Science*, *26*, 1025–1047, 1991. [Cited on page 118.]

Krall, J., J. Huba, G. Joyce, and T. Yokoyama, Density enhancements associated with equatorial spread f, in *Annales Geophysicae*, vol. 28, pp. 327–337, Copernicus GmbH, 2010. [Cited on page 118.]

Krishna Murthy, B., S. Hari, and V. Somayajulu, Nighttime equatorial thermospheric meridional winds from ionospheric h'f data, *Journal of Geophysical Research: Space Physics*, *95*, 4307–4310, 1990. [Cited on pages 29, 119, and 133.]

Kudeki, E., B. G. Fejer, D. Farley, and H. Ierkic, Interferometer studies of equatorial f region irregularities and drifts, *Geophysical Research Letters*, *8*, 377–380, 1981. [Cited on page 148.]

Kudeki, E., A. Akgiray, M. Milla, J. L. Chau, and D. L. Hysell, Equatorial spread-f initiation: Post-sunset vortex, thermospheric winds, gravity waves, *Journal of Atmospheric and Solar-Terrestrial Physics*, *69*, 2416–2427, 2007. [Cited on page 21.]

Kumar, A., D. Chakrabarty, K. Pandey, B. Fejer, S. Sunda, G. Seemala, S. Sripathi, and A. Yadav, Evidence for the significant differences in response times of equatorial ionization anomaly crest corresponding to plasma fountains during daytime and post-sunset hours, *Journal of Geophysical Research: Space Physics*, *126*, e2020JA028,628, 2021. [Cited on pages 27 and 31.]

Kumar, A., D. Chakrabarty, K. Pandey, and A. Yadav, Solar flux dependence of post-sunset enhancement in vertical total electron content over the crest region of equatorial ionization anomaly, *Journal of Geophysical Research: Space Physics*, *127*, e2021JA030,156, 2022a. [Cited on page 31.]

Kumar, S., B. Veenadhari, S. T. Ram, S.-Y. Su, and T. Kikuchi, Possible relationship between the equatorial electrojet (EEJ) and daytime vertical E× B drift velocities in F region from ROCSAT observations, *Advances in Space Research*, *58*, 1168–1176, 2016. [Cited on page 31.]

Kumar, S., D. Pallamraju, P. Suryawanshi, T. Vijayalakshmi, and G. K. Seemala, On the latitudinal variation in OI 630.0 nm dayglow emissions in response to the equatorial electrodynamic processes and neutral winds, *Advances in Space Research*, *69*, 926–938, 2022b. [Cited on pages 95 and 134.]

Lakshmi Narayanan, V., S. Gurubaran, and K. Emperumal, Airglow imaging observations of small-scale structures driven by convective instability in the upper mesosphere over Tirunelveli (8.7^0N), *J. Geophys. Res.*, *115*, 2010. [Cited on pages 27 and 118.]

Laskar, F. I., D. Pallamraju, T. V. Lakshmi, M. A. Reddy, B. M. Pathan, and S. Chakrabarti, Investigations on vertical coupling of atmospheric regions using combined multiwavelength optical dayglow, magnetic, and radio measurements, *J. Geophys. Res.*, *118*, 4618–4627, 2013. [Cited on pages 28 and 118.]

Laskar, F. I., D. Pallamraju, and B. Veenadhari, Vertical coupling of atmospheres: dependence on strength of sudden stratospheric warming and solar activity, *Earth, Planets and Space*, *66*, 94, 2014. [Cited on page 118.]

Laskar, F. I., D. Pallamraju, B. Veenadhari, T. V. Lakshmi, M. A. Reddy, and S. Chakrabarti, Gravity waves in the thermosphere: Solar activity dependence, *Adv. Space Res.*, *55*, 1651 – 1659, 2015. [Cited on pages 28 and 118.]

Le Huy, M., and C. Amory-Mazaudier, Magnetic signature of the ionospheric disturbance dynamo at equatorial latitudes:"ddyn", *Journal of Geophysical Research: Space Physics*, *110*, 2005. [Cited on page 32.]

Lee, C.-C., J.-Y. Liu, B. Reinisch, W.-S. Chen, and F.-D. Chu, The effects of the prereversal exb drift, the eia asymmetry, and magnetic activity on the equatorial spread f during solar maximum, in *Annales Geophysicae*, vol. 23, pp. 745–751, Copernicus GmbH, 2005. [Cited on page 21.]

Lei, J., L. Liu, W. Wan, and S.-R. Zhang, Variations of electron density based on long-term incoherent scatter radar and ionosonde measurements over millstone hill, *Radio science*, *40*, 1–10, 2005. [Cited on page 30.]

Li, G., B. Ning, C. Wang, M. Abdu, Y. Otsuka, M. Yamamoto, J. Wu, and J. Chen, Storm-enhanced development of postsunset equatorial plasma bubbles around the meridian 120°E/ 60°W on 7–8 September 2017, *Journal of Geophysical Research: Space Physics*, *123*, 7985–7998, 2018. [Cited on page 159.]

Lin, C., J. Liu, T. Fang, P. Chang, H. Tsai, C. Chen, and C. Hsiao, Motions of the equatorial ionization anomaly crests imaged by FORMOSAT-3/COSMIC, *Geophysical Research Letters*, *34*, 2007. [Cited on page 13.]

Link, R., and L. Cogger, A reexamination of the OI 6300-Å nightglow, *Journal of Geophysical Research: Space Physics*, *93*, 9883–9892, 1988. [Cited on pages 78 and 79.]

Link, R., J. McConnell, and G. Shepherd, A self-consistent evaluation of the rate constants for the production of the oi 6300 Å airglow, *Planetary and Space Science*, *29*, 589–594, 1981. [Cited on page 78.]

Lomb, N. R., Least-squares frequency analysis of unequally spaced data, *Astrophys. Space Sci.*, *39*, 447–462, 1976. [Cited on pages 67 and 153.]

Luan, X., P. Wang, X. Dou, and Y. C.-M. Liu, Interhemispheric asymmetry of the equatorial ionization anomaly in solstices observed by cosmic during 2007–2012, *Journal of Geophysical Research: Space Physics*, *120*, 3059–3073, 2015. [Cited on page 13.]

Lühr, H., S. Maus, and M. Rother, Noon-time equatorial electrojet: Its spatial features as determined by the champ satellite, *Journal of Geophysical Research: Space Physics*, *109*, 2004. [Cited on pages 31 and 32.]

Makela, J., and M. Kelley, Field-aligned 777.4-nm composite airglow images of equatorial plasma depletions, *Geophysical Research Letters*, *30*, 2003. [Cited on pages 21, 22, and 147.]

Makela, J., and E. Miller, Optical observations of the growth and day-to-day variability of equatorial plasma bubbles, *Journal of Geophysical Research: Space Physics*, *113*, 2008. [Cited on page 163.]

Makela, J., B. Ledvina, M. Kelley, and P. Kintner, Analysis of the seasonal variations of equatorial plasma bubble occurrence observed from haleakala, hawaii, *22*, 3109–3121, 2004. [Cited on pages 27, 146, and 148.]

Makela, J. J., A review of imaging low-latitude ionospheric irregularity processes, *Journal of atmospheric and solar-terrestrial physics*, *68*, 1441–1458, 2006. [Cited on pages 19 and 157.]

Makela, J. J., J. W. Meriwether, J. P. Lima, E. S. Miller, and S. J. Armstrong, The remote equatorial nighttime observatory of ionospheric regions project and the international heliospherical year, *Earth, Moon, and Planets*, *104*, 211–226, 2009. [Cited on page 26.]

Makela, J. J., S. Vadas, R. Muryanto, T. Duly, and G. Crowley, Periodic spacing between consecutive equatorial plasma bubbles, *Geophysical Research Letters*, *37*, 2010. [Cited on pages xxiii, 146, 147, 166, 167, and 168.]

Makela, J. J., J. W. Meriwether, Y. Huang, and P. J. Sherwood, Simulation and analysis of a multi-order imaging Fabry–Perot interferometer for the study of thermospheric winds and temperatures, *Appl. Opt.*, *50*, 4403–4416, 2011. [Cited on page 26.]

Makela, J. J., D. J. Fisher, J. W. Meriwether, R. A. Buriti, and A. F. Medeiros, Near-continual ground-based nighttime observations of thermospheric neutral winds and temperatures over equatorial Brazil from 2009 to 2012, *J. Atmos. Sol. Terr. Phys.*, *103*, 94 – 102, 2013. [Cited on page 27.]

Makela, J. J., et al., Validation of icon-mighti thermospheric wind observations: 1. nighttime red-line ground-based fabry-perot interferometers, *Journal of Geophysical Research: Space Physics*, *126*, e2020JA028,726, 2021. [Cited on page 28.]

Mallat, S. G., A theory for multiresolution signal decomposition: the wavelet representation, *IEEE Trans. Pattern Anal. Mach. Intell.*, *11*, 674–693, 1989. [Cited on page 68.]

Mandal, S., and D. Pallamraju, Thermospheric gravity wave characteristics in the daytime over low-latitudes during geomagnetic quiet and disturbed conditions, *Journal of Atmospheric and Solar-Terrestrial Physics*, *211*, 105,470, 2020. [Cited on pages 29 and 119.]

Mandal, S., D. Pallamraju, and T. K. Pant, Vertical propagation speeds of gravity waves in the daytime as a precursor to the onset of the equatorial spread-f, *Journal of Geophysical Research: Space Physics*, p. e2022JA030401. [Cited on page 147.]

Mandal, S., D. Pallamraju, D. K. Karan, K. A. Phadke, R. P. Singh, and P. Suryawanshi, On deriving gravity wave characteristics in the daytime upper atmosphere using radio technique, *Journal of Geophysical Research: Space Physics*, *124*, 6985–6997, 2019. [Cited on page 29.]

Mandal, S., D. Pallamraju, and P. Suryawanshi, Changes in the daytime thermospheric gravity wave propagation characteristics over low-latitudes in response to the variation in solar flux, *Journal of Atmospheric and Solar-Terrestrial Physics*, *209*, 105,414, 2020. [Cited on page 29.]

Marshall, R. A., S. Smith, J. Baumgardner, and S. Chakrabarti, Continuous ground-based multiwavelength airglow measurements, *J. Geophys. Res.*, *116*, 2011. [Cited on page 44.]

Martinis, C., J. Eccles, J. Baumgardner, J. Manzano, and M. Mendillo, Latitude dependence of zonal plasma drifts obtained from dual-site airglow observations, *Journal of Geophysical Research: Space Physics*, *108*, 2003. [Cited on pages 159 and 163.]

Martinis, C., J. Baumgardner, M. Mendillo, S. Su, and N. Aponte, Brightening of 630.0 nm airglow depletions observed at midlatitudes, *J. Geophys. Res*, *114*, A06,318, 2009. [Cited on page 118.]

Martyn, D., Theory of height and ionization density changes at the maximum of a chapman-like region, taking account of ion production, decay, diffusion and tidal drift, *Physics of the Ionosphere*, p. 254, 1955. [Cited on page 12.]

Maruyama, T., and N. Matuura, Longitudinal variability of annual changes in activity of equatorial spread f and plasma bubbles, *Journal Of Geophysical Research: Space Physics*, *89*, 10,903–10,912, 1984. [Cited on pages 146 and 148.]

Matsushita, S., Sq and l current systems in the ionosphere, *Geophysical Journal International*, *15*, 109–125, 1968. [Cited on page 7.]

Mayr, H. G., I. Harris, and N. W. Spencer, Some properties of upper atmosphere dynamics, *Rev. Geophys.*, *16*, 539–565, 1978. [Cited on page 119.]

Medeiros, A., H. Takahashi, P. Batista, D. Gobbi, and M. J. Taylor, Observations of atmospheric gravity waves using airglow all-sky CCD imager at Cachoeira Paulista (23° S, 45° W), *Geofísica Internacional*, *43*, 29, 2004. [Cited on page 27.]

Meinel, A., et al., Oh emission bands in the spectrum of the night sky. ii., *The Astrophysical Journal*, *112*, 120, 1950. [Cited on page 76.]

Meinel, I., OH emission bands in the spectrum of the night sky. i, *The Astrophysical Journal*, *111*, 555, 1950. [Cited on page 76.]

Mendillo, M., and J. Baumgardner, Airglow characteristics of equatorial plasma depletions, *J. Geophys. Res.*, *87*, 7641, 1982. [Cited on pages 21, 27, 118, 147, 159, and 163.]

Mendillo, M., and A. Tyler, Geometry of depleted plasma regions in the equatorial ionosphere, *Journal of Geophysical Research: Space Physics*, *88*, 5778–5782, 1983. [Cited on pages 21 and 147.]

Mendillo, M., J. Baumgardner, X. Pi, P. J. Sultan, and R. Tsunoda, Onset conditions for equatorial spread f, *Journal of Geophysical Research: Space Physics*, *97*, 13,865–13,876, 1992. [Cited on page 21.]

Mendillo, M., J. Baumgardner, D. Nottingham, J. Aarons, B. Reinisch, J. Scali, and M. Kelley, Investigations of thermospheric-ionospheric dynamics with 6300$\AA$ images from the arecibo observatory, *J. Geophys. Res.*, *102*, 7331–7343, 1997. [Cited on page 159.]

Meriwether, J. W., P. Shih, T. L. Killeen, V. B. Wickwar, and R. G. Roble, Nighttime thermospheric winds over Sondre Stromfjord, Greenland, *Geophys. Res. Lett.*, *11*, 931–934, 1984. [Cited on page 26.]

Meriwether, J. W., J. W. Moody, M. A. Biondi, and R. G. Roble, Optical interferometric measurements of nighttime equatorial thermospheric winds at Arequipa, Peru, *J. Geophys. Res.*, *91*, 5557–5566, 1986. [Cited on pages 26, 27, and 137.]

Meriwether Jr, J. W., A review of the photochemistry of selected nightglow emissions from the mesopause, *Journal of Geophysical Research: Atmospheres*, *94*, 14,629–14,646, 1989. [Cited on page 76.]

Meriwether Jr, J. W., M. A. Biondi, and D. N. Anderson, Equatorial airglow depletions induced by thermospheric winds, *Geophysical research letters*, *12*, 487–490, 1985. [Cited on pages xx, 26, 119, 137, and 139.]

Miller, K., D. Torr, and P. Richards, Meridional winds in the thermosphere derived from measurement of f 2 layer height, *Journal of Geophysical Research: Space Physics*, *91*, 4531–4535, 1986. [Cited on pages 29 and 119.]

Mitra, S., Geomagnetic control of region f 2 of the ionosphere, *Nature*, *158*, 668–669, 1946. [Cited on page 12.]

Morlet, J., G. Arens, E. Fourgeau, and D. Glard, Wave propagation and sampling theory—Part I: Complex signal and scattering in multilayered media, *Geophysics*, *47*, 203–221, 1982. [Cited on page 68.]

Mukherjee, G., Studies of equatorial f-region depletions and dynamics using multiple wavelength nightglow imaging, *Journal of atmospheric and solar-terrestrial physics*, *65*, 379–390, 2003. [Cited on pages 147 and 148.]

Mukherjee, G., L. Carlo, S. Mahajan, and P. Patil, First results of all-sky imaging from india, *Earth, planets and space*, *50*, 119–127, 1998. [Cited on page 58.]

Mukherjee, G., L. Carlo, and S. Mahajan, 630 nm nightglow observations from 17 n latitude, *Earth, planets and space*, *52*, 105–110, 2000. [Cited on page 26.]

Murthy, B. K., and K. S. Gupta, A method for estimation of f-region vertical velocities from nighttime nh profiles, *Journal of Atmospheric and Terrestrial Physics*, *34*, 1155–1159, 1972. [Cited on page 29.]

Nade, D., A. Sharma, S. Nikte, P. Patil, R. Ghodpage, M. Rokade, S. Gurubaran, A. Taori, and Y. Sahai, Zonal velocity of the equatorial plasma bubbles over kolhapur, india, in *Annales Geophysicae*, vol. 31, pp. 2077–2084, Copernicus GmbH, 2013. [Cited on pages 159 and 163.]

Narayanan, R., J. N. Desai, N. K. Modi, R. Raghavarao, and R. Sridharan, Dayglow photometry: a new approach, *Appl. Opt.*, *28*, 2138–2142, 1989. [Cited on page 28.]

Narayanan, V. L., and S. Gurubaran, Statistical characteristics of high frequency gravity waves observed by oh airglow imaging from tirunelveli (8.7 n), *Journal of atmospheric and solar-terrestrial physics*, *92*, 43–50, 2013. [Cited on page 118.]

Narayanan, V. L., S. Gurubaran, and K. Emperumal, Imaging observations of upper mesospheric nightglow emissions from tirunelveli (8.7 o n), *92.60. hw; 92.60. hh; 92.60. hc*, 2009. [Cited on page 58.]

Narayanan, V. L., A. Taori, A. Patra, K. Emperumal, and S. Gurubaran, On the importance of wave-like structures in the occurrence of equatorial plasma bubbles: A case study, *Journal of Geophysical Research: Space Physics*, *117*, 2012. [Cited on pages 147 and 170.]

Narayanan, V. L., S. Gurubaran, K. Emperumal, and P. Patil, A study on the night time equatorward movement of ionization anomaly using thermospheric airglow imaging technique, *Journal of Atmospheric and Solar-Terrestrial Physics*, *103*, 113–120, 2013. [Cited on pages 13, 91, 105, 119, and 175.]

Narcisi, R., and A. Bailey, Mass spectrometric measurements of positive ions at altitudes from 64 to 112 kilometers, *Journal of Geophysical Research*, *70*, 3687–3700, 1965. [Cited on page 4.]

Nicolet, M., Nitrogen oxides in the chemosphere, *Journal of Geophysical Research*, *70*, 679–689, 1965. [Cited on page 4.]

Ossakow, S. L., Spread-f theories—a review, *Journal of Atmospheric and Terrestrial Physics*, *43*, 437–452, 1981. [Cited on page 19.]

Ossakow, S. L., and P. Chaturvedi, Morphological studies of rising equatorial spread f bubbles, *Journal of Geophysical Research: Space Physics*, *83*, 2085–2090, 1978. [Cited on page 21.]

Otsuka, Y., K. Shiokawa, T. Ogawa, and P. Wilkinson, Geomagnetic conjugate observations of equatorial airglow depletions, *Geophysical Research Letters*, *29*, 43–1, 2002. [Cited on pages xii, 22, 23, 27, and 157.]

Otsuka, Y., T. Kadota, K. Shiokawa, T. Ogawa, S. Kawamura, S. Fukao, and S.-R. Zhang, Optical and radio measurements of a 630-nm airglow enhancement over japan on 9 september 1999, *Journal of Geophysical Research: Space Physics*, *108*, 2003. [Cited on pages 119 and 140.]

Pallam Raju, D., R. Sridharan, R. Narayanan, N. K. Modi, R. Raghavarao, and B. H. Subbaraya, Ground-based optical observations of daytime auroral emissions from Antarctica, *J. Atmos. Terr. Phys.*, *57*, 1591–1597, 1995. [Cited on page 28.]

Pallam Raju, D., R. Sridharan, S. Gurubaran, and R. Raghavarao, First results from ground-based daytime optical investigation of the development of the equatorial ionization anomaly, *Ann. Geophys.*, *14*, 238–245, 1996. [Cited on pages 28, 90, and 91.]

Pallamraju, D., Errors in airglow & auroral emission measurements, 2003. [Cited on page 53.]

Pallamraju, D., and S. Chakrabarti, Contributions of imaging Echelle spectrographs to daytime optical aeronomy, *J. Atmos. Sol. Terr. Phys.*, *68*, 1459 – 1471, 2006. [Cited on page 44.]

Pallamraju, D., and R. Sridharan, Ground-based optical measurements of daytime auroral emissions: A new means of investigating space-weather related processes, *Proceedings of the Indian Academy of Sciences - Earth and Planetary Sciences*, *107*, 203–211, 1998a. [Cited on page 28.]

Pallamraju, D., and R. Sridharan, High resolution 2-D maps of OI 630.0 nm thermospheric dayglow from equatorial latitudes, *Ann. Geophys.*, *16*, 997–1006, 1998b. [Cited on page 12.]

Pallamraju, D., J. Baumgardner, and S. Chakrabarti, A multiwavelength investigation of the ring effect in the day sky spectrum, *Geophys. Res. Lett.*, *27*, 1875–1878, 2000. [Cited on page 44.]

Pallamraju, D., J. Baumgardner, S. Chakrabarti, and T. R. Pedersen, Simultaneous ground based observations of an auroral arc in daytime/twilighttime OI 630.0 nm emission and by incoherent scatter radar, *J. Geophys. Res.*, *106*, 5543–5549, 2001. [Cited on pages 28 and 91.]

Pallamraju, D., J. Baumgardner, and S. Chakrabarti, HIRISE: A ground-based high-resolution imaging spectrograph using echelle grating for measuring daytime airglow/auroral emissions, *J. Atmos. Sol. Terr. Phys.*, *64*, 1581–1587, 2002. [Cited on pages 28, 44, and 50.]

Pallamraju, D., U. Das, and S. Chakrabarti, Short- and long-timescale thermospheric variability as observed from OI 630.0 nm dayglow emissions from low latitudes, *J. Geophys. Res.*, *115*, 2010. [Cited on pages 14, 28, 90, and 118.]

Pallamraju, D., F. I. Laskar, R. P. Singh, J. Baumgardner, and S. Chakrabarti, MISE: A multiwavelength imaging spectrograph using echelle grating for daytime optical aeronomy investigations , *J. Atmos. Sol. Terr. Phys.*, *103*, 176 – 183, 2013. [Cited on pages 28 and 44.]

Pallamraju, D., D. K. Karan, and K. A. Phadke, First three dimensional wave characteristics in the daytime upper atmosphere derived from ground-based multiwavelength oxygen dayglow emission measurements, *Geophys. Res. Lett.*, *43*, 5545–5553, 2016. [Cited on pages 28 and 118.]

Pallamraju, D., et al., Daytime wave characteristics in the mesosphere lower thermosphere region: Results from the balloon-borne investigations of regional-atmospheric dynamics experiment, *Journal of Geophysical Research: Space Physics*, *119*, 2229–2242, 2014. [Cited on pages 28 and 118.]

Pandey, K., R. Sekar, B. G. Anandarao, S. P. Gupta, and D. Chakrabarty, Estimation of nighttime dip-equatorial E-region current density using measurements and models, *Journal of Atmospheric and Solar-Terrestrial Physics*, *146*, 160–170, 2016, http://dx.doi.org/10.1016/j.jastp.2016.06.002. [Cited on page 10.]

Parihar, N., and A. Taori, An investigation of long-distance propagation of gravity waves under cawses india phase ii programme, in *Annales Geophysicae*, vol. 33, pp. 547–560, Copernicus GmbH, 2015. [Cited on page 118.]

Parihar, N., S. M. Radicella, B. Nava, Y. O. Migoya-Orue, P. Tiwari, and R. Singh, An investigation of the ionospheric f region near the eia crest in india using oi 777.4 and 630.0 nm nightglow observations, in *Annales Geophysicae*, vol. 36, pp. 809–823, Copernicus GmbH, 2018. [Cited on page 90.]

Parkinson, B. W., and J. J. Spilker, *Progress in astronautics and aeronautics: Global positioning system: Theory and applications*, vol. 164, Aiaa, 1996. [Cited on page 31.]

Patra, A., P. Rao, V. Anandan, and A. Jain, Radar observations of 2.8 m equatorial spread-f irregularities, *Journal of Atmospheric and Solar-Terrestrial Physics*, *59*, 1633–1641, 1997. [Cited on page 30.]

Patra, A., A. Taori, P. Chaitanya, and S. Sripathi, Direct detection of wavelike spatial structure at the bottom of the f region and its role on the formation of equatorial plasma bubble, *Journal of Geophysical Research: Space Physics*, *118*, 1196–1202, 2013. [Cited on page 147.]

Patra, A., P. Srinivasulu, P. P. Chaitanya, M. D. Rao, and A. Jayaraman, First results on low-latitude e and f region irregularities obtained using the gadanki ionospheric radar interferometer, *Journal of Geophysical Research: Space Physics*, *119*, 10–276, 2014. [Cited on pages 30 and 146.]

Patra, A., et al., Simultaneous radar observations of meter-scale f region irregularities at and off the magnetic equator over india, *Journal of Geophysical Research: Space Physics*, *110*, 2005. [Cited on page 30.]

Paxton, L. J., et al., Global ultraviolet imager (guvi): Measuring composition and energy inputs for the nasa thermosphere ionosphere mesosphere energetics and dynamics (timed) mission, in *Optical spectroscopic techniques and instrumentation for atmospheric and space research III*, vol. 3756, pp. 265–276, SPIE, 1999. [Cited on page 31.]

Pedatella, N., J. Forbes, A. Maute, A. Richmond, T.-W. Fang, K. Larson, and G. Millward, Longitudinal variations in the f region ionosphere and the topside ionosphere-plasmasphere: Observations and model simulations, *Journal of Geophysical Research: Space Physics*, *116*, 2011. [Cited on pages xi and 7.]

Pfaff Jr, R. F., M. H. Acuña, P. A. Marionni, and N. B. Trivedi, Dc polarization electric field, current density, and plasma density measurements in the daytime equatorial electrojet, *Geophysical Research Letters*, *24*, 1667–1670, 1997. [Cited on pages 7, 11, and 32.]

Picone, J., A. Hedin, D. P. Drob, and A. Aikin, Nrlmsise-00 empirical model of the atmosphere: Statistical comparisons and scientific issues, *Journal of Geophysical Research: Space Physics*, *107*, SIA–15, 2002. [Cited on pages 64 and 79.]

Pimenta, A., P. R. Fagundes, J. A. Bittencourt, Y. Sahai, D. Gobbi, A. F. d. Medeiros, M. J. Taylor, and H. Takahashi, Ionospheric plasma bubble zonal drift: a methodology using oi 630 nm all-sky imaging systems, *Advances in Space Research*, *27*, 1219–1224, 2001. [Cited on pages xxii, 159, and 160.]

Pimenta, A., P. Fagundes, Y. Sahai, J. Bittencourt, and J. Abalde, Equatorial f-region plasma depletion drifts: latitudinal and seasonal variations, in *Annales Geophysicae*, vol. 21, pp. 2315–2322, Copernicus GmbH, 2003. [Cited on pages 146, 147, and 159.]

Prakash, S., D. Pallamraju, and H. Sinha, Role of the equatorial ionization anomaly in the development of the evening prereversal enhancement of the equatorial zonal electric field, *Journal of Geophysical Research: Space Physics*, *114*, 2009. [Cited on page 157.]

Press, W. H., and G. B. Rybicki, Fast algorithm for spectral analysis of unevenly sampled data, *The astrophysical journal*, *338*, 277–280, 1989. [Cited on page 67.]

Raghavarao, R., and B. G. Anandarao, Vertical winds as a plausible cause for equatorial counter electrojet, *Geophys. Res. Lett.*, *7*, 357–360, 1980. [Cited on page 11.]

Raghavarao, R., P. Sharma, and M. R. Sivaraman, Correlation of ionization anomaly with the intensity of the electrojet, *Space Res.*, *18*, 277–280, 1978. [Cited on pages 14, 90, 95, 96, 112, 118, and 124.]

Raghavarao, R., S. Gupta, R. Sekar, R. Narayanan, J. Desai, R. Sridharan, V. Babu, and V. Sudhakar, In situ measurements of winds, electric fields and electron densities at the onset of equatorial spread-F, *J. Atmos. Terr. Phys.*, *49*, 485 – 492, 1987. [Cited on page 157.]

Raghavarao, R., M. Nageswararao, J. H. Sastri, G. Vyas, and M. Sriramarao, Role of equatorial ionization anomaly in the initiation of equatorial spread f, *Journal of Geophysical Research: Space Physics*, *93*, 5959–5964, 1988a. [Cited on page 157.]

Raghavarao, R., R. Sridharan, J. H. Sastri, V. V. Agashe, B. C. N. Rao, P. B. Rao, and V. V. Somayajulu, *The equatorial ionosphere; WITS handbook. World Ionosphere/Thermosphere Study, vol 1.*, SCOSTEP Secretariat, University of Illinois, Urbana, 1988b. [Cited on pages 14 and 90.]

Raghavarao, R., L. E. Wharton, N. W. Spencer, H. G. Mayr, and L. H. Brace, An equatorial temperature and wind anomaly (ETWA), *Geophys. Res. Lett.*, *18*, 1193–1196, 1991. [Cited on pages xii, 15, 16, 31, and 90.]

Raghavarao, R., W. R. Hoegy, N. W. Spencer, and L. E. Wharton, Neutral temperature anomaly in the equatorial thermosphere- A source of vertical winds, *Geophys. Res. Lett.*, *20*, 1023–1026, 1993. [Cited on page 16.]

Raghavarao, R., R. Suhasini, W. Hoegy, H. Mayr, and L. Wharton, Local time variation of equatorial temperature and zonal wind anomaly (etwa), *Journal of atmospheric and solar-terrestrial physics*, *60*, 631–642, 1998. [Cited on page 16.]

Rajesh, P., J. Liu, H. Sinha, and S. Banerjee, Appearance and extension of airglow depletions, *Journal of Geophysical Research: Space Physics*, *115*, 2010. [Cited on pages 21 and 147.]

Rama Rao, P., S. Gopi Krishna, K. Niranjan, and D. Prasad, Temporal and spatial variations in tec using simultaneous measurements from the indian gps network of receivers during the low solar activity period of 2004-2005, in *Annales Geophysicae*, vol. 24, pp. 3279–3292, Copernicus GmbH, 2006. [Cited on page 31.]

Rao, P., A. Jain, P. Kishore, P. Balamuralidhar, S. Damle, and G. Viswanathan, Indian mst radar 1. system description and sample vector wind measurements in st mode, *Radio Science*, *30*, 1125–1138, 1995. [Cited on page 30.]

Rao, P. R., S. G. Krishna, K. Niranjan, and D. Prasad, Temporal and spatial variations in tec using simultaneous measurements from the indian gps network of receivers during the low solar activity period of 2004-2005, 2006. [Cited on page 13.]

Rao, V., and P. Kulkarni, 6300 Å night airglow enhancements in low latitudes, *Journal of Atmospheric and Terrestrial Physics*, *35*, 193–206, 1973. [Cited on pages 27 and 119.]

Rastogi, R. G., Lunar effects in the counter electrojet near the magnetic equator, *Journal of Atmospheric and Terrestrial Physics*, *36*, 167–170, 1974, http://dx.doi.org/10.1016/0021-9169(74)90074-9. [Cited on page 32.]

Rastogi, R. G., On the criterion of geomagnetic field at the time of disappearance of equatorial Esq layer, *Indian Journal of Radio & Space Physics*, *04*, 1–5, 1975, http://nopr.niscair.res.in/handle/123456789/37649. [Cited on page 11.]

Rastogi, R. G., and H. Chandra, Response of equatorial ionosphere during the super geomagnetic storm of April 2000, *Indian Journal of Radio & Space Physics*, *41*, 524–535, 2012, http://nopr.niscair.res.in/handle/123456789/36904. [Cited on page 32.]

Rastogi, R. G., and K. N. Iyer, Quiet day variation of geomagnetic H-field at low latitudes, *Journal of Geomagnetism and Geoelectricity*, *28*, 461–479, 1976, http://dx.doi.org/10.5636/jgg.28.461. [Cited on pages 32 and 62.]

Rastogi, R. G., and J. A. Klobuchar, Ionospheric electron content within the equatorial F2 layer anomaly belt, *J. Geophys. Res.*, *95*, 19,045–19,052, 1990. [Cited on pages 12, 32, and 91.]

Rastogi, R. G., and A. Patil, Complex structure of equatorial electrojet current, *Current Science*, *55*, 433–436, 1986. [Cited on pages 32 and 62.]

Ratcliffe, J., The microscopic mechanism for the absorption of radio waves in the ionosphere, *Vistas in Astronomy*, *2*, 791–798, 1956. [Cited on page 6.]

Rayleigh, L., The aurora line in the spectrum of the night sky, *Proceedings of the Royal Society of London. Series A, Containing Papers of a Mathematical and Physical Character*, *100*, 367–378, 1922. [Cited on page 25.]

Reinisch, B. W., et al., New digisonde for research and monitoring applications, *Radio Science*, *44*, 2009. [Cited on page 59.]

Richmond, A., Equatorial electrojet—ii. use of the model to study the equatorial ionosphere, *Journal of Atmospheric and Terrestrial Physics*, *35*, 1105–1118, 1973. [Cited on pages xi and 11.]

Rishbeth, H., Thermospheric winds and the F-region: A review, *J. Atmos. Terr. Phys.*, *34*, 1 – 47, 1972. [Cited on page 17.]

Rishbeth, H., Dynamics of the equatorial f-region, *Journal of atmospheric and terrestrial physics*, *39*, 1159–1168, 1977. [Cited on pages xii, xx, 13, 130, and 131.]

Rishbeth, H., The equatorial f-layer: progress and puzzles, in *Annales Geophysicae*, vol. 18, pp. 730–739, Copernicus GmbH, 2000. [Cited on pages 90 and 91.]

Rishbeth, H., and O. K. Garriott, *Introduction to Ionospheric Physics*, Academic Press, 1969. [Cited on page 7.]

Rishbeth, H., A. Lyon, and M. Peart, Diffusion in the equatorial f layer, *Journal of Geophysical Research*, *68*, 2559–2569, 1963. [Cited on pages 12 and 13.]

Roach, F., and J. L. Gordon, The night airglow or nightglow, in *The Light of the Night Sky*, pp. 47–81, Springer, 1973. [Cited on page 48.]

Rodrigues, F., J. Smith, M. Milla, and R. Stoneback, Daytime ionospheric equatorial vertical drifts during the 2008–2009 extreme solar minimum, *Journal of Geophysical Research: Space Physics*, *120*, 1452–1459, 2015. [Cited on page 12.]

Roesler, F., and R. J. Sica, The application of imaging detectors for fabry–perot spectroscopy, *Coupled Energetics and Dynamics of Atmospheric Regions (CEDAR) Volume II: Detailed Facilities Development*, pp. 250–254, 1986. [Cited on page 53.]

Röttger, J., Equatorial spread-f by electric fields and atmospheric gravity waves generated by thunderstorms, *Journal of Atmospheric and Terrestrial Physics*, *43*, 453–462, 1981. [Cited on page 147.]

Rush, C. M., and A. D. Richmond, The relationship between the structure of the equatorial anomaly and the strength of the equatorial electrojet, *J. Atmos. Terr. Physics*, *35*, 1171 – 1180, 1973. [Cited on pages 14 and 95.]

Saha, S., and D. Pallamraju, Latitudinal variations in the nocturnal behaviour of OI 630 nm airglow emissions and their relationship with equatorial electrodynamics, *Journal of Atmospheric and Solar-Terrestrial Physics*, *241*, 105,965, 2022. [Cited on pages 13, 113, and 175.]

Saha, S., D. Pallamraju, T. K. Pant, and S. Chakrabarti, On the cause of the post-sunset nocturnal oi 630 nm airglow enhancement over low-latitude thermosphere, *Journal of Geophysical Research: Space Physics*, *126*, e2021JA029,146, 2021. [Cited on pages 26, 27, 29, 91, 99, 100, 134, and 176.]

Saha, S., D. Pallamraju, and R. N. Ghodpage, Investigations of equatorial plasma bubbles as observed in the OI 630 nm nightglow emissions over off-equatorial and low-latitudinal locations over indian longitudes, *Advances in Space Research*, *70*, 3686–3698, 2022. [Cited on pages 170 and 177.]

Sahai, Y., J. Aarons, M. Mendillo, J. Baumgardner, J. Bittencourt, and H. Takahashi, Oi 630 nm imaging observations of equatorial plasma depletions at 16 s dip latitude, *Journal of Atmospheric and Terrestrial Physics*, *56*, 1461–1475, 1994. [Cited on page 157.]

Sahai, Y., P. Fagundes, and J. Bittencourt, Transequatorial f-region ionospheric plasma bubbles: solar cycle effects, *Journal of Atmospheric and Solar-Terrestrial Physics*, *62*, 1377–1383, 2000. [Cited on page 148.]

Salah, J. E., and J. M. Holt, Midlatitude thermospheric winds from incoherent scatter radar and theory, *Radio Science*, *9*, 301–313, 1974. [Cited on page 119.]

Sampath, S., and T. S. G. Sastry, AC electric fields associated with the plasma instabilities in the equatorial electrojet-III, *Journal of Geomagnetism and Geoelectricity*, *31*, 391–400, 1979, http://doi.org/10.5636/jgg.31.391. [Cited on page 31.]

Sampath, S., and T. S. G. Sastry, Results from in situ measurements of ionospheric currents in the equatorial region-I, *J. Geomag. Goelect.*, *31*, 373–379, 1979. [Cited on pages xi and 11.]

Sastri, J. H., Equatorial anomaly in F-region - A Review, *Indian Journal of Radio & Space Physics*, *19*, 225–240, 1990, http://nopr.niscair.res.in/handle/123456789/36285. [Cited on page 13.]

Sastri, J. H., and H. R. Rao, Optical interferometer measurements of thermospheric temperature at kavalur (12.5 n, 78.5 e), india, *Journal of atmospheric and terrestrial physics*, *56*, 775–782, 1994. [Cited on pages 140 and 141.]

Sastri, J. H., K. Ramesh, and H. R. Rao, Transient composite electric field disturbances near dip equator associated with auroral substorms, *Geophysical research letters*, *19*, 1451–1454, 1992. [Cited on pages xvii and 109.]

Sastri, J. H., H. Ranganath Rao, V. Somayajulu, and H. Chandra, Thermospheric meridional neutral winds associated with equatorial midnight temperature maximum (mtm), *Geophysical research letters*, *21*, 825–828, 1994. [Cited on pages 119 and 141.]

Sastry, T. S. G., Diurnal changes in the parameters of the equatorial electrojet as observed by rocket-borne magnetometers, *Space Research X*, pp. 778–785, 1970. [Cited on page 31.]

Scannapieco, A. J., and S. L. Ossakow, Nonlinear equatorial spread f, *Geophysical Research Letters*, *3*, 451–454, 1976. [Cited on page 21.]

Scargle, J. D., Studies in astronomical time series analysis. II - Statistical aspects of spectral analysis of unevenly spaced data, *Astrophys. J.*, *263*, 835–853, 1982. [Cited on pages 66, 67, and 153.]

Scherliess, L., and B. G. Fejer, Radar and satellite global equatorial f region vertical drift model, *Journal of Geophysical Research: Space Physics*, *104*, 6829–6842, 1999. [Cited on pages xii, 17, 18, 19, 31, and 111.]

Schuster, A., On the investigation of hidden periodicities with application to a supposed 26 day period of meteorological phenomena, *Terrestrial Magnetism*, *3*, 13–41, 1898. [Cited on page 66.]

Sechrist Jr, C., A theory of the winter absorption anomaly at middle latitudes, *Journal of Atmospheric and Terrestrial Physics*, *29*, 113–136, 1967. [Cited on page 4.]

Sekar, R., and M. Kelley, On the combined effects of vertical shear and zonal electric field patterns on nonlinear equatorial spread f evolution, *Journal of Geophysical Research: Space Physics*, *103*, 20,735–20,747, 1998. [Cited on page 147.]

Sekar, R., and R. Raghavarao, Role of vertical winds on the rayleigh-taylor mode instabilities of the night-time equatorial ionosphere, *Journal of atmospheric and terrestrial physics*, *49*, 981–985, 1987. [Cited on page 21.]

Sekar, R., E. Kherani, P. Rao, and A. Patra, Interaction of two long-wavelength modes in the nonlinear numerical simulation model of equatorial spread f, *Journal of Geophysical Research: Space Physics*, *106*, 24,765–24,775, 2001. [Cited on pages 147 and 170.]

Sekar, R., D. Chakrabarty, R. Narayanan, S. Sripathi, A. Patra, and K. Subbarao, Characterization of vhf radar observations associated with equatorial spread f by narrow-band optical measurements, in *Annales Geophysicae*, vol. 22, pp. 3129–3136, Copernicus GmbH, 2004. [Cited on pages 27 and 30.]

Sekar, R., D. Chakrabarty, S. Sarkhel, A. Patra, C. Devasia, and M. Kelley, Identification of active fossil bubbles based on coordinated vhf radar and airglow measurements, in *Annales Geophysicae*, vol. 25, pp. 2099–2102, Copernicus GmbH, 2007. [Cited on pages 27, 30, and 146.]

Sekar, R., D. Chakrabarty, R. Narayanan, and A. Patra, Equatorial spread f structures and associated airglow intensity variations observed over gadanki, in *Annales Geophysicae*, vol. 26, pp. 3863–3873, Copernicus GmbH, 2008. [Cited on pages 19, 30, and 146.]

Sekar, R., D. Chakrabarty, and D. Pallamraju, Optical signature of shear in the zonal plasma flow along with a tilted structure associated with equatorial spread F during a space weather event, *J. Atmos. Sol. Terr. Phys.*, *75–76*, 57 – 63, 2012a. [Cited on page 147.]

Sekar, R., D. Chakrabarty, and D. Pallamraju, Optical signature of shear in the zonal plasma flow along with a tilted structure associated with equatorial spread f during a space weather event, *Journal of atmospheric and solar-terrestrial physics*, *75*, 57–63, 2012b. [Cited on page 148.]

Setty, C., Some studies of bifurcation of the ionospheric f-layer into f1 and f2, *Journal of Atmospheric and Terrestrial Physics*, *19*, 82–87, 1960. [Cited on page 6.]

Sharma, A., D. Nade, S. Nikte, R. Ghodpage, P. Patil, M. Rokade, R. Vhatkar, and S. Gurubaran, Development of fast image analysis technique for all-sky images, 2014. [Cited on pages xiv, 26, 58, and 149.]

Sharma, P., and R. Raghavarao, Simultaneous occurrence of ionization ledge and counterelectrojet in the equatorial ionosphere: observational evidence and its implications, *Can. J. Phys.*, *67*, 166–172, 1989. [Cited on page 13.]

Shepherd, G. G., et al., WINDII, the wind imaging interferometer on the Upper Atmosphere Research Satellite, *J. Geophys. Res.*, *98*, 10,725–10,750, 1993. [Cited on page 28.]

Shepherd, G. G., et al., The Wind Imaging Interferometer (WINDII) on the Upper Atmosphere Research Satellite: A 20 year perspective, *Rev. Geophys.*, *50*, 2012. [Cited on page 28.]

Shinagawa, H., H. Jin, Y. Miyoshi, H. Fujiwara, T. Yokoyama, and Y. Otsuka, Daily and seasonal variations in the linear growth rate of the rayleigh-taylor instability in the ionosphere obtained with gaia, *Progress in Earth and Planetary Science*, *5*, 1–14, 2018. [Cited on page 21.]

Shiokawa, K., Y. Otsuka, T. Ogawa, and P. Wilkinson, Time evolution of high-altitude plasma bubbles imaged at geomagnetic conjugate points, in *Annales Geophysicae*, vol. 22, pp. 3137–3143, Copernicus GmbH, 2004. [Cited on pages xii, 22, 23, 118, and 157.]

Shiokawa, K., Y. Otsuka, and T. Ogawa, Quasiperiodic southward moving waves in 630-nm airglow images in the equatorial thermosphere, *J. Geophys. Res.*, *111*, 2006. [Cited on page 27.]

Shiokawa, K., Y. Otsuka, S. Oyama, S. Nozawa, M. Satoh, Y. Katoh, Y. Hamaguchi, Y. Yamamoto, and J. Meriwether, Development of low-cost sky-scanning fabry-perot interferometers for airglow and auroral studies, *Earth, planets and space*, *64*, 1033–1046, 2012. [Cited on page 26.]

Shiokawa, K., et al., Development of airglow temperature photometers with cooled-ccd detectors, *Earth, planets and space*, *59*, 585–599, 2007. [Cited on page 26.]

Shuman, B. M., Rocket measurement of the equatorial electrojet, *Journal of Geophysical Research*, *75*, 3889–3901, 1970. [Cited on page 31.]

Sibanda, P., and L. McKinnell, Topside ionospheric vertical electron density profile reconstruction using gps and ionosonde data: possibilities for south africa, in *Annales Geophysicae*, vol. 29, pp. 229–236, Copernicus GmbH, 2011. [Cited on page 30.]

Singh, D., S. Gurubaran, and M. He, Evidence for the influence of DE3 tide on the occurrence of equatorial counterelectrojet, *Geophysical Research Letters*, *45*, 2145–2150, 2018. [Cited on pages 11 and 32.]

Singh, R. P., and D. Pallamraju, On the latitudinal distribution of mesospheric temperatures during sudden stratospheric warming events, *J. Geophys. Res.*, *120*, 2926–2939, 2015. [Cited on pages 26, 27, and 118.]

Singh, R. P., and D. Pallamraju, Near infrared imaging spectrograph (NIRIS) for ground-based mesospheric OH (6-2) and O2 (0-1) intensity and temperature measurements, *J. Earth Syst. Sci.*, *126*, 2017. [Cited on pages 26, 27, and 118.]

Sinha, H., P. Rajesh, R. Misra, and N. Dutt, Multi-wavelength imaging observations of plasma depletions over kavalur, india, in *Annales Geophysicae*, vol. 19, pp. 1119–1131, Copernicus GmbH, 2001. [Cited on page 21.]

Sirk, M. M., et al., Design and performance of the icon euv spectrograph, *Space science reviews*, *212*, 631–643, 2017. [Cited on page 31.]

Sivakandan, M., I. Paulino, T. Ramkumar, A. Taori, A. Patra, S. Sripathi, K. Niranjan, and A. Bilibio, Multi-instrument investigation of troposphere-ionosphere coupling and the role of gravity waves in the formation of equatorial plasma bubble, *Journal of Atmospheric and Solar-Terrestrial Physics*, *189*, 65–79, 2019. [Cited on pages 146 and 147.]

Slipher, V., Emissions of the spectrum of the night sky, *Popular Astronomy*, *37*, 327, 1929. [Cited on page 25.]

Sobral, J., M. Abdu, C. Zamlutti, and I. Batista, Association between plasma bubble irregularities and airglow disturbances over brazilian low latitudes, *Geophysical Research Letters*, *7*, 980–982, 1980. [Cited on pages 21 and 27.]

Sobral, J., M. Abdu, H. Takahashi, M. J. Taylor, E. De Paula, C. Zamlutti, M. De Aquino, and G. Borba, Ionospheric plasma bubble climatology over brazil based on 22 years (1977–1998) of 630nm airglow observations, *Journal of Atmospheric and Solar-Terrestrial Physics*, *64*, 1517–1524, 2002. [Cited on page 148.]

Sobral, J. H. A., and M. Abdu, Solar activity effects on equatorial plasma bubble zonal velocity and its latitude gradient as measured by airglow scanning photometers, *Journal of Atmospheric and Terrestrial Physics*, *53*, 729–742, 1991. [Cited on page 148.]

Solomon, S. C., and V. J. Abreu, The 630 nm dayglow, *J. Geophys. Res.*, *94*, 6817–6824, 1989. [Cited on pages 31 and 75.]

Sousasantos, J., M. A. Abdu, A. Santos, I. Batista, A. Silva, and L. E. Loures, Further complexities on the pre-reversal vertical drift modeling over the brazilian region: A comparison between long-term observations and model results, *Journal of Space Weather and Space Climate*, *10*, 20, 2020. [Cited on page 19.]

Spencer, N. W., L. Wharton, H. Niemann, A. Hedin, G. Carignan, and J. Maurer, The Dynamics Explorer wind and the temperature spectrometer, *Space Science Instrumentation*, *5*, 417–428, 1981. [Cited on page 31.]

Sridharan, R., S. Gurubaran, R. Raghavarao, and R. Suhasini, Co-ordinated thermospheric and F-region measurements from low latitudes, *J. Atmos. Terr. Phys.*, *53*, 515–519, 1991. [Cited on pages 26, 27, 119, and 138.]

Sridharan, R., S. A. Haider, S. Gurubaran, R. Sekar, and R. Narayanan, OI 630.0-nm dayglow in the region of equatorial ionization anomaly: Temporal variability and its causative mechanism, *J. Geophys. Res.*, *97*, 13,715–13,721, 1992. [Cited on page 28.]

Sridharan, R., R. Narayanan, N. K. Modi, and D. P. Raju, A Novel mask design for multiwavelength dayglow photometry, *Appl. Opt.*, *32*, 4178–80, 1993a. [Cited on page 28.]

Sridharan, R., R. Sekar, and S. Gurubaran, Two-dimensional high-resolution imaging of the equatorial plasma fountain, *J. Atmos. Terr. Phys.*, *55*, 1661 – 1665, 1993b. [Cited on pages xvii, 12, 13, 90, 91, 102, 103, 105, 118, 119, and 175.]

Sridharan, R., D. P. Raju, R. Raghavarao, and P. V. S. Ramarao, Precursor to equatorial spread-F in OI 630.0 nm dayglow, *Geophys. Res. Lett.*, *21*, 2797–2800, 1994. [Cited on pages 28, 146, and 157.]

Sridharan, R., N. K. Modi, D. P. Raju, R. Narayanan, T. K. Pant, A. Taori, and D. Chakrabarty, A multiwavelength daytime photometer - a new tool for the investigation of atmospheric processes, *Meas. Sci. Technol.*, *9*, 585, 1998. [Cited on page 28.]

Sridharan, R., D. P. Raju, V. Somayajulu, A. Taori, D. Chakrabarty, and R. Raghavarao, Imprint of equatorial electrodynamical processes in the OI 630.0 nm dayglow, *J. Atmos. Sol. Terr. Phys.*, *61*, 1143 – 1155, 1999. [Cited on pages 14, 28, and 95.]

Stolle, C., H. Lühr, M. Rother, and G. Balasis, Magnetic signatures of equatorial spread f as observed by the champ satellite, *Journal of Geophysical Research: Space Physics*, *111*, 2006. [Cited on pages 31 and 32.]

Strutt, R. J., On a night sky of exceptional brightness, and on the distinction between the polar aurora and the night sky, *Proceedings of the Royal Society of London. Series A, Containing Papers of a Mathematical and Physical Character*, *131*, 376–381, 1931. [Cited on page 25.]

Subbarao, K., and B. Murthy, F-region vertical velocity & its fluctuations at the magnetic equator, 1983. [Cited on page 133.]

Sullivan, H., Seasonal variation of the twilight sodium layer, *Journal of Atmospheric and Terrestrial Physics*, *33*, 573–579, 1971. [Cited on page 76.]

Sultan, P., Linear theory and modeling of the rayleigh-taylor instability leading to the occurrence of equatorial spread f, *Journal of Geophysical Research: Space Physics*, *101*, 26,875–26,891, 1996. [Cited on page 21.]

Takahashi, H., M. J. Taylor, J. Sobral, A. Medeiros, D. Gobbi, and D. Santana, Fine structure of the ionospheric plasma bubbles observed by the OI 6300 and 5577 airglow images, *Advances in Space Research*, *27*, 1189–1194, 2001. [Cited on pages 21, 24, and 146.]

Takahashi, H., P. Essien, C. Figueiredo, C. Wrasse, D. Barros, M. Abdu, Y. Otsuka, K. Shiokawa, and G. Li, Multi-instrument study of longitudinal wave structures for plasma bubble seeding in the equatorial ionosphere, *Earth and Planetary Physics*, *5*, 368–377, 2021. [Cited on page 146.]

Takahashi, H., et al., Simultaneous observation of ionospheric plasma bubbles and mesospheric gravity waves during the spreadfex campaign, in *Annales Geophysicae*, vol. 27, p. 1477, European Geosciences Union, 2009. [Cited on pages 147 and 166.]

Taylor, M. J., J. Eccles, J. LaBelle, and J. Sobral, High resolution OI (630 nm) image measurements of f-region depletion drifts during the guará campaign, *Geophysical Research Letters*, *24*, 1699–1702, 1997. [Cited on page 159.]

Taylor, M. J., W. Pendleton, C. Gardner, et al., Comparison of terdiurnal tidal oscillations in mesospheric oh rotational temperature and Na lidar temperature measurements at mid-latitudes for fall/spring conditions, *Earth, planets and space*, *51*, 877–885, 1999. [Cited on page 26.]

Thampi, S. V., M. Yamamoto, R. T. Tsunoda, Y. Otsuka, T. Tsugawa, J. Uemoto, and M. Ishii, First observations of large-scale wave structure and equatorial spread f using certo radio beacon on the c/nofs satellite, *Geophysical Research Letters*, *36*, 2009. [Cited on page 147.]

Tinsley, B., Field aligned airglow observations of transequatorial bubbles in the tropical f-region, *Journal of Atmospheric and Terrestrial Physics*, *44*, 547–557, 1982. [Cited on page 22.]

Tsunoda, R. T., Control of the seasonal and longitudinal occurrence of equatorial scintillations by the longitudinal gradient in integrated e region pedersen conductivity, *J. Geophys. Res.*, *90*, 447–456, 1985. [Cited on pages 146 and 148.]

Tsunoda, R. T., On the enigma of day-to-day variability in equatorial spread f, *Geophysical research letters*, *32*, 2005. [Cited on pages 30 and 147.]

Tsunoda, R. T., and B. R. White, On the generation and growth of equatorial backscatter plumes 1. wave structure in the bottomside f layer, *Journal of Geophysical Research: Space Physics*, *86*, 3610–3616, 1981. [Cited on page 148.]

Tsunoda, R. T., R. C. Livingston, J. McClure, and W. Hanson, Equatorial plasma bubbles: Vertically elongated wedges from the bottomside f layer, *Journal of Geophysical Research: Space Physics*, *87*, 9171–9180, 1982. [Cited on page 148.]

Tsunoda, R. T., D. M. Bubenik, S. V. Thampi, and M. Yamamoto, On large-scale wave structure and equatorial spread f without a post-sunset rise of the f layer, *Geophysical research letters*, *37*, 2010. [Cited on page 147.]

Tsunoda, R. T., S. Saito, and T. T. Nguyen, Post-sunset rise of equatorial f layer—or upwelling growth?, *Progress in Earth and Planetary Science*, *5*, 1–28, 2018. [Cited on page 21.]

Tulasi Ram, S., P. Rama Rao, K. Niranjan, D. Prasad, R. Sridharan, C. Devasia, and S. Ravindran, The role of post-sunset vertical drifts at the equator in predicting the onset of vhf scintillations during high and low sunspot activity years, *24*, 1609–1616, 2006. [Cited on pages 21, 146, and 157.]

Tulasi Ram, S., S.-Y. Su, C. Liu, B. Reinisch, and L.-A. McKinnell, Topside ionospheric effective scale heights (ht) derived with rocsat-1 and ground-based ionosonde observations at equatorial and midlatitude stations, *Journal of Geophysical Research: Space Physics*, *114*, 2009. [Cited on page 30.]

Vadas, S., and D. Fritts, Reconstruction of the gravity wave field from convective plumes via ray tracing, *27*, 147–177, 2009. [Cited on page 167.]

Vadas, S. L., and G. Crowley, Sources of the traveling ionospheric disturbances observed by the ionospheric tiddbit sounder near wallops island on 30 october 2007, *Journal of Geophysical Research: Space Physics*, *115*, 2010. [Cited on pages xxiii, 167, and 168.]

Vadas, S. L., and H.-l. Liu, Generation of large-scale gravity waves and neutral winds in the thermosphere from the dissipation of convectively generated gravity waves, *Journal of Geophysical Research: Space Physics*, *114*, 2009. [Cited on page 167.]

Valladares, C., J. Villalobos, R. Sheehan, and M. Hagan, Latitudinal extension of low-latitude scintillations measured with a network of gps receivers, *22*, 3155–3175, 2004. [Cited on page 157.]

Venkatesh, K., P. Rama Rao, P. Saranya, D. Prasad, and K. Niranjan, Vertical electron density and topside effective scale height (H_T) variations over the indian equatorial and low latitude stations, in *Annales Geophysicae*, vol. 29, pp. 1861–1872, Copernicus GmbH, 2011. [Cited on page 30.]

Venkatesh, K., P. R. Fagundes, D. V. Prasad, C. M. Denardini, A. De Abreu, R. De Jesus, and M. Gende, Day-to-day variability of equatorial electrojet and its role on the day-to-day characteristics of the equatorial ionization anomaly over the indian and brazilian sectors, *Journal of Geophysical Research: Space Physics*, *120*, 9117–9131, 2015. [Cited on page 90.]

Vichare, G., and R. Rajaram, Global features of quiet time counterelectrojet observed by ørsted, *Journal of Geophysical Research: Space Physics*, *116*, 2011. [Cited on pages 7, 11, and 32.]

Vineeth, C., T. K. Pant, C. V. Devasia, and R. Sridharan, Atmosphere-Ionosphere coupling observed over the dip equatorial MLTI region through the quasi 16-day wave, *Geophys. Res. Lett.*, *34*, L12,102, 2007. [Cited on page 118.]

Whalen, J. A., Dependence of equatorial bubbles and bottomside spread f on season, magnetic activity, and e× b drift velocity during solar maximum, *Journal of Geophysical Research: Space Physics*, *107*, SIA–3, 2002. [Cited on page 21.]

Woodman, R. F., and C. La Hoz, Radar observations of f region equatorial irregularities, *Journal of Geophysical Research*, *81*, 5447–5466, 1976. [Cited on pages 30, 90, 146, and 148.]

Woodman, R. F., J. L. Chau, and R. R. Ilma, Comparison of ionosonde and incoherent scatter drift measurements at the magnetic equator, *Geophysical research letters*, *33*, 2006. [Cited on pages 29 and 126.]

Yabuzaki, T., and T. Ogawa, Rocket measurement of sq ionospheric currents over kagoshima, japan, *Journal of Geophysical Research*, *79*, 1999–2001, 1974. [Cited on page 7.]

Yamazaki, Y., and A. Maute, Sq and EEJ—a review on the daily variation of the geomagnetic field caused by ionospheric dynamo currents, *Space Science Reviews*, *206*, 299–405, 2017. [Cited on pages xi and 8.]

Yntema, L., On the brightness of the sky and total amount of starlight, *Publications of the Kapteyn Astronomical Laboratory Groningen*, *22*, 1–55, 1909. [Cited on page 25.]

Yokoyama, T., A review on the numerical simulation of equatorial plasma bubbles toward scintillation evaluation and forecasting, *Progress in Earth and Planetary Science*, *4*, 1–13, 2017. [Cited on page 19.]

Zaka, K., A. Kobea, P. Assamoi, O. Obrou, V. Doumbia, K. Boka, B.-P. Adohi, and N. Mene, Latitudinal profile of the ionospheric disturbance dynamo magnetic signature:

Comparison with the dp2 magnetic disturbance, in *Annales Geophysicae*, vol. 27, pp. 3523–3536, Copernicus GmbH, 2009. [Cited on page 32.]

Zalesak, S., and S. Ossakow, Nonlinear equatorial spread f: Spatially large bubbles resulting from large horizontal scale initial perturbations, *Journal of Geophysical Research: Space Physics*, *85*, 2131–2142, 1980. [Cited on page 166.]

Zalesak, S., S. Ossakow, and P. Chaturvedi, Nonlinear equatorial spread f: The effect of neutral winds and background pedersen conductivity, *Journal of Geophysical Research: Space Physics*, *87*, 151–166, 1982. [Cited on page 147.]

List of Publications

Publications in Journals

1. Saha, S., Pallamraju, D., Pant, T. K., & Chakrabarti, S. (2021). On the cause of the post-sunset nocturnal OI 630 nm airglow enhancement over low-latitude thermosphere. Journal of Geophysical Research: Space Physics, 126, e2021JA029146. https://doi.org/10.1029/2021JA029146.

2. Saha, S., Pallamraju, D., & Ghodpage, R. (2022). Investigations of Equatorial Plasma Bubbles as observed in the OI 630 nm Nightglow Emissions over Off-equatorial and Low-latitudinal Locations over Indian Longitudes. Advances in Space Research, 70, 3686-3698. https://doi.org/10.1016/j.asr.2022.08.023.

3. Saha, S. & Pallamraju, D. (2022). Latitudinal Variations in the Nocturnal behaviour of OI 630 nm Airglow Emissions and Their Relationship with the Equatorial Electrodynamics. Journal of Atmospheric and Solar-Terrestrial Physics, 241, 105965. https://doi.org/10.1016/j.jastp.2022.105965.

4. Pallamraju, D., Suryawanshi, P., Urmalia, S., Kumar, S., Saha, S., Singh, R. P., Kushwaha, P., & Soni, M. (2023). CDAP: A portable CCD-based daytime airglow photometer for investigations of ionosphere-thermosphere phenomena. Journal of Atmospheric and Solar-Terrestrial Physics, 244, 106025. https://doi.org/10.1016/j.jastp.2023.106025.

5. Saha, S. & Pallamraju, D. Nocturnal OI 630.0 nm emission behaviour over low latitudes under varying solar fluxes and changing geomagnetic activity. (Under-preparation)

Presentations at Conferences

1. **Sovan Saha**, Duggirala Pallamraju, and Rupesh N. Ghodpage, "Investigation of Gravity Wave Scale Sizes present in the low-/ equatorial latitude upper atmosphere with and without Plasma Bubbles as seen in the OI 630.0 nm Nightglow Emissions ", American Geophysical Union Fall meeting, Chicago, USA, 12-16 December 2022. [Oral by SS]

2. **Sovan Saha**, and Duggirala Pallamraju, "Latitudinal Movement seen in the OI 630.0 nm Nightglow Emissions in Poleward and Equatorward Directions and their relationship with Equatorial Electrodynamics", American Geophysical Union Fall meeting, Chicago, USA, 12-16 December 2022. [Poster]

3. **Sovan Saha**, and Duggirala Pallamraju, "Effect of Equatorial Electric Fields seen in the Latitudinal Movement of the OI 630 nm Nocturnal Emissions over Indian Longitude", 16^{th} International Symposium on Equatorial Aeronomy (ISEA-16), Kyoto University, Japan, 12-16 September 2022. [Poster]

4. **Sovan Saha**, Duggirala Pallamraju, and Rupesh N. Ghodpage, "Characteristics Gravity Wave Scale Sizes present in the Plasma Bubbles as seen in the OI 630 nm Nightglow Emissions over Low-Latitudes", 16^{th} International Symposium on Equatorial Aeronomy (ISEA-16), Kyoto University, Japan, 12-16 September 2022. [Poster]

5. Duggirala Pallamraju, **Sovan Saha**, Sunil Kumar, "Variations in OI 630 nm Dayglow and Nightglow emissions over low- /equatorial latitudes and their dependence on neutral winds and equatorial electric fields". Presented at 44^{th} scientific assembly COSPAR-2022, Athens, Greece, 16-24 July 2022. [Oral by DP]

6. **Sovan Saha**, Duggirala Pallamraju, and Rupesh N. Ghodpage, "Dynamics and Structure of Plasma bubble observed in the OI 630 nm nightglow emissions over low and off-equatorial latitudes". Presented at the 15^{th} Quadrennial Solar-Terrestrial Physics

(STP-15) symposium, Indian Institute of Geomagnetism, Navi Mumbai, India, 21-25 February 2022. (presented online) [Oral by SS]

7. **Sovan Saha** and Duggirala Pallamraju, "Latitudinal movement of the EIA crest as seen in OI 630 nm nightglow emissions over low-latitudinal region of Indian longitude". Presented at the 15^{th} Quadrennial Solar-Terrestrial Physics (STP-15) symposium, Indian Institute of Geomagnetism, Navi Mumbai, India, 21-25 February 2022. (presented online) [Oral by SS]

8. **Sovan Saha**, Duggirala Pallamraju, and Tarun K. Pant, "OI 630 nm nightglow variability during post-sunset time over low-latitude thermosphere". Presented at the 21^{th} National Space Science Symposium (NSSS-2022), IISER, Kolkata, 31 January - 04 February 2022. (presented online) [Oral by SS]

9. **Sovan Saha** and Duggirala Pallamraju, "Influence of Seasonal and Solar Flux Variations on the Low-latitude OI 630 nm Thermospheric Nightglow". Presented at the Joint Scientific Assembly IAGA-IASPEI-2021, CSIR-NGRI, Hyderabad, 21-27 August 2021. (presented online) [Oral by SS]

10. **Sovan Saha**, Duggirala Pallamraju, and Rupesh N. Ghodpage, "Coupling of the Ionospheric Plasma as investigated using OI 630 nm Emissions from Low- and Off-equatorial Latitude locations in Indian Longitudes". Presented at the Joint Scientific Assembly IAGA-IASPEI-2021, CSIR-NGRI, Hyderabad, 21-27 August 2021. (presented online) [Oral by SS]

11. **Sovan Saha**, Duggirala Pallamraju, and Tarun K. Pant, "On the Cause of Post-sunset Enhancement in OI 630 nm Airglow Emission over Low-latitude Thermosphere". Presented at the Joint Scientific Assembly IAGA-IASPEI-2021, 21-27 August 2021. (presented online) [Oral by SS]

12. **Sovan Saha** and Duggirala Pallamraju, "Investigation of the Variability in OI 630 nm Nightglow Emission over Low-latitude Thermosphere". Presented at the CEDAR workshop-2021, 20-25 June 2021. (presented online) [Poster]

13. Subir Mandal, Duggirala Pallamraju, Deepak Kumar Karan, Ravindra Pratap Singh, Pradip Suryawanshi, and **Sovan Saha**, "Gravity wave characteristics over low-latitude

upper atmospheric region obtained by Digisonde". Presented at 20^{th} National Space Science Symposium (NSSS-2019), Savitribai Phule Pune University, Pune, 29-31 January 2019. [Poster]

14. **Sovan Saha** and Duggirala Pallamraju, "OI 630.0 nm nightglow emission variability from Gurushikhar, Mt. Abu, a region under the crest of equatorial plasma fountain effect". Space and Atmospheric Science (NCSAS-2019), Sanjay Ghodawat University, Kolhapur, 10-11 May 2019. [Poster]

Recognition

Student/ Early career convener in the AGU Fall meeting 2022 of the session SA004-Advances in the Understanding of the Equatorial Ionization Anomaly (EIA) and Ionospheric Irregularities (e.g., Scintillations, Equatorial Plasma Bubbles, Spread-F) Using Measurements and Modeling.

Publications attached with the thesis

1. Saha, S., Pallamraju, D., Pant, T. K., & Chakrabarti, S. (2021). On the cause of the post-sunset nocturnal OI 630 nm airglow enhancement over low-latitude thermosphere. Journal of Geophysical Research: Space Physics, 126, e2021JA029146. https://doi.org/10.1029/2021JA029146.

2. Saha, S., Pallamraju, D., & Ghodpage, R. (2022). Investigations of Equatorial Plasma Bubbles as observed in the OI 630 nm Nightglow Emissions over Off-equatorial and Low-latitudinal Locations over Indian Longitudes. Advances in Space Research, 70, 3686-3698. https://doi.org/10.1016/j.asr.2022.08.023.

3. Saha, S. & Pallamraju, D. (2022). Latitudinal Variations in the Nocturnal behaviour of OI 630 nm Airglow Emissions and Their Relationship with the Equatorial Electrodynamics. Journal of Atmospheric and Solar-Terrestrial Physics, 241, 105965. https://doi.org/10.1016/j.jastp.2022.105965.

Check for updates

AGU ADVANCING EARTH AND SPACE SCIENCE

JGR Space Physics

RESEARCH ARTICLE
10.1029/2021JA029146

On the Cause of the Post-Sunset Nocturnal OI 630 nm Airglow Enhancement Over Low-Latitude Thermosphere

Sovan Saha[1,2], **Duggirala Pallamraju**[1], **Tarun K. Pant**[3], **and Supriya Chakrabarti**[4]

[1]Space and Atmospheric Sciences Division, Physical Research Laboratory, Ahmedabad, India, [2]Indian Institute of Technology, Gandhinagar, India, [3]Space Physics Laboratory, Vikram Sarabhai Space Centre, Thiruvananthapuram, India, [4]University of Massachusetts, Lowell, MA, USA

Key Points:

- Enhancement in OI 630 nm red line emissions observed during the post-sunset time from a low-latitude location
- Column integrated volume emission rate and relative meridional wind variations have been calculated using digisondes at two locations
- Poleward meridional winds play an important role in causing the observed enhancements in the post-sunset OI 630 nm emissions

Correspondence to:

D. Pallamraju,
raju@prl.res.in

Citation:

Saha, S., Pallamraju, D., Pant, T. K., & Chakrabarti, S. (2021). On the cause of the post-sunset nocturnal OI 630 nm airglow enhancement over low-latitude thermosphere. *Journal of Geophysical Research: Space Physics*, *126*, e2021JA029146. https://doi.org/10.1029/2021JA029146

Received 29 JAN 2021
Accepted 17 JUN 2021

Abstract Airglow emissions serve as good tracers of the altitudinal regions at which they originate. OI 630 nm (red line) nocturnal emissions originate from around 250 km altitude. A total of 142 nights of data corresponding to the months of January, February, and March in the years 2013, 2014, and 2016, obtained from Mt. Abu (24.6°N, 72.7°E, 16°N Mag), Gurushikhar, India, a low-latitude location, are investigated. These are compared with the column integrated emission rates calculated using, as inputs, the measured electron density profiles obtained from a digisonde from Ahmedabad (AMD, 23.0°N, 72.6°E, 15°N Mag), India. Following the expected monotonic decrement in the emissions after sunset, an enhancement is observed on several nights that peaks at around 20–21 local time (LT). The cause for this enhancement has been investigated in detail and it is found that the neutral winds, as obtained using digisondes at two locations, show almost a very good correlation between a poleward directed wind or cessation of equatorward wind over AMD and the observed airglow emission enhancement in the post-sunset time. Further, the percentage enhancement in emissions also shows a decrease in magnitudes from January to March which has a broad similarity to the decrease in the model climatological meridional wind magnitudes in the same duration. Based on the data spanning over different years, it is inferred that, during geomagnetic quiet periods, almost all of the nocturnal variability in OI 630 nm emissions is due to the variations in the neutral wind.

Plain Language Summary Some atoms in the Earth's upper atmosphere emit light due to internal processes known as airglow. The processes prevalent at those altitudes can be understood by remotely observing the modulations/variations of this airglow brightness. One such emission at 630 nm, known as redline airglow showed large enhancements in post-sunset time over a low-latitude location. While such redline emission enhancements can, on occasions, possibly occur due to a process at magnetic equator, known as pre-reversal enhancement in electric field, systematic measurements carried out in this study over a three year duration in the months of January to March revealed that the meridional wind at thermospheric altitudes is the dominant cause of such enhancements. This conclusion has been made by measuring the relative variations in winds in the post-sunset times that vary from night-to-night and the climatological model output that shows a broad month-to-month variation. We use the fact that poleward winds bring in electrons, one of the ingredients that produces redline emission, to low-latitudes thereby causing these emission enhancements.

1. Introduction

Neutral species and charged particles co-exist in the Earth's upper atmosphere, that is, the thermosphere and ionosphere. The thermospheric-ionospheric system is tightly coupled and shows intriguing behavior. Optical emissions from the upper atmosphere act as good tracers to investigate the behavior of the altitude region of their origin. This passive remote sensing method has been used to investigate various aspects of the thermosphere-ionosphere system, such as the vertical coupling of atmosphere (e.g., Laskar et al., 2013, 2014), wave activity in the upper atmosphere (e.g., Chakrabarty et al., 2004; Karan & Pallamraju, 2017; Laskar et al., 2015; Pallamraju et al., 2010, 2014, 2016), mesospheric temperature and wave dynamics (e.g., Lakshmi Narayanan et al., 2010; Lakshmi Narayanan & Gurubaran, 2013; Parihar & Taori, 2015; Singh & Pallamraju, 2015, 2017; Vineeth et al., 2007), and plasma irregularities in the ionosphere (e.g., Krall et al., 2010; Martinis et al., 2009; Mendillo & Baumgardner, 1982; Shiokawa et al., 2004).

The off-equatorial low-latitude regions are connected to the equatorial region through the geomagnetic field lines. Equatorial electrodynamics, such as, the equatorial ionization anomaly (EIA) and the pre-reversal enhancement (PRE) in electric field can influence the plasma distribution over the low-latitude regions (Raghavarao et al., 1978). It is known that the change in the direction of zonal winds over the equator during sunset time causes the initiation of the generation in PRE (Farley et al., 1986). These wind magnitudes and the times of reversals vary as a function of season. Their effectiveness in generating values of PRE is found to be high during equinoxes when the magnetic field lines are closely aligned with that of the solar terminator. The EIA refers to the formation of two crests in ionization on either side of the magnetic equator brought-in essentially due to the plasma fountain effect which results in a trough in the electron densities over the magnetic equator in the daytime. At the time of sunset, on occasions, enhanced vertical drifts at the magnetic equator due to the PRE in electric field can cause a resurgence of the plasma fountain effect, thereby bringing additional ionization to latitudes further away from the equator in the evening and nighttimes (e.g., Klobuchar et al., 1990; Sridharan et al., 1993).

Optical emissions are very sensitive to the changes in the upper atmospheric dynamics. Nighttime OI 630 nm emission is produced due to the dissociative recombination of molecular oxygen ion which results in excited atomic oxygen (^{1}D state). The transition of the O(^{1}D) state to the ground state of O(^{3}P) releases 630 nm photons (Chamberlain, 1957). There are several reports in the literature on the effect of equatorial electrodynamics on the off-equatorial dayglow emission variations (e.g., Karan et al., 2016; Pallamraju et al., 2010, 2014; Sridharan et al., 1994). Signature of reversal of EIA was observed using all-sky imaging Fabry-Perot spectrometer (Sridharan et al., 1993) from an off-equatorial location, Mt. Abu (24.6°N, 72.7°E, 16°N Mag). Plasma plume structures have been observed in the post-sunset emissions from latitude close to the magnetic equator (Sekar et al., 2012) and low-latitudinal locations (e.g., Makela, 2006; Martinis et al., 2009; Mendillo & Baumgardner, 1982; Otsuka et al., 2002; Park et al., 2003).

Meridional winds also play an important role in the distribution of plasma in the off-equatorial region, which results in the variation of the airglow emission rates. Meridional winds in the upper atmosphere have been conventionally obtained by the measurements of Doppler shifts in the nighttime OI 630 nm emissions (e.g., Gurubaran & Sridharan, 1993; Meriwether et al., 1985; Sridharan et al., 1991) and incoherent scatter radar (e.g., Salah & Holt, 1974). An alternate method of measurement of meridional winds using ionograms from latitudinally separated locations has also been presented (Krishna Murthy et al., 1990; Medeiros et al., 1997; Miller et al., 1986). The strengths of the daytime electric field, the EIA, the PRE, and the neutral winds vary from day-to-day, season, and solar activity even during geomagnetic quiet times. During geomagnetic disturbances, these phenomena are further modified as changes that are imposed on the equatorial electric fields due to both prompt-penetration and disturbance dynamo processes, affect the neutral wind magnitudes, their direction of propagations, and electron densities globally (e.g., Karan & Pallamraju, 2018; Mandal & Pallamraju, 2020; Mayr et al., 1978; Salah & Holt, 1974).

In this study, the effects of both equatorial electrodynamics and meridional winds have been investigated to understand the observed variations in the post-sunset emissions in the OI 630 nm airglow over the low-latitude location, Mt. Abu.

2. Observations and Data Analysis

2.1. OI 630 nm Nightglow Emission

Ground-based measurements of airglow emissions can be used to understand the behavior of the thermospheric-ionospheric system. In earlier studies, optical instruments at high spectral resolutions (0.07–0.015 nm at 630 nm wavelength) have been developed to obtain the optical emissions in both day and nighttimes (e.g., Pallamraju et al., 2002, 2013; Sridharan et al., 1994, 1998). In the present study, nightglow emission measurements of the red line are made from Gurushikhar, Mt. Abu, a region typically under the crest of the EIA anomaly, using the High Throughput Imaging Echelle Spectrograph (HiTIES) (Chakrabarti et al., 2001).

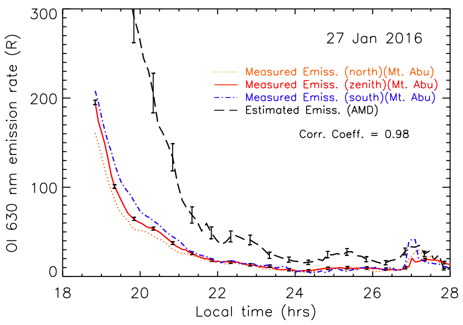

Figure 1. Sample variation of OI 630 nm emissions measured from Mt. Abu (solid red line) for zenith and those estimated over Ahmedabad (dashed black line). The southern and northern directions as viewed from Mt. Abu are separated by ∼250 km.

2.1.1. Optical Data Analysis

HiTIES is a slit spectrograph that yields a high spectral resolution (0.06 nm at 630 nm) image of 54° field-of-view. It uses a 1 K × 1 K CCD chip, however, it is binned (1 × 16) in the spatial direction to improve the signal-to-noise ratio (SNR). The data cadence used for this analysis is 5 min. The scattered light, which can arise due to the star light, zodiacal light, is also eliminated by subtracting the light falling in the spectral region adjacent (separated by 0.1 nm) to the OI 630 nm emission line. The red colored solid line in Figure 1 shows zenith emissions (from Mt. Abu) obtained for a sample night. The *x*-axis shows the local time (LT) in hours and the *y*-axis shows the OI 630 nm emission rates in Rayleigh. The SNR of the instrument varies in the range of 50.6–7.1 for a signal brightness 100–10 R. Therefore, the uncertainty in the measurement typically varies in the range of 1–3 R as shown (for a few times) in Figure 1.

2.2. Estimation of Emission Rate Over AMD

Photochemical calculations have been carried out over Ahmedabad (AMD, 23.0°N, 72.6°E, 15°N Mag), to obtain the OI 630 nm volume emission rate (VER). The OI 630 nm emissions through dissociative recombination (Cogger et al., 1980; Link & Cogger, 1988; Link et al., 1981) over AMD are calculated using the digisonde measured electron densities over AMD as inputs to the model. The information on neutral densities and temperature have been obtained from NRLMSISE-00 model (Picone et al., 2002). The ion densities, ion, and electron temperatures have been obtained from the IRI-16 model (Bilitza et al., 2017). The peak altitude of the OI 630 nm emissions vary typically from 240 to 300 km, with full width at half maxima varying between 80 and 100 km. In the present study, we have calculated the emission rates integrating the VER over a height range from 100 to 700 km. These computed nightglow intensities are compared to the measured ones over Mt. Abu, located around 180 km away. Figure 1 shows the estimated emission rate of OI 630 nm (dashed black line) over AMD for the same night (January 27, 2016) of measured emissions over Mt. Abu. Uncertainty in the estimated emission rate over AMD that incorporates the uncertainties in measurement of electron densities (around 2%–6%) and of the model (around 15%) is shown at intervals of 30 min. Since the two locations, AMD and Mt. Abu, are reasonably close to one another, the variations in the estimated and measured airglow emission rates from these two locations are compared with one another.

Due to the absence of the solar photons after the sunset, a monotonic decrement of nightglow emission rate is observed during 18–22 LT. The differences were seen in the emission rates between the measured (over Mt. Abu) and the estimated (over AMD) values are most likely due to the location of the EIA crest region near or south of the location of AMD. This can also be ascertained by the spatial variation in emissions as obtained by HiTIES, as the emission rates measured toward the southern (dash-dot line) direction from Mt. Abu (toward EIA crest) are greater in magnitude than those measured toward the northern (dotted line) direction (away from the EIA crest), with intermediary values over the zenith. Further, on almost all the nights it is seen that as the night progresses the measured and estimated emissions become nearly equal to one another (as shown in Figures 1, 2, and 4). This conclusion is also highlighted by the fact that the connection between the variabilities estimated (from AMD) vs. measured (over Mt. Abu) during 19–28 LT is extremely high with a correlation coefficient value of 0.98. Such a high correlation is also seen on other nights. The nocturnal variability in the OI 630 nm emissions as shown in Figure 2, the correlation coefficients between the measured and estimated emissions are, in general, greater than 0.9. In this present study, we have considered geomagnetic quiet nights (*Ap* <20) in the months of January, February, and March in the years 2013, 2014, and 2016. A total of 142 clear nights of data are considered for the investigation of thermosphere-ionosphere interactions.

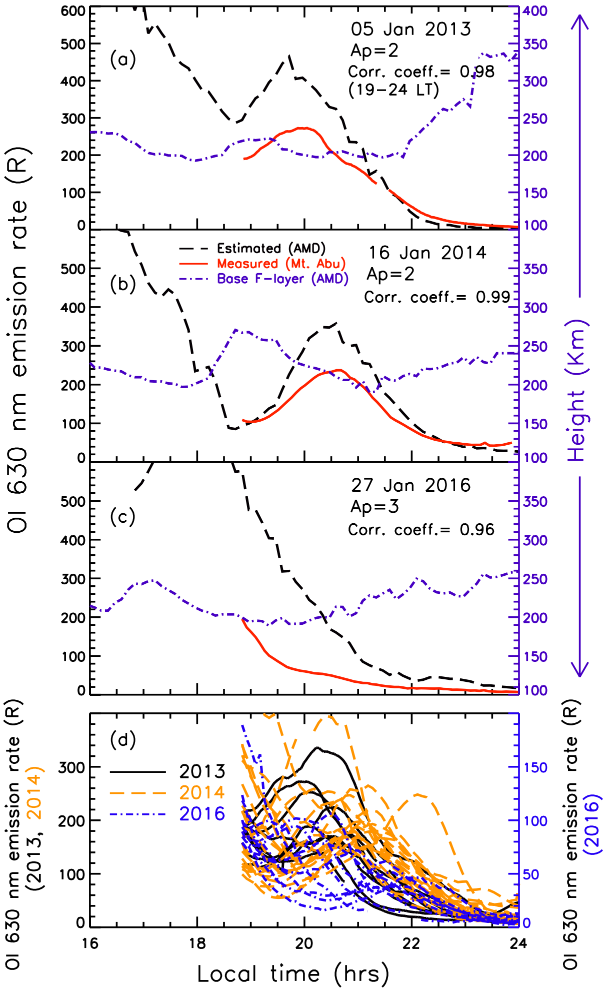

Figure 2. Panels (a–c) show the emissions measured from zenith at Mt. Abu (solid red line) and estimated (dashed black line) emissions along with the base F-layer height (dash-dot blue line) over Ahmedabad (AMD) for three selected nights from different years. Both Panels (a, b) show the presence of post-sunset enhancement in emissions, whereas, Panel (c) shows no such enhancement after the sunset. Correlation coefficients between the measured emissions at Mt. Abu and estimated emissions at AMD during 19–24 LT are also shown. Panel (d) depicts variations in the measured emissions on around 38 nights with significant post-sunset enhancements.

2.3. Digisonde Data

Digisonde Portable Sounder (DPS4D) located at AMD (off-equatorial location) and Trivandrum (TVM) (equatorial location), have been used in this study. The digisonde data from TVM are used to estimate the strength of the PRE on all the days under consideration during January, February, and March months of the years 2013, 2014, and 2016. Further, digisonde data on the nights without equatorial spread F (ESF) occurrence have been used to derive meridional winds as described in Section 3.3.

2.4. EEJ Data

Geomagnetic data over Indian sector are used to calculate the equatorial electrojet strength. Following earlier studies (Chandra & Rastogi, 1974), geomagnetic field data of Tirunelveli (TIR) (equatorial location) and Alibag (ABG) (off-equatorial location) are used to calculate the EEJ strength. Variations of corresponding nighttime base values of each location are subtracted to eliminate the geomagnetic contributions at those latitudes. Then, magnetic data of ABG are subtracted from that of TIR to eliminate the contribution of magnetospheric currents, if any, and thereby obtain the electrojet strength over the equator. Hourly geomagnetic data of TIR and ABG that have been used to calculate the EEJ strength, are obtained from http://wdciig.res.in/WebUI/Home.aspx.

3. Observations and Results

The main focus of this study is to understand the thermosphere-ionosphere behavior in the low- and equatorial-latitudes using nocturnal 630 nm airglow variations. We consider the zenith emission measurements as obtained from Mt. Abu. It has been observed that out of a total 142 nights as mentioned earlier, emission enhancement exists on 85 nights (around 60%). Figure 2 shows two sample nights (Figures 2a and 2b) with enhancements in the emission during the post-sunset time, one each in the years 2013 and 2014. Figure 2c shows a case without any post-sunset enhancement, and Figure 2d shows 38 nights of nightglow emission variations showing significant enhancements of at least 15 R during post-sunset time. The *x*-axis depicts the LT. In Figures 2a–2c, the left-side *y*-axis shows the measured emission rate in Rayleighs and the right-side *y*-axis shows the base F-layer height in km over AMD. An enhancement in the emission rates observed over Mt. Abu centered around 20 LT on January 05, 2013 is shown in Figure 2a (solid red line). The emission rates calculated over AMD (dashed black line) also show an enhancement around this time. The correlation coefficient calculated between the measured and the estimated emission rates during 19–24 LT is shown in each of the panels of Figures 2a–2c. The blue dash-dot line depicts the variation in the base height of the F-layer (estimated from *h*'F) over AMD obtained by the Digisonde. It may be noted that this is anti-correlated with the variations in the measured emission rate and can be understood that when the F-layer height increases (in the duration of 18.5–19.5 LT and after 21.5 LT in Figure 2a), the electrons in the ionosphere are lifted above the peak altitude region of 630 nm emission thereby resulting in a decrease in the emission rate. Figure 2b also shows post-sunset enhancement for another night in the OI 630 nm emission rate which is anti-correlated with the variation of the base F-layer height over AMD. Figure 2c shows a monotonic decrease in emissions beginning in twilight time and no enhancement during the post-sunset time. On this night, the base of the F-layer too did not show any changes in its height variation. The black solid lines, orange dashed lines and the blue dash-dot lines show the emission rates corresponding to the years of 2013, 2014, and 2016, respectively, in Figure 2d. The enhancements in emissions are observed to be of Gaussian shaped mostly around 19–21 LT, typically 2–3 h following the monotonic decrement after sunset. Emissions in the year 2016 were fainter (magnitudes given in the right-side *y*-axis) as compared to the other years which can be understood to be due to relative decrease in the electron densities as compared to other years commensurate with the decrease in solar flux. The emissions have been observed to range between 270 and 15 R depending on the solar activity. Therefore, considering 15 R as the lower limit there were 38 nights with post-sunset emission enhancement.

As the goal of our study is to gain a systemic understanding of the cause of such post-sunset enhancement of OI 630 nm emissions, we have investigated the role of the equatorial electric fields, and neutral winds on the variability of the nightglow emissions in the low-latitude region.

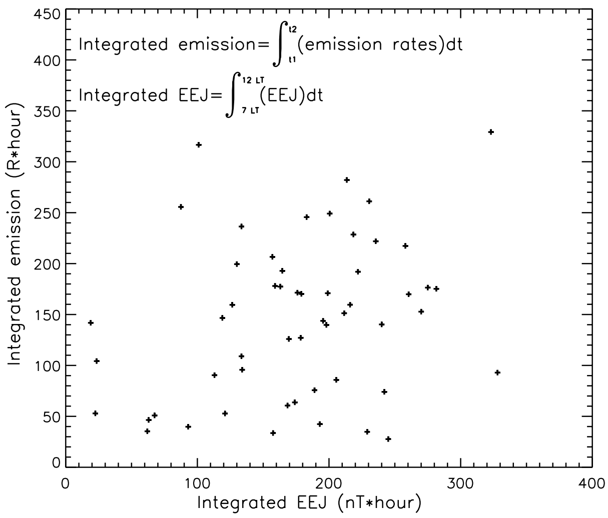

Figure 3. The Integrated EEJ values during 7–12 Local time and the integrated nightglow emission rates centered at the time of peak emissions from Mt. Abu integrated for one hour. Here, $t1$ = Peak Time −30 min; $t2$ = Peak Time +30 min. This result shows that the post-sunset OI 630 nm emission enhancements are not correlated with the integrated EEJ strength of that day.

3.1. The Role of Daytime Electric Fields

It is known that equatorial electrodynamic phenomena, like the EIA and PRE, can cause redistribution of plasma by bringing in excess electrons from the equatorial-to low-latitudes. It has been established in earlier studies that the EIA strength is proportional to the daytime EEJ strength (Karan et al., 2016; Raghavarao et al., 1978). Therefore, to explore if this is the cause, we have characterized the post-sunset emission enhancement by taking the area under the curve of the observed emissions with the duration of one hour with respect to the peak emission as the center and compared it with the integrated strength of the EEJ (depicted in Figure 3). Figure 3 shows this comparison where in it can be clearly noted that these two parameters are not correlated (correlation coefficient values are −0.17, 0.2, 0.08 in the years 2013, 2014, 2016, respectively). This result is not unexpected as the electron density enhancement due to the development of EIA can take around 3 h to affect the off-equatorial regions. Therefore, the effects due to EEJ, if any, would be noticed by the sunset time over Mt. Abu location, and not beyond that time.

3.2. Role of Pre-Reversal Enhancement in Electric Field

Another factor that can be considered as a possible source for the measured enhancements in the emissions over off-equatorial locations is the PRE during sunset time over the magnetic equator. A strong PRE in the equatorial region can contribute to an increase in electron densities over the off-equatorial regions through the plasma fountain process, as discussed above, which, in turn, can contribute to the enhancement in the nighttime emissions through the dissociative recombination mechanism.

To investigate the effect of equatorial electrodynamics over an off-equatorial location, the variations in the heights of the base and peak of F-layer and their time rate of change over TVM were considered. Figure 4 shows both the OI 630 nm measured and estimated emission rates with varying magnitudes of post-sunset emissions (top panel), F-layer height variation over TVM (middle panel) and the time rate of change of F-layer base height ($d\left(h'\mathrm{F}\right)/dt$) over TVM (bottom panel), which is proportional to the PRE in electric

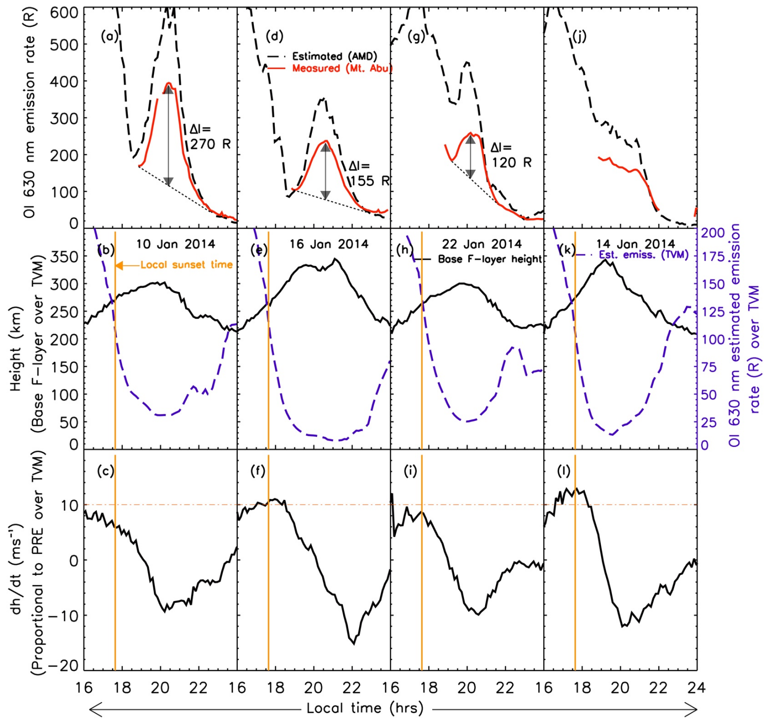

Figure 4. Top row shows the measured (solid red line) and estimated (dashed black line) emission variability on four sample nights in the year 2014. Middle row shows the base F-layer height (h'F) over Trivandrum (TVM), the equatorial location, for the same nights (solid black line). The dashed blue line of the middle row shows the estimated red line emission rate over TVM. The bottom row shows the time rate of change of the base of the F-layer height (dh / dt) over the magnetic equator TVM, which is proportional to the strength of PRE of equatorial electric field. The vertical lines in the middle and bottom rows show the time of ground sunset over TVM. To aid the eye, a horizontal dash-dot line is drawn for the plots in the bottom row at 10 m s^{-1}.

field (Goel et al., 1990; Woodman et al., 2006) on a few sample nights. The vertical solid yellow line in the middle and bottom panels show the local sunset time (at TVM). The middle panel of Figure 4 also shows the estimated OI 630 nm emission rates over TVM, wherein a monotonic decrease is observed after the sunset, which is a clear consequence of the upward movement of the F-layer. Over Mt. Abu, however, larger emission enhancements are seen during post-sunset time in the first three nights (January 10, 16, and 22, 2014), wherein emissions as large as 400−240 R have been observed. The data gap shown in Figure 4j, during 22–23.5 LT is due to presence of moonlight in the FOV of the instrument and the estimated emission (dashed black line) confirms that there is no enhancement in emission during that time. It is pertinent to note that the PRE is, in general, considered as the most likely cause of such enhancements in nightglow over off-equatorial locations as observed in the present study (Sridharan et al., 1993), as plasma from the equatorial latitudes is then transported to the off-equatorial latitudes which can then participate in the dissociative recombination process to produce OI 630 nm emissions. To investigate if this was the cause for the observed emission enhancement in these nights, the variations in the F-layer heights and, more importantly, the PRE in electric field over TVM have been obtained. As expected, base of the F-layer of the

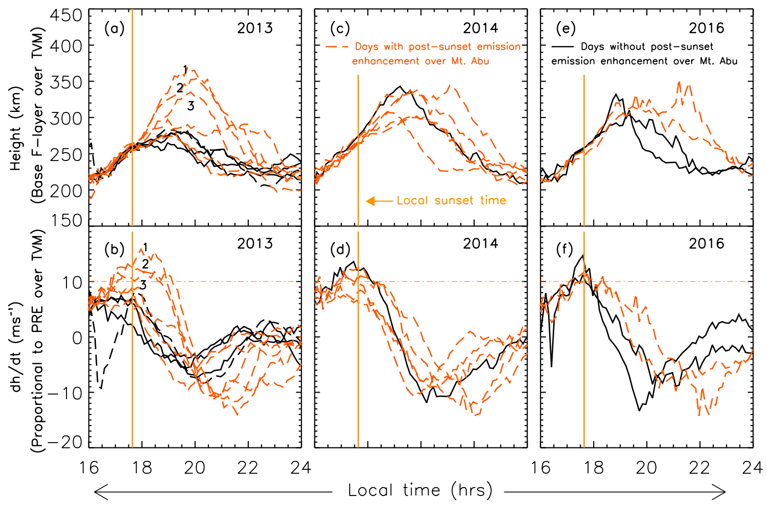

Figure 5. The top panels show the base F-layer height over Trivandrum (TVM) and the bottom panels show the time rate of change of the base F-layer height ($dh\ /\ dt$). Different years 2013, 2014, and 2016 are depicted. The yellow vertical line in the plots indicates the local sunset time over TVM. Dashed red lines show the nights with enhanced emissions over Mt. Abu and solid black lines show the nights without such enhancements in emission during post-sunset time.

ionosphere moves up (middle row) due to both recombination of ionization in the bottom side and vertical drift due to the PRE in electric field. To assess the extent of contribution of the PRE in electric field on each of the nights the dh/dt is shown in the bottom panel. To aid the eye a horizontal line is drawn at the value of 10 m s^{-1}. It can be noted that on January 10, 2014 (leftmost column) the PRE is the smallest at the sunset time and beyond and on January 14, 2014 (the rightmost column) the value of PRE is the largest among all the days in consideration. We have compared the dh/dt values with the magnitude of enhancements (ΔI), which is calculated by taking differences between the peak value and the interpolated emission value at that time if the peak was not present. ΔI is seen to be the largest on January 10 with 270 R and least on January 22 with 120 R, although both nights have similar dh/dt values. The dh/dt value for January 16 (11 m s^{-1}) is slightly higher compared to January 10 (9 m s^{-1}), however, the ΔI is smaller on January 16 (155 R) compared to January 10 (270 R). The data on January 14, in fact, showed the highest values (13 m s^{-1}) of dh/dt among all the four nights, but did not show the presence of any post-sunset enhancement in emissions. The magnitudes of the drifts fall off sharply on all the days after the sunset over the equator. While these results are intriguing, in order to gain a greater understanding of the systemic nature of nocturnal emissions, these investigations are extended to several nights.

Figure 5 shows a consolidated picture of equatorial electrodynamics for several geomagnetically quiet nights (Ap <20). As the occurrence of ESF renders the estimation of h'F ambiguous, only non-ESF nights are considered for comparison with the optical emission data. A total of 19 nights' data are included in this figure in which on twelve post-sunset emissions were present. This figure depicts the variations in the F-region heights and the vertical drifts for several nights. The plots in the top row show dashed red lines indicating the behavior of the equatorial F-region on the nights that showed emission enhancements over Mt. Abu in the post-sunset time, whereas, the solid black lines depict the data on the nights that did not show any such airglow emission enhancements. The vertical yellow lines indicate the average time of local sunset at the ground over TVM in that duration. Similarly, the plots in the bottom row show the variation in PRE indicated as the $dh\ /\ dt$. The base of F-layer height variations over TVM for the years 2014 and 2016 (Figures 5c and 5e) do not show any differences between the two categories, namely with and without

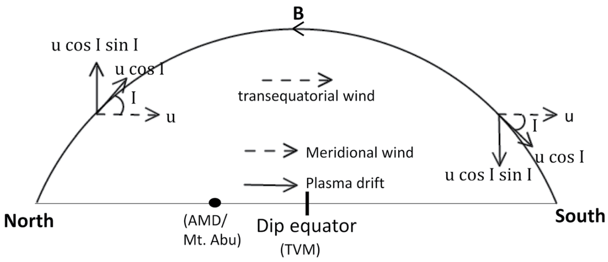

Figure 6. Schematic showing the movement of ionospheric plasma in response to meridional winds (Adapted from Rishbeth, 1977).

having post-sunset emission enhancements of nightglow emissions measured over Mt. Abu. Similarly, the variations in PRE in electric field over TVM for those nights also did not show any contrasting behavior (Figures 5d and 5f). For the year 2013 as well, except for the three days marked in Figures 5a and 5b, the base of the F-layer height and PRE over TVM do not show any differences among those nights with or without any post-sunset enhancement in the variations in the nightglow emissions over Mt. Abu. Data for the three days marked as 1, 2, and 3, correspond to January 01, January 05, and March 04, 2013, respectively, and show higher values of F-layer height and higher magnitudes of PRE prior to the occurrence of emission enhancements measured over Mt. Abu. These three nights have been investigated in greater detail and their results are described in the next section (# 4). Considering all the relevant data presented so far, in Figures 4 and 5, it is clear that the post-sunset enhancement in the equatorial electric fields do not seem to be playing a decisive role that explains the observed OI 630 nm nightglow emission enhancements measured over low-latitudes during the post-sunset hours.

3.3. Role of Meridional Winds

Another factor that can influence plasma distribution over low-latitude regions is the sense and magnitude of meridional wind. Figure 6 depicts a schematic of the effect of the equatorward and the poleward meridional winds (either transequatorial or otherwise) on the movement of plasma at different latitudes. In the presence of meridional wind of speed U, plasma moves along the geomagnetic field lines with an effect of $U\cos(I)$, where, I is the dip angle of the location. Therefore, this results in the displacement of plasma vertically upward or downward by a magnitude of $U\cos(I)\sin(I)$ depending on either equatorward or poleward directed meridional wind (Rishbeth, 1977). As shown in Figure 2 and described above, upward movement of F-layer (due to the equatorial wind) causes a decrease in OI 630 nm emissions over Mt. Abu as the available ionization density in the altitude region of airglow emissions is reduced. Similarly, a downward movement of plasma (due to poleward wind) causes an enhancement in the emissions as it brings in more electrons in the altitude region of emissions. Hence, the change in meridional wind is an extremely potent cause for the observed enhancements in the 630 nm airglow emission rates over Mt. Abu. As there are no neutral wind measurements from this location for this duration, we have estimated the variability in the meridional winds using the ionospheric data from two locations. They are AMD, an off-equatorial location, where we want to estimate the meridional winds and TVM, an equatorial location. From Figure 6, we note that meridional winds do not contribute to a change in the F-region height over the magnetic equator owing to horizontal nature of the magnetic field lines, whereas, for any latitude away from the equatorial latitudes ($>\pm3°$) the ionospheric heights do get affected by the presence of a meridional wind.

The extent of vertical movement of the F-layer measured at any location can be expressed as,

$$V = V_d\cos(I) - U\cos(I)\sin(I) - W_d\sin^2(I), \tag{1}$$

where, V_d is the vertical $E \times B$ drift over the magnetic equator, U is the meridional wind (positive poleward), W_d is the plasma diffusion, and I is the dip angle. Note that at the magnetic equatorial location, as the dip angle is zero, to the first order, the measured vertical drift of the F-layer corresponds to the $E \times B$ drift (V_d).

By rearranging the terms in Equation 1 the meridional wind (U) at a given location can be written as,

$$U = \frac{2\left(V_d \cos(I) - V\right)}{\sin(2I)} - W_d \tan(I), \tag{2}$$

However, the measured vertical drift is the sum of true vertical ($E \times B$) drift (V_{true}) and apparent vertical drift (V_{apparent}). V_{apparent} results due to recombination of charges at lower altitudes of the ionosphere, as also discussed above, and can be estimated as a product of the rate of recombination coefficient β and scale height H. If, $(V_T)_{\text{meas}}$, $\beta_T H_T$, and $(V_A)_{\text{meas}}$, $\beta_A H_A$ represent the measured and apparent vertical drifts at TVM and AMD, respectively, then, $(V_T)_{\text{meas}}$, $(V_A)_{\text{meas}}$ can be written as,

$$(V_T)_{\text{meas}} = (V_T)_{\text{true}} + (V_T)_{\text{apparent}};\ (V_T)_{\text{meas}} = (V_T)_{\text{true}} + \beta_T H_T, \tag{3a}$$

$$(V_A)_{\text{meas}} = (V_A)_{\text{true}} + (V_A)_{\text{apparent}};\ (V_A)_{\text{meas}} = (V_A)_{\text{true}} + \beta_A H_A, \tag{3b}$$

Therefore,

$$(V_T)_{\text{true}} = (V_T)_{\text{meas}} - \beta_T H_T, \tag{4a}$$

$$(V_A)_{\text{true}} = (V_A)_{\text{meas}} - \beta_A H_A, \tag{4b}$$

Now, $(V_T)_{\text{true}}$ is equal to the $E \times B$ drift over the equator (V_d). Therefore, using Equations 4a and 4b, and V for $(V_A)_{\text{true}}$, in Equation 2, the expression becomes,

$$U = \frac{2\left((V_T)_{\text{meas}} \cos(I) - (V_A)_{\text{meas}}\right)}{\sin(2I)} - \frac{2\left(\beta_T H_T \cos(I) - \beta_A H_A\right)}{\sin(2I)} - W_d \tan(I), \tag{5}$$

H is calculated as $N(dH / dN)$ (Subbarao & Krishna Murthy, 1983), wherein, we have used two frequencies 2.0 and 2.5 MHz in the calculation of meridional wind over AMD. The value of dip angle *(I)* corresponding to the years under consideration is taken from IGRF model (http://wdc.kugi.kyoto-u.ac.jp/igrf/point/index.html). The uncertainty in the calculation of meridional wind has been computed to be ± 23.7 m s^{-1} considering the uncertainty in the measurement of height from the digisonde to be of 5 km and a data cadence of 7.5 min, mentioned in Figure 7 at 45 min interval.

This approach had been carried out earlier using the digisondes at TVM and SHAR (Krishna Murthy et al., 1990) over Indian longitudes. In the present work as the geomagnetic quiet times are considered (Ap <20), we assume that there are no interlocational changes in the neutral temperature and that the electric field variation over the off-equatorial location to be a cosine*(I)* factor of that of the equatorial region. Under these assumptions, we obtain the relative variations in meridional winds using this method. Considering the lack of true information on the magnitudes of other parameters such as the thermospheric temperature and electric field, this method can only yield information on the relative variations in winds and not their absolute magnitudes. With this understanding, let us now explore as to how these variations compare with those of the measured airglow emissions.

As discussed earlier, Mt. Abu and AMD are two close by locations, and the variability in estimated emission rates over AMD show an excellent correlation (about >0.9) with the measured emission rates over Mt. Abu. With this background, one can compare the variations in the meridional wind over AMD with that of the measured OI 630 nm emissions over Mt. Abu. These are shown in Figure 7 for several nights in the years 2013, 2014, and 2016 including those depicted in Figure 4. The x-axis shows the LT, and the left side y-axis

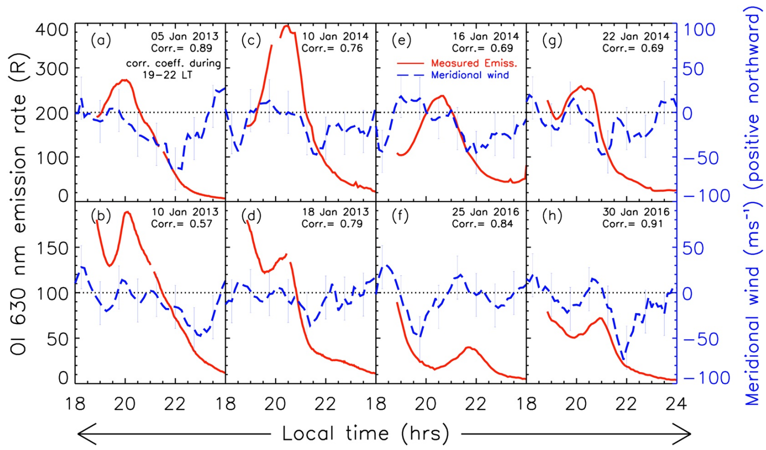

Figure 7. Variations in the measured 630 nm emission (solid red lines) over Mt. Abu and the relative variations of meridional wind (dashed blue lines) calculated for Ahmedabad (positive poleward) are shown. The horizontal dotted lines indicate the zero value of the meridional wind. The correlation coefficient between variations in the measured emissions and calculated winds are also shown in each of the panels.

shows the emission rates in Rayleighs. Please note the differences in the ranges of left side *y*-axes between the top and the bottom panels. The right side *y*-axis depicts the derived relative meridional wind values. The small gaps in the measured emissions in some nights are due to removal of data due to the presence of star light (in Figures 7a and 7b) and moon light (in Figures 7c and 7d) in the field-of-view. The poleward meridional winds in the daytime turn equatorward after the sunset. Qualitatively, these plots show that there is an association of enhancement in the emission in the post-sunset time with the turning of meridional wind from equatorward to poleward or cessation of equatorward directed winds. Similarly, when the wind again turns in the equatorward direction, the nightglow emission rates start decreasing (Figures 7a–7h). As discussed earlier, the poleward wind brings down the F-layer height thereby bringing electrons to lower altitudes resulting in enhancement in emissions as measured in our data. It may be noted that the variability between emission rate and meridional winds shows extremely good correlations (in the duration of 19–22 LT) as shown in these plots. In some cases, time differences have been observed to be varying from around 15–45 min between the measured airglow emissions in response to the meridional wind variations, which could be due to the small spatial separation between the two locations. Also, physical parameters like plasma lifetime, diffusion constant, ion drag, and viscous drag can create time delays in the response of ionosphere with the imposed meridional wind. Beyond 22 LT, the electron density becomes so small that meridional wind does not have any perceptible effect in the airglow emission variabilities, especially during the geomagnetic quiet and non-ESF nights that are considered here.

In spite of the independent nature of these two data sets, namely, one being measurements of optical OI 630 nm airglow emission variability over Mt. Abu and the other being relative meridional wind variations obtained by digisondes at two locations, the high correlation (many of the cases, the correlation coefficient values are more than 0.75) between them is remarkable and reinforces the inference that the cause of the variability in the measured OI 630 nm emission brightness over low-latitudes during geomagnetic quiet times is most likely due to the variation in the meridional winds.

4. Discussion

In this study, we have carried out a detailed investigation to understand the possible cause of the enhancements in the measured airglow emissions during the post-sunset time over the low-latitude location, Mt. Abu. The PRE in electric field over the magnetic equator did not show any contrasting behavior between the nights having and not having post-sunset emission enhancements. However, it is seen that the emission enhancements were sensitive to the variations in the meridional winds. While discussing about the meridional winds, there are two aspects that are implicit in it, one is the sense of winds and the other is the electron densities that are present at that given time. From the panels in Figure 7, it can be readily noted that the changes in the magnitude of meridional winds from equatorward to poleward portray almost good relationship with the emission enhancements as seen by the correlation coefficient values. "Almost," because the electron density is also involved. Sufficient electron number density is required for significant changes to be seen in the nocturnal emissions. This is the reason why near or after midnight, the emission variations do not correlate with the variations in the calculated meridional winds. The values of the electron densities are proportional to the solar flux. The solar flux values in the present study were such that they can be considered to represent moderate, high, and low solar activity periods in the years 2013, 2014, and 2016, respectively. Thus, the results obtained in this study are independent of the variation in solar flux. Nevertheless, the changes in the meridional winds correlate well with the variation in the measured airglow emission enhancements during the post-sunset time. For example, in Figures 7c and 7e, during the post-sunset time, relative changes in meridional winds from equatorward to poleward are quite similar, however, the magnitude of emissions are different (400R and 230R). This is explained to be due to the higher solar flux on January 10, 2014 (solar flux unit, sfu, of 170) (1 sfu = 10^{-22} W m^{-2} Hz^{-1}) compared to January 16, 2014 (sfu of 117). The electron density values at 250 km at the time of peak emissions were 2.34×10^6 and 1.3×10^6 cm^{-3} on these two nights. It is striking to note that all these parameters, namely, emission brightness, sfu, and electron densities, scale by a similar value of around 1.7.

In Figures 5a and 5b, three days showed greater F-region heights, and vertical drifts (dh / dt), over TVM on January 01, 2013, January 05, 2013, and March 04, 2013 (identified as 1, 2, and 3, respectively) compared to the other days in that year. The equatorial base F-layer height (top row), dh / dt (middle row), and nocturnal emissions of these nights along with another night January 18, 2013, where post-sunset emission enhancement was also present (bottom row), are shown in Figure 8. It may be noted that in the absence of OI 630 nm emission measurements from Mt. Abu, for data of 1 and 3 the comparison is made with the OI 630 nm column integrated emission rates estimated using the measured electron densities from the digisonde at AMD as inputs to the photochemical calculations, as these two show good correlated with each other (corr. coeff. >0.9). The correlation coefficients between estimated emission rates and derived meridional wind during 19–22 LT have been calculated for these nights and are shown in the bottom panels of Figure 8. All these nights showed enhancements in emissions around the time 20–21 LT. However, the behavior in the variability of emission magnitudes over Mt. Abu/AMD vs. the F-region over equator was in stark contrast. For the sake of consistency the estimated column integrated emission values are compared on all the nights for the following discussion. Also, as in Figures 4 and 5, a horizontal line is drawn at 10 m s^{-1} drift speed values to aid the eye. The emission variability on the first two nights (January 05, 2013 and March 04, 2013) depicted in columns 1 and 2 of Figure 8, showed contrasting emission magnitudes (460 vs. 620 R) even though the F-region behavior (F-region base height and the dh / dt values) was similar. When one compares this with the other two nights (January 01, 2013 and January 18, 2013) in columns 3 and 4 of Figure 8, the F-region behavior over the equatorial location was quite different while the emission magnitudes were nearly similar (around 280 R at 21 LT). Though, having larger vertical drift values on January 01, 2013 compared with January 05, 2013 and March 04, 2013, the magnitude of enhanced emission is much smaller. Nevertheless, it is to be noted that on all these nights the values of the correlation coefficient between the relative variations in meridional wind and optical emissions are quite good. Therefore, the one common parameter that comes forth from these four nights is that the 630 nm nightglow emission variability over low-latitude location, such as Mt. Abu, is primarily due to the poleward turning (or cessation of equatorward directed) meridional winds.

The electric field variation over low-latitudes is considered to be proportional to the equatorial electric field. Any small deviations from this proportionality may contribute to changes in the ionospheric height

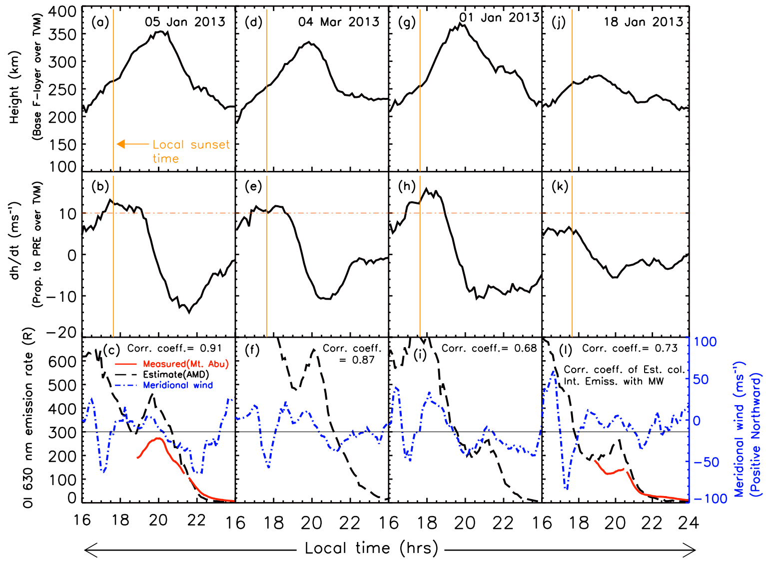

Figure 8. The top panels show the base F-layer height variation over Trivandrum (TVM). Middle panels show the dh / dt variation over TVM for the same days as above. The bottom panels show the post-sunset variation in the optical 630 nm emissions and calculated meridional wind for the same days as above. Plots (c, l) show both the measured and estimated emissions, whereas, (f, i) show estimated emissions only due to unavailability of optical data.

variation. During geomagnetic quiet times, as considered in the present study, these are not expected to change independent of the equatorial region. In any case, there is no way to ascertain such variations, if any, in the electric field at such high temporal cadence, as no studies exist on these aspects so far over low-latitudes. There are, however, ample evidence in the literature that showed using ground-based measurements that meridional winds do change over short timescales of an hour (e.g., Meriwether et al., 1985). The measurements from Mt. Abu carried out during February, 1991, using a Fabry-Perot spectrometer (Sridharan et al., 1991), showed the presence of poleward wind in the post-sunset time with a magnitude of around 100–150 m s^{-1} that varied within 1–2 h duration (Gurubaran & Sridharan, 1993). Many other ground-based observations from different locations also showed variations of meridional wind in short time scales ranging from a fraction of an hour to a couple of hours (Biondi & Sipler, 1985; Harper, 1973; Meriwether et al., 1985).

In Figure 8, we have seen that the differences in emission magnitudes for two nights were commensurate with the increase in solar fluxes on those individual nights. To explore, if that is the case in all the existing (38 nights of) data, we have plotted the enhancement in emissions (ΔI) and percentage enhancement in emissions ($[\Delta I/I]$*100) as a function of sfu variations in Figures 9a and 9b, respectively. It is interesting to note from Figure 9a that the enhancement in emissions is reasonably correlated with sfu. As we have seen above in Figure 7, this is related to enhancement in electron densities due to increase in solar flux, which varied from 90 to 210 sfu. As the average background emission also increases with increasing solar flux, the percentage enhancements in emissions remain broadly independent of the variation in solar flux as shown in Figure 9b. As this percentage variation in $\Delta I/I$ is reasonably free from that in the solar flux, these variations for three different years have been organized as a function of the Day of year (DOY) in Figure 9c to investigate the seasonal variations in them, if any. Here we have considered January 1 of each year as the DOY = 1. It is seen that there is a broad decrease in the percentage enhancement in emissions from January 1 to March 30. Poleward winds over Ahmedabad at 20 LT, a representative time of the observations in

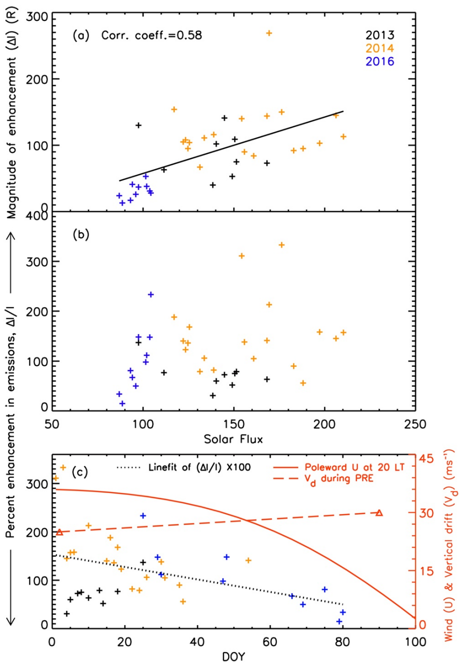

Figure 9. The variation of magnitude of enhancement (ΔI) and percentage enhancement in emissions ([$\Delta I/I$]*100) with solar fluxes are shown in the top two panels. Panel c shows the percentage variation in ($\Delta I/I$) with day of the year for three different years.

emission enhancements, obtained using the HWM-14 (Drob et al., 2015) are also plotted (solid red line). Being a climatological model, night-to-night comparison is not possible from HWM-14 wind values, however, the broad seasonal trend in them as a function of the DOY (season) can be readily noted. This decrease in poleward directed winds is consistent with the decrease in $\Delta I/I$ in post-sunset emissions as measured over a low-latitude location. We further compare these variations with the model values of vertical drifts at the post-sunset time as presented by the vertical drift model (Fejer et al., 2008). Values for winter solstice and equinox times are considered and are also plotted in Figure 9c (dashed line). As it is known, the PRE values are larger in the equinoxes as compared to the winters, which is in stark contrast with the observed values of $\Delta I/I$.

In conclusion, considering all the observational datasets, namely, (a) ionospheric F-region height variations over TVM and AMD, (b) PRE in electric field over the magnetic equatorial location (TVM) in Indian longitudes, (c) measured column integrated OI 630 nm emission variations over Mt. Abu, an off-equatorial location, (d) the column integrated emission rates estimated using Digisonde measured electron density over AMD and TVM, and (e) the relative meridional wind variations derived from the measured values of electron densities at separate latitudes during the non-ESF quiet periods, it seems that the enhancements in nighttime OI 630 nm nocturnal airglow emissions over Mt. Abu in the post-sunset period are due to the variations in those of meridional winds, for all solar flux conditions. This conclusion is further reinforced by the similar nature of the model meridional wind variation and that in the observed percentage enhancement in emissions as a function of DOY (representing the changing seasons from winter to equinox).

What is presented here is the circumstantial evidence of the significant role of meridional winds in causing the observed OI 630 nm emission enhancements. Measurements of neutral winds from the same location at an earlier time and from other longitudes do show that the meridional winds do change in their magnitudes and direction in short times scales (half an hour to couple of hours' duration). Simultaneous Fabry-Perot interferometric measurements of neutral winds and temperatures are planned in the future from AMD/Mt. Abu. These measurements will enable quantification of the calculated meridional winds from the digisonde measurements as described in this study. That study will also enable assessment of relative contribution of winds and the PRE in governing the OI 630 nm emission variability in such low-latitude locations on a night-to-night basis.

5. Summary

Enhancements in OI 630 nm nightglow emissions were observed on several nights from Mt. Abu. OI 630 nm emission photochemical model has been developed which uses the measured electron densities as inputs obtained from the Digisonde, located at AMD and the neutral and plasma parameters from NRLMSISE-00 and IRI-16 models, respectively. The equatorial electrodynamics and the meridional wind variations have been investigated to understand the plausible causes for the observed post-sunset enhancement in the OI 630 nm nightglow emissions over a period of three years. Daytime EEJ strengths do not show any similarity with the measured post-sunset nightglow emission enhancements. Variations in the base of F-layer height and PRE in electric field over an equatorial location, TVM, have been studied around the sunset time and they too do not show any contrast in their behavior between the nights with and without post-sunset enhancement in the OI 630 nm nightglow emissions measured over Mt. Abu. Meridional wind variability estimated over AMD using ionosonde data of two locations shows a very good correlation with that of the observed airglow emission variability over Mt. Abu during the post-sunset hours. Whenever the meridional wind turns poleward from equatorward or a cessation in the equatorward wind occurs, a clear enhancement has been noticed in the measured OI 630 nm nightglow emissions during post-sunset hours over the low-latitude location. The magnitudes in the measured emission enhancements depend on the electron density that is present on a given night. The variabilities in the OI 630 nm emissions correlate well with the calculated relative meridional wind variations on all of the nights on which radio data were available over TVM during non-ESF and geomagnetic quiet times. These variations in emission enhancements are also consistent with those in the model meridional winds, which add strength to the conclusion arrived at in this study. The observations of emission spanned over the years 2013, 2014, and 2016 with varying solar activity, which asserts that the results are independent of the solar flux variation.

Data Availability Statement

The nighttime optical data, used in this study, has been obtained by the Physical Research Laboratory. The hourly geomagnetic data which have been used to calculate the electrojet strength has been obtained from the ground-magnetometers maintained by the Indian Institute of Geomagnetism http://wdciig.res.in/WebUI/Home.aspx. The digisonde data of the locations at AMD and TVM are obtained from the Physical Research Laboratory, Ahmedabad and Space Physics Laboratory, Trivandrum, respectively. The data used for this work represented in figures can be accessed from https://osf.io/ubcaz.

Acknowledgments

S. Chakrabarti's efforts were supported by Lowell Center for Space Science and Technology (LoCSST). S. Saha thanks Subir Mandal and Sunil Kumar for the useful discussions during the course of this work. This work is supported by the Department of Space, Government of India.

References

Bilitza, D., Altadill, D., Truhlik, V., Shubin, V., Galkin, I., Reinisch, B., & Huang, X. (2017). International reference ionosphere 2016: From ionospheric climate to real-time weather predictions. *Space Weather*, *15*, 418–429. https://doi.org/10.1002/2016SW001593

Biondi, M. A., & Sipler, D. P. (1985). Horizontal and vertical winds and temperatures in the equatorial thermosphere: Measurements from Natal, Brazil during August–September 1982, *Planetary and Space Science*, *33*(7), 817–823. https://doi.org/10.1016/0032-0633(85)90035-2

Chakrabarti, S., Pallamraju, D., Baumgardner, J., & Vaillancourt, J. (2001). HiTIES: A high throughput imaging Echelle spectrograph for ground-based visible airglow and auroral studies. *Journal of Geophysical Research*, *106*(A12), 30337–30348. https://doi.org/10.1029/2001JA001105

Chakrabarty, D., Sekar, R., Narayanan, R., Pant, T. K., & Niranjan, K. (2004). Thermospheric gravity wave modes over low and equatorial latitudes during daytime. *Journal of Geophysical Research*, *109*, A12309. https://doi.org/10.1029/2003JA010169

Chamberlain, J. W. (1957). Oxygen red lines in the airglow Twilight and night excitation process. *Astrophysical Journal*, *127*, 54. https://doi.org/10.1029/JA092iA02p01231

Chandra, H., & Rastogi, R. G. (1974). Geomagnetic storm effects on ionospheric drifts and the equatorial E_s over the magnetic equator. *Indian Journal of Radio and Space Physics*, *3*, 332–336.

Cogger, L. L., Walker, J. C. G., & Meriwether, J. W., Jr. (1980). F region airglow are ground-based observations consistent with recent satellite results. *Journal of Geophysical Research*, *85*(A6), 3013–3020. https://doi.org/10.1029/JA085iA06p03013

Drob, D. P., Emmert, J. T., Meriwether, J. W., Makela, J. J., Doornbos, E., Conde, M., et al. (2015). An update to the Horizontal Wind Model (HWM): The quiet time thermosphere. *Earth and Space Science*, *2*(7), 301–319. https://doi.org/10.1002/2014EA000089

Farley, D. T., Bonelli, E., Fejer, B. G., & Larsen, M. F. (1986). The prereversal enhancement of the zonal electric field in the equatorial ionosphere. *Journal of Geophysical Research*, *91*(A12), 13723–13728. https://doi.org/10.1029/JA091iA12p13723

Fejer, B. G., Jensen, J. W., & Su, S.-Y. (2008). Quiet time equatorial F region vertical plasma drift model derived from ROCSAT-1 observations. *Journal of Geophysical Research*, *113*, A05304. https://doi.org/10.1029/2007JA012801

Goel, M. K., Singh, S. S., & Rao, B. C. N. (1990). Postsunset rise of F layer height in the equatorial region and its relation to the F layer dynamo polarization fields. *Journal of Geophysical Research*, *95*(A5), 6237–6246. https://doi.org/10.1029/JA095iA05p06237

Gurubaran, S., & Sridharan, R. (1993). Effect of meridional winds and neutral temperatures on the F layer heights over low latitude. *Journal of Geophysical Research*, *98*(A7), 11629–11635. https://doi.org/10.1029/92JA02029

Harper, R. M. (1973). Nighttime meridional neutral winds near 350 km at low to mid-latitudes. *Journal of Atmospheric and Terrestrial Physics*, *35*, 2023–2034. https://doi.org/10.1016/0021-9169(73)90116-5

Karan, D. K., & Pallamraju, D. (2017). Small-scale longitudinal variations in the daytime equatorial thermospheric wave dynamics as inferred from oxygen dayglow emissions. *Journal of Geophysical Research: Space Physics*, *122*, 6528–6542. https://doi.org/10.1002/2017JA023891

Karan, D. K., & Pallamraju, D. (2018). Effect of geomagnetic storms on the daytime low-latitude thermospheric wave dynamics. *Journal of Atmospheric and Solar-Terrestrial Physics*, *170*, 35–47. https://doi.org/10.1016/j.jastp.2018.02.003

Karan, D. K., Pallamraju, D., Phadke, K. A., Vijayalakshmi, T., Pant, T. K., & Mukherjee, S. (2016). Electrodynamic influence on the diurnal behavior of neutral daytime airglow emissions. *Annales Geophysicae*, *34*, 1019–1030. https://doi.org/10.5194/angeo-34-1019-2016

Klobuchar, J. A., Anderson, D. N., & Doherty, P. H. (1990). Model studies of the latitudinal extent of the equatorial anomaly during equinoctial conditions. *Radio Science*, *26*(4), 1025–1047. https://doi.org/10.1029/91RS00799

Krall, J., Huba, J. D., Joyce, G., & Yokoyama, T. (2010). Density enhancements associated with equatorial spread F, *Annales Geophysicae*, *28*, 327–337. https://doi.org/10.5194/angeo-28-327-2010

Krishna Murthy, B. V., Hari, S. S., & Somayajulu, V. V. (1990). Night-time equatorial thermospheric meridional winds from ionospheric h'F data. *Journal of Geophysical Research*, *95*(A4), 4307–4310. https://doi.org/10.1029/JA095iA04p04307

Lakshmi Narayanan, V., & Gurubaran, S. (2013). Statistical characteristics of high frequency gravity waves observed by OH airglow imaging from Tirunelveli (8.7°N). *Journal of Atmospheric and Solar-Terrestrial Physics*, *92*, 43–50. https://doi.org/10.1016/j.jastp.2012.09.002

Lakshmi Narayanan, V., Gurubaran, S., & Emperumal, K. (2010). Airglow imaging observations of small-scale structures driven by convective instability in the upper mesosphere over Tirunelveli (8.7°N). *Journal of Geophysical Research*, *115*, D19119. https://doi.org/10.1029/2009JD012937

Laskar, F. I., Pallamraju, D., Lakshmi, T. V., Reddy, M. A., Pathan, B. M., & Chakrabarti, S. (2013). Investigations on vertical coupling of atmospheric regions using combined multiwavelength optical dayglow, magnetic, and radio measurements. *Journal of Geophysical Research: Space Physics*, *118*(7), 4618–4627. https://doi.org/10.1002/jgra.50426

Laskar, F. I., Pallamraju, D., & Veenadhari, B. (2014). Vertical coupling of atmospheres: Dependence on strength of sudden stratospheric warming and solar activity. *Earth, Planets and Space*, *66*(1), 94. https://doi.org/10.1186/1880-5981-66-94

Laskar, F. I., Pallamraju, D., Veenadhari, B., Vijaya Lakshmi, T., Anji Reddy, M., & Chakrabarti, S. (2015). Gravity waves in the thermosphere: Solar activity dependence. *Advances in Space Research*, *55*, 1651–1659. https://doi.org/10.1016/j.asr.2014.12.040

Link, R., & Cogger, L. L. (1988). A re-examination of the OI 6300-Å nightglow. *Journal of Geophysical Research*, *93*(A9), 9883–9892. https://doi.org/10.1029/JA093iA09p09883

Link, R., McConnell, J. C., & Shepherd, G. G. (1981). A self-consisting evaluation of the rate constants for the production of the OI 6300 Å airglow, *Planetary and Space Science*, *29*, 589. https://doi.org/10.1016/0032-0633(81)90106-9

Makela, J. J. (2006). A review of imaging low-latitude ionospheric irregularity processes. *Journal of Atmospheric and Solar-Terrestrial Physics*, *68*, 1441–1458. https://doi.org/10.1016/j.jastp.2005.04.014

Mandal, S., & Pallamraju, D. (2020). Thermospheric gravity wave characteristics in the daytime over low-latitudes during geomagnetic quiet and disturbed conditions. *Journal of Atmospheric and Solar-Terrestrial Physics*, *211*, 105470. https://doi.org/10.1016/j.jastp.2020.105470

Martinis, C., Baumgardner, J., Mendillo, M., Su, S.-Y., & Aponte, N. (2009). Brightening of 630.0 nm airglow depletions observed at midlatitudes. *Journal of Geophysical Research*, *114*, A06318. https://doi.org/10.1029/2008JA013931

Mayr, H. G., Harris, I., & Spencer, N. W. (1978). Some properties of upper atmosphere dynamics. *Reviews of Geophysics*, *16*, 539–565. https://doi.org/10.1029/RG016i004p00539

Medeiros, R. T., Abdu, M. A., & Batista, I. S. (1997). Thermospheric meridional wind at low latitude from measurements of F layer peak height. *Journal of Geophysical Research*, *102*(A7), 14531–14540. https://doi.org/10.1029/97JA00799

Mendillo, M., & Baumgardner, J. (1982). Airglow characteristics of equatorial plasma depletions. *Journal of Geophysical Research*, *87*(A9), 7641–7652. https://doi.org/10.1029/JA087iA09p07641

Meriwether, J. W., Jr., Biondi, M. A., & Anderson, D. N. (1985). Equatorial airglow depletions induced by thermospheric winds. *Geophysical Research Letters*, *12*, 487. https://doi.org/10.1029/GL012i008p00487

Miller, K. L., Torr, D. G., & Richards, P. G. (1986). Meridional winds in the thermosphere derived from measurement of F_2 layer height. *Journal of Geophysical Research*, *91*(A4), 4531–4535. https://doi.org/10.1029/JA091iA04p04531

Otsuka, Y., Shiokawa, K., Ogawa, T., & Wilkinson, P. (2002). Geomagnetic conjugate observations of equatorial airglow depletions. *Geophysical Research Letters*, *29*, 1753. https://doi.org/10.1029/2002GL015347

Pallamraju, D., Baumgardner, J., & Chakrabarti, S. (2002). HIRISE: A ground-based high-resolution imaging spectrograph using echelle grating for measuring daytime airglow/auroral emissions. *Journal of Atmospheric and Solar-Terrestrial Physics*, *64*, 1581–1587. https://doi.org/10.1016/S1364-6826(02)00095-0

Pallamraju, D., Baumgardner, J., Singh, R. P., Laskar, F. I., Mendillo, C., Cook, T., et al. (2014). Daytime wave characteristics in the mesosphere lower thermosphere region: Results from the balloon-borne investigations of regional-atmospheric dynamics experiment. *Journal of Geophysical Research*, *119*, 2229–2242. https://doi.org/10.1002/2013JA019368

Pallamraju, D., Das, U., & Chakrabarti, S. (2010). Short- and long-timescale thermospheric variability as observed from OI 630.0 nm dayglow emissions from low latitudes. *Journal of Geophysical Research*, *115*, A06312. https://doi.org/10.1029/2009JA015042

Pallamraju, D., Karan, D. K., & Phadke, K. A. (2016). First three dimensional wave characteristics in the daytime upper atmosphere derived from ground-based multiwavelength oxygen dayglow emission measurements. *Geophysical Research Letters*, *43*, 5545–5553. https://doi.org/10.1002/2016GL069074

Pallamraju, D., Laskar, F. I., Singh, R. P., Baumgardner, J., & Chakrabarti, S. (2013). MISE: A multiwavelength imaging spectrograph using echelle grating for daytime optical aeronomy investigations. *Journal of Atmospheric and Solar-Terrestrial Physics*, *103*, 176–183. https://doi.org/10.1016/j.jastp.2012.12.003

Parihar, N., & Taori, A. (2015). An investigation of long-distance propagation of gravity waves under CAWSES India Phase II Program. *Annales Geophysicae*, *33*, 547–560. https://doi.org/10.5194/angeo-33-547-2015

Park, J., Min, K. W., Lee, J.-J., Kil, H., Kim, V. P., Kim, et al. (2003). Plasma blob events observed by KOMPSAT-1 and DMSP F15 in the low latitude nighttime upper ionosphere. *Geophysical Research Letters*, *30*(21), 2114. https://doi.org/10.1029/2003GL018249

Picone, J. M., Hedin, A. E., Drob, D. P., & Aikin, A. C. (2002). NRLMSISE-00 empirical model of the atmosphere: Statistical comparisons and scientific issues. *Journal of Geophysical Research*, *107*(A12), 1468. https://doi.org/10.1029/2002JA009430

Raghavarao, R., Sharma, P., & Sivaraman, M. R. (1978). Correlation of Ionization anomaly with the intensity of the electrojet. *Space Research*, *18*, 277–280. https://doi.org/10.1016/b978-0-08-022021-5.50063-x

Rishbeth, H. (1977). Dynamics of the equatorial F-region. *Journal of Atmospheric and Solar-Terrestrial Physics*, *39*, 1159–1168. https://doi.org/10.1016/0021-9169(77)90024-1

Salah, J. E., & Holt, J. M. (1974). Midlatitude thermospheric winds from incoherent scatter radar and theory. *Radio Science*, *9*(2), 301–313. https://doi.org/10.1029/RS009i002p00301

Sekar, R., Chakrabarty, D., & Pallamraju, D. (2012). Optical signature of shear in the zonal plasma flow along with a tilted structure associated with equatorial spread F during a space weather event. *Journal of Atmospheric and Solar-Terrestrial Physics*, *75–76*, 57–63. https://doi.org/10.1016/j.jastp.2011.05.009

Shiokawa, K., Otsuka, Y., Ogawa, T., & Wilkinson, P. (2004). Time evolution of high-altitude plasma bubbles imaged at geomagnetic conjugate points. *Annales Geophysicae*, *22*, 3137–3143. https://doi.org/10.5194/angeo-22-3137-2004

Singh, R. P., & Pallamraju, D. (2015). On the latitudinal distribution of mesospheric temperatures during sudden stratospheric warming events. *Journal of Geophysical Research: Space Physics*, *120*, 2926–2939. https://doi.org/10.1002/2014JA020355

Singh, R. P., & Pallamraju, D. (2017). Large- and small-scale periodicities in the mesosphere as obtained from variations in O_2 and OH nightglow emissions. *Annales Geophysicae*, *35*, 227–237. https://doi.org/10.5194/angeo-35-227-2017

Sridharan, R., Gurubaran, S., Raghavarao, R., & Suhasini, R. (1991). Coordinated thermospheric and F-region measurements from low latitudes. *Journal of Atmospheric and Solar-Terrestrial Physics*, *53*(6/7), 515–519. https://doi.org/10.1016/0021-9169(91)90078-L

Sridharan, R., Modi, N. K., Pallam Raju, D., Narayanan, R., Pant, T. K., Taori, A., & Chakrabarty, D. (1998). A Multiwavelength daytime photometer—A new tool for the investigation of atmospheric processes. *Measurement Science and Technology*, *9*, 585–591. https://doi.org/10.1088/0957-0233/9/4/005

Sridharan, R., Pallamraju, D., Raghavarao, R., & Ramarao, P. V. S. (1994). Precursor to equatorial spread-F in OI 630.0 nm dayglow. *Geophysical Research Letters*, *21*, 2797–2800. https://doi.org/10.1029/94GL02732

Sridharan, R., Sekar, R., & Gurubaran, S. (1993). Two-dimensional high-resolution imaging of the equatorial plasma fountain. *Journal of Atmospheric and Solar-Terrestrial Physics*, *55*, 1661–1665. https://doi.org/10.1016/0021-9169(93)90170-4

Subbarao, K. S. V., & Krishna Murthy, B. V. (1983). F-region vertical velocity and its fluctuations at the magnetic equator. *Indian Journal of Radio and Space Physics*, *12*, 94–96.

Vineeth, C., Pant, T. K., Devasia, C. V., & Sridharan, R. (2007). Atmosphere-ionosphere coupling observed over the dip equatorial MLTI region through the quasi 16 day wave. *Geophysical Research Letters*, *34*, L12102. https://doi.org/10.1029/2007GL030010

Woodman, R. F., Chau, J. L., & Ilma, R. R. (2006). Comparison of ionosonde and incoherent scatter drift measurements at the magnetic equator. *Geophysical Research Letters*, *33*, L01103. https://doi.org/10.1029/2005gl023692

Available online at www.sciencedirect.com

ScienceDirect

Advances in Space Research 70 (2022) 3686–3698

ADVANCES IN SPACE RESEARCH
(a COSPAR publication)

www.elsevier.com/locate/asr

Investigations of equatorial plasma bubbles as observed in the OI 630 nm nightglow emissions over off-equatorial and low-latitudinal locations over Indian longitudes

Sovan Saha [a,b], Duggirala Pallamraju [a,*], Rupesh N. Ghodpage [c]

[a] *Physical Research Laboratory, Ahmedabad, India*
[b] *Indian Institute of Technology, Gandhinagar, India*
[c] *Medium Frequency Radar Facility, Indian Institute of Geomagnetism, Shivaji University Campus, Kolhapur, India*

Received 3 April 2022; received in revised form 8 July 2022; accepted 7 August 2022
Available online 11 August 2022

Abstract

Equatorial plasma bubbles (EPBs), generated over the dip-equator during the sunset time, get mapped over to the low-latitudes through the geomagnetic field lines and contribute to structures of different scales in the nighttime thermosphere-ionosphere system. In the present study, the EPBs are observed in the OI 630 nm nightglow emissions over Mt. Abu and Kolhapur using a High Throughput Imaging Echelle spectrograph (HiTIES) and All-Sky Imager (ASI), respectively. Similar periodicities obtained in these measurements consistently corroborate the presence of the EPBs at both these locations. The strength of the Pre-Reversal Enhancement (PRE) in the zonal electric field has been investigated using the ionosonde data over Trivandrum, a dip-equatorial location. The strength of PRE decides the latitudinal extent of the EPBs. The eastward movement of the EPBs has been estimated to be in the range of 190–90 ms^{-1}, decreasing in magnitude from post-sunset to midnight. The wave number analysis carried out using the observed OI 630 nm emissions in the zonal direction has resulted in a contrasting behaviour during the presence/absence of the EPBs. Based on the analysis of around 1300 images of data, it is revealed that the scale sizes in the range of 250–300 km are omnipresent, whereas, shorter scale sizes (50–250 km) are present only during the presence of EPBs. It is inferred that these shorter scale size gravity waves played a significant role in the seeding the perturbation of the EPBs.

Keywords: OI 630 nm nightglow; Equatorial plasma bubbles; Equatorial electrodynamics; Gravity waves; Ionosphere-thermosphere system; High-resolution spectrographs

1. Introduction

Equatorial ionospheric irregularities can extend to large spatial distances in latitudes, which pose significant adverse impacts on trans-ionospheric radio wave propagation during their presence. The GPS receiver shows scintillations in the signals due to loss in phase locks. This brings practical difficulties in navigation and satellite-based communication, and so it motivates the scientific community working in the ionospheric studies to understand these phenomena in greater detail. The sharp plasma density gradient in the ionospheric F-region altitudes during sunset time sets the stage for the onset of ionospheric irregularities. These irregularities span a wide range of scale sizes from a few centimetres to several thousand kilometres, as observed in different techniques. Some of the manifestations of these irregularities are the spread in reflected echoes (spread-F) of radio frequency as seen in ionograms, plasma bubbles as seen in optical imagers, plasma plumes as observed using radars,

* Corresponding author.

https://doi.org/10.1016/j.asr.2022.08.023
0273-1177/

and plasma scintillations as seen in VHF and GPS measurements (e.g., Farley et al., 1970; Woodman and La Hoz, 1976; Abdu et al., 1983; Kelley, 1985; Takahashi et al., 2001, 2021; Huang et al., 2013; Patra et al., 2014; Abadi et al., 2015; Huang and Roddy, 2016; Sivakandan et al., 2019; Takahashi et al., 2021). Generalised Rayleigh-Taylor instability (RTI) generates the bubble-like structures, which, to the first order, are understood to be responsible for the generation of such plasma irregularities over the magnetic equator (Balsley et al., 1972; Kelley, 1985). The RTI growth rate is dependent on the magnitude and the sense of the equatorial eastward electric field and neutral winds, gravitational force, ion-neutral collision frequency, electron density gradient, and vertically downward winds, among other factors (Haerendel et al., 1992; Kelley, 1985; Sekar and Raghavarao, 1987; Sultan, 1996). Numerous investigations have been carried out, which brought out several important aspects/factors with regard to this plasma irregularity formation and morphology. Some of them that play a significant role in the generation and growth of the plasma instability are: the strength of equatorial ionization anomaly (EIA) in the daytime (e.g., Kelley, 1985; Raghavarao et al., 1988; Sridharan et al., 1994; Pallamraju et al., 2004; Prakash et al., 2009), the pre-reversal enhancement in the electric field, field-line integrated conductivity of the medium (Abdu et al., 1982; Tsunoda et al., 1985), neutral winds (both vertical and meridional), (Maruyama and Matuura, 1984; Sekar and Raghavarao, 1987; Raghavarao et al., 1987, 1993) and gravity waves (GWs) (Kelley et al., 1981; Kelley and Hysell, 1991; Abdu et al., 2009). Modelling studies have evolved over the decades to understand the linear, non-linear growth of plasma bubbles, the effect of the electric field, and winds in the generation and growth of plasma bubbles (e.g., Ossakow, 1981; Sekar and Raghavarao, 1987; Haerendel et al., 1992, Sekar et al., 1994, 2001; Sultan, 1996; Huba et al., 2008; Krall et al., 2009). In parallel, observational studies have been carried out using ground-based and satellite-borne measurements (e.g., Tsunoda et al., 1982; Kil et al., 2009; Karan et al., 2020; Park et al.,2022), which increased our understanding of the plasma instabilities, and their structure, and zonal drifts.

Optical emissions have been used extensively in the investigations of equatorial plasma bubbles (EPBs). OI 630.0 nm and 777.4 nm emissions originating from around 250 km and peak F-layer, respectively, are more commonly used for the investigations of EPBs (Mendillo and Baumgardner, 1982; Kelley et al., 2002; Makela and Kelley, 2003; Mukherjee et al., 2003; Rajesh et al., 2010; Sekar et al., 2012; Ghodpage et al., 2014) as the electron densities play an important role in the production of these emissions. The plasma bubbles which are generated over the dip-equator rise to higher altitudes in response to the eastward electric fields and come down to the low-latitudes along the geomagnetic field lines due to ambipolar diffusion and pressure gradient forces. The apex altitudes to which the bubbles reach can be as high as 1700 km. These plasma bubbles are aligned along the magnetic field lines as demonstrated by the simultaneous observation from two geomagnetic conjugate locations (e.g., Otsuka et al., 2002; Shiokawa et al., 2004), wherein, the structures of the plasma bubbles and their bifurcations at the conjugate locations do match fairly well with one another. Several characteristics of the plasma bubbles, like, westward tilt of the bubble structures and eastward movements, have been investigated from different longitude sectors (Mendillo and Tyler, 1983; Makela and Kelley, 2003; Mukherjee et al., 2003; Pimenta et al., 2001; Sekar et al., 2012; Ghodpage et al., 2014; Gurav et al., 2019; Karan et al., 2020). The neutral wind measurement using the Fabry-Perot interferometer over the Brazilian sector had been shown to match very well with the zonal plasma drift as well as with the zonal drift of plasma bubbles (Chapagain et al., 2012, 2013).

In this study, we present the results obtained from observations of OI 630 nm nocturnal emissions carried out during January to March in the year of 2014 from two different locations, namely, Mt. Abu (24.6°N, 72.7°E, 19°N Mag) and Kolhapur (16.8°N, 74.2°E, 10.4°N Mag). Mt. Abu is typically located at the northern edge of the EIA crest, whereas, Kolhapur is located between the magnetic equator and the northern crest of the EIA. Signature of the plasma bubble has been observed in the OI 630 nm emissions from these two locations using two different optical instruments, High throughput Imaging Echelle Spectrograph (HiTIES) over Mt. Abu and All-sky Imager (ASI) over Kolhapur. This passive remote sensing of the upper atmosphere has resulted in improving our understanding of the signatures of nighttime GW behaviour both in zonal and meridional directions. The plasma bubbles are clearly seen as depletions in emissions in the imager and the spectrograph. The zonal plasma drift, horizontal scale sizes as obtained from the imager data, and the plasma bubble periodicity obtained from two locations will be discussed in detail.

2. Observations and data used

2.1. OI 630 nm nightglow emissions

The OI 630 nm airglow emissions originate at an altitude centred at 250 km with around 100 km full-width half maxima during nighttime. The nighttime OI 630 nm emission is produced following a two-step mechanism. Firstly, the O^+ charge exchanges with O_2 to produce O_2^+. Then the dissociative recombination of O_2^+ produces excited atomic oxygen ($O(^1D)$) in the presence of background thermal electrons, which, on the transition to the ground state, releases 630 nm photons. This forbidden state of $O(^1D)$ has radiative lifetime of 110 sec, so it has enough time to equilibrate with the thermospheric dynamics. Thus, the OI 630 nm nightglow emission variation provides information on the thermospheric-ionospheric interaction and enables investigations of the upper atmospheric dynamics.

2.1.1. HiTIES observations

HiTIES is a high spectral resolution slit spectrograph (Chakrabarti et al., 2001) which is in operation from Mt. Abu, India. HiTIES has a spectral resolution of 0.06 nm at 630 nm. It uses 1024 × 1024 pixels CCD which are binned 1 × 16 in the spatial direction, to improve the signal-to-noise ratio. The field-of-view (FOV) of HiTIES is around 54° along the slit, which is oriented in the geomagnetic north–south direction for this experiment. The data cadence is 5 min. Dark count, vignetting effects, and Van Rhijn effects have been considered in the images before further analyses are carried out. Greater information on the instrument, its working, and data processing has been reported in earlier works (Chakrabarti et al., 2001, Saha et al., 2021).

2.1.2. All-sky imager observation

The data set from an all-sky imager located at an off-equatorial station, Kolhapur, is used in this study. The 1024 × 1024 pixels CCD-based ASI gives 140° FOV, which covers around 1200 km distance (Sharma et al., 2014). To avoid the curvature and non-linear effects that exist in the image at larger incident angles, we have taken around 100° FOV, which corresponds to around 600 km horizontal distance both in the zonal and meridional directions in our analysis. Around 20 nights of clear sky (cloud-free) data have been obtained during the period Jan to Feb in the year 2014.

2.2. Digisonde

Radio-sounding data using Digisonde Portable Sounder (DPS-4D) from two locations Trivandrum (8.5°N, 76.9°E, 0.03°N Mag) (dip equatorial location) and Ahmedabad (23.0°N, 72.6°E, 17.3°N Mag) (a low-latitude location) have been used in this study. The digisonde provides the ionospheric information every 7.5 min. During the presence of plasma irregularities, spread in reflected radio echoes are seen in the ionograms rendering the measurement of the height of the F-region ambiguous. Therefore, during the absence of spread-F and until the occurrence of spread-F, we have estimated the plasma drifts over the equator. Further, in order to avoid uncertainty in the estimation of plasma drifts which can arise due to the recombination in the bottom side of the F-region (Bittencourt and Abdu, 1981), we have used 7 MHz isoelectron density contours, which are typically above 300 km, to calculate the sunset time F-layer vertical drift over the dip-equator.

3. Observations and results

Different types of variability in the OI 630 nm nightglow emissions have been observed from a low-latitude location, Mt. Abu. After the sunset, as the electrons recombine rapidly, OI 630 nm emissions decrease monotonically from 18:45 LT, when the HiTIES observations begin in a programmed mode (Fig. 1a). The different colours represent emissions that originate from different directions as viewed from HiTIES, as mentioned in this figure. On several nights, we have observed an enhancement in emissions after around 1.5 h of local sunset (Fig. 1b) at around 21 LT. A poleward meridional wind which brings down the plasma to the 630 nm emission altitudes, has been found to be the cause of such emission enhancements (Saha et al., 2021). Apart from that, we have observed excursions in emissions on some nights (as shown in Fig. 1c, d). There are four depletions in emissions that have been observed on 26 Feb 2014 at 20:30, 21:25, 22:45, and 24:35 LT (Fig. 1c). A close inspection indicates that the emissions decrease at the same time and with the same magnitudes in all directions, north, zenith and south at 21:25 LT. Whereas, for the other depletions, the southern side emissions (dashed blue line) show a much sharper and deeper decrease than that on the northern side. Similarly, the depletions in emissions seen on the other night, 05 Mar 2014, have different rates of decrease in different directions. All these differences are the tell-tale signature of the plasma bubbles, their latitudinal and longitudinal extents, etc., as will be clear once the data from other datasets are presented and discussed as given below. Out of 68 moonless clear sky nights during Jan-Mar of the year 2014, 26 nights showed such sudden depletions in emissions.

The simultaneous digisonde measurement from nearby location in Ahmedabad indicated the presence of spread-F in the ionogram during the times of depletions in the nightglow emissions observed from Mt. Abu. These locations of spread-F are indicated with the shaded region (pink coloured horizontal lines) in Fig. 1c and 1d. It should be mentioned here that the other two nights in Fig. 1a and 1b are non-spread-F nights. The presence of spread-F at the time of depletions in emissions suggests the presence of strong plasma irregularities over this region. The presence of depletions in emissions over Mt. Abu coincides on all (100 %) of the occasions with the spread-F seen over Ahmedabad, indicating the extent of large-scale size plasma irregularities at least until 19° magnetic latitude on those nights. However, only on 69 % nights of spread-F observations over Ahmedabad coincides with the occurrence of plasma depletion over Mt. Abu, which indicates that the bubbles did not extend beyond 17° magnetic latitude on 31 % of nights.

To ascertain that such sharp fluctuations as obtained in our measurements over Mt. Abu are due to plasma depletions, we have also investigated the OI 630 nm all-sky images obtained from Kolhapur, which is situated between the magnetic equator (Trivandrum) and low-latitude region (Mt. Abu/ Ahmedabad). We have around 20 clear nights of data from the imager during the same period of Jan-Mar in the year of 2014. Fig. 2 shows OI 630 nm nightglow variation from both the places, Mt. Abu and Kolhapur. The meridional segment (12 km over zenith × 600 km along south-north) from each of the images obtained from Kolhapur is arranged with time to form a keogram and is shown in the bottom panels of the Fig. 2. In the top panels,

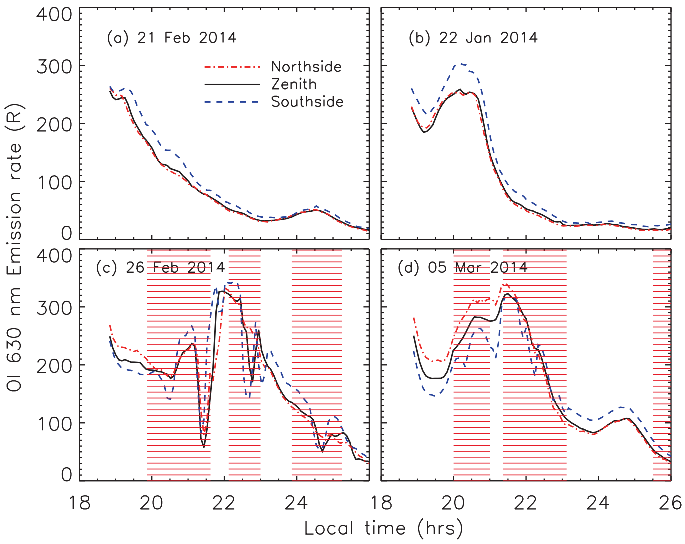

Fig. 1. Typical nightglow variations of OI 630 nm emissions are depicted here. The total FOV of HiTIES is segmented into three sections, one towards North, one South, and Zenith, as indicated in these different colour and line styles. Panel (a) shows monotonic decrease in emissions after the sunset, whereas, panel (b) shows the enhancement in emission during post-sunset time. Panels (c) and (d) show multiple excursions in emissions. The shaded regions in the panels (c) and (d) indicate the time duration of spread-F observed in digisonde, which is situated about 1.5° southward of Mt. Abu.

the OI 630 nm nightglow variations obtained from Mt. Abu are shown. The data gap in the bottom panels is due to non-availability of the data at that time. Interestingly, for four nights, 24 Feb, 26 Feb, 04 Mar, and 05 Mar (Fig. 2a-h), all the depletions in emissions observed over Mt. Abu have a clear correspondence with plasma bubbles seen in all-sky images obtained over Kolhapur in simultaneity, which confirms that the depletion signatures observed over Mt. Abu are due to the plasma bubbles present over latitudes corresponding to that of Mt. Abu. There are several examples of nights when the plasma bubbles did not reach over to Mt. Abu although they had been observed over Kolhapur. For example, on the nights of 24 and 25 Mar (Fig. 2i-l), only one or two bubbles have reached over Mt. Abu, although many more are seen over Kolhapur. It is important to take into cognisance that the distance between the northernmost location presented in the ASI data and the southernmost view direction, as presented in Fig. 2, is around 400 km. Thus, it is understandable that not all plasma bubbles seen in the ASI data from Kolhapur will be present in the HiTIES data over Mt. Abu. Another important aspect that can be noticed is that the depletions in emissions are not equal in all the three different directions (north, zenith, and south) as observed from Mt. Abu, with relatively deeper and also sometimes wider in the emission variability towards south. As the plasma bubbles are aligned along the magnetic field lines and as the different latitudes are mapped to different apex altitudes over the dip equator, it can be inferred that the electron density depletion is greater at lower altitudes over the magnetic equator as compared to those higher above.

Although visually the depletions in both the HiTIES and ASI data seem similar, to make a qualitative assessment, we have carried out spectral analysis of the data, wherein, the emissions obtained from the southernmost direction from HiTIES (around 125 km away from the zenith of Mt. Abu) are compared with the emissions obtained in the northern-most segment of the ASI imager (around 300 km away from the zenith of Kolhapur). The result from the Lomb-Scargle time period analysis (Lomb, 1976; Scargle, 1982) for these two datasets is shown in Fig. 3 for two sample nights with a 90 % confidence level (shown in a horizontal line) out of the nights as shown in Fig. 2. The solid black line indicates the normalized power spectral density (PSD) for different periodicities over southernside of Mt. Abu, whereas, the dashed blue line indicates normalized PSD over northernside of Kolhapur. Fig. 3a shows the presence of periodic fluctuations of less than 1 hr for 24 Feb 2014, whereas, Fig. 3b indicates the periodicities greater than 2 hrs for 04 Mar 2014. The similar periodicities as observed in plasma bubble depletions from the analysis as discussed above and depicted in Fig. 3a and 3b suggest that these are consistently present at both the locations for these and other nights as well (not shown here). As already mentioned above, the physical separation between the locations from these two datasets is around

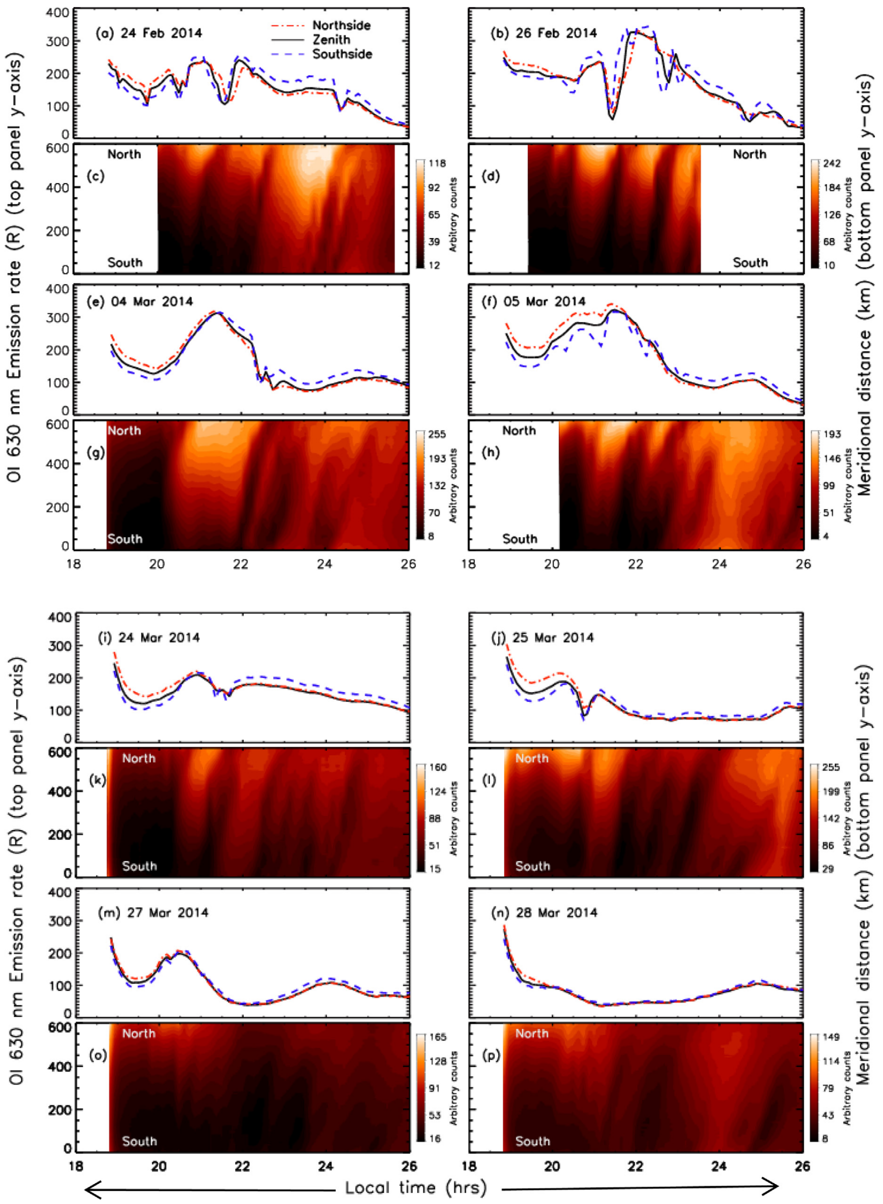

Fig. 2. OI 630 nm emission variations for eight nights as observed over Mt. Abu are shown in top panels a, b, e, f, i, j, m, and n, whereas, the keograms in the bottom panels c, d, g, h, k, l, o, and p show OI 630 nm emission variations in the south-north direction over Kolhapur. The y-axis of the top panels indicates that the OI 630 nm emission rates as observed over Mt. Abu whereas, the y-axis for the bottom panels indicates the south-north distance with Kolhapur as the zenith. Whenever the plasma depletions are observed over Mt. Abu, plasma bubbles are also observed over Kolhapur simultaneously, but the converse is not true.

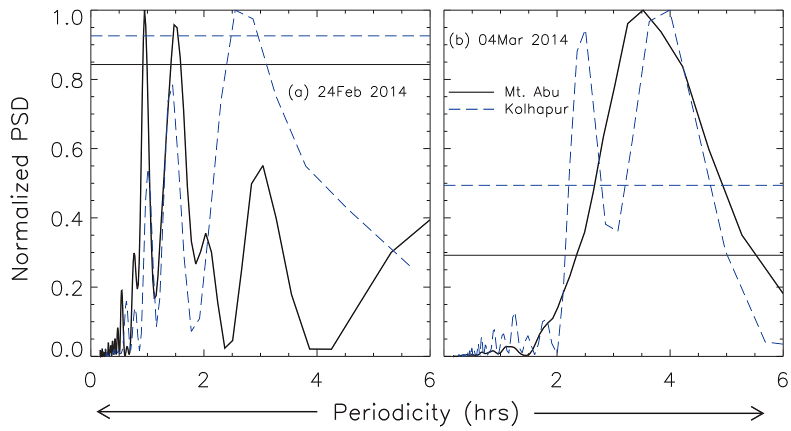

Fig. 3. The Lomb-Scargle periodicities obtained for two sample nights as observed over both the places, Mt. Abu and Kolhapur are presented. Emissions obtained from the Southernmost view direction from Mt. Abu and northern-most as viewed from Kolhapur, which are separated by around 400 km are used in these analyses.

400 km, and therefore, it is expected that not all the periodicities are present with similar strengths at both the locations. A case in point can be seen on 24 Feb 2014 (Fig. 3a), wherein all the periodicities around 1.0, and 1.5 are seen in data at Mt. Abu, while a period of 2.5 hr is present in data at Kolhapur. Nevertheless, the periodicities of 1.0 and 1.5 hr in data at Kolhapur and 2.5 hr in data at Mt. Abu are conspicuous, albeit with lower strength than their respective confidence limits. In Fig. 3b, it can be noted that there are more number of significant periodicities in the data of Kolhapur, which is closer to the magnetic equator and so, it is more likely to record signature of plasma bubbles that extend only closer to the magnetic equator.

The apex altitude to which these bubbles are required to be raised is over 1000 km at the magnetic equator in order for them to reach the latitudes of Mt. Abu. The vertical uplift of the plasma during the sunset time depends upon the strength of the PRE in the zonal electric field during that time (Abadi et al., 2015). The rate of change in the height of the F-layer is used as a proxy for the eastward electric field. An increase in the height of the F-layer happens during sunset time due to an increase in PRE in the electric field. At lower altitudes, due to the recombination of plasma, the ionospheric F-layer shows apparent vertical drift. Bittencourt and Abdu (1981) showed that the effect of recombination is negligible when the F-layer height reaches above 300 km. To minimize the uncertainty in vertical drift measurements that can arise due to recombination at the lower F-region altitudes, we have used the rate of change of the height corresponding to the returned echo of 7 MHz isoelectron density contour to calculate the F-layer vertical drift over Trivandrum. The strength of the PRE has been characterized by taking 30 min average centred at the time of occurrence of peak value in PRE. Out of the 51 nights of available PRE data over Trivandrum, we have found around 21 nights when the optical emissions over Mt. Abu showed sharp depletions due to plasma bubbles. Fig. 4 depicts the variation of PRE strength with the day of year (DOY). The red points indicate the values of the PRE on the nights when the plasma depletions extended until the latitudes of Mt. Abu. On all these nights spread-F had occurred as observed over Trivandrum (except for two; DOY 22 and 52). The red circles indicate the days when EPBs are observed over Kolhapur which are used in this study. It can be seen whenever the plasma

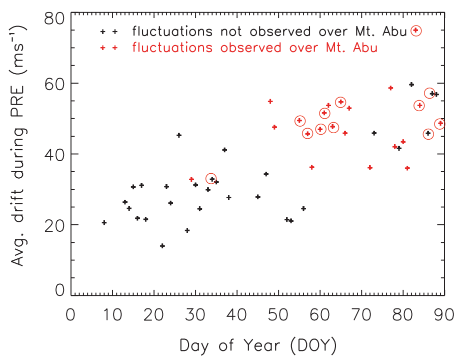

Fig. 4. Avg. PRE strength with day of year (DOY) during Jan-Mar in the year of 2014 is shown. The points in red colour indicate the presence of plasma depletions as observed in the OI 630 nm emission data over Mt. Abu. The EPBs observed in the all-sky imager data used in this study over Kolhapur is indicated in red circles. With the observation of these nights, it can be seen that whenever the depletions are observed over Mt. Abu, the EPBs have been observed over Kolhapur.

depletions are seen over Mt. Abu, the EPBs have been observed over Kolhapur. Due to the high strength of PRE, the plasma bubbles were lifted up to high altitudes (greater than1000 km) which enabled them to reach over Mt. Abu. The plasma depletions over Mt. Abu have been observed on most of the occasions when the PRE values are in the range of 40–60 ms^{-1}. Here, it is emphasised that PRE plays an important role in extending the depletion of electron densities to be mapped over the latitudes along the geomagnetic field lines rather than PRE as the seeding factor (as the discussion corresponds to the developments after the bubble generation). On some occasions, the plasma bubble was absent over Mt. Abu, although large values of PRE were present (for example, DOY: 73, 79, 82, 86, 87, 88). However, plasma bubbles were seen in the ASI data over Kolhapur on the two nights of available data (DOY: 86 & 87) as also shown in Fig. 2o, and 2p (27, 28 Mar). On the night of DOY 87, spread-F was not even observed in the digisonde data at Ahmedabad (although located equatorward of Mt. Abu). We have also looked into the concurrent observation of the C/NOFS satellite data which has an inclination angle of 13° to explore the electron density variation near the equatorial region during these nights when the all-sky imager data were unavailable. As per the availability of C/NOFS data, the electron densities are shown to exhibit sharp decreases on all nights (not shown here) not only when the depletions were observed over Mt. Abu, but also when the depletions were not observed over Mt. Abu on the days mentioned above (DOY: 73, 86, 87, 88). Several factors, such as, elec-

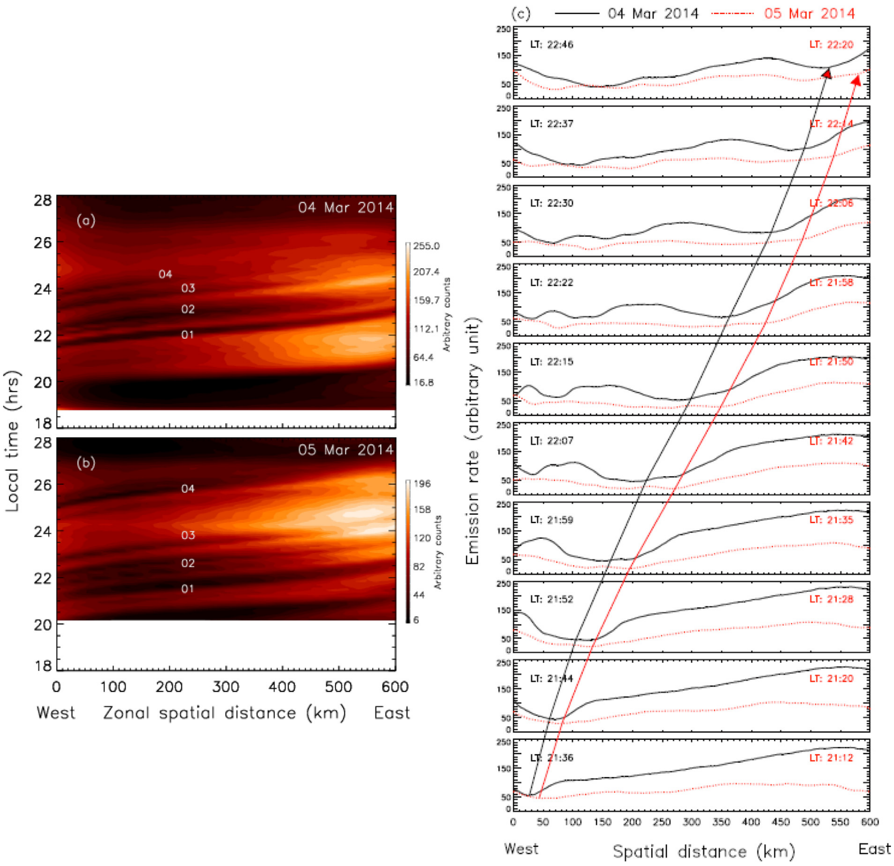

Fig. 5. Zonal variations in OI 630 nm emissions have been depicted with time for two neighbouring nights in panels (a) and (b). A zonal strip for each image (12 km centred over zenith × 600 km) is considered. The zonal movement of the plasma bubble marked as '01' for the nights 04 Mar and 05 Mar 2014 has been shown over the time in panel (c).

tric fields, and neutral winds, could have prevented the plasma bubbles from reaching to Mt. Abu later in the night in spite of large magnitudes of PRE earlier on those nights. This will be taken up in different study.

We have calculated the zonal drift speeds in the plasma depletions using the nightly images as the bubbles move zonally with time. The zonal (12 km over zenith × 600 km along west-east) segment in each image is considered and they are stacked one above the other as shown in Fig. 5. By observing the spatial movement with time of depletions in emissions caused due to the plasma bubbles, we have calculated their zonal drift speeds. As can be seen from Fig. 5a and 5b for 04 and 05 Mar 2014, different bubbles keep appearing as time progresses (as shown in the y-axis), beginning from the westernmost location of the FOV, moving eastwards, and disappearing. The times corresponding to the bubbles' appearance and disappearance are noted along with the spatial distances to calculate the average zonal drift speeds of each plasma bubble. Four plasma bubbles have been marked on these nights in the figure. It can be seen that the bubble 01 is seen to be present over the whole 600 km in the west-east direction for a long duration on both nights, whereas, the other bubbles do not last that long. Further, the first bubble is the deepest and widest of all. Such behaviour in the zonal extent has been seen on the other nights also (not shown here). There is another bubble that can be seen on 05 Mar around 20 LT (before the one marked by 01), and as this was present even before the first image was obtained on that night, it is not used for the estimation of the drift speed. The spatial movements of the plasma bubble 01 for the night 04 Mar and 05 Mar 2014 as seen over zonal strip centered over zenith are depicted in solid black and dotted red lines, respectively (Fig. 5c). The time evolution of each frame of the Fig. 5c is mentioned on the left and right sides for the nights of 04 Mar and 05 Mar 2014, respectively. From the time evolution of the depletions seen in the frames as shown in Fig. 5c, it can be seen that they have travelled around 510 km and 540 km with zonal speeds of around 121.4 and 132.4 ms^{-1} for 04 Mar and 05 Mar 2014, respectively. Similarly, the zonal drift values for the other plasma bubbles for different nights have also been calculated and are shown in Fig. 6.

Fig. 6 shows the zonal drift values of the plasma bubbles for a total 14 nights which include those plasma bubbles that have crossed the zenith location. It can be seen that the zonal speeds are higher during the post-sunset time, and they decrease as the night progresses. The orange line in the Fig. 6 shows the temporal variation of average zonal drift where all the values in a given 30 min duration are averaged. In an earlier study over Brazilian sector, the zonal speeds were shown to be different at different sides of plasma bubble structures, like, western wall, central depletion and eastern wall (Pimenta et al., 2001). It was reported in that work that the eastern wall showed an increase in speed of around 40 % as compared with the western wall, whereas, the central depletion showed an

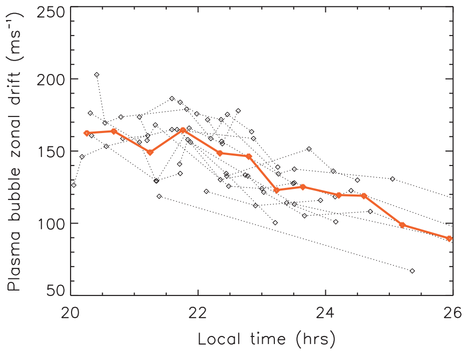

Fig. 6. Zonal drift speeds of the plasma bubbles are depicted for 14 nights. The orange line shows the 30-minutes average values.

increase by 10–20 %. The present investigations over Indian longitudes reported here did not reveal such differential variations in speeds for different sides of plasma walls. The current result of the plasma bubble drift speed matches well with the earlier reports over Indian sector (Mukherjee et al., 2003, Gurav et al., 2018; Ghodpage et al., 2021). The background plasma and the plasma bubble zonal drift showed good correlation with the measured eastward neutral winds (Chapagain et al., 2012, 2013). The similarity in the variation in the zonal drifts of the EPBs and the zonal wind speeds had been interpreted to be due to the internal space–time dynamics of the EPBs as the perturbed electric field generated inside the EPBs can affect the drift motion.

4. Discussion

In the previous section, we have discussed about the plasma depletions observed over two low-latitudinal regions, Mt. Abu and Kolhapur. As discussed, the 100° FOV of the all-sky imager data provides spatial coverage with a range of 300 km radius centred over Kolhapur. We have carried out the wave number spectral analysis from the OI 630 nm images using the Lomb-Scargle periodogram analysis by taking 600 km west-east strip over the zenith for each image of a given night. This analysis yields the information of zonal scales of that particular time. In Fig. 7, we depict the contour plot using the information of zonal scale sizes that are obtained by such spectral analysis at different times on a given night. A contrasting behaviour of zonal scale size has been noticed between the nights when the plasma bubbles are present (03 Feb and 24 Feb 2014) and when they are absent (04 Feb and 25 Feb 2014). Fig. 7a, b and 7c, d show the data from two neighbouring nights which clearly depicts a clear contrast between these nights. The 99 % confidence level for various frequencies has been estimated, and it is 0.2 or smaller in terms of the normalized PSD. It can also be

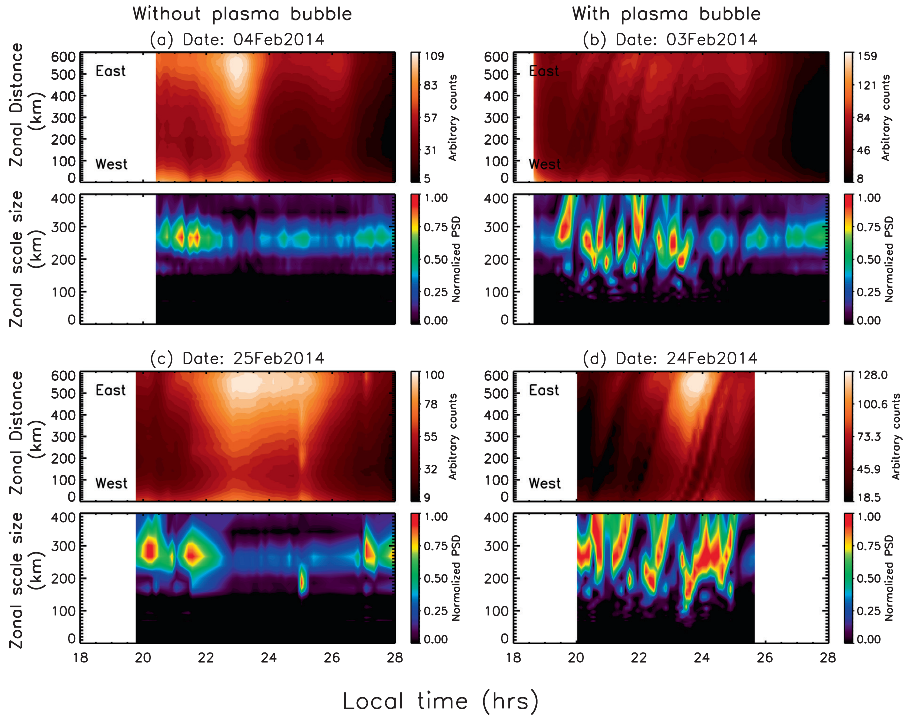

Fig. 7. The zonal spatial variation and scale sizes are shown in OI 630 nm emissions as observed over Kolhapur for four different nights. The values of scale sizes show contrasting behaviour between the nights with the occurrence of EPBs and those with the absence of the EPBs.

noted that for all the nights the scale sizes in the range of 250–300 km are present with larger power in comparison to those of 150–200 km range. On the nights that showed the presence of EPBs, several smaller scale sizes were noticed (Fig. 7b, d) which is in stark contrast with the nights that did not show any presence of EPBs (Fig. 7a, c).

Different scale sizes are significant (as seen in the PSD values) at different times. Therefore, the percentage occurrence and the averaged PSD value of a given range of scale size are obtained for a given night. The estimated scale sizes have been binned in 50 km grids as shown in Fig. 8a-d with the number of occurrences for a given range of scale size, whereas, the Fig. 8e-h shows the average PSD value for that particular range of scale size. Suppose for different scale size bins, λ_i (i = 1, 2, 3, 4, ...), the number of occurrences is found to be n_i, the percentage of occurrences in a given scale size bin has been calculated as, $(n_i/\Sigma n_i) \times 100\,\%$. Now, for a given scale size bin, λ_i, if the number of occurrences of that bin is n_i and normalized PSD values of each occurrence are p_k (k = 1, 2, ..., n_i), then the average PSD value has been calculated as, $\Sigma p_k/n_i$ for that given scale size bin. The data corresponding to the nights as shown in Fig. 7 are depicted in Fig. 8. Scale sizes above the 99 % confidence level have been considered in this representation. A clear contrast is seen in terms of the percentage occurrences of different scale sizes between the nights with and without the presence of EPBs. The dominant 150–200 km and 250–300 km zonal scale sizes on the nights without EPBs (Fig. 8a, c) are interpreted to be the typical scale sizes of the GWs present in the ionosphere-thermosphere region, as these are also present on the nights with the EPB occurrences (Fig. 8b, d). However, the shorter scale sizes can be seen on the nights with the EPB occurrence only (Fig. 8b, d). Moreover, not only does the percentage occurrence of shorter scale sizes, but also their average PSD values show an increase during the nights with the occurrence of EPBs (Fig. 8f, h). This clearly shows the significance of shorter scales during the nights with EPB occurrence. This type of contrast in scale sizes is seen for the other nights as well. Thus, the plasma bubble characteristics associated with it, like the inter-bubble separation(s), bifurcation of bubbles, widths of the bubble, etc., change with time. The contrast in scale sizes as observed between EPB and non-EPB nights provides important information on the state of nighttime ionosphere thermosphere regions during the presence of plasma bubbles. Such characterization in the zonal GW

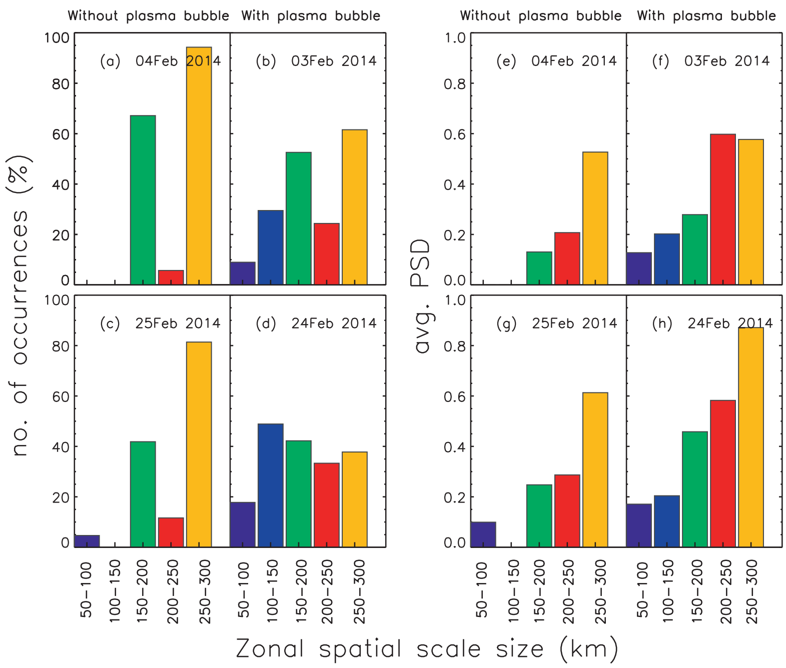

Fig. 8. The scale sizes are put in 50 km grid which are shown in x-axis. The percentage occurrence of a given scale size and the average PSD values of the corresponding scale sizes are shown in the y-axis of the left and right-side figures, respectively.

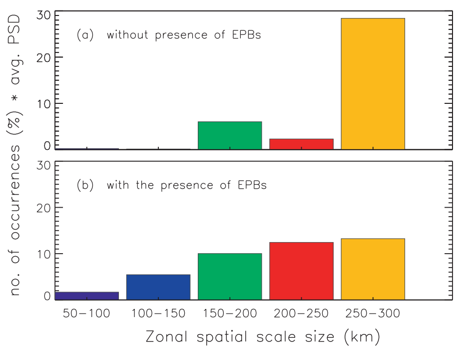

Fig. 9. The scale sizes which are segregated in 50 km grids are compared between the cases when the bubbles appeared in the image and when they did not. In the y-axis the collective effect of number of occurrence and PSD value for a given scale size has been shown by calculating the product of these two. The top panel includes all the images when the bubbles were not observed and the bottom panel shows the distribution of scale sizes when the plasma bubbles were observed in the images.

behaviour using the information of multiple number of nights has not been presented in the literature so far, to the best of our knowledge.

The GWs are one of the potential factors in the seeding of the plasma bubbles that triggers the Rayleigh-Taylor instability (e.g., Kelley et al., 1981; Huang and Kelley, 1996; Makela et al., 2010). The 250–300 km scale sizes have been found to be omnipresent irrespective of the presence/absence of plasma bubbles indicating that this is a neutral GW scale size typically existing at all times in the upper atmosphere. Further, smaller length scales are found to be present during the nights when EPBs were observed. The GWs with smaller scale sizes seem to be playing an effective role in the generation of plasma bubbles. These scale sizes on the nights with EPB occurrence also coincide with the inter-bubble distance. From the literature reported earlier, the inter-bubble spacings had been shown to have a good correlation with the horizontal GW wavelengths (Takahashi et al., 2009; Makela et al., 2010; Das et al., 2020). The inter-bubble spacing measured from radar data over Gadanki in Indian longitudes, has been shown to be following a linear relationship with the horizontal wavelengths of GWs as estimated from the collocated data from ionosonde (Das et al., 2020). In an earlier report, Makela et al. (2010) categorized the plasma bubble spacings as seen over Chile, low-latitude location in the southern hemisphere, using three years of optical data. With the support of ray tracing method as discussed by Vadas and Crowley

(2010), these bubble spacings were considered as evidence of horizontal wavelength of GWs, which are mostly secondary GWs present at this thermospheric altitudes. The presence of the small-scale wave-like structure (SSWS) as seen in the inter-bubble depletion is discussed in some earlier reports with some numerical simulation (Sekar et al., 2001) and a case study (Narayanan et al., 2012). Our result experimentally establishes the presence of such smaller-scale wave structures using the observation of around 14 nights during the period Feb-Mar in the year of 2014 when the EPBs were observed. It is proposed that these smaller scale size GWs in the zonal direction in the range of 50–150 km are potential seeds that triggered the occurrence of plasma bubbles.

To buttress the proposition further, we have considered both the factors, number of occurrence of a given range of scale size and the normalized strength on each occasion, as depicted in Fig. 8 and have shown the result in Fig. 9. Fig. 9 shows distribution of scale sizes between the two categories of presence of EPBs and absence of EPBs. Here, we have first calculated the scale sizes for each of the images that are present at 7–8 min cadance and obtained a product of the average PSD value of a given scale size and the percentage of occurrence of that scale size for a given night. This takes into account, both, their strength and number of occurrences of a given scale size. Around 1290 images have been analysed for 20 nights among which 688 images showed the presence of plasma bubble signatures, which is around 53 %. Therefore, this analysis can be considered to yield a fair comparison between the behaviour of the zonal GW characteristics in both the categories of existence and absence of EPBs. It is evident from Fig. 9 that there is strong occurrence of 250–300 km scale size in non-EPB images (similar to that seen in 04, 25 Feb 2014 in Fig. 8), whereas, when the EPBs are present, the power corresponding to zonal scale sizes shorter than 250 km is also seen to be increasing. The power in the 250–300 km scale sizes seems to be redistributed among the shorter scale sizes like 200–250 km, 150–200 km, 100–150 km. As also stated above, these scale sizes give a fair indication of the inter-bubble spacings. The crests of the GW in the zonal direction are likely to give rise to the density depletion as the low-density plasma from lower altitudes is lifted upwards over the equator, which is mapped as a bubble along a given longitude as seen in optical all-sky images over Kolhapur. In this comprehensive study, we have shown experimental evidence of the presence of GW scale size less than 250 km, possibly serving as the seed perturbation of EPBs for a given night.

5. Summary

OI 630 nm nighttime airglow emissions have been investigated over Mt. Abu, a low-latitude location. Multiple excursions have been found in the OI 630 nm emissions on some nights. Simultaneous radio observations using ionosonde from a nearby location, Ahmedabad, exhibited spread in the reflected echoes exactly at the times when depletions were observed in the nightglow emissions. We have also analysed the OI 630 nm emissions obtained using an all-sky imager from Kolhapur, which is situated between the low-latitude and the dip equatorial locations. Whenever depletions in the OI 630 nm nightglow are seen at Mt. Abu, plasma bubbles are seen in simultaneity over Kolhapur. The strength of the PRE was found to be larger on the nights when the depletions in emissions were observed in the OI 630 nm emission over Mt. Abu, indicating that the bubbles rose over 1000 km at the magnetic equator on those occasions. The plasma bubbles generated due to Rayleigh-Taylor instability over the magnetic equator move eastwards as the night progresses along with the zonal wind. The zonal speeds of the plasma bubbles estimated from all-sky imager data over Kolhapur have been found to be varying in the range around 190–90 ms^{-1}, decreasing in magnitudes from post-sunset to midnight. Further, we have also carried out wave number analyses for the emissions in the zonal direction for around 1300 images with nearly equal number with occurrence and absence of EPBs. It is found that, typically, during nighttime the zonal scale sizes are in the range of 150–200 km and 250–300 km (with a greater strength in the latter scale-size) on geomagnetic quiet nights without the presence of any plasma bubbles. The zonal scale sizes show contrasting behaviour between the nights with the EPB and without the occurrence of EPBs. The scale sizes of GWs smaller than 250 km have been observed on almost all the times whenever the plasma bubbles were present, which correspond to the inter-bubble separation distance. As the bubble depletions over the magnetic equator most likely occur at the crest location of the GW, the zonal distances between the bubbles, as seen in a location close to the magnetic equator can be assumed to represent the zonal scale sizes of GWs over the equator. Therefore, it is proposed that the GW scale sizes in the zonal direction of smaller than 250 km, if present, in the evening could potentially act as the triggers for the generation of plasma bubbles.

Declaration of Competing Interest

The authors declare that they have no known competing financial interests or personal relationships that could have appeared to influence the work reported in this paper.

Acknowledgement

The nighttime spectrograph data used in this study have been obtained from PRL's optical aeronomy observatory at Gurushikhar which is maintained by the Physical Research Laboratory. All-sky imager data are obtained from Indian Institute for Geomagnetism, Shivaji University campus, Kolhapur, India. The digisonde data of the locations at AMD and TVM are obtained from the Physical Research Laboratory, Ahmedabad and Space Physics Laboratory, Trivandrum, respectively. The C/NOFS data have been obtained from https://cdaweb.gsfc.nasa.gov/index.html. SS acknowledges the discussions carried out with Sunil Kumar, Subir Mandal, and Dupinder Singh during this work. This work is supported by the Department of Space, Government of India.

References

Abadi, P., Otsuka, Y., Tsugawa, T., 2015. Effects of pre-reversal enhancement of E × B drift on the latitudinal extension of plasma bubble in Southeast Asia. Earth Planet and Space 67–74. https://doi.org/10.1186/s40623-015-0246-7.

Abdu, M.A., Batista, I.S., Kantor, I.J., Sobral, J.H.A., 1982. Gravity wave induced ionization layers in the night F-region over Cachoeira Paulista (22°S, 45°W). J. Atmos. Terr. Phys. 44 (9), 759–767. https://doi.org/10.1016/0021-9169(82)90004-6.

Abdu, M.A., De Medeiros, R.T., Bittencourt, J.A., Batista, I.S., 1983. Vertical ionization drift velocities and range type spread F in the evening equatorial ionosphere. J. Geophys. Res. Space Phys. 88 (A1), 399–402. https://doi.org/10.1029/JA088iA01p00399.

Abdu, M.A., Alam Kherani, E., Batista, I.S., De Paula, E.R., Fritts, D.C., Sobral, J.H.A., 2009. Gravity wave initiation of equatorial spread F/plasma bubble irregularities based on observational data from the SpreadFEx campaign. Ann. Geophys. 27 (7), 2607–2622. https://doi.org/10.5194/angeo-27-2607-2009.

Balsley, B.B., Haerendel, G., Greenwald, R.A., 1972. Equatorial spread F: recent observations and a new interpretation. J. Geophys. Res. 77 (28), 5625–5628. https://doi.org/10.1029/JA077i028p05625.

Bittencourt, J.A., Abdu, M.A., 1981. Theoretical comparison between apparent and real vertical ionization drift velocities in the equatorial F region. J. Geophys. Res. 86, 2451–2454. https://doi.org/10.1029/JA086iA04p02451.

Chakrabarti, S., Pallamraju, D., Baumgardner, J., Vaillancourt, J., 2001. HiTIES: a high throughput imaging echelle spectrograph for ground-based visible airglow and auroral studies. J. Geophys. Res. 106 (A12), 30337–30348. https://doi.org/10.1029/2001JA001105.

Chapagain, N.P., Makela, J.J., Meriwether, J.W., Fisher, D.J., Buriti, R. A., Medeiros, A.F., 2012. Comparison of nighttime zonal neutral winds and equatorial plasma bubble drift velocities over Brazil. J. Geophys. Res.: Space Phy. 117 (A6). https://doi.org/10.1029/2012JA017620.

Chapagain, N.P., Fisher, D.J., Meriwether, J.W., Chau, J.L., Makela, J.J., 2013. Comparison of zonal neutral winds with equatorial plasma bubble and plasma drift velocities. J. Geophys. Res. Space Phys. 118 (4), 1802–1812. https://doi.org/10.1002/jgra.50238.

Farley, D.T., Balsey, B.B., Woodman, R.F., McClure, J.P., 1970. Equatorial spread F: implications of VHF radar observations. J. Geophys. Res. 75 (34), 7199–7216. https://doi.org/10.1029/JA075i034p07199.

Ghodpage, R.N., Taori, A., Patil, P.T., Gurubaran, S., Sripathi, S., Banola, S., Sharma, A.K., 2014. Simultaneous optical measurements of equatorial plasma bubble (EPB) from Kolhapur (16.8°N, 74.2°E) and Gadanki (13.5°N, 79.2°E). J. Atmos. Terr. Phys. 121, 196–205. https://doi.org/10.1016/j.jastp.2014.05.008.

Ghodpage, R. N., Gurav, O. B., Taori, A., Sau, S., Patil, P. T., Erram, V. C., & Sripathi, S., 2021. Observation of an intriguing equatorial plasma bubble event over Indian sector. Journal of Geophysical Research: Space Physics, 126(5), e2020JA028308. https://doi.org/10.1029/2020JA028308.

Das, S.K., Patra, A.K., Kherani, E.A., Chaitanya, P.P., Niranjan, K., 2020. Relationship between presunset wave structures and interbubble spacing: the seeding perspective of equatorial plasma bubble. Journal of Geophysical Research: Space Physics, 125(8), 2020JA028122. https://doi.org/10.1029/2020JA028122.

Gurav, O.B., Sharma, A.K., Ghodpage, R.N., Nade, D.P., Chavan, G.A., Gaikwad, H.P., Patil, P.T., 2018. Zonal drift velocity of equatorial plasma bubbles during ascending phase of 24th solar cycle using all sky imager over Kolhapur, India. J. Geophys. Res. Sp. Phys. https://doi.org/10.1029/2018JA025810.

Gurav, O.B., Narayanan, V.L., Sharma, A.K., Ghodpage, R.N., Gaikwad, H.P., Patil, P.T., 2019. Airglow imaging observations of some evolutionary aspects of equatorial plasma bubbles from Indian sector. Adv. Space Res. 64, 385–399. https://doi.org/10.1016/j.asr.2019.04.008.

Haerendel, G., Eccles, J.V., Cakir, S., 1992. Theory for modeling the equatorial evening ionosphere and the origin of the shear in the horizontal plasma flow. J. Geophys. Res. Space Phys. 97 (A2), 1209–1223. https://doi.org/10.1029/91JA02226.

Huang, C.S., de La Beaujardiere, O., Roddy, P.A., Hunton, D.E., Ballenthin, J.O., Hairston, M.R., 2013. Long-lasting daytime equatorial plasma bubbles observed by the C/NOFS satellite. J. Geophys. Res. Space Phys. 118 (5), 2398–2408. https://doi.org/10.1002/jgra.50252.

Huang, C.S., Kelley, M.C., 1996. Non-linear evolution of equatorial spread F: 2. Gravity wave seeding of Rayleigh-Taylor instability. J. Geophys. Res.: Space Phys. 101 (A1), 293–302. https://doi.org/10.1029/95JA02210.

Huang, C.S., Roddy, P.A., 2016. Effects of solar and geomagnetic activities on the zonal drift of equatorial plasma bubbles. J. Geophys. Res. Space Phys. 121 (1), 628–637. https://doi.org/10.1002/2015JA021900.

Huba, J.D., Joyce, G., Krall, J., 2008. Three-dimensional equatorial spread F modeling. Geophys. Res. Lett. 35, L10102. https://doi.org/10.1029/2008GL033509.

Karan, D.K., Daniell, R.E., England, S.L., Martinis, C.R., Eastes, R.W., Burns, A.G., McClintock, W.E., 2020. First zonal drift velocity measurement of Equatorial Plasma Bubbles (EPBs) from a geostationary orbit using GOLD data. Journal of Geophysical Research: Space Physics, 125(9),2020JA028173. https://doi.org/10.1029/2020JA028173.

Kelley, M.C., 1985. Equatorial spread F: Recent results and outstanding problems. J. Atmos. Terr. Phys. 47 (8–10), 745–752. https://doi.org/10.1016/00219169(85)90051-0.

Kelley, M.C., Hysell, D.L., 1991. Equatorial spread-F and neutral atmospheric turbulence. a review and a comparative anatomy. J. Atmos. Sol. Terr. Phys. 53, 695–708. https://doi.org/10.1016/0021-9169(91)90122-N.

Kelley, M.C., Larsen, M.F., LaHoz, C., McClure, J.P., 1981. Gravity wave initiation of equatorial spread F: a case study. J. Geophys. Res. 86, 9087. https://doi.org/10.1029/JA086iA11p09087.

Kelley, M.C., Makela, J.J., Ledvina, B.M., Kintner, P.M., 2002. Observations of equatorial spread-F from Haleakala, Hawaii. Geophys. Res. Lett. 29 (20). https://doi.org/10.1029/2002GL015509.

Kil, H., Paxton, L.J., Oh, S.J., 2009. Global bubble distribution seen from ROCSAT-1 and its association with the evening prereversal enhancement. J. Geophys. Res. Space Phys. 114. https://doi.org/10.1029/2008JA013672 A06307.

Krall, J., Huba, J.D., Martinis, C.R., 2009. Three-dimensional modeling of equatorial spread F airglow enhancements. Geophys. Res. Lett. 36 (10). https://doi.org/10.1029/2009GL038441.

Lomb, N.R., 1976. Least-squares frequency analysis of unequally spaced data. Astrophys. Space Sci. 39 (2), 447–462. https://doi.org/10.1007/BF00648343.

Makela, J.J., Kelley, M.C., 2003. Field-aligned 777.4-nm composite airglow images of equatorial plasma depletions. Geophys. Res. Lett. 30 (8). https://doi.org/10.1029/2003GL017106.

Makela, J.J., Vadas, S.L., Muryanto, R., Duly, T., Crowley, G., 2010. Periodic spacing between consecutive equatorial plasma bubbles. Geophys. Res. Lett. 37 (14). https://doi.org/10.1029/2010GL043968.

Maruyama, T., Matuura, N., 1984. Longitudinal variability of annual changes in activity of equatorial spread F and plasma bubbles. J. Geophys. Res. Space Phys. 89 (A12), 10903–10912. https://doi.org/10.1029/JA089iA12p10903.

Mendillo, M., Baumgardner, J., 1982. Airglow characteristics of equatorial plasma depletions. J. Geophys. Res. Space Phys. 87 (A9), 7641–7652. https://doi.org/10.1029/JA087iA09p07641.

Mendillo, M., Tyler, A., 1983. Geometry of depleted plasma regions in the equatorial ionosphere. J. Geophys. Res. 88 (A7), 5778–5782. https://doi.org/10.1029/JA088iA07p05778.

Mukherjee, G.K., 2003. Studies of equatorial F-region depletions and dynamics using multiple wavelength nightglow imaging. J. Atmos. Sol. Terr. Phys. 65 (3), 379–390. https://doi.org/10.1016/S1364-6826(02)00214-6.

Narayanan, V.L., Taori, A., Patra, A.K., Emperumal, K., Gurubaran, S., 2012. On the importance of wave-like structures in the occurrence of equatorial plasma bubbles: a case study. J. Geophys. Res. 117, A01306. https://doi.org/10.1029/2011JA017054.

Ossakow, S.L., 1981. Spread-F theories—a review. J. Atmos. Terr. Phys. 43 (5–6), 437–452. https://doi.org/10.1016/0021-9169(81)90107-0.

Otsuka, Y., Shiokawa, K., Ogawa, T., Wilkinson, P., 2002. Geomagnetic conjugate observations of equatorial airglow depletions. Geophys. Res. Lett. 29, 1753. https://doi.org/10.1029/2002GL015347.

Pallamraju, D., Chakrabarti, S., Valladares, C.E., 2004. Magnetic storm-induced enhancement in neutral composition at low latitudes as inferred by O(1D) dayglow measurements from Chile. Ann. Geophys. 22, 3241–3250. https://doi.org/10.5194/angeo-22-3241-2004.

Park, J., Huang, C.-S., Eastes, R.W., Coster, A.J., 2022. Temporal evolution of low-latitude plasma blobs identified from multiple measurements: ICON, GOLD, and Madrigal TEC. Journal of Geophysical Research: Space Physics, 127, e2021JA029992. https://doi.org/10.1029/2021JA029992.

Patra, A.K., Srinivasulu, P., Chaitanya, P.P., Rao, M.D., Jayaraman, A., 2014. First results on low-latitude E and F region irregularities obtained using the Gadanki Ionospheric Radar Interferometer. J. Geophys. Res. Space Phys. 119, 10276–10293. https://doi.org/10.1002/2014JA020604.

Pimenta, A.A., Fagundes, P.R., Bittencourt, J.A., Sahai, Y., Gobbi, D., Medeiros, A.F., Taylor, M.J., 2001. Ionospheric plasma bubble zonal drift: a methodology using OI 630 nm all-sky Imaging systems. Adv. Space Res. 27 (2001), 1219–1224. https://doi.org/10.1016/S0273-1177(01)00201-0.

Prakash, S., Pallamraju, D., Sinha, H.S.S., 2009. Role of the equatorial ionization anomaly in the development of the evening prereversal enhancement of the equatorial zonal electric field. J. Geophys. Res. 114, A02301. https://doi.org/10.1029/2007JA012808.

Raghavarao, R., Gupta, S.P., Sekar, R., Narayanan, R., Desai, J.N., Sridharan, R., Babu, V.V., Sudhakar, V., 1987. In situ measurements of winds, electric fields and electron densities at the onset of equatorial spread-F. J. Atmos. Terr. Phys. 49 (5), 485–492. https://doi.org/10.1016/0021-9169(87)90042-0.

Raghavarao, R., Nageswararao, M., Sastri, J.H., Vyas, G.D., Sriramarao, M., 1988. Role of equatorial ionization anomaly in the initiation of equatorial spread F. J. Geophys. Res. 93 (A6), 5959–5964. https://doi.org/10.1029/JA093iA06p05959.

Raghavarao, R., Hoegy, W.R., Spencer, N.W., Wharton, L.E., 1993. Neutral temperature anomaly in the equatorial thermosphere-a source of vertical winds. Geophys. Res. Lett. 20 (11), 1023–1026. https://doi.org/10.1029/93GL01253.

Rajesh, P.K., Liu, J.Y., Sinha, H.S.S., Banerjee, S.B., 2010. Appearance and extension of airglow depletions. J. Geophys. Res.: Space Phys. 115 (A8). https://doi.org/10.1029/2009JA014952.

Saha, S., Pallamraju, D., Pant, T.K. and Chakrabarti, S., 2021. On the Cause of the Post-Sunset Nocturnal OI 630 nm Airglow Enhancement Over Low-Latitude Thermosphere. Journal of Geophysical Research: Space Physics, 126(7), 2021JA029146. https://doi.org/10.1029/2021JA029146.

Scargle, J.D., 1982. Studies in astronomical time series analysis. II. statistical aspects of spectral analysis of unevenly spaced data. Astron. J. 263 (2), 835–853. https://doi.org/10.1086/160554.

Sekar, R., Kherani, E.A., Rao, P.B., Patra, A.K., 2001. Interaction of two long-wavelength modes in the non-linear numerical simulation model of equatorial spread F. J. Geophys. Res. Space Phys. 106 (A11), 24765–24775. https://doi.org/10.1029/2000JA000361.

Sekar, R., Chakrabarty, D., Pallamraju, D., 2012. Optical signature of shear in the zonal plasma flow along with a tilted structure associated with equatorial spread F during a space weather event. J. Atmos. Sol. Terr. Phys. 75–76, 57–63. https://doi.org/10.1016/j.jastp.2011.05.009.

Sekar, R., Raghavarao, R., 1987. Role of vertical winds on the Rayleigh-Taylor mode instabilities of the nighttime equatorial ionosphere. J. Atmos. Terr. Phys. 49 (10), 981–985. https://doi.org/10.1016/0021-9169(87)90104-8.

Sekar, R., Suhasini, R., Raghavarao, R., 1994. Effects of vertical winds and electric fields in the non-linear evolution of equatorial spread F. J. Geophys. Res. Space Phys. 99 (A2), 2205–2213. https://doi.org/10.1029/93JA01849.

Sharma, A.K., Nade, D.P., Nikte, S.S., Ghodpage, R.N., Patil, P.T., Rokade, M.V., et al., 2014. Development of fast image analysis technique for all-sky images. Curr. Sci., 1–9

Shiokawa, K., Otsuka, Y., Ogawa, T., Wilkinson, P., 2004. Time evolution of high-altitude plasma bubbles imaged at geomagnetic conjugate points. Ann. Geophys. 22, 3137–3143. https://doi.org/10.5194/angeo-22-3137-2004.

Sivakandan, M., Paulino, I., Ramkumar, T.K., Taori, A., Patra, A.K., Sripathi, S., Niranjan, K., Bilibio, A.V., 2019. Multi-instrument investigation of troposphere-ionosphere coupling and the role of gravity waves in the formation of equatorial plasma bubble. J. Atmos. Sol. Terr. Phys. 189, 65–79. https://doi.org/10.1016/j.jastp.2019.04.006.

Sridharan, R., Pallamraju, D., Raghavarao, R., Ramarao, P.V.S., 1994. Precursor to equatorial spread-F in OI 630.0 nm dayglow. Geophys. Res. Lett. 21, 2797–2800. https://doi.org/10.1029/94GL02732.

Sultan, P.J., 1996. Linear theory and modeling of the Rayleigh-Taylor instability leading to the occurrence of equatorial spread F. J. Geophys. Res. 101 (A12), 26875–26891. https://doi.org/10.1029/96JA00682.

Takahashi, H., Taylor, M.J., Sobral, J.H.A., Medeiros, A.F., Gobbi, D., Santana, D.C., 2001. Fine structure of the ionospheric plasma bubbles observed by the OI 6300 and 5577 airglow images. Adv. Space Res. 27 (6–7), 1189–1194. https://doi.org/10.1016/S0273-1177(01)00159-4.

Takahashi, H., Taylor, M.J., Pautet, P.-D., Medeiros, A.F., Gobbi, D., Wrasse, C.M., et al., 2009. Simultaneous observation of ionospheric plasma bubbles and mesospheric gravity waves during the SpreadFEx Campaign. Ann. Geophys. 27, 1477–1487. https://doi.org/10.5194/angeo-27-1477-2009.

Takahashi, H., Essien, P., Figueiredo, C.A.O.B., Wrasse, C.M., Barros, D., Abdu, M.A., Otsuka, Y., Shiokawa, K., Li, G., 2021. Multi-instrument study of longitudinal wave structures for plasma bubble seeding in the equatorial ionosphere. Earth Planet. Phys. 5 (5), 368–377. https://doi.org/10.26464/epp2021047.

Tsunoda, R.T., 1985. Control of the seasonal and longitudinal occurrence of scintillations by the longitudinal gradient in integrated *E* region Pedersen conductivity. J. Geophys. Res. 90 (A1), 447–456. https://doi.org/10.1029/JA090iA01p00447.

Tsunoda, R.T., Livingston, R.C., McClure, J.P., Hanson, W.B., 1982. Equatorial plasma bubbles: vertically elongated wedges from the bottomside F layer. J. Geophys. Res. 87 (A11), 9171–9180. https://doi.org/10.1029/JA087iA11p09171.

Vadas, S.L., Crowley, G., 2010. Sources of the traveling ionospheric disturbances observed by the ionospheric TIDDBIT sounder near Wallops Island on 30 October 2007. Journal of Geophysical Research: Space Physics, 115(A7). https://doi.org/10.1029/2009JA015053.

Woodman, R.F., La Hoz, C., 1976. Radar observations of F region equatorial irregularities. J. Geophys. Res. 81 (31), 5447–5466. https://doi.org/10.1029/JA081i031p05447.

Journal of Atmospheric and Solar–Terrestrial Physics 241 (2022) 105965

Contents lists available at ScienceDirect

Journal of Atmospheric and Solar-Terrestrial Physics

journal homepage: www.elsevier.com/locate/jastp

Latitudinal variations in the nocturnal behaviour of OI 630 nm airglow emissions and their relationship with equatorial electrodynamics

Sovan Saha [a,b], Duggirala Pallamraju [a,*]

[a] Space and Atmospheric Sciences Division, Physical Research Laboratory, Ahmedabad, India
[b] Indian Institute of Technology, Gandhinagar, India

ARTICLE INFO

Keywords:
OI 630 nm nightglow
Low-latitude thermosphere-ionosphere
Equatorial electric fields
Equatorial ionization anomaly
Reversal of EIA
Optical spectrographs

ABSTRACT

Airglow emissions from the thermosphere act as tracers of the behaviour of the upper atmosphere. OI 630 nm nightglow emissions that originate from an altitude of around 250 km in the thermosphere have been investigated using a large field-of-view ground-based optical spectrograph from Mt. Abu (24.6°N, 72.7°E, 19°N Mag.), a low-latitudinal location in India. The latitudinal movement of the crest of the equatorial ionization anomaly (EIA) in both poleward in the evening and equatorward in the night has been reported using the OI 630 nm nightglow emissions. The EIA crest is found to shift away from the equator after the sunset, which has been shown to be directly related to the strength of the twilighttime equatorial electrodynamics. Later in the night, after 20 LT, a clear movement of the crest back towards the equator, known as the reversal of EIA, has been observed. The speeds of the EIA reversals for forty nights in the years 2014 and 2015 have been obtained and are found to be in the range of 10–55 ms^{-1}. As the global equatorial electric fields ($\boldsymbol{E}$) are irrotational in nature ($\nabla \times \boldsymbol{E} = 0$), simultaneous variations in the daytime electrojet strength over Jicamarca in the American sector have been compared with the nighttime reversal speeds of the EIA over the Indian sector, which show a remarkable relationship with each other. Thus, it is hereby demonstrated that the reversal in EIA as inferred by the OI 630 nm nightglow emissions in our measurements is due to the westward equatorial electric field. It is hereby proposed that the reversal speed derived from optical nightglow measurements can serve as a proxy for the determination of westward electric field over equator for that longitude sector.

1. Introduction

The behaviour of the upper atmosphere depends upon the movement of both neutrals and ions in response to electrodynamic forces. The OI 630 nm (red line) airglow emissions that originate from around 250 km altitude serve as a tracer of the dynamics that is prevalent at those altitudes. In the nighttime, the 630 nm photons are generated as a result of dissociative recombination of molecular oxygen ions with the ambient electrons, where the molecular oxygen ions are produced following the charge exchange process between the oxygen molecule and atomic oxygen ions. Thus, the variation in the emission rates of OI 630 nm depends on both the density of electrons and oxygen molecules present at a given altitude. Thereby, the emission rates are also significantly affected by the changes in the local electron densities in that region (Chamberlain, 1961; Sridharan et al., 1992; Saha et al., 2021). The electrons present in a location could be (i) those that are generated due to photoionization during the day, and (ii) those that are brought in from the equatorial region due to transport under the influence of equatorial electrodynamics or winds. Both these factors show a day-to-day variability. Optical photometers, spectrographs, and imagers have been developed to measure the nighttime airglow emissions over varying fields-of-view (e.g., Chakrabarti et al., 2001; Mukherjee et al., 2006; Rajesh et al., 2012; Narayanan et al., 2013; Phadke et al., 2014; Singh and Pallamraju, 2016, 2017) to infer the upper atmospheric dynamics prevalent at those locations in the nighttime.

The electric field in the upper atmosphere is eastward in the daytime (Fejer et al., 1991). Owing to the horizontal nature of the magnetic fields (**B**) over the dip-equator, this eastward electric field (**E**) gives rise to a **E** × **B** vertical drift, which is charge and mass independent. This drift causes an uplift of the plasma to higher altitudes over the equator. Plasma, thus lifted up, comes down to the off-equatorial regions along the magnetic field lines due to the gravitational and pressure gradient forces following the ambipolar diffusion, thereby creating a fountain like distribution in plasma with two crests in the electron density on

* Corresponding author.
E-mail address: raju@prl.res.in (D. Pallamraju).

https://doi.org/10.1016/j.jastp.2022.105965
Received 4 August 2022; Received in revised form 28 September 2022; Accepted 8 October 2022
Available online 13 October 2022

either side of the dip-equator. This is called the equatorial ionization anomaly (EIA) (e.g., Sastri, 1990; Rishbeth, 2000), which typically takes 2–3 h for the plasma to reach over the off-equatorial regions from the magnetic equator. It has been shown that the strength and the location of the EIA crest vary with the strength of the equatorial electric field. As the eastward equatorial electrojet (EEJ) is formed due to this primary eastward electric field (e.g., Woodman, 1970; Raghavarao et al., 1988, 1991; Hysell and Burcham, 2000), it has been considered to serve as a good proxy for the equatorial F-region electric field. Further, it has also been shown that the strength of the EEJ is directly proportional to the strength of the EIA (Raghavarao et al., 1978). The pre-reversal enhancement (PRE) in the zonal electric field is observed during sunset time, whose magnitude varies with season and solar activity (Farley et al., 1986). The PRE causes upward vertical drift, which can contribute to a resurgence of plasma in low-latitudinal regions in a manner similar to that of the daytime equatorial electric field. As mentioned above, the PRE magnitudes are dependent on the solar flux and season, and they can even be larger than those in the daytime, especially during equinoxes (Fejer et al., 2008; Fesen et al., 2000). Therefore, the latitudinal extent and magnitude of enhancement in electron densities at the EIA crest are also solar flux and season dependent. The signatures of the EIA can be noticed in the OI 630 nm ionospheric airglow emissions as well due to the temporal and latitudinal variations in electron densities. Nightglow observations of OI 630 nm emissions have been carried out earlier, and the results on many important thermospheric phenomena such as, ionospheric irregularities (e.g., Otsuka et al., 2002; Makela et al., 2004; Sekar et al., 2007, 2012; Saha et al., 2022), enhancement in nightglow emissions in the post-sunset hours (e.g., Rao and Kulkarni, 1973; Saha et al., 2021), atmospheric waves (e.g., Shiokawa et al., 2006), neutral wind and temperature (e.g., Gurubaran and Sridharan, 1993), midnight temperature maximum (e.g., Faivre et al., 2006), etc., have been reported in the literature. A resurgence or redevelopment in the crest of the EIA takes place due to the PRE, and its consequence can be seen after the sunset time for 1–2 h. After the cessation of PRE, the F-region electric field over the dip-equator becomes westward as measured by the Jicamarca incoherent scatter radar (ISR) (Fejer et al., 1991). Under the influence of this nocturnal electric field over the equator, the EIA crest can be expected to move equatorward. However, there are not many reports of studies on this aspect in the literature. It could be due to a large decrease in electron densities preventing reliable measurements using ionosondes. In this backdrop, the OI 630 nm emission variability provides an efficient means to monitor such movement, as (i) the emission rates are extremely sensitive to the variation in electron densities, and (ii) these emissions are integrated in an altitude region of around 100 km, with major contribution arising from the bottomside of the F-region of the ionosphere. Thus, as demonstrated in earlier works, these emissions have been shown to be able to capture very subtle features present in the ionosphere-thermosphere regions (Sridharan et al., 1993; Pallamraju et al., 2001; Sekar et al., 2012; Narayanan et al., 2013; Saha et al., 2021, 2022).

In this study, we have used spectral imaging observations of the nocturnal OI 630 nm emissions over Mt. Abu (24.6°N, 72.7°E, 19°N Mag), a low-latitudinal location, usually situated under the northern crest region of the EIA in the Indian longitudes. Latitudinal movement of the EIA crest during the nighttime has been investigated in this study. During the high solar activity year 2014, we have observed that the location of the EIA crest is within the field-of-view (FOV) of the instrument during three months of the observation duration (Jan–Mar). Equatorward movement of the crest has been observed later in the night on many occasions. In this study, we present the results obtained on the movement of the crest, both away from the equator and towards the equator, as a direct result of the changes in the equatorial electrodynamics. To the best of our knowledge, such results on the movement of the EIA crest, both away and towards the equator, have not been reported before in the literature. These results provide insights into the dynamical nature of the nocturnal variation in the OI 630 nm airglow emissions over a low-latitude location vis-à-vis its response to the equatorial ionospheric electrodynamics.

2. Data used

2.1. Optical data (OI 630 nm nightglow emissions)

High throughput Imaging Echelle Spectrograph (HiTIES) is used to observe the optical OI 630 nm emissions in the nighttime, which emanate from around 250 km altitude. The observations have been carried out from a low-latitude location in Indian longitudes, Mt Abu. The transition of O(^{1}D) to O(^{3}P) results in the emission of photons at 630 nm. The formation of excited atomic oxygen is due to a two-step process. The first is the formation of O_2^+ due to charge exchange between ambient O_2 and O^+, and the second one is dissociative recombination of O_2^+ with ambient thermal electrons. The radiative lifetime of OI 630 nm is 110 s. HiTIES has a FOV of 54°, and the slit is aligned along the meridional direction. It covers around 254 km in the north-south direction for a central emission altitude of 250 km. The whole spatial region has been segregated into five independent directions. These are: one along zenith, two regions along the northern direction, and two along the southern direction. The data are integrated for a 5-min duration to increase the signal-to-noise ratio (SNR), thereby, the uncertainty in the data is significantly reduced. Different types of nocturnal variations in terms of their magnitudes across latitudes are seen on different nights, which are shown in Fig. 1 and described in section 3.

2.2. Radio data (electron density)

Data from the Digisonde Portable Sounder (DPS-4D) at Trivandrum (TVM) (8.5°N, 76.9°E, 1.1°N Mag) (a dip-equatorial location) has been

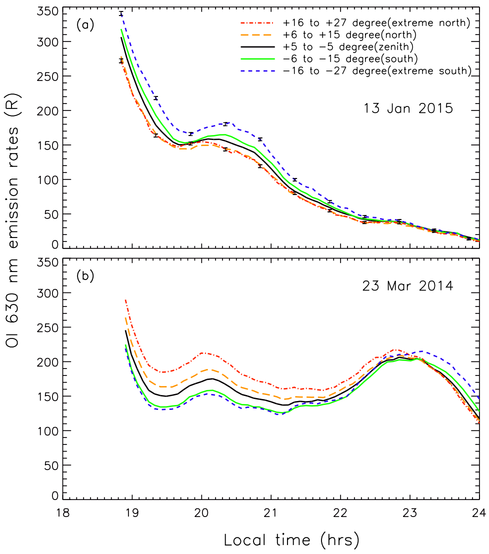

Fig. 1. Panel (a, b) Emission variations over the whole field-of-view of observations which have been segregated into five spatially independent directions as shown by different line styles and colours. Nocturnal variations in emissions on two sample nights are shown with different regions of enhancements corresponding to the enhanced electron densities due to the EIA crest.

used in this study to assess the equatorial ionospheric condition on a given day/night. F-region ionospheric vertical drifts during sunset time have been obtained using this data set at 7.5 min cadence. We have calculated the vertical drift of the ionospheric F-layer by monitoring the heights of the iso-electron density contours at 7 MHz.

2.3. Magnetic data (equatorial electrojet)

Hourly EEJ values have been obtained using the geomagnetic data from a dip-equatorial location, Tirunelveli (TIR) (8.7°N, 77.7°E, 0.2°N Mag), and an off-equatorial location, Alibag (ABG) (18.6°N, 72.9°E, 12.4°N Mag). Nighttime geomagnetic intensity values have been subtracted from those at each of the locations to remove the contribution due to the local geomagnetic field. Then, the magnetic data of ABG is subtracted from that of TIR to remove the magnetospheric currents, which thereby results in the magnitude of the equatorial electrojet over the Indian longitudes, as demonstrated in earlier studies (Chandra and Rastogi, 1974). The hourly geomagnetic data of TIR and ABG have been obtained from http://wdciig.res.in/WebUI/Home.aspx. Magnetometer data of minute resolution from Jicamarca (11.9°S, 283.1°E, 0.05°S Mag) and Piura (5.2°S, 279.4°E, 6.4°N Mag) have been obtained from http://lisn.igp.gob.pe, which have been used to calculate the daytime EEJ strengths in the American sector. The EEJ strength over Jicamarca is obtained by subtracting the magnetometer data of the off-equatorial location, Piura, in the same way as described for the estimation of the strength of EEJ over Indian longitudes.

3. Observations and results

Fig. 1 shows nocturnal variations of the OI 630 nm emissions of two sample nights that depict the different types of variabilities observed during nighttime over this low-latitudinal location. The whole FOV of the instrument has been segregated into five directions, as mentioned above, which are shown in different colours. The vignetting and Van-Rhijn effects have been corrected during the image processing. The data cadence is 5 min, and the uncertainty, σ, in each measurement varies typically from 1 to 3 R (as shown in Fig. 1a for emissions along two different directions). It can be noted that for most of the duration, the emission rates along all these view directions, and especially those along (i) the extreme south (zenith angle, 16°-27°), (ii) extreme north (zenith angle, 16°-27°), and (iii) the zenith, show magnitudes that are independent of each other as they are away by ±1σ (uncertainty) values of each other during most of the post-sunset hours. Fig. 1a shows larger emissions along the southern direction as viewed from Mt. Abu, whereas, Fig. 1b shows larger emissions along the northern direction after the sunset time. These different features, as depicted in Fig. 1, indicate the dynamic nature of the thermospheric behaviour, as the red line emissions readily respond to such variations. We have investigated the magnitudes of variation in emissions between the northern and southern directions, which is considered to be a result of the latitudinal movement of the crest in the EIA after the sunset time. The nights where the magnitudes of emissions between the two view directions differ by at least 2σ values at a given time are considered to determine this movement. Under this criterion, there exists a total of 122 nights of clear sky data (excluding moonlit and cloudy nights) obtained during the months of Jan, Feb, and Mar in the year 2014 (72 nights) and Jan and Feb in 2015 (50 nights) that are used for analysis. Crests have been found in the northern side (similar to Fig. 1b) on around 47% nights out of these 122 nights.

The different types of OI 630 nm nocturnal emission variations across latitudes, as seen along different view directions in the given FOV of HiTIES, are depicted in Fig. 1. Variations are seen during the course of the night as well. Variations are such that, on some nights during the sunset time, the emissions in the southern direction are larger as compared to those in the northern direction (e.g., Fig. 1a) and completely opposite on some other (e.g., Fig. 1b). This is most likely a consequence of transport processes in terms of the movement of the EIA crest across latitudes, which is different on different nights. From the production mechanism of the OI 630 nm nightglow discussed above, it can be noted that almost all the variabilities in the emissions are essentially due to the changes in the electron densities in the region of emissions, as also established in one of our earlier studies (Saha et al., 2021). We have shown in that study that the base of the F-layer height and the OI 630 nm emission magnitudes are anti-correlated. The variations in the F-layer height can bring in/take away the electrons to/from the altitudinal regions of OI 630 nm nightglow emissions. In other words, when the F-layer moves to higher (lower) altitudes, the molecular oxygen density decreases (increases) which affects the charge exchange process. Thereby, the emission rate decreases (increases). It was shown in that study that the emission rates estimated using the measured electron densities (from Ahmedabad, AMD, 23.0°N, 72.57°E) as inputs into the photochemical model showed a very high correlation (>0.9) with those observed over Mt. Abu. Thus, these variabilities are essentially due to the varying strengths of equatorial electrodynamics from one night to the other. In order to quantify such latitudinal movement of OI 630 nm emission after the sunset, ratios between emissions along the north-most (from now on represented as N) to the south-most (henceforth, S) view directions with respect to Mt. Abu have been considered. These two view directions correspond to a separation of about 2.3° in latitude. Therefore, the emission ratio of N to S greater than one can be attributed to the presence of the EIA crest northward of Mt. Abu. The increase in the values of the ratios is an indication of the intensification of the strength of the EIA crest and of its location further away towards north from Mt. Abu. This is because the column integrated emissions along N would cut across a larger number densities of reactants ($[N_e]$ and $[O_2^+]$) as compared to that towards S. We have investigated various possible causes that determine the motion of the EIA crest away from the dip-equator towards the low-latitudes, such as the EEJ and PRE.

3.1. Effect of the EEJ strength on the ratio of latitudinal emission rates

Earlier studies have shown that there exists a good correlation between the strengths of EIA and EEJ (Rush and Richmond, 1973; Raghavarao et al., 1978). The latitudinal extent of the plasma fountain is larger for greater strengths of EIA. As we are investigating the movement of EIA crest during post-sunset, we have considered integrated EEJ values for the whole day (7–17 LT) for comparing with the OI 630 nm nightglow emission measurements. The nightglow observations start every night in a programmed manner at 18.75 LT. Therefore, these integrated EEJ values have been compared with the N to S emission ratios for a duration of about 15 min (18.75–19.00 LT) soon after the start of the nocturnal emission observations. The variation in the ratios of the emissions clearly shows an increasing nature with the day of year (DOY). This indicates the changes that occur with the season as one traverses from winter time to equinoxes (January to March) (Fig. 2a). Here, the values of ratios corresponding to different months are shown in different colours. As the integrated EEJ strength serves as a proxy to the equatorial electric fields (Raghavarao et al., 1978; Sridharan et al., 1999; Hysell and Burcham, 2000), and thereby to the EIA strength, the variation in emission ratios has been compared with the integrated EEJ strengths as shown in Fig. 2b. A linear fit is drawn between these two and the linear correlation coefficient is calculated which is also shown in Fig. 2b. The nightglow emission ratio of the initial period shows a small increasing trend with the integrated EEJ variation within the given limitations. The limitation here is that the observations are available beginning only at 18.75 LT and not before. The airglow emission ratios were calculated for a constant time duration of 18.75–19.00 LT for all three months. As the plasma diffusion time for the movement of ionization from equatorial to low-latitudes is of the order of around 3 h, and so, the electron densities corresponding to the EIA crest could have also been formed even before the starting time of the observations of OI 630

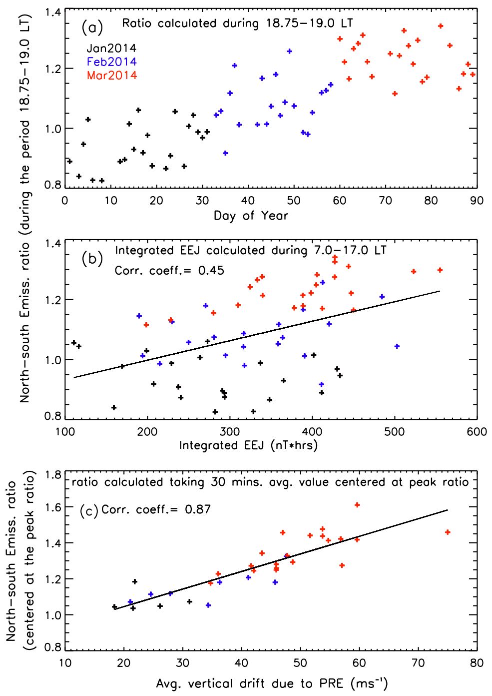

Fig. 2. Panels a and b show the variation in ratios of emissions obtained along extreme-north (N) and extreme-south (S) as viewed from Mt. Abu during 18.75–19.0 LT with respect to the DOY and integrated EEJ, respectively. Panel c shows the variation of ±15 min averaged ratio centered at the peak emission ratio of PRE. The PRE values are averaged (±15 min) around the peak.

nm nightglow emissions. Further, for the sake of completeness, we have also compared the variation of these ratios with the EEJ data integrated for the pre-noon hours as well, as carried out in some earlier studies (Raghavarao et al., 1978), and it has been noted that there exists no relation between them (not shown here). Therefore, a clear role of the daytime integrated EEJ strength on the observed emission ratios might not be revealed when only a fixed time duration of 18.75–19.0 LT nighttime airglow measurements are considered. Nevertheless, as it is known that the plasma diffusion initiated in the day is assisted and sometimes rejuvenated by the effect of the PRE at sunset time, the strength of PRE is considered as described below.

3.2. Effect of PRE on the variation in the ratio of latitudinal emission rates

PRE that occurs at the time of sunset over the dip-equator can cause a resurgence of plasma fountain, similar to that caused in the daytime EIA by the F-region electric fields. The strength of the PRE in electric field has been determined from the vertical drift by calculating the rate of change of height variation of the electron density at 7 MHz over TVM. The echoes of 7 MHz correspond to altitudes above 300 km, and so the effect of recombination on them is negligible (Bittencourt and Abdu, 1981). The strength of the PRE on a given day has been characterized by taking the average of ±15 min centered at the peak value of PRE occurrence. The time of occurrence of peak value in PRE is different in different months as the sunset times vary from January (18.3 LT) to March (18.6 LT). The peaks in the N–S emissions ratios have been found to occur over times varying from around 30–90 min from the time of occurrence of the peak PRE, as the relative strengths vary from one day to the other.

Around 33 nights have been found, wherein, the EIA crest crossed the zenith and moved towards the north, and a clear peak in the N–S emission ratios has been found. The data for around the first seven nights in the months of January and a few nights in each of the months have been excluded either due to unavailability of equatorial ionosonde data or due to the presence of moonlight in the FOV. Fig. 2c shows the integrated (for ±15 min centered at peak PRE value) PRE versus the peak ratio (integrated for ±15 min centered at peak ratio value) as obtained over different times, which are well correlated (correlation coefficient of 0.87). Therefore, the strength of the PRE seems to be deciding the extent of northward movement of the crest after the sunset over low-latitudes.

3.3. Reversal in the EIA crest

So far, we have discussed the northward movement of the EIA crest by considering the emission ratios between the northern and southern directions. During the month of March, the values of the ratios are higher, which indicate that the likely position of the EIA crest is towards latitudes further away in the northern direction as compared to other months (January and February). This is most likely due to the effect of a stronger PRE in March as compared to that in January (Fejer et al., 1991). In Fig. 3, the airglow emission variations for 12 nights (four nights for each of the three months in the year 2014) are shown. Higher emissions along N have been observed on all these nights. Interestingly, as we move from January to March, the differences in magnitudes of emission rates between those obtained in the north and the south increase, with larger values towards North. In this context, it may be noted that the emission rates for February and March are larger, and the values are depicted on the right-side of the y-axis. This is understood to be due to larger plasma densities being brought over to the low-latitudes from the equatorial locations, displaying a clear effect of plasma transport that varies from month to month. After sunset, the rate of decrease in the magnitude of emissions becomes smaller along N compared to that of S. In contrast to this, the emission magnitudes that were larger along N decrease at a rate faster as compared to those at S at a later time. This is inferred to be due to the process of initiation in the reverse movement of the EIA crest as a function of time. As discussed in section 1, the daytime eastward electric field causes the upward plasma vertical drift, the strength of which decides the latitudinal location and the plasma density of the crest of the EIA. Thus, the reversal in the EIA crest in the night can be inferred to be due to the night time westward electric field over the magnetic equator. Further, in order to explore if meridional winds can contribute to the increase in emissions as observed in the southern direction (towards the equator), we have studied their typical variation during the nights. The increase in emissions in the southern direction is observed during 21–24 LT, at which time the meridional winds are typically equatorward (Drob et al., 2015; Saha et al., 2021). It is known that the equatorward meridional winds cause an uplift of the plasma along the field lines to higher altitudes, and consequently, a decrease of OI 630 nm emissions is seen (Saha et al., 2021), and not an increase as seen in the present case. Therefore, it can be inferred that the meridional winds at this time cannot contribute to the observed increase in OI 630 nm emissions in the southern direction.

To investigate the reverse movement of the EIA crest, ratios in emissions from N to S have been estimated for all the times, unlike only around peak values as shown in Fig. 2. The variation in the N–S ratios on the nights shown in Fig. 3 is depicted in Fig. 4. On a given night, the maximum value in ratios suggests that the crest is located in the northern region, and the time corresponding to the maximum ratio is considered to indicate the time when the EIA crest has reached that

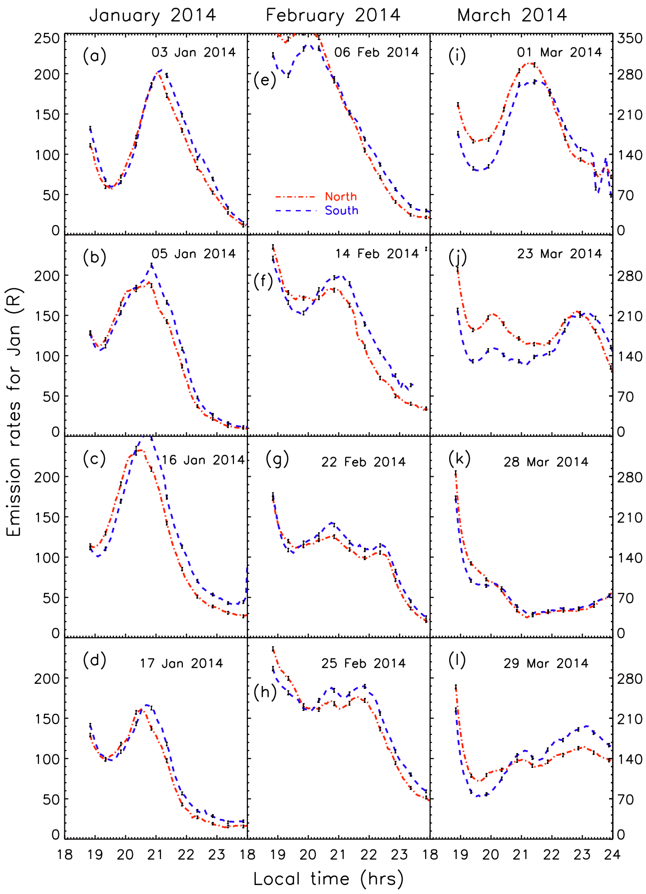

Fig. 3. The columns show emission variations along the two directions (N and S) for 12 nights during Jan–Mar 2014, 4 nights for each of the months. The left side y-axis corresponds to the month of Jan, and the right one corresponds to those for Feb and Mar. Uncertainty in the measurements is small (±1.4 – ±2.4 R), as shown in each of the figures.

location. As the crest moves in the southward direction it crosses the value of one, which indicates that emissions over the northern and southern sides of the view direction are almost equal. The minimum values in the ratio indicate that the EIA crest is located in the southernmost view direction of HiTIES on a given night. To identify the times of maximum or minimum values in the ratios, we have considered those times only when the differences between the emissions along N and S are greater than 10 R, which is at least 3 to 4 times greater than the value of the measurement uncertainty (σ). After the time of occurrence in the minimum value, the ratios trace back to around a value of one with time as the poleward side of the EIA crest moves further southward and away from the HiTIES FOV, and so, the airglow emissions at both N and S decrease to the nightly 'background' values. On some nights, e.g., 22 Feb and 25 Feb 2014, after the maximum values in emission ratios were observed, there were one or more excursions in emissions before the ratios reached to the value of one. Such observations are possibly due to the latitudinal structures that may exist in the EIA on a given night. In the present work, during the high solar activity year 2014, we have noted the reverse movement of the EIA crest on many nights. On some nights, there are data gaps due to the presence of moonlight in the FOV. Also, there are other nights wherein equatorial spread-F occurred. These two effects, when present over large spatial extents in the given FOV, prevent unambiguous determination of the reversal times in the EIA all through the FOV. Therefore, for these nights, a portion of the distance, either from north to zenith or zenith to south is considered for the estimation of reversal speeds.

To provide a visual picture of this reversal in the equatorial ionization anomaly, we reproduce a figure from the work of Sridharan et al. (1993) as Fig. 5. An all-sky Imaging Fabry-Perot Spectrometer was used to measure the OI 630 nm nocturnal emissions from Mt. Abu. Images of Fabry-Perot interferometric rings were reported in that work which serves as a clear observation of the equatorward movement of the EIA crest as observed on the night of 05 Jan 1992. Each image of this figure shows Fabry-Perot fringes corresponding to data obtained for half an hour over a 140° FOV. The fiducial shows the orientation of the magnetic north. From the sequence of images, it is clear that during

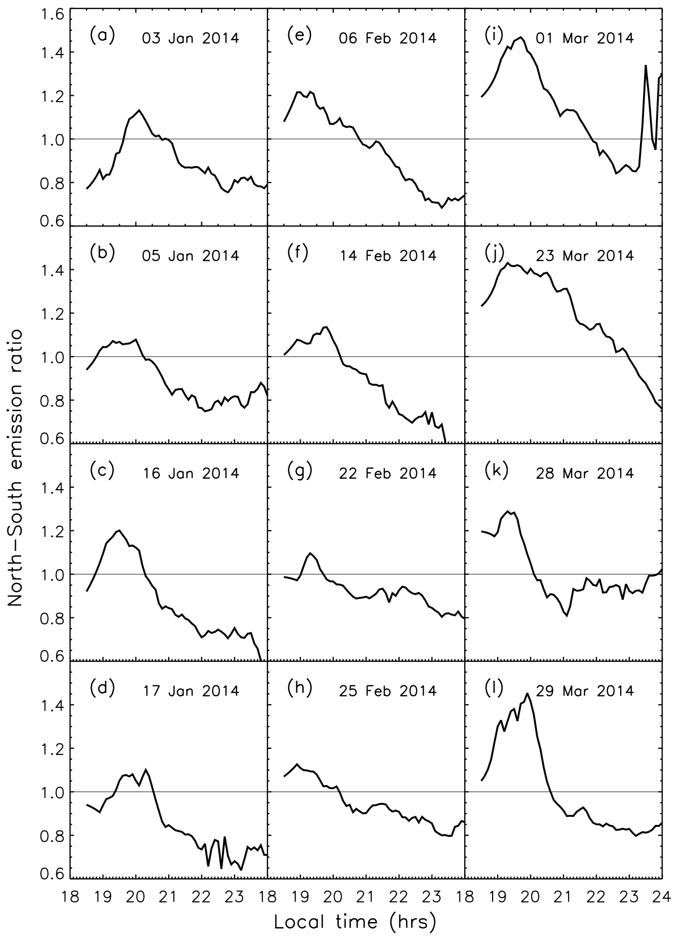

Fig. 4. The N to S ratios obtained in the OI 630 nm emission rates are shown for the 12 nights whose nocturnal emission rates along N and S are depicted in Fig. 3.

1916–1946 LT, the emission rates are higher towards north, indicating that the crest of the EIA is northward of Mt. Abu on that night during the high solar activity period (the solar flux was 257.7 solar flux units on this day, 1 sfu = 10^{-22} $Wm^{-2}Hz^{-1}$). As time progresses, it can be seen that the brightness in emission sequentially shows a southward movement. In the images obtained during 2051–2153 LT, the emission intensity in all the fringes seems to be equal in all directions. Later, this enhancement in emission rates moved further southwards, and by 0137 h of 06 Jan 1992, the EIA crest had moved away from the FOV of the instrument. Based on these measurements, the speed of the movement was reported to be 1.4° lat.hrs^{-1} or 42 ms^{-1}.

In the present study, we have estimated the speeds of the equatorward movement of the EIA by taking the time differences of the crests at north and south. The distance between the centre of northern and southern directions is considered for the estimation of the speed of the reversals. The uncertainties in the location arise due to the spatial extent considered for each directional segment (north and south), and we have taken the centre-to-centre distance between two segments while calculating the speeds. We have also checked the available optical data in January and February in the year 2015 and calculated the speed of the movement of the EIA crest. A total of 40 nights, 25 in 2014 and 15 in 2015, have been considered for estimation of the speeds of the EIA crest. The speeds obtained from the present data fall in the range of 10–55 ms^{-1} with uncertainty in them of around 6-30 ms^{-1} as shown in Fig. 6.

In an earlier work that was based on optical imager measurements from Kolhapur (16.8°N, 74.1°E, 11.1°N Mag), the reversal speeds in EIA were reported to be in the range of 25–90 ms^{-1} for nights during January–March in the year 2008 (Narayanan et al., 2013). We have also included those values reported in that work in Fig. 6.

As discussed so far, the upward vertical drift during sunset causes the poleward movement of the EIA crest, and then, in the nighttime, as the zonal electric field reverses its direction, the vertical drift becomes downward. Thus, the base of the F-layer height is pushed down, and as a consequence, it gives rise to larger emissions in the southern direction.

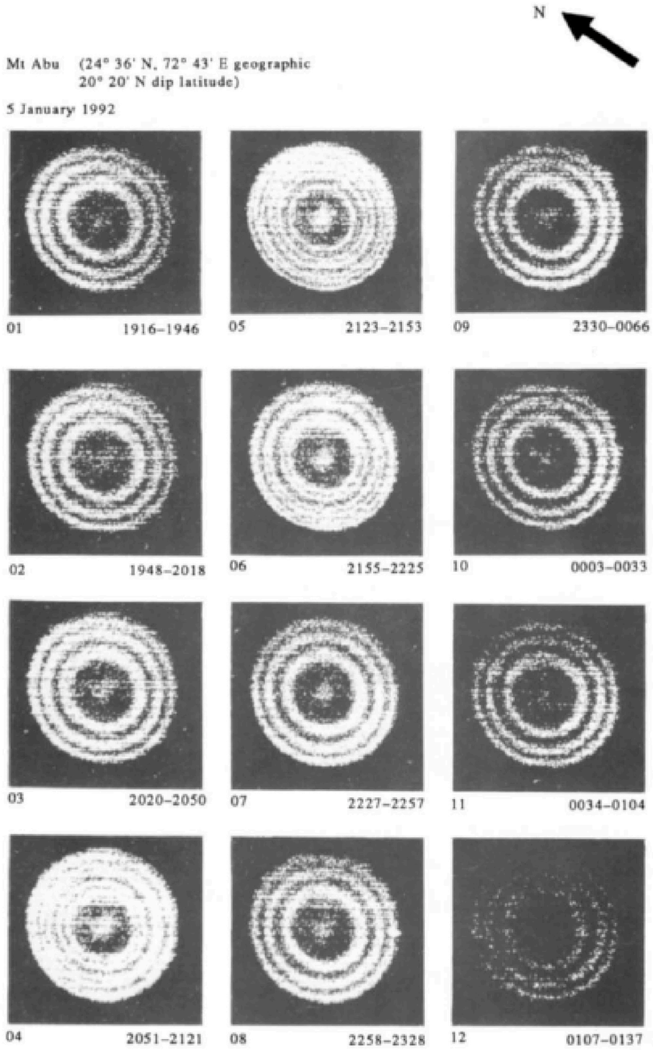

Fig. 5. Equatorward movement of EIA crest obtained from Mt. Abu on Jan 05, 1992 using the all-sky imaging Fabry-Perot spectrometer [Reproduced from Fig. 1 of Sridharan et al., 1993].

To explore the relationships of the speeds of reversal with the background plasma density, meridional neutral winds, and evening time equatorial electrodynamics, if any, we have plotted them with respect to the solar flux, day of the year (seasons), and PRE strength in Fig. 6.

Fig. 6a depicts the variation in the speeds of EIA crest movement with solar flux values corresponding to the years 2014 and 2015. The reversal speeds reported in earlier studies in 1992 (Sridharan et al., 1993) and 2008 (Narayanan et al., 2013) are also included in this figure. Estimated speeds from Narayanan et al. (2013) show large excursions within a small variation in solar flux, which was calculated during the year 2008. In the years 2014 and 2015, the solar flux values were comparatively higher than those in 2008. The average speed of the crest decreased during the high solar active year 2014–2015 compared to that calculated over Kolhapur in 2008. We do recognize that there could probably be differences in the reversal speeds with respect to magnetic latitudes, as Mt. Abu and Kolhapur are far apart. Nevertheless, a decrease is seen in the values of the reversal speeds of EIA with solar flux, although the nature of its variation does not indicate any conclusive result in the given extent of the data.

Fig. 6b depicts the variation in the reversal speeds with respect to the

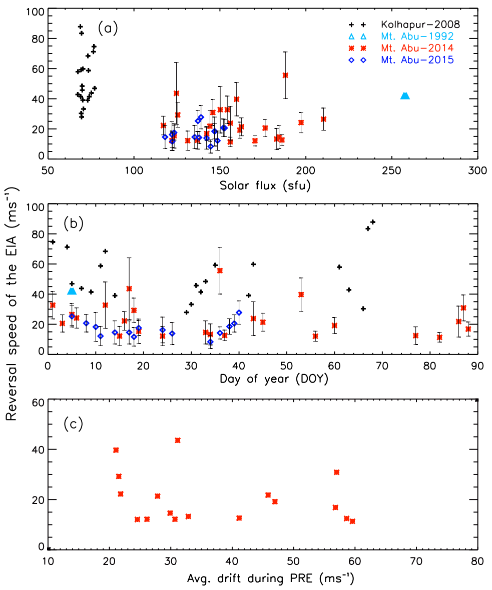

Fig. 6. (a) The reversal speeds of the EIA crest movement with solar flux variation are depicted for a total of 61 nights. Results from earlier published results from different studies are also included. The speeds calculated for the emissions obtained from Mt. Abu for two different years, 2014 and 2015, are shown in red and blue colour, respectively. (b) Reversal speeds of the EIA crest for the same nights have been depicted with the day of year (DOY). (c) The reversal speed of the EIA crest is shown along with the available average vertical drifts obtained during PRE in the year 2014.

DOY, wherein, all the available data are plotted. Even though it may appear that the envelope of higher values in reversal speeds shows a decreasing trend with DOY (season), unambiguous inferences cannot be made as the data are biased with a larger number of nights during the months of January and February as compared to that during March. Although the seasonal behaviour of vertical drift over the dip-equator shows an increasing nature (Fejer et al., 1991), and the poleward meridional wind a decreasing behaviour from January to March (Drob et al., 2015), the variation in reversal speeds, however, does not show any relation whatsoever with model meridional winds or the solar flux.

From the results presented in this study, it is quite clear that the northward extent of the EIA crest is solely dependent upon the strength of the vertical drifts generated by PRE electric fields in the evening time. Therefore, we have explored if the variation in the reversal speeds observed in the EIA movement has any relation with the strength of the PRE. On the basis of the available data on equatorial vertical drift, reversal speeds for seventeen nights during 2014 have been obtained and are depicted in Fig. 6c, and it can be readily noted that these two do not show any relation with each other.

4. Discussion

From the measurement of vertical plasma drifts over the magnetic equator as presented by Fejer et al. (1991), it is known that the drifts are vertically downward in the nighttime, indicating a westward electric field. It was also shown that the magnitude and the variability of the downward plasma drift undergoes significant changes, both during the course of a night and from night-to-night. Therefore, it can be expected that the equatorward movement of the crest of the EIA is due to such westward electric field over the equator. However, this has not been demonstrated in any of the studies so far. This is because direct measurements of the westward equatorial electric fields have been mainly restricted to the American longitudes where an ISR exists. Further, satellite measurement of ion-drifts or electric fields over the magnetic equator are not available over the Indian longitudes during the nighttime. Few passes of C/NOFS over Indian longitudes during our observational period, whenever available, were above 500 km altitude, and the electron densities were low. Presumably, due to these factors, the vertical drift measurements on-board C/NOFS, whenever present, showed large fluctuations (not shown here).

Therefore, in the absence of any direct measurement(s), we ascertain the veracity of our interpretation on the westward electric field being the cause for the equatorward movement of the EIA by taking recourse to the fact that the equatorial electric fields are global in nature. The ionospheric electric fields are governed by $\oint \boldsymbol{E}.\boldsymbol{dl} = 0$, where $\boldsymbol{E}$ is the electric field at a given location and $\boldsymbol{dl}$ is the element of length along the dip-latitude. Therefore, it is imperative that larger eastward electric field in a longitude sector will be compensated by a simultaneous westward electric field in the opposite sector (Fejer et al., 1991). In this background, we consider the findings of an earlier study as a beacon to go forward, in which Sastri et al. (1992) showed that the effects of prompt-penetration during substorm event over two equatorial locations in the opposite longitudes, Kodaikanal in the Indian sector and Huancayo in the South American sector, were greatly related. In that study, it was shown that an increase in polar cap potential decreases the F-layer height over Kodaikanal, which was in simultaneity with an increase in height of the F-layer over Huancayo. Subsequently, the decrease in polar cap potential causes an increase in the F-layer height over Kodaikanal and a decrease over Huancayo (Fig. 7). Another example in which the daytime upward vertical drift over Jicamarca was perfectly anti-correlated with the nighttime downward vertical drift over India was presented for the geomagnetic storm event of Apr 17, 2002 (Kelley et al., 2007). The results reported in these two studies are a clear demonstration of the irrotational nature of the global ionospheric equatorial electric field. However, these events were during geomagnetic disturbed conditions, wherein the effects are known to get accentuated. Such results motivated us to explore whether this effect can be established during geomagnetic quiet conditions also, to which our present experimental results pertain to. To the best of our knowledge, there has been no experimental evidence depicting the irrotational nature of the global ionospheric electric field that has been reported for geomagnetic quiet times by simultaneous measurements. This is most likely due to the subtle nature of changes, especially in the night side. This irrotational nature of the equatorial electric field, which satisfies the equation $\oint \boldsymbol{E}.\boldsymbol{dl} = \oint \boldsymbol{Bv}.\boldsymbol{dl} = 0$, is used in the process of generation of the global empirical ionospheric vertical plasma drift model by Scherliess and Fejer (1999). Here, we have tried to show simultaneous variation in the day and nighttime electric field variations using nighttime vertical drifts and daytime EEJ strengths from two opposite longitude sectors during geomagnetic quiet time periods. The vertical drifts measured from ISR over Jicamarca are used to serve as a proxy for nighttime ionospheric electric field, whereas, the daytime EEJ variation measured from Indian sector is used to serve as a proxy of daytime electric field. Such simultaneous variation of the nighttime vertical drifts and daytime EEJ strengths for one non-ESF night over Jicamarca is shown in Fig. 8. The temporal variation of the vertical drift on the nightside shows a clear anti-correlation with the EEJ variation on the dayside. Similarly, in reciprocity, the variation in the EEJ over Jicamarca sector indicates the variation in the nighttime electric fields over Indian sector.

In this background, we have attempted to explore the equatorial electrodynamic behaviour at opposite longitudes in simultaneity with those of our measurements over Indian longitudes. In order to do that,

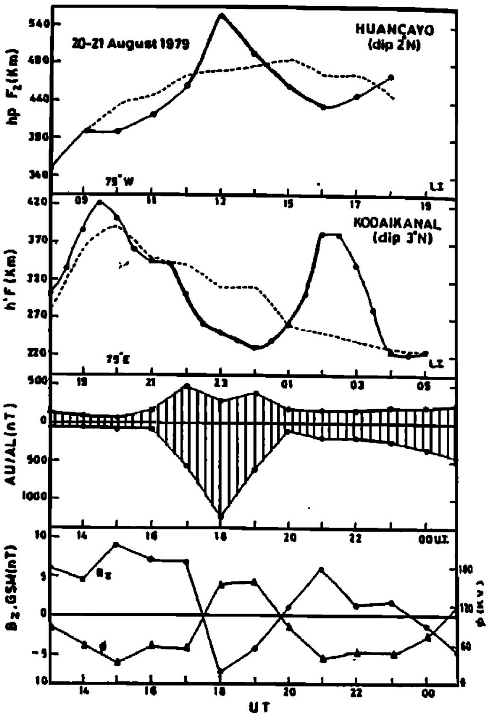

Fig. 7. The top panels show the ionospheric height variation at Huancayo and Kodaikanal on 20–21 Aug 1979. The bottom panels indicate the presence of strong geomagnetic disturbance on that day [Reproduced from Fig. 2 of Sastri et al., 1992].

we have considered the daytime EEJ strength integrated for pre-noon (duration 8–12 LT for Jicamarca) as a proxy of the daytime equatorial F-region over the American longitudes (e.g., Raghavarao et al., 1978; Hysell and Burcham, 2000). We have compared this with the nighttime reversal speeds of the EIA crest obtained in simultaneity using the optical measurements over the Indian sector as shown in Fig. 9. As discussed earlier, the reversal of EIA depends on the variation of the nighttime westward electric field, therefore, the speeds of the reversal of EIA crest have been compared with the strengths of the daytime EEJ at Jicamarca. It is remarkable that these two proxies correlate very well (correlation coefficient of 0.78). Here, the nights in the year 2014 when the EIA crest had reached the latitude of Mt. Abu as seen in the emissions have been considered. On many nights in the year 2015, the EIA crest did not reach Mt. Abu, most likely due to the decreased solar activity in 2015 compared with 2014, and hence, these have not been included in this analysis. It should be mentioned here that the three points with speeds greater than 40 ms^{-1} have not been considered for the calculation of the correlation coefficient. The large deviation in the speeds on these three nights could not be understood, at present, especially as these were geophysically quiet days and also as the rest of the values are around 30 ms^{-1} or less. For the sake of completeness, we have compared and calculated the correlations between the integrated EEJ over American longitude with the reversal speeds for other time durations also, such as, 8–13 LT (corr. coeff. 0.74), 8–14 LT (corr. coeff. 0.68), 9–12 LT (corr. coeff. 0.74), 9–13 LT (corr. coeff. 0.7), and 10–13 LT (corr. coeff. 0.64) and it can be noted that they all are positively correlated.

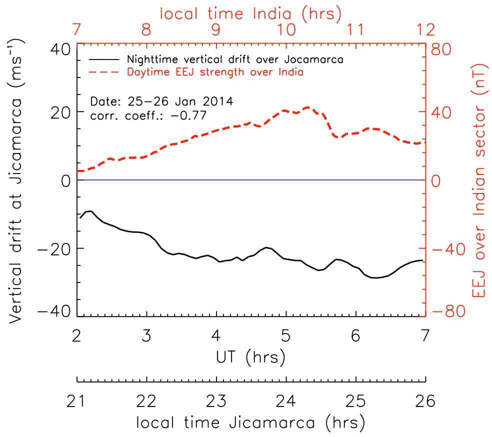

Fig. 8. The variation of nighttime vertical drift over Jicamarca is shown with simultaneous variation of EEJ over Indian sector of a given day which is a non-ESF night over Jicamarca. The universal time and corresponding local times at Jicamarca and Indian sector are shown in different x-axes. These variations show a clear anti-correlation behaviour between these two.

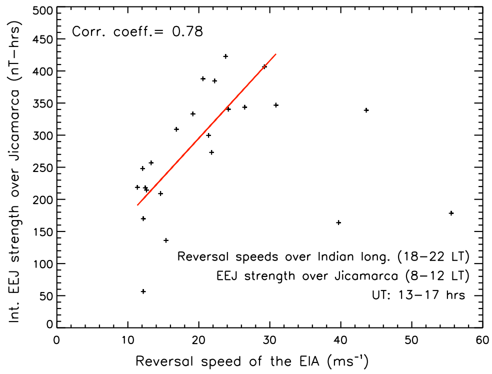

Fig. 9. Integrated EEJ variation for the duration 8–12 LT over Jicamarca is compared with the reversal speed of EIA depicted in Fig. 6b over Indian sector for the year 2014. The three nights when the speeds were >40 ms^{-1} have not been considered in obtaining the linear fit and the correlation coefficient.

The present results are particularly interesting as they show the experimental evidence of the global nature of equatorial electric fields during the geomagnetic quiet time periods. In doing so, two proxies for electric fields integrated EEJ strength in the daytime and reversal speeds of EIA in the nighttime, as seen in OI 630 nm airglow emissions, have also been characterized. The electric fields are extremely difficult to measure during nighttime. Due to recombination among neutrals and ions, and low electron densities in the nighttime ionosphere, it is not possible to obtain unambiguous information of nighttime electric field from the digisonde data over the equator. That is the reason why we consider the variation in the height of 7 MHz of the digisonde frequency, as the height of reflection is greater than 300 km for this frequency in the evening time which is used to obtain the information on PRE. Therefore, only measurements from an ISR located over the magnetic equator can yield accurate information on the equatorial electric fields. However, it is practically impossible to install an ISR over several longitudes around the globe. In contrast, it is more viable to obtain the OI 630 nm nightglow measurements over a large FOV at different longitudinal sectors, which could give information on relative variations in the electric field. It is expected that simultaneous measurements of westward electric fields from ISR, Jicamarca and estimation of reversal speeds in EIA as measured from optical emissions from the American longitude sector will enable a direct comparison and enable quantification of the EIA reversal speeds with the equatorial electric fields. Models and simulation studies will also help in quantifying the extent of correspondence between the reversal speed and nighttime electric field variations, which will be carried out in the future.

5. Summary

OI 630 nm emission data from a large FOV optical instrument, HiTIES, is used to investigate the latitudinal movement of the EIA crest during the post-sunset time for geomagnetic quiet conditions. The latitudinal movement of the EIA crest has been observed in the both direction, poleward movement for around 1 h after the sunset and then, reverses its direction towards the equator. During March (and towards the end of February), it has been observed that the airglow emissions along northern direction are larger after the sunset time as compared to those along the southern direction when viewed from Mt. Abu. The ratios in emissions towards north and south directions have been investigated with the equatorial electrodynamical phenomena, like daytime integrated EEJ and the PRE strength of electric field. A good relationship between the vertical drift due to PRE in electric field at sunset time and N–S emission ratios in the nightglow has been obtained. As the strength of the PRE increases, plasma rises to higher altitudes over the dip-equator, and due to the well-known plasma fountain effect, it moves to latitudes farther away. As the night progresses, the ambient plasma is continually lost due to recombination resulting in a decrease of emissions. The crest formed at the northern location traces back towards the equator, which, in turn, shows larger airglow emission values in the southern region (as compared to those in the northern) later in the night. The speeds of the reverse movement of the crest have been estimated for different nights and are found to be varying in the range of 10–55 ms^{-1} with more number of nights having values closer to the lower range. These were compared with the variations in the equatorial PRE, solar flux, and seasons, but except for a weak trend in decrease in speeds with the increase in solar flux, no clear correspondence was noted. Thus, in this study, it is clearly shown that the primary reason for the variation in the speeds of reversal in EIA is due to the variation in nocturnal westward electric fields over the magnetic equator. Considering the data from other longitude sectors and given the fact that the equatorial electric fields are global in nature ($\oint E.dl = 0$), we have compared the reversal speeds in the EIA crest obtained from Indian longitude sectors using optical emissions with the daytime integrated EEJ strength from opposite longitude sector (Jicamarca). The pre-noon time EEJ strength over Jicamarca shows good relationship with the observed reversal speeds in the present study, which confirms our interpretation and establishes an empirical evidence to show that the observed variation in the equatorward movement of the EIA crest is indeed due to the nighttime westward electric field. The present results are particularly interesting as they show the experimental evidence of the global nature of equatorial electric fields during the geomagnetic quiet time periods. In doing so, through this work, the speeds of equatorward movement of the EIA emerge as a viable proxy to determine the temporal behaviour of the nightly westward electric fields – which are otherwise difficult to obtain. It is envisaged that such remote sensing measurements of optical OI 630 nm nightglow emissions at different latitudes, either from ground-based or space-borne platforms, can yield information on the relative nightly variation in the westward equatorial electric fields.

Declaration of competing interest

The authors declare that they have no known competing financial interests or personal relationships that could have appeared to influence the work reported in this paper.

Data availability

Data will be made available on request.

Acknowledgement

The nighttime optical data used in this study, have been obtained from PRL's optical aeronomy observatory at Gurushikhar which is maintained by the Physical Research Laboratory. The geomagnetic data used for calculation of the electrojet strength have been obtained from the ground-based magnetometers maintained by the Indian Institute of Geomagnetism http://wdciig.res.in/WebUI/Home.aspx. The magnetometer data over Jicamarca sector is obtained from http://wdciig.res.in/WebUI/Home.aspx. The Jicamarca ISR data have been obtained from http://millstonehill.haystack.mit.edu/list. The quasi-dipole coordinate of a given location is obtained from http://www.geomag.bgs.ac.uk/. The digisonde data of the locations at AMD and TVM are obtained from the Physical Research Laboratory, Ahmedabad, and Space Physics Laboratory, Trivandrum, respectively. This work is supported by the Department of Space, Government of India.

References

Bittencourt, J.A., Abdu, M.A., 1981. Theoretical comparison between apparent and real vertical ionization drift velocities in the equatorial F region. J. Geophys. Res. 86, 2451–2454. https://doi.org/10.1029/JA086iA04p02451.

Chakrabarti, S., Pallamraju, D., Baumgardner, J., Vaillancourt, J., 2001. HiTIES: a high throughput imaging Echelle spectrograph for ground-based visible airglow and auroral studies. J. Geophys. Res. 106 (A12) https://doi.org/10.1029/2001JA001105, 30,337-30,348.

Chamberlain, J.W., 1961. Physics of the Aurora and Airglow. Academic Press.

Chandra, H., Rastogi, R.G., 1974. Geomagnetic storm effects on ionospheric drifts and the equatorial Es over the magnetic equator. Indian J. Radio Space Phys. 3, 332–336. http://nopr.niscair.res.in/handle/123456789/37843.

Drob, D.P., Emmert, J.T., Meriwether, J.W., Makela, J.J., Doornbos, E., Conde, M., et al., 2015. An update to the Horizontal Wind Model (HWM): the quiet time thermosphere. Earth Space Sci. 2 (7), 301–319. https://doi.org/10.1002/2014EA000089.

Faivre, M., Meriwether, J., Fesen, C., Biondi, M., 2006. Climatology of the midnight temperature maximum phenomenon at Arequipa, Peru. J. Geophys. Res.: Space Phys. 111 (A6) https://doi.org/10.1029/2005JA011321.

Farley, D.T., Bonelli, E., Fejer, B.G., Larsen, M.F., 1986. The prereversal enhancement of the zonal electric field in the equatorial ionosphere. J. Geophys. Res. 91 (A12), 13723–13728. https://doi.org/10.1029/JA091iA12p13723.

Fejer, B.G., de Paula, E.R., Gonzalez, S.A., Woodman, R.F., 1991. Average vertical and zonal F region plasma drifts over Jicamarca. J. Geophys. Res. 96 (A8), 13901–13906. https://doi.org/10.1029/91JA01171.

Fejer, B.G., Jensen, J.W., Su, S.-Y., 2008. Quiet time equatorial F region vertical plasma drift model derived from ROCSAT-1 observations. J. Geophys. Res. 113, A05304 https://doi.org/10.1029/2007JA012801.

Fesen, C., Crowley, G., Roble, R., Richmond, A., Fejer, B.G., 2000. Simulation of the pre-reversal enhancement in the low latitude vertical ion drifts. Geophys. Res. Lett. 27 (13), 1851–1854. https://doi.org/10.1029/2000GL000061.

Gurubaran, S., Sridharan, R., 1993. Effect of meridional winds and neutral temperatures on the F layer heights over low latitude. J. Geophys. Res. 98 (A7), 635. https://doi.org/10.1029/92JA02029, 11,629-11.

Hysell, D.L., Burcham, J.D., 2000. Ionospheric electric field estimates from radar observations of the equatorial electrojet. J. Geophys. Res. 105 (A2), 2443–2460. https://doi.org/10.1029/1999JA900461.

Kelley, M.C., Nicolls, M.J., Anderson, D., Anghel, A., Chau, J.L., Sekar, R., Subbarao, K.S. V., Bhattacharyya, A., 2007. Multi-longitude case studies comparing the interplanetary and equatorial ionospheric electric fields using an empirical model. J. Atmos. Sol. Terr. Phys. 69, 1174–1181. https://doi.org/10.1016/j.jastp.2006.08.014.

Makela, J., Ledvina, B., Kelley, M., Kintner, P., 2004. Analysis of the seasonal variations of equatorial plasma bubble occurrence observed from Haleakala, Hawaii. Ann. Geophys. 22, 3109–3121. https://doi.org/10.5194/angeo-22-3109-2004.

Mukherjee, G., Parihar, N., Niranjan, K., Manju, G., 2006. Signature of midnight temperature maximum (MTM) using OI 630 nm airglow. Indian J. Radio Space Phys. 35 (1), 14–21. http://nopr.niscair.res.in/handle/123456789/3993.

Narayanan, V.L., Gurubaran, S., Emperumal, K., Patil, P., 2013. A study on the night time equatorward movement of ionization anomaly using thermospheric airglow imaging technique. J. Atmos. Sol. Terr. Phys. 103, 113–120. https://doi.org/10.1016/j.jastp.2013.03.028.

Otsuka, Y., Shiokawa, K., Ogawa, T., Wilkinson, P., 2002. Geomagnetic conjugate observations of equatorial airglow depletions. Geophys. Res. Lett. 29, 1753. https://doi.org/10.1029/2002GL015347.

Pallamraju, D., Baumgardner, J., Chakrabarti, S., Pedersen, T.R., 2001. Simultaneous ground based observations of an auroral arc in daytime/twilighttime OI 630.0 nm emission and by incoherent scatter radar. J. Geophys. Res. 106 (A4), 5543–5549. https://doi.org/10.1029/2000JA000244.

Phadke, K.A., Narayanan, R., Singh, R.P., Pallamraju, D., 2014. An automated CCD-based multi-wavelength airglow photometer (CMAP) for optical aeronomy studies. PRL Tech. Note. https://doi.org/10.13140/RG.2.1.2641.7520. PRL-TN-2014-107.

Raghavarao, R., Sharma, P., Sivaraman, M.R., 1978. Correlation of Ionization anomaly with the intensity of the electrojet. Space Research 18, 277–280. https://ui.adsabs.harvard.edu/abs/1978spre.conf..277R/abstract.

Raghavarao, R., Sridharan, R., Sastri, J.H., Agashe, V.V., Rao, B.C.N., Rao, P.B., Somayajulu, V.V., 1988. The Equatorial Ionosphere; WITS Handbook. World Ionosphere/Thermosphere Study, vol. 1. SCOSTEP Secretariat, University of Illinois, Urbana.

Raghavarao, R., Wharton, L., Spencer, N., Mayr, H., Brace, L., 1991. An equatorial temperature and wind anomaly (ETWA). Geophys. Res. Lett. 18 (7), 1193–1196. https://doi.org/10.1029/91GL01561.

Rajesh, P., Liu, J., Lin, C., Chen, A., Hsu, R., Su, H., 2012. Airglow observation over equatorial and low-latitudes in the extreme solar minimum of 2007-2008, 94.20. Ac; 94.20. dt; 96.60. qd. http://nopr.niscair.res.in/handle/123456789/14042.

Rao, V.R., Kulkarni, P., 1973. 6300 Å night airglow enhancements in low latitudes. J. Atmos. Terr. Phys. 35 (2), 193–206. https://doi.org/10.1016/0021-9169(73)90087-1.

Rishbeth, H., 2000. The equatorial f-layer: progress and puzzles. Ann. Geophys. 18, 730–739. https://doi.org/10.1007/s00585-000-0730-6.

Rush, C.M., Richmond, A.D., 1973. The relationship between the structure of the equatorial anomaly and the strength of the equatorial electrojet. J. Atmos. Terr. Phys. 35, 1171–1180. https://doi.org/10.1016/0021-9169(73)90013-5.

Saha, S., Pallamraju, D., Pant, T.K., Chakrabarti, S., 2021. On the cause of the post-sunset nocturnal OI 630 nm airglow enhancement over low-latitude thermosphere. J. Geophys. Res.: Space Phys. 126, e2021JA029146 https://doi.org/10.1029/2021JA029146.

Saha, S., Pallamraju, D., Ghodpage, R., 2022. Investigation of equatorial plasma bubbles as observed in the OI 630 nm nightglow emissions over off-equatorial and low-latitudinal locations over Indian longitudes. Adv. Space Res. https://doi.org/10.1016/j.asr.2022.08.023.

Sastri, J.H., 1990. Equatorial anomaly in F-region—a review. Indian J. Radio Space Phys. 19, 225–240. http://nopr.niscair.res.in/handle/123456789/36285.

Sastri, J.H., Ramesh, K.B., Rao, H.N.R., 1992. Transient composite electric field disturbances and near dip equator associated with auroral sub storms. Geophys. Res. Lett. 19 https://doi.org/10.1029/92GL01447, 0094– 8276.

Scherliess, L., Fejer, B.G., 1999. Radar and satellite global equatorial F region vertical drift model. J. Geophys. Res. 104 (A4), 6829–6842. https://doi.org/10.1029/1999JA900025.

Sekar, R., Chakrabarty, D., Pallamraju, D., 2012. Optical signature of shear in the zonal plasma flow along with a tilted structure associated with equatorial spread F during a space weather event. J. Atmos. Sol. Terr. Phys. 75–76, 57–63. https://doi.org/10.1016/j.jastp.2011.05.009.

Sekar, R., Chakrabarty, D., Sarkhel, S., Patra, A., Devasia, C., Kelley, M., 2007. Identification of active fossil bubbles based on coordinated VHF radar and airglow measurements. Ann. Geophys. 25, 2099–2102. https://doi.org/10.5194/angeo-25-2099-2007.

Shiokawa, K., Otsuka, Y., Ogawa, T., 2006. Quasiperiodic southward moving waves in 630-nm airglow images in the equatorial thermosphere. J. Geophys. Res.: Space Phys. 111 (A6) https://doi.org/10.1029/2005JA011406.

Singh, R.P., Pallamraju, D., 2016. Effect of cyclone Nilofar on mesospheric wave dynamics as inferred from optical nightglow observations from Mount Abu, India. J. Geophys. Res.: Space Phys. 121, 5856–5867. https://doi.org/10.1002/2016JA022412.

Singh, R.P., Pallamraju, D., 2017. Large- and small-scale periodicities in the mesosphere as obtained from variations in O_2 and OH nightglow emissions. Ann. Geophys. 35, 227–237. https://doi.org/10.5194/angeo-35-227-2017.

Sridharan, R., Haider, S.A., Gurubaran, S., Sekar, R., Narayanan, R., 1992. OI 630.0-nm dayglow in the region of equatorial ionization anomaly: temporal variability and its causative mechanism. J. Geophys. Res.: Space Phys. 97 (A9), 13715–13721. https://doi.org/10.1029/92JA00674.

Sridharan, R., Sekar, R., Gurubaran, S., 1993. Two-dimensional high-resolution imaging of the equatorial plasma fountain. J. Atmos. Sol. Terr. Phys. 55, 1661–1665. https://doi.org/10.1016/0021-9169(93)90170-4.

Sridharan, R., Pallam Raju, D., Somayajulu, V.V., Taori, A., Chakrabarty, D., Raghavarao, R., 1999. Imprint of equatorial electrodynamical processes in the OI 630.0 nm dayglow. J. Atmos. Sol. Terr. Phys. 61, 1143–1155. https://doi.org/10.1016/S1364-6826(99)00064-4.

Woodman, R.F., 1970. Vertical drift velocities and east-west electric fields at the magnetic equator. J. Geophys. Res. 75 (31), 6249–6259. https://doi.org/10.1029/JA075i031p06249.